UNIVERSITÀ DEGLI STUDI DI NAPOLI "FEDERICO II"
DIPARTIMENTO DI INGEGNERIA INDUSTRIALE

DOTTORATO DI RICERCA IN INGEGNERIA AEROSPAZIALE,
NAVALE E DELLA QUALITÀ

XXVII CICLO

TESI DI DOTTORATO

Investigation of Synthetic Jets Heat Transfer and Flow Field

Carlo Salvatore Greco

Tutori:
Prof. Ing. Gennaro Cardone
Prof. Ing. Andrea Ianiro

Coordinatore:
Prof. Ing. Luigi de Luca

Marzo 2015

“La sapienza è figliola della sperienza.”

“Wisdom is daughter of experience.”

Leonardo da Vinci

Table of Contents

Abstract

The present thesis deals with the investigation of synthetic jets heat transfer and flow field behaviour. Synthetic jets are devices used mainly for flow control and heat transfer. Such devices are able to “synthetize” a jet from the ambient in which they are embedded through a simple membrane oscillation inside a cavity with an orifice. Such features make them high reliable, silent and easy to be miniaturized. For these reasons, they are widely investigated also as electronic cooling devices. State of art literature shows that the heat transfer performance of these devices are promising. Under these considerations, the present research is focused on the design and analysis of a different type of synthetic jet device with respect to its classical configuration. Such a device is experimentally characterized through the study of its free and impinging flow field. Furthermore the heat transfer rate has been evaluated. The novel configurations are compared to the performance of a classical synthetic jet device.

Nomenclature

a	Fluid acceleration (m/s^2)
b	Jet width (m)
Bi	Biot number
c	Air speed of sound (m/s)
C_1, C_2	First and second universal radiation constants (Wm^2 and Km)
c_p	Stainless steel specific heat (J/(Kg K))
D	Nozzle/Orifice exit diameter (m)
D^*	Sensitivity figure of merit of the infrared detector detectivity (cmHz$^{1/2}$/W)
d_p	Particle diameter (m)
D_p	Piston diameter (m)
dT_w/dt	Time derivative of wall temperature (K/s)
E^b	Total hemispherical emissive power (W/m^2)
f	Actuation frequency (Hz)
$f/\#$	Numerical aperture of the camera
f_2	Acquisition frequency (Hz)
f_H	Helmholtz resonance frequency (Hz)
Fo_f	Modified Fourier number
f_p	Phenomenon frequency (Hz)
g	Acceleration due to gravity (m/s^2)
h	Convective heat transfer coefficient (W/(m^2 K))
$\bar{h}$	Time-average convective heat transfer coefficient (W/(m^2 K))
H	Nozzle/orifice-to-plate distance (m) ($H=z$)
H/D	Dimensionless nozzle/orifice-to-plate distance
I	Energy flux per wavelength emitted by a real body in the hemisphere outside its surface (W/m^3)
I'	Total radiation detected by the camera (W/m^3)
I^b	Energy flux per wavelength emitted by a black body in the hemisphere outside its surface (W/m^3)
I^b_{amb}	Black body radiation intensity corresponding to the (effective) temperature of the object surroundings T_{amb} (W/m^3)

I^b_{atm}	Radiation intensity corresponding to a black body at the temperature of the atmosphere T_{atm} (W/m³)
I^b_{obj}	Radiation intensity corresponding to a black body at the object temperature (W/m³)
k	Air thermal conductivity (W/(m K))
k_{loss}	Head loss
l	Jet-axes-distance (m)
L	Nozzle length (m)
L'	Effective pipe length (m)
L_0	Stroke length (m)
$L_0^{(f)}$	Synthetic jet formation stroke length (m)
l_p	Half piston stroke (m)
n	Integer number of period of membrane oscillation
N	Number of flow field of the same phase
$NDiv$	Number of sampled phases
$\overline{Nu}$	Time-average Nusselt number
Nu'	Standard deviation Nusselt number phase-average
Nu_φ	Phase-average Nusselt number
p_c	Cavity pressure (Pa)
p_{amb}	Ambient pressure (Pa)
q'_k	Tangential conduction heat flux (W/m²)
$\overline{q'_k}$	Time-average tangential conduction heat flux (W/m²)
q	Normalized diameter
q'_j	Joule heat flux (W/m²)
q'_n	Natural convection heat flux (W/m²)
q'_r	Radiation heat flux (W/m²)
$\overline{q'_r}$	Time-average radiation heat flux (W/m²)
Q_c	Q-criterion value (1/s²)
r	Radial coordinate (m)
R, B, F	Calibration parameters
Re	Reynolds number
s	Foil thickness (m)
Sr	Strouhal number

t	Time (s)
T	Temperature (K)
T_{amb}	Ambient temperature (K)
T_{atm}	Atmosphere temperature (K)
T_{aw}	Adiabatic wall temperature (K)
$\overline{T_{aw}}$	Time-average adiabatic wall temperature (K)
T_{obj}	Object temperature (K)
T_w	Wall temperature (K)
$\overline{T_w}$	Time-average wall temperature (K)
$\overline{TKE}$	Time-average turbulent kinetic energy
<TKE>	Phase-average turbulent kinetic energy
u	Instantaneous radial velocity (along the *x* axis) (m/s)
<*u*>	Phase-average radial velocity (along the *x* axis) (m/s)
$\tilde{u}$	Instantaneous radial phase-correlated organized contribution to the velocity (along the *x* axis) (m/s)
$\overline{\tilde{u}^2}$	Mean-squared radial phase-correlated organized contribution to the velocity (along the *x* axis) (m^2/s^2)
$\overline{u'^2}$	Mean-squared radial turbulent velocity (along the *x* axis) (m^2/s^2)
<u'^2>	Phase-average mean-squared radial turbulent velocity (along the *x* axis) (m^2/s^2)
U	Time-average radial velocity (along the *x* axis) (m/s)
U_0	Reference/Characteristic velocity (m/s)
U_A	Velocity at the exit plane of the nozzle/orifice (m/s)
U_D	Detected signal
U_f	Fluid velocity (m/s)
U_g	Gravitationally induced velocity (m/s)
U_P	Particle velocity (m/s)
U_S	Velocity lag (m/s)
Vol	Sub-cavity volume (m^3)
w	Instantaneous axial velocity (along the *z* axis) (m/s)
<*w*>	Phase-average axial velocity (along the *z* axis) (m/s)
$\tilde{w}$	Instantaneous axial phase-correlated organized contribution to the velocity (along the *z* axis) (m/s)

$\overline{\tilde{w}^2}$ Mean-squared axial phase-correlated organized contribution to the velocity (along the *z* axis) (m^2/s^2)

$\overline{w'^2}$ Mean-squared axial turbulent velocity (along the *z* axis) (m^2/s^2)

$\langle w'^2 \rangle$ Phase-average mean-squared axial turbulent velocity (along the *z* axis) (m^2/s^2)

$\overline{\tilde{w}\tilde{u}}$ Time-average phase-correlated organized contribution to the velocity Reynolds stress (m^2/s^2)

$\overline{w'u'}$ Time-average turbulent Reynolds stress (m^2/s^2)

$\langle w'u' \rangle$ Phase-average turbulent Reynolds stress (m^2/s^2)

W Time-average axial velocity (along the *z* axis) (m/s)

W_c Time-average centreline axial velocity (along the *z* axis) (m/s)

x Abscissa axis(m)

y Ordinate axis(m)

z Axial axis (m)

Greek symbols

α Thermal diffusivity (m^2/s)

α_r Absorptivity coefficient

β Stefan-Boltzmann's constant ($W/m^2 K^4$)

ε Total hemispherical emissivity coefficient

φ Phase (°)

λ Radiation wavelength (m)

λ_f Foil thermal conductivity (W/(m K))

λ_l Light wavelength (m)

λ^* Wavelength at which the black body emits its maximum spectral emissive power (m)

μ Fluid dynamic viscosity (Kg/(m s))

ρ Fluid density (Kg/m^3)

ρ_p Tracer particle density (Kg/m^3)

ρ_r Reflectivity coefficient

ρ_{foil} Stainless steel density (Kg/m^3)

Σ Dimensionless jet-axes-distance

τ Actuation period (s)

τ_r	Transmissivity coefficient
τ_S	Relaxation time (s)

Acronym

FOV	Field of view
FPA	Focal plane array
HPIV	Holographic Particle Image Velocimetry
IFOV	Instantaneous field of view (mrad)
IR	Infrared
LSV	Laser Speckle Velocimetry
MCCD	Multigrid cross-correlation digital
MTF_{IR}	Modulation Transfer Function
MWIR	Middle wavelength infrared
NETD	Noise equivalent temperature difference (mK)
NIR	Near infrared
PIV	Particle Image Velocimetry
PTV	Particle Tracking Velocimetry
SSJ	Single synthetic jet
SWIR	Short wavelength infrared
TSJ	Twin synthetic jet

Introduction

The continuous technology improvement is causing a proliferation of electronic systems in our society. Nowadays human society is completely dependent on such electronic devices; hence, the reliability of these systems is mandatory. The failure of these systems can be caused by many factors such as high temperature, electrical overstress and material fatigue.

The system failure is mostly due to the thermal overstress caused by a continuous request of intense work. Although the majority of the electronic devices have a high efficiency, a continuous use can cause an increase in temperature which can affect the device performance until the failure. Electronic components are designed to operate within a certain temperature range thus need for a cooling system. Such a cooling system has to be designed to dissipate all the thermal power to maintain a suitable temperature and guarantee electronic component safety without affecting working performance.

According to Moore's law (1965), the number of transistors on an integrated circuit doubles every one and a half year and the transistor density is expected to be very high. Moreover, the size of these transistors decreases exponentially as silicon microfabrication processes are improved. These two components lead to an increase in the heat power which has to be carried away by cooling devices in order to let the electronic systems work properly within a suitable temperature range.

Conventional cooling techniques such as heat sink, fans and liquid cooling need to be continuously optimized to face this continuous request of higher heat power dissipation and miniaturization.

Such needs have led researchers to focus their efforts on the design of new technology cooling devices.

Synthetic jets are an innovative device with promising features in the heat dissipation field. According to Lasance and Aarts. (2008), the benefits and improvements of synthetic jets, compared with a fan, are:

- Lower noise level,
- Better efficiency,
- Design-friendly,
- Intrinsic higher reliability,

- Easier miniaturisation,
- Simple noise cancellation.

Synthetic jets are jets with zero-net-mass-flux synthesized directly from the fluid present in the system in which the jet device is embedded (Smith and Glezer, 1998). Such a feature obviates the need for an external input piping, making them ideal for low cost and low space applications. A synthetic jet is generated by a membrane oscillation in a cavity which produces a periodic volume change and thus pressure variation. As the membrane oscillates, fluid is periodically entrained into and expelled out from the orifice. During the injection part of the cycle the flow field could be considered as one inducted by a sink, which coincides with the orifice, while during the ejection part of the cycle, a vortex ring can form near the orifice and, under certain operating conditions (Holman et al., 2005), convects away from the orifice to form a time-average jet (Smith and Glezer, 1998). Several studies have been carried out to characterize and describe the heat transfer behaviour of a classical synthetic jet (Gutmark et al., 1982, Mahalingam and Glezer 2005, Valiorgue et al., 2008, Chaudhari et al., 2010a, Persoons et al., 2011, Arik and Icoz ,2012, Greco et al. 2014). In order to improve the heat transfer performances of synthetic jets in practical applications, some recent studies are focused on the design of different configurations. For instance, Rylatt and O'Donovan (2013) decided to confine the impinging synthetic air jet asserting that, with such a configuration, cold air was drawn from a remote location into the jet flow. Chaudhari et al. (2011) realized a particular synthetic jet device by means of a centre orifice surrounded by multiple satellite orifices. Laxmikant and Chaudhari (2015) designed also synthetic jets with diamond and oval shape orifice. Luo et al. (2006) proposed a new generation of synthetic jet consisting in two cavities sharing the same piezoelectric actuator. Lasance ans Aarts (2008) and Lasance et al. (2008) replaced the two slots with two orifices and the piezoelectric with a loudspeaker creating the so-called "dipole cooler". This double configuration was found to be advantageous because of noise reduction (Russell et al., 1999) and improvement of heat transfer performances (Lasance et al., 2008) without a characterization of its flow field behaviour.

The object of this research is:

- to design a similar experimental apparatus with variable jet-axes-distance;
- to deeply investigate and characterize the jets free and impinging flow field;
- to evaluate and explain the jets heat transfer performance;
- to compare the results with the classical single synthetic jet (under the same operating conditions).

Moreover, as also reported in Persoons et al. (2011): "*Although information is available for free synthetic jets insufficient knowledge is available for impinging synthetic jets, which could be the focus of future research.*", thus a study on the classical single synthetic jet impinging flow field behaviour, varying the operating parameters, has also been carried out.

The thesis has been divided as following: Chapter 1 reviews current literature, Chapter 2 describes the measurements techniques employed in present investigation, in Chapter 3 the experimental rigs are shown, Chapters 4 and 5 discuss the results, for the free and impinging configurations, Chapter 6 draws final conclusions and Chapter 7 opens the path for future works.

Chapter 1

Literature Review

1.1 Historical Background and Flow Field

The generation of synthetic jets is based on the phenomenon that an oscillating boundary or transmission of sound can induce a fluid stream.

The first to develop a theory on this topic has been Lord Rayleigh (1883) who stated: "*Experimenters in acoustics have discovered more than one set of phenomena, apparently depending for their explanation upon the existence of regular currents of air resulting from vibratory motion. . . .such currents, involving as they do circulation of the fluid, could not arise in the absence of friction. . . . And even when we are prepared to include the influence of friction, we have no chance of reaching an explanation if, as usual, we limit ourselves to the supposition of infinitely small motion and neglect the squares and higher powers. . . .*".

Lord Rayleigh (1896) performed the following experiment: *". . . . when the corresponding fork, strongly excited, was held to the mouth of the Helmholtz resonator a wind of considerable force issued from the nipple at the opposite side. This effect may rise to such intensity as to blow out a candle upon whose wick the stream is directed. . . . Closer examination revealed the fact that at the sides of the nipple the outward flowing stream was replaced by one in the opposite direction, so that a tongue of flame from a suitable placed candle appeared to enter the nipple at the same time that another candle situated immediately in front was blown away.*".

Subsequently Eckart (1948) developed a systematic account of the theory of second-order acoustic effects. This mathematical theory was useful to obtain a calculation of the steady flow produced by a sound beam of circular cross section.

Based on the theory of streaming caused by sound waves showed in Eckart (1948), a synthetic jet flow was first observed by Ingard and Labate (1950). They studied the acoustical streaming phenomena around the orifice by the use of smoke particles. Their study employed diameters ranging from 3.5 mm to 20 mm and velocities ranging from 0 m/s to 7 m/s. Acoustic waves were used to form the sinusoidal motion that was characterized through stroboscopic illumination.

Medinkov and Novitskii (1975) used an acoustically driven conical tube to produce an air jet. Using a low frequency oscillating plane (10-100 Hz), the observed average streaming velocities was up to 17 m/s.

Subsequently Lighthill (1978) investigated how turbulent jets could be generated by a sound and suggested two methods for generating fluid streams. The first is based on the transmission of pressure waves through a compressible medium while the second is related to viscous effects at a boundary.

Lebedeva (1980) obtained a jet formation with a velocity up to 10 m/s by using a high amplitude sound wave (with a frequency ranging from 500 to 1600 Hz) passing through an orifice of 0.75cm diameter located at the end of tube.

Coe et al. (1994) and then Allen and Glezer (1995) proposed for the first time an innovative device called synthetic jet actuator (whose classical sketch is depicted in Fig. 1.1).

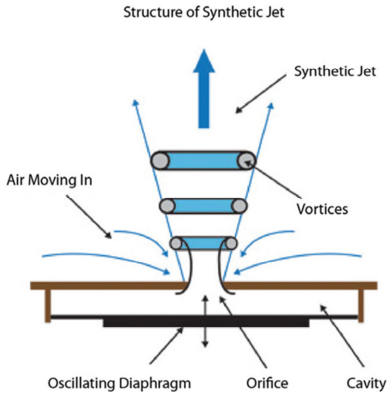

Fig. 1.1 Sketch of a classical synthetic jet device (from http://www.designworldonline.com/lighting-the-way-for-led-development/)

The dimensionless parameters that have been identified to govern the synthetic jets phenomenon are the Reynolds number and the Strouhal number defined as:

$$Re = \frac{\rho U_0 D}{\mu} \tag{1.1}$$

$$St = \frac{fD}{U_0} = \frac{D}{L_0} \tag{1.2}$$

where ρ is fluid density, μ is fluid dynamic viscosity, U_0 is a characteristic velocity, D is the nozzle/orifice exit diameter, f is the actuation frequency and L_0 is the stroke length (defined as U_0/f) that is associated to the quantity of fluid pulled in the ambient during the expulsion cycle.

Several definitions of the characteristic velocity U_0 exist in literature (Kral et al., 1997; Mallinson et al., 1999, Smith and Glezer, 1998 and Cater and Soria, 2002). Kral et al. (1997) chose as characteristic velocity the maximum value obtained during the expulsion phase on the exit orifice while Mallinson et al. (1999) selected a time-average velocity at some distance from the orifice exit. The most used definition for the characteristic velocity in literature are owed to Smith and Glezer (1998) and Cater and Soria (2002).

Such a characteristic velocity was defined by Smith and Glezer (1998) as the mean velocity over the ejection half of the cycle:

$$U_0 = \frac{1}{\tau}\int_0^{\tau/2} U_A(t)\, dt \tag{1.3}$$

where τ is the actuation period and U_A is the velocity at the exit plane of the orifice. Differently Cater and Soria (2002) defined their characteristic velocity as the mean squared integral of the velocity profile over an oscillation period (momentum flow velocity):

$$U_0 = \sqrt{\frac{4}{\pi D^4 \tau}\int_0^{\tau}\int_0^{D/2} 2rw(r,t)w(r,t)\, dr\, dt} \tag{1.4}$$

where w is the axial velocity at the exit plane of the orifice/nozzle and r is the radial coordinate.

Several studies have been carried out during last decades aiming at the characterization of the synthetic jets flow field. Such a characterization was based on a comparison between the synthetic jet flow field and the continuous jet one.

James et al. (1996) experimentally investigated a round turbulent submerged water jet produced by a resonantly driven diaphragm mounted flush with a wall. The synthetic jet was generated only for high amplitudes of oscillation which caused cavitation bubbles formation at the diaphragm surface. Hence the jet formation was due to the motion caused

by the periodic formation and collapse of bubbles. The jet shows a spreading which is less than that of conventional jets at a similar source Reynolds number. A similar result was found also by Smith and Glezer (1998). They studied the main properties of slot (2-D) synthetic jets comparing them to conventional 2-D jets. They found that the increase of the width of synthetic jets and the volume flow rate are lower than those of continuous jets. Furthermore they obtained that the streamwise decrease of the jet centreline velocity, for synthetic jets, is lower than that of the continuous jets. Differently from those, Cater and Soria (2002) investigated experimentally a round synthetic jet observing that it had a cross-stream velocity distribution similar to that of a conventional continuous jet but with a larger spreading rate. They also characterized the near field of a synthetic jet as function of the Strouhal number and the Reynolds number defining four different flow field behaviours: laminar jets, laminar rings, transitional jets and turbulent jets.

Glezer and Amitay (2002) presented a review on most of the studies carried out on synthetic jets. They described the synthetic jet formation and characterized the synthetic jets flow field (composed by the near and far field). They found that the near field "*depends critically on the details of the formation and advection of the discrete vortices in the presence of the time-periodic reversed flow*". They characterized the vortex behaviour determining the trajectory and celerity. They also observed, in the near field, that:" *The time-periodic reversal in flow direction along the jet centreline during the blowing and suction strokes leads to the time-periodic appearance of a stagnation (saddle) point on the centreline (between the recent vortex and the jet exit plane) that moves along the centreline during the suction stroke*." In the far field they highlighted the difference between synthetic and continuous jets, stating that : "*although cross-stream distributions of the time-averaged streamwise and cross-stream velocity components and the corresponding rms velocity fluctuations appear to collapse in the usual similarity coordinates, the streamwise scaling of other variables (e.g., the centreline velocity, jet width, volume flow rate, etc.) do not match corresponding scaling for conventional jets*.". The comparison between the synthetic and continuous jets was also presented by Smith and Swift (2003). They compare synthetic jets to continuous jets at the same Reynolds number showing that, in the far field, they have the same velocity shape, as occurs in Glezer and Amitay (2002). Moreover they observed that, in the near field, synthetic jets are dominated by vortex pairs that entrained more fluid than continuous ones generating a more rapidly growth both in terms of jet width and volume flux. These latter findings are different from those

obtained by Smith and Glezer (1998) because of the different operating condition (Reynolds number and Strouhal number). Shuster and Smith (2007) demonstrated that the round synthetic jet is uniquely identified by the dimensionless stroke length L_0/D and showed that for a distance from the nozzle lower than L_0 the flow is dominated by the vortex ring formed at the nozzle exit while only after one stroke length there is a transition to a nominally steady turbulent jet. They also found that for values of the stroke length higher than 1 the Reynolds number (ranging between 1000 and 10000) does not affect the streamwise variation of the mean jet centreline velocity and the jet width. They also stated that the vortex ring behaviour depends only on the stroke length showing that its streamwise convection is a linear function of such a parameter. The effect of varying stroke length on the flow morphology of free synthetic jets was studied by McGuinn et al. (2013) with high speed PIV and hot wire anemometry. According to Gharib et al. (1998), the power of a vortex ring is enhanced with stroke length increasing up to L_0/D = 4; for higher L_0/D a trailing jet is formed which adversely affects the stability of the primary vortex. Analogously, synthetic jets without impingement (McGuinn et al., 2013) are characterized by a monotonous increase in vortex strength up to L_0/D =4. For L_0/D higher than 4 and up to 8 the flow field is characterized by additional fluid ejected after the formation of the vortex ring and forming a trailing jet following and widening the vortex ring. A maximum ejection velocity occurs in the trailing jet and destabilizes the vortex ring promoting mixing for L_0/D between 8 and 16. For higher L_0/D the most relevant flow feature is represented by the trailing jet: the ejected fluid remaining once the primary vortex was fully formed and propagated, overtook the vortex ring resulting in a highly turbulent intermittent jet flow.

1.2 Heat Transfer and Impinging Flow Field

The characterization of synthetic jets flow field has been used by researchers to understand the behaviour of these devices. Such studies have led to several fields of applications for synthetic jets as: flow control, heat transfer, enhancement of mixing between fluid currents and generation of microthrust for propulsion.

Focusing the attention on the heat transfer field many works in literature have showed promising performances of synthetic jets used as cooling devices in an impinging configuration. Indeed the high heat transfer rate obtainable with impinging continuous jets is widely recognized and explained in scientific literature (Jambunathan et al., 1992

and Martin, 1997). The use of impinging continuous jets is very popular in many industrial applications such as paper drying, glass tempering and turbine blades cooling. For these reasons the most intuitive application of synthetic jets in the heat transfer field is the impinging configuration.

The first literature work on synthetic jets used as cooling devices was presented by Gutmark et al. (1982) that showed heat transfer data on synthetic jet used to enhance both natural and forced convection. The results revealed that the acoustically excited airflow can increase the overall heat-transfer coefficient by a factor of four. Later Mahalingam and Glezer (2005) studied the design and thermal performance of a heat sink for high power dissipation in electronics enhanced with synthetic jet impingement. The results revealed a case temperature decrease from 71.5 to 36°C with synthetic jets operation and a power dissipation of 20-40% higher with respect to the same heat sink with a fan in the flow rate range of 3-5 cubic feet per minute. Valiorgue et al. (2009) studied synthetic jets impinging at nozzle-to-plate distance equal to 2 D and for various stroke lengths. The heat transfer rate (that obviously increases with increasing Reynolds number) was found to increase linearly with L_0/H increasing up to L_0/H = 2.5, then being constant for further increasing L_0/H values. This effect was ascribed to the formation of a time-average recirculating vortex located at $r/D \simeq 2$ for L_0/H = 2.5. The promising performances of synthetic jets were later confirmed by the studies of Chaudhari et al. (2010a). They carried out experiments on the cooling of a flat plate by using a synthetic jet generated through a circular orifice. Such experiments for Reynolds number in the range 1500-4200 and nozzle-to-plate distance in the range 0-25 D showed that the heat transfer rate is comparable with that of continuous axisymmetric jets at low Reynolds number (up to 4000), expecting it to be higher at greater values of Reynolds number. Furthermore Chaudhari et al. (2010b) investigated also the effect of the orifice on the heat transfer behaviour of an impinging synthetic jet. Several kind of orifices were considered: square, circular and rectangular (of different ratio raging between 1 and 20). Experiments were undertaken at a Reynolds number ranging between 950 and 4000 while the nozzle-to-plate distance varied between 1 and 25. They found that for nozzle-to-plate distance higher than 5 diameters the square orifice enhances the heat transfer while, for smaller distances, the rectangular orifice with a ratio of 3 and 5 shows the best performance.

As for steady jets, heat transfer correlations have been developed also for synthetic jets (Arik and Icoz, 2012 and Persoons et al., 2011). Arik and Icoz (2012) established a

closed form empirical correlation to predict the heat transfer coefficient as a function of Reynolds number, axial distance, orifice size and jet driving frequency. They observed that the heat transfer coefficient on a vertical surface increases with the driving voltage; it has a peak at the resonance frequency and the effect of the axial distance on the heat transfer becomes stronger as the jet driving frequency increases. The empirical correlation proposed by Arik and Icoz (2012) is valid for $Re < 2900$, $5 < H/D < 20$ and actuation frequency between 0.16 times the resonance frequency and the resonance frequency itself. Persoons et al. (2011) compared the stagnation point heat transfer performance of an axisymmetric synthetic jet versus established steady jet correlations. Such a research led to a general correlation for the stagnation point Nusselt number including the effect of all appropriate scaling parameters: Reynolds number ($500 < Re < 1500$), orifice-to-plate distance ($2 < H/D < 16$) and stroke length ($2 < L_0/D < 40$). Based on such a correlation, Persoons et al. (2011) defined four heat transfer regimes, each one identified by a different range of values acquired by the ratio $(L_0-L_0^{(f)})/H$ (where $L_0^{(f)}$ is the synthetic jet formation stroke length, i.e., practically the escape length of the vortex ring in order to not be swallowed again in the orifice during the suction phase). McGuinn et al. (2013) also studied the impinging flow field of synthetic jets with high speed PIV and hot wire anemometry. They also accounted for the presence of the plate with the non-dimensional parameter $(L_0-L_0^{(f)})/H$, as previously done by Persoons et al. (2011). In the study by McGuinn et al. (2013) $L_0^{(f)}$ was constant and equal to 2 D, H/D varied between 2 and 16, L_0/D between 3 and 32 and Reynolds number was equal to 1500. The first regime is for $(L_0-L_0^{(f)})/H<0.5$, which corresponds to a stroke length slightly higher than the formation one; as a consequence the momentum of the jet reaching the surface is very weak. Accordingly, the heat transfer increases with increasing $(L_0-L_0^{(f)})/H$ up to $(L_0-L_0^{(f)})/H = 1$. Further increase of the stroke length is seen to promote radial spreading of the jet causing reduction in time-average velocity approaching the impingement region point for $1 < (L_0-L_0^{(f)})/H \leq 2$ while for $(L_0-L_0^{(f)})/H >2$ the flow field was dominated by the trailing jet. Also few numerical studies have been undertaken in order to correlate the heat transfer and the impinging flow field of synthetic jets. Silva and Ortega (2013) numerically studied the relationship between the flow field and the heat transfer of a purely oscillatory jet (that is not influenced by exit geometry). They solved the problem by using a fully unsteady, two dimensional finite volume approach to determine the complex time dependent flow field varying several parameters: driving frequency (400-1200 Hz), Reynolds number (203-

508) and orifice-to-plate distance (5-20 *D*). They found that the merging of vortices led to a lower heat transfer and that, by using the point to point correlations, the instantaneous local Nusselt number was strongly correlated to the axial impinging velocity. Furthermore Tehrani et al. (2011) analysed the nozzle-to-plate distance (ranging between 2-8) and frequency (equal to 16, 80 and 400 Hz) influence on the heat transfer and flow field of an impinging synthetic jet at Reynolds number equal to 3386 with a turbulence intensity set as 10%. They found that a recirculation zone is generated at *H/D* equal to 2 and 4 which causes a decrease in the heat transfer performance. Such a region disappears for higher nozzle-to-plate distances leading to an increase of the heat transfer. This recirculation region reduces the effective heat transfer because stops the counter current flow field which helps to remove the heated air and supplying fresh incoming air. They also noticed that the heat transfer rate is enhanced as the frequency increases. This is ascribed to the recirculation region which causes a strong reversed flow generating flow separation and, consequently, poor heat transfer. Such a recirculation region decreases as the frequency increases promoting a higher heat transfer rate. Indeed, for high frequencies, such an improvement provides an heat transfer rate greater than a steady jet whose velocity is the same of the maximum expulsion velocity of the synthetic jet (during its ejection phase). Moreover they stated that the vortex motion influences the heat transfer: an increase in the local heat transfer is obtained while the vortex ring is sweeping the impinging wall. Such an enhancement decreases as the vortex ring moves farther from the stagnation point.

These studies tried to understand how the operating parameters (i.e. Reynolds number, Strouhal number, nozzle-to-plate distance etc.) of an impinging synthetic jets influence the heat transfer in order to enhance it. The same scope (i.e. heat transfer enhancement) has been seek by other authors who focused on the design of devices different from the classical single configuration of synthetic jets. Several innovative configurations were based on the generation of two synthetic jets by using a unique device. Luo et al. (2006) proposed a new generation of synthetic jet actuators consisting in two cavities sharing the same wall equipped with a single piezoelectric diaphragm and a slide block separating the two exit slots at an appropriate distance. Their numerical simulation resulted in a device which not only doubles the function of the existing synthetic jet with a single diaphragm but also resolves the problems of pressure loading and energy inefficiency of the existing synthetic jet. Subsequently Luo et al. (2011) carried

out PIV measurements of such a dual synthetic jets actuator at Reynolds number and Strouhal number equal to 2500 and 0.17, respectively. In the near field, they found a more complex flow field characterized by a "*self-support*" phenomenon between the two synthetic jets while in the far field the two jets merged in a single and more stable synthetic jet. Differently from Luo et al. (2006 and 2011), Persoons et al. (2009) studied two adjacent synthetic jets, with slot orifice, which allowed directing the flow by changing the phase between the jets. Both PIV and IR thermography heat transfer measurements were carried out, at a fixed Reynolds number, equal to 600, and dimensionless stroke length L_0/D =29 in order to quantify the local convective heat transfer and flow field for different values of phase and jet-to-surface spacing H/D (6, 12 and 24). This work reported a 90% enhancement of the maximum and the overall cooling rate, compared to a single jet, for a phase equal to 120° and a jet-to-surface spacing H/D equal to 12. Lasance and Aarts (2008) replaced the classical circular single jet configuration with a double circular configuration. The double configuration was found to be advantageous because of noise reduction (Russell et al., 1999) and improvement of heat transfer performances (Lasance et al., 2008).

Other devices were based on the innovative idea of changing the orifice shape or exit configuration. Chaudhari et al. (2011) realized a particular synthetic jet device by means of a centre orifice surrounded by multiple satellite orifices. All the experiments were carried out varying both the Reynolds number ($1000 < Re < 2600$) and the normalized axial distance ($1 < H/D < 30$). Such an innovative configuration shows a maximum heat transfer coefficient which is approximately 30% more than the one of the conventional single orifice jet. A different configuration was employed by Rylatt et al. (2013) who decided to confine the impinging synthetic air jet asserting that, with such a configuration, cold air was drawn from a remote location into the jet flow. The experiments showed that the ducted configuration, achieves an heat transfer enhancement of up to 36% in the stagnation region. Bhapkar et al. (2014) studied the acoustical aspects and average heat transfer characteristics of an elliptic impinging synthetic jet comparing it with circular, rectangular and square orifice. Acoustically the synthetic jet shows the same behaviour independently from the orifice shape. The elliptical case shows its maximum heat transfer rate for an orifice-to-plate distance equal to 3 diameters. For an orifice-to-plate distance lower than 6 the elliptical orifice performs better than other shapes while, at higher orifice-to-plate distance, circular and square orifices still outperform. They explained that

such a behaviour is mainly due to the high spreading rates. The last configuration found in literature is the new synthetic jet featured with a diamond and oval shape orifice studied by Laxmikant and Chaudhari (2015). They studied the heat transfer and acoustic behaviour of these two different shapes comparing to the circular case. They found an average heat transfer enhancement of 17% and 7%, for diamond and oval orifices respectively and a decrease of 7 dB of the sound pressure level for both cases.

The knowledge about impinging synthetic jets flow field is insufficient (as also reported by Persoons et al., 2011) differently from continuous jets. Indeed, as previously reported, very few experimental (McGuinn et al., 2013) and numerical (Silva and Ortega, 2013 and Therani et al., 2011) works deal with the characterization of the impinging flow field of synthetic jets. Some studies have found similar aspects between synthetic and continuous jets. For this reason a brief review on the behaviour of impinging continuous jets is reported in the following.

The flow field of an impinging continuous jet is sketched in Fig 1.2. The jet emerges from a nozzle or an opening with a velocity and temperature profile and with turbulence characteristics dependent on the upstream flow and on nozzle shape (Schetz and Fuhs, 1999). For a pipe-shaped nozzle the flow develops into the parabolic velocity profile common to pipe flow plus a moderate amount of turbulence developed upstream. In contrast, a flow delivered by the application of differential pressure across a thin, flat orifice will create an initial flow with a fairly flat velocity profile, less turbulence, and a downstream flow contraction (vena contracta). Typical jet nozzle designs use either a round jet with an axis-symmetric flow profile or a slot jet, a long, thin jet with a two-dimensional flow profile.

After it exits the nozzle, the emerging jet may pass through a region where it is sufficiently far from the impingement surface to behave as a free submerged jet. In the free jet region, the velocity gradients lead to a shear-driven interaction of the exiting jet with the ambient that produces entrainment of mass, momentum, and energy. The net effects include the development of a non-uniform radial velocity profile within the jet, the expansion of the jet, an increase of total mass flow rate, and the modification of the jet temperature. In the process, the jet loses energy and the velocity profile is widened in spatial extent and decreased in magnitude along the sides of the jet.

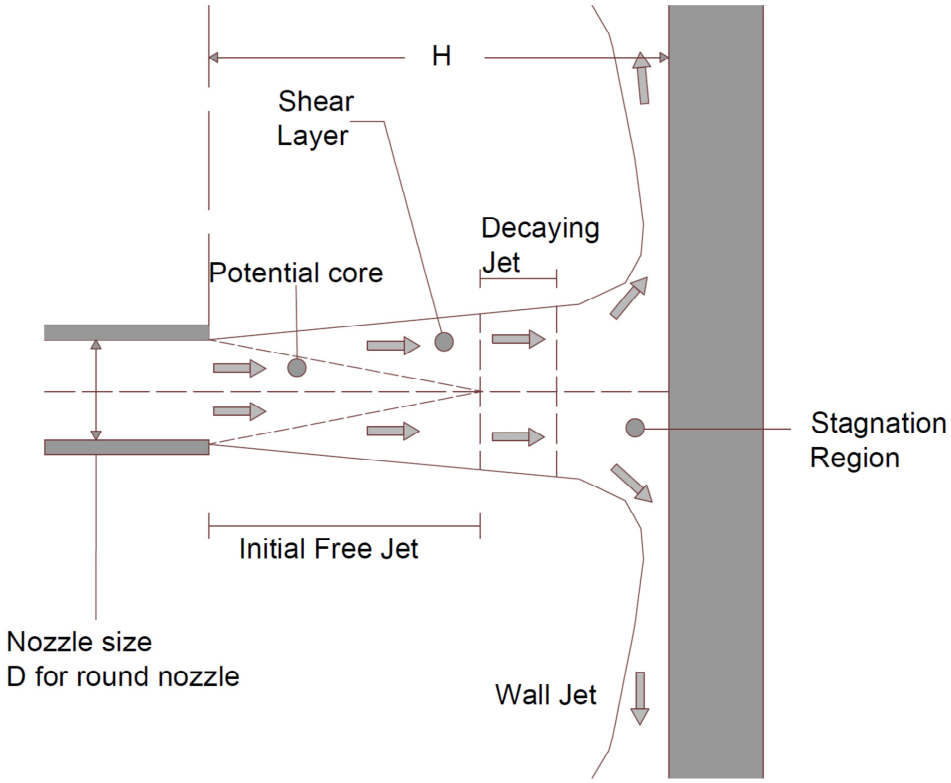

Fig. 1.2 The flow regions of an impinging continuous jet

The flow interior to the progressively widening shear layer remains unaffected by this momentum transfer and forms a core region (called potential core) with a higher total pressure, though it may experience a drop in velocity and a pressure decay resulting from velocity gradients present at the nozzle exit. Despite of that, it has to be remarked that a free jet region may not exist if the nozzle lies within a distance of two diameters (2D) from the target. In such cases, the nozzle is close enough to the elevated static pressure in the stagnation region for this pressure to influence the flow immediately at the nozzle exit. According to Viskanta (1993),at small separation distances, the velocity profile of the jet does not have sufficient room to develop and the arrival velocity is essentially uniform. Thus, impingement occurs within the potential core of the jet and the pressure distribution well agrees with the inviscid solution.

If the shear layer expands toward the centre of the jet before reaching the target, a region of core decay forms. The length of the potential core is dependent on the turbulence intensity in the nozzle exit and the initial velocity profile. Livingood and Hrycak (1973) show that the potential core zone extends 6-7 diameters from the nozzle

exit for axis-symmetric jets and 4.7-7.7 slot widths for slot jets. This decaying jet begins four to eight nozzle diameters or slot-widths downstream of the nozzle exit. In the decaying jet, the axial velocity component decreases and according to Reichardt (1943), a Gaussian velocity distribution best fit experimental measurements in this zone. Other investigations show that in the fully developed zone the jet broadens linearly and that the decay of the axial velocity is also linear. Martin (1977) provides a collection of equations for predicting the velocity in the free jet and decaying jet region.

As the flow approaches the wall, it loses axial velocity and turns in a region called stagnation region. The flow builds up a higher static pressure on and above the wall, transmitting the effect of the wall upstream. The non-uniform turning flow experiences high normal and shear stresses in the deceleration region, which greatly influence local transport properties. After turning, the flow enters a wall jet region where the flow moves laterally outward parallel to the wall. So the wall parallel velocity component, initially increasing from zero must reach a maximum at a given distance from the stagnation point. Due to the presence of a shear layer influenced by both the velocity gradient with respect to the stationary fluid at the wall (no-slip condition) and the velocity gradient with respect to the fluid outside the wall jet, the boundary layer thickness for the wall jet is defined as the height at which wall-parallel flow speed in the wall jet is maximum at a given radial position. The boundary layer within the wall jet begins in the stagnation region, where it has a typical thickness of no more than 1% of the jet diameter. As the wall jet progresses, it entrains flow and grows in thickness, and its average flow speed decreases as the location of highest flow speed shifts progressively farther from the wall; thus the maximum speed in the wall jet finally tends to zero in the fully developed wall jet proportionally with the distance from the centre of impingement r^{-1} for the axis-symmetric jet. Whereas the stabilizing effect of the acceleration keeps the boundary layer laminar in the stagnation zone, transition to turbulence generally occurs in the decelerating flow region immediately after the coordinate at which the flow reaches the maximum velocity. The turbulent kinetic energy, gives a measure of the intensity of the turbulent flow field. The downstream flow and heat transfer characteristics are sensitive to both the steady time-average nozzle velocity profile and fluctuations in the velocity over time. Knowledge of these turbulent fluctuations and the ability to model them, including associated length scales, are vital for understanding and comparing the behaviour and performance of impinging jets. In the initial jet region the primary source

of turbulence is the shear flow on the edges of the jet. This shear layer may start as thin as a knife-edge on a sharp nozzle, but naturally grows in area along the axis of the jet. The shear layer generates flow instability, similar to the Kelvin–Helmholtz instability.

If Reynolds number is high enough (e.g. $Re > 1000$), the destabilizing effects of shear forces may overcome the stabilizing effect of fluid viscosity/momentum diffusion. The position of the shear layer and its velocity profile may develop oscillations in space, seemingly wandering from side to side over time. Downstream the magnitude and the spatial extent of the oscillations grow to form large-scale vortices along the sides of the jet.

The largest eddies have a length scale of the same order of magnitude as the jet diameter and persist until they either independently break up into smaller eddies or meet and interact with other downstream flow features (vortex pairing). The pressure field of the stagnation region further stretches and distorts the eddies, displacing them laterally until they arrive at the wall (Violato et al., 2011). Clearly, as shown already in the seventies by Hoogendorn (1977), the development of turbulence in the free jet is critical in influencing the arrival conditions of the flow on the plate. In the decaying jet region the shear layer extends throughout the centre of the jet and this shearing promotes flow turbulence, but on smaller scales. The flow in the decaying jet may form small eddies and turbulent pockets within the centre of the jet, eventually developing into a unstructured turbulent flow field with little or no coherent structures in the entire jet core. In the deceleration region, additional mechanisms take part in influencing flow field turbulence. The pressure gradients within the flow field cause the flow to turn, influencing the shear layer and turning and stretching large-scale structures thus increasing the turbulence; also the deceleration of the flow creates normal strains and stresses, which promote turbulence. Large-scale turbulent flow structures in the free jet have a great effect upon transfer in the stagnation and the wall jet region. The vortices formed in the free jet-shear layer may penetrate into the boundary layer and exchange fluids of differing kinetic energy and temperature (or concentration). This vortex dynamically scrubs away the boundary layer, as it travels against and along the wall. The turbulent flow field along the wall may also cause formation of additional vortices categorized as secondary vortices. Turbulent fluctuations in lateral/radial velocity and associated pressure gradient fluctuations can produce local flow reversals along the wall, initiating separation and the formation of the secondary vortices as shown in Fig. 1.3 (Hadziabdic and Hanjalic, 2002) and Fig. 1.4 (Rohlfs et al., 2012).

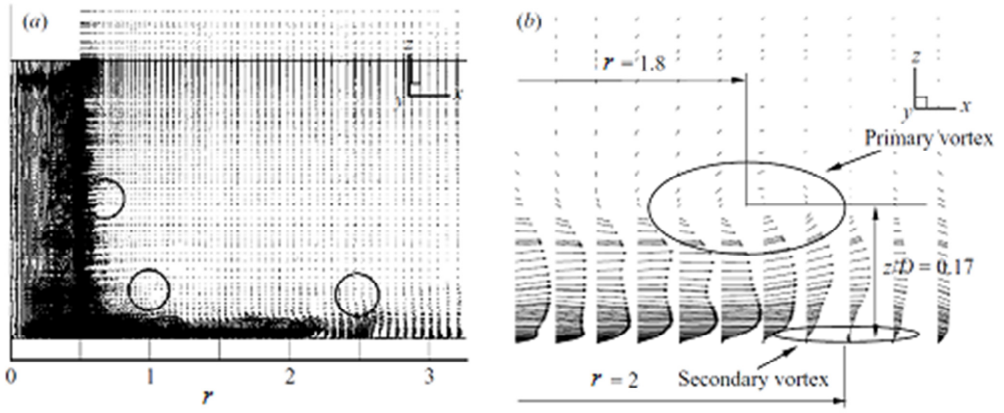

Fig. 1.3 Instantaneous velocity-vector field: (a) a full view with three vortical cores(encircled); (b) an enlargement in the wall-jet region around r/D=2 (from Hadziabdic and Hanjalic 2008)

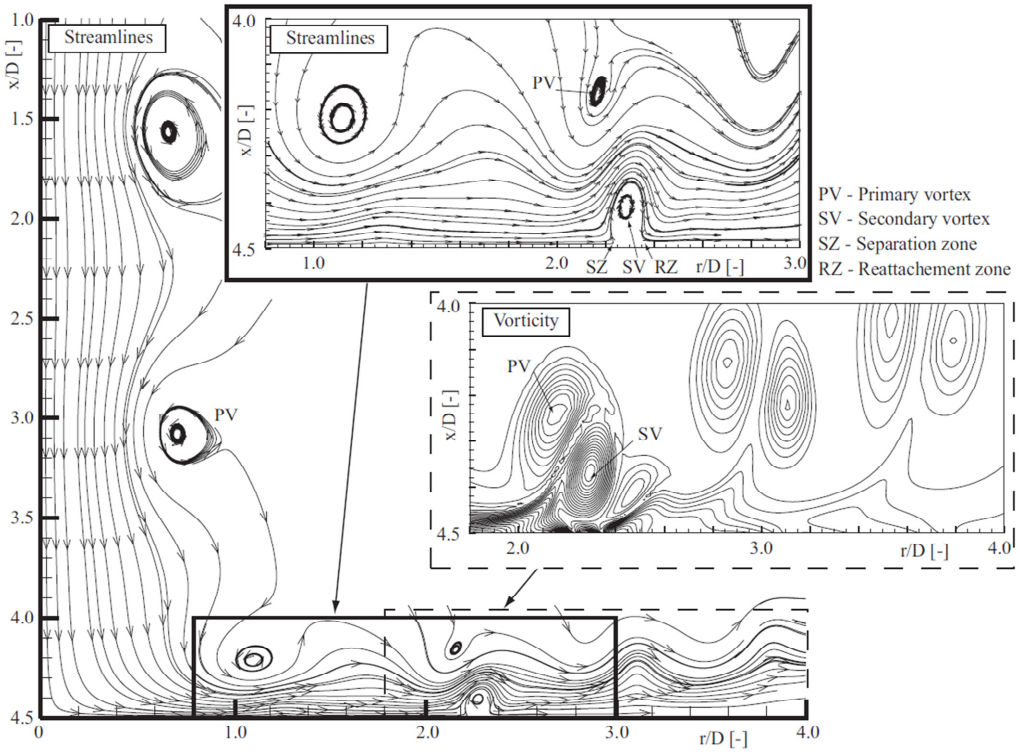

Fig. 1.4 Instantaneous velocity field of the disturbed flow (from Rholfs et al., 2012)

Chapter 2

Measurement Techniques

2.1 InfraRed Thermography

Measuring heat fluxes in thermo-fluid-dynamics requires both a thermal sensor (with its related thermo-physical model) and temperature transducers. Where temperature is measured with sensors such as thermocouples, resistance temperature detectors (RTDs) etc., each transducer yields either the heat flux at a single point, or the space-averaged one; hence, in terms of spatial resolution, the sensor itself has to be considered as zero-dimensional. This limitation makes measurements particularly troublesome whenever the temperature, and/or heat flux, fields exhibit high spatial variations. Instead, the infrared (IR) camera constitutes a truly two-dimensional transducer, allowing for accurate measurements of surface temperature maps even in the presence of relatively high spatial gradients. Accordingly, the heat flux sensor also becomes two-dimensional, as long as the necessary corrections are applied.

When compared to standard techniques, the use of the infrared camera as a temperature transducer in convective heat transfer measurements appears advantageous from several points of view. In fact, since IR camera is fully two-dimensional (up to 1 Mpixels), besides producing a whole temperature field, it permits an easier evaluation of errors due to radiation and tangential conduction; furthermore, it is non-intrusive (e.g., allowing conduction removal through thermocouple or RTD wires), it has high sensitivity (down to 20 mK) and low response time (down to 20 μs). As such, IR thermography can be effectively employed to measure convective heat fluxes with both steady and transient techniques.

The first IR cameras were developed in the 1960s as offshoots of military programmes but without accuracy features, not mandatory for the existing needs. The 1970s energy crisis brought government support in Sweden and so the first radiometric thermal imagers were developed by AGA and Bofors, both Swedish companies. These cameras used a single detector, the image two-dimensionality being achieved by rotating, or oscillating, mirrors and/or refractive elements (such as prisms) which scanned the

field of view (FOV) in both vertical and horizontal directions; in fact, they were also called infrared scanning radiometers.

The detector of these radiometers was the photon one, where the release of electrons is directly associated with photon absorption, its main features being a quite short response time and limited spectral response. Such detector requires cooling, well below ambient temperature to allow for rapid scanning, high sensitivity and low noise. In fact, the sensor was often located in the wall of a Dewar vessel filled with liquid nitrogen (77 K). Subsequent scanning radiometers used various types of cooled photon detectors with lower time constants allowing frame rates of 15- 30 Hz. All real time commercial cameras used cooled photon single detectors with optomechanical scanning well into the 1980s, when (staring) infrared Focal Plane Array (FPA) detectors, having quite adequate time constants to achieve 30-60 Hz frame rates, were introduced. By using these staring arrays, the infrared camera, long restricted to a point sensing instrument, became an effective two dimensional transducer. IR cameras based on non-cooled FPA thermal detectors (such as microbolometers) emerged in the mid 1990s and led to the development and diffusion of thermal imagers requiring no cooling.

The earliest attempts to measure heat transfer coefficients arose in the hypersonic regime and were performed by using scanners operating in the middle IR band (3÷6 μm) of the infrared spectrum, at the time called short wave IR band. In particular, the AGA Thermovision 680SWB camera was employed by Thomann and Frisk (1968) to measure the heat flux distribution on the surface of an elastomeric paraboloid in a hypersonic wind tunnel at Mach number equal to 7. The thin-film sensor was used to determine convective heat transfer coefficients, which showed good agreement with data already obtained with other techniques, and was encouraging in view of using IR systems for heat flux measurements. Once the method was shown to work, efforts were mainly oriented towards comprehension of potential errors sources which could affect measurement accuracy and especially to developing devices which could ease IR camera use. Compton (1972), at NASA Ames, realized that the bottleneck of IR thermography was data acquisition, storage and processing. The solution was devised in the automation of data processing and this concept finally brought to the systems currently in use.

Apart from heat flux evaluation, the characterization of flow field behaviour, with location of boundary layer transition to turbulence and of flow separation and reattachment zones, constituted a subject of great interest to aerodynamicists and efforts

were devoted to acquire information on IR camera capability to deal with these phenomena. The boundary layer transition over a flat plate was examined by Peake et al. (1977), who detected the different adiabatic wall temperatures that occur amongst laminar and turbulent flows.

A first analysis of heat transfer measurements by IR thermography and a review of some of their applications were presented by Carlomagno and de Luca (1989). Gartenberg and Roberts (1992) reported an extensive retrospective on aerodynamic research with infrared cameras. In this Chapter, the principles of radiation necessary to perform IR thermography are briefly discussed and the IR camera with its main features are revised.

2.1.1 Fundamental principles of radiation heat transfer

Heat transfer by radiation (Siegel and Howell, 1992) is an energy transport mechanism that occurs in the form of electromagnetic waves. Via this heat transfer mode, energy can also travel in vacuum and may be partially absorbed and reflected by a body, or even pass through it. By denoting with α_r the radiation fraction being absorbed by the body, with ρ_r the fraction being reflected by it and with τ_r the fraction being transmitted (which passes through), energy conservation requires:

$$\alpha_r + \rho_r + \tau_r = 1 \tag{2.1}$$

where α_r, ρ_r and τ_r are respectively called absorptivity, reflectivity and transmissivity coefficients of the body under consideration and may depend on both radiation wavelength (spectral) and propagation direction (directional). Radiation is emitted by all bodies at an absolute temperature $T > 0$ and, for non-transparent bodies ($\tau_r = 0$), it origins from their surface only. The body which emits the greatest amount of energy at a given temperature is called black body.

The law that prescribes the energy flux (energy rate per unit body area) per wavelength (spectral hemispherical emissive power) $I^b(\lambda)$, which is emitted by a black body in the hemisphere outside its surface, is the Planck's law of radiation:

$$I^b(\lambda) = {C_1}\Big/{\lambda^5\left(e^{\left({C_2}/{\lambda T}\right)} - 1\right)} \tag{2.2}$$

where λ is the radiation wavelength (m), T the absolute black body temperature (K) and C_1 and C_2 the first and the second universal radiation constants, respectively equal to 3.7418 x 10^{-16} Wm^2 and 1.4388 x 10^{-2} Km. Eq. 2.2 represented in Fig. 2.1, shows that I^b leads to zero for both $\lambda \to 0$ and $\lambda \to \infty$.

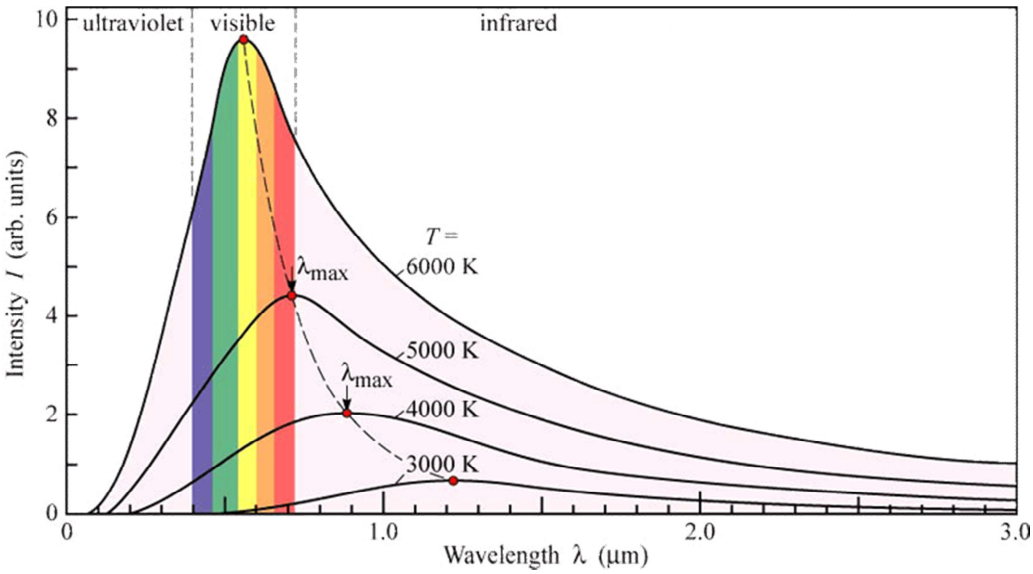

Fig. 2.1 Black-body radiation curves

It has to be noted that, for a black body, the radiation intensity (per unit solid angle) based on the body area projected normally to the direction of emission is independent of the latter. The electromagnetic spectrum is roughly divided into a number of wavelength intervals called bands. The infrared spectral band, of interest within the present context, is generally sub-divided into four smaller bands with arbitrarily chosen boundaries: near infrared (0.75÷3 μm), middle infrared (3÷6 μm), far or long infrared (6÷15 μm) and extreme infrared (15÷1000 μm). Most currently used IR camera detectors are sensitive in the middle (MWIR) and the long (LWIR) spectral bands, but the band between ~5 and ~7.5 μm is seldom used because of its rather high atmospheric absorption. Detectors are also available in the near infrared (NIR), sometimes called short wavelength (SWIR), and in the extreme infrared bands, but they are not generally used for thermo-fluid dynamic applications. By deriving and integrating with respect to λ, Planck's law leads, respectively, to the following two other laws:

Wien's displacement law: the wavelength λ^* at which the black body emits its maximum spectral emissive power is a function of the absolute black body temperature according to:

$$\lambda^* T = 2897.8\ \mu m\ K \tag{2.3}$$

i.e., the maximum value of I^b moves towards shorter wavelengths as the body temperature increases. E.g., at liquid nitrogen temperature (77 K) $\lambda^* \approx 38$ μm, at room temperature $\lambda^* \approx 10$ μm, while the sun (at about 6000 K) emits yellow light peaking around 0.5 μm in the visible light spectrum. This explains why IR cameras mainly operate in MWIR and LWIR bands.

Stefan-Boltzmann's law: The total (over all wavelengths) hemispherical emissive power E^b (W/m^2) also depends on the absolute black body temperature alone, according to:

$$E^b = \sigma T^4 \tag{2.4}$$

where σ is the Stefan-Boltzmann's constant, which is equal to 5.6704 x 10-8 W/m^{2}K^4. However, since infrared camera detectors capture only a limited band of the whole electromagnetic spectrum, while making measurements with IR thermography, Planck's law (Eq. 2.2), rather than Stefan-Boltzmann's law (Eq. 2.4), has to be applied. Real objects almost never comply with the above-described laws even if they may approach the black body behaviour in certain spectral bands and conditions. A real object generally emits only a fraction $I(\lambda)$ of the radiation emitted by the black body $I^b(\lambda)$ at the same temperature and wavelength. For the sake of ease, $I(\lambda)$ is always referred to the spectral hemispherical emissive power. By introducing the spectral emissivity coefficient, defined as:

$$\varepsilon(\lambda) = I(\lambda)/I^b(\lambda) \tag{2.5}$$

Eq. 2.2 can be rewritten for real bodies by simply multiplying its second term by *ε(λ)*:

$$I(\lambda) = {\varepsilon(\lambda)C_1}\Big/{\lambda^5(e^{\left({C_2}/{\lambda T}\right)} - 1)} \tag{2.6}$$

Bodies having their emissivity independent of λ are called grey bodies. Kirchhoff's law states that the spectral emissivity coefficient is equal to the spectral absorptivity coefficient $\alpha_r(\lambda)$, that is the absorbed fraction of the radiation of wavelength λ. Therefore, for non-transparent bodies, such as those generally used in infrared thermography, Eq. 2.1 becomes:

$$\varepsilon(\lambda) + \rho(\lambda) = 1 \tag{2.7}$$

Therefore, materials with low emissivity ε (such as metallic ones) not only emit less energy, but also reflect a large amount of the radiation coming from the ambient and impinging on them. Whenever possible, they should not be employed in IR thermography or, if they must be necessarily used and transient heat transfer is not involved, the viewed body should be covered with a thin layer of thermally black paint.

2.1.1 Infrared cameras: hardware, performance and calibration

The core of the IR camera system is the radiation detector. Detector technologies are mainly separated into two classes: thermal detectors, that are sensitive to the incident energy flux, and quantum detectors, whose sensitivity depends on photon absorption. A currently common type of thermal detector is the uncooled microbolometer, made of metal compound or semiconductor material. The microbolometer typically has a lower cost and broadband IR spectral response, but is less sensitive and quite slower (response time in the milliseconds domain) than quantum detectors. The latter ones are made from materials such as InSb, HgCdTe (MCT), and layered GaAs/AlGaAs for QWIP (Quantum Well Infrared Photon) detector. Quantum detectors have a low response time (microseconds domain) and higher sensitivity than thermal ones, but strong cooling is still required. In actual cameras, miniature Stirling coolers easily achieve temperatures around 70 K.

In Fig. 2.2, the spectral responses of some of the most sensitive, largely used, cooled and uncooled infrared detectors and their relative detectivity are indicated. The response curves are shown in terms of *D** (detectivity star) for a specific exposure time, as a function of the spectral wavelength. *D** is the sensitivity figure of merit of the infrared detector detectivity, so that higher *D*s* indicate better performance.

Modern quantum detectors and QWIP tend to approach the ideal (top curves) detector behaviour. Nowadays, non-cooled microbolometers are typically employed in both MWIR and LWIR spectral bands. Instead, because of their respectively higher *D*s* (see Fig. 2.2), quantum detectors usually utilize InSb in MWIR band and HgCdTe, or QWIP, in LWIR band. To carry out IR thermography, the choice of the most appropriate working spectral band (MWIR, or LWIR) depends on several factors often linked to object surface nature and to atmospheric absorption. Cameras in LWIR band, because of their band, thanks to low atmospheric absorption (except for very high water vapour content) and high thermal contrast, generally allow for high accuracy measurements; in particular, they are able to take data also in the presence of air plasma that typically does not emit in 8-12 μm band (Cardone, 2007). However, frequently MWIR cameras are preferred because of their lower cost detectors and optics, higher detectivity *D** for quantum detectors and since some surfaces have a higher emissivity coefficient in the middle infrared band. It has to be noted that, for temperatures higher than about 10°C, temperature sensitivity is generally better for MWIR than for LWIR quantum detectors. When high sensitivity and very short response time are not required, the best and most cost-effective actual choice is a camera with non-cooled microbolometers. The standard instantaneous output of each thermal image is generally constituted by a matrix of data from 105 up to 106 elements. Therefore, as already stated, a digital data processing is mandatory, although easy to perform since practically all cameras have a digital output. The temperature range usually measured spans from −20 up to +1500°C, but it can be further extended to higher values by filtering the oncoming radiation. Typically, MWIR cameras use silicon optics, while the LWIR ones use germanium optics. Most of the available IR cameras offer also telescopes, expander lenses and supplementary close-up microscope lenses, i.e., the possibility of changing their optics, in order to adapt working distances to the scene one is looking at.

The performance of an infrared camera is conventionally evaluated in terms of thermal sensitivity, scan speed, image resolution and intensity resolution. Thermal sensitivity is generally defined in terms of (mean) noise equivalent temperature

difference (NETD), which is the time-average standard deviation over all pixels of a blackbody scene and is expressed in terms of mK. Some modern FPA systems are able to detect temperature differences of less than 20 mK at ambient temperature.

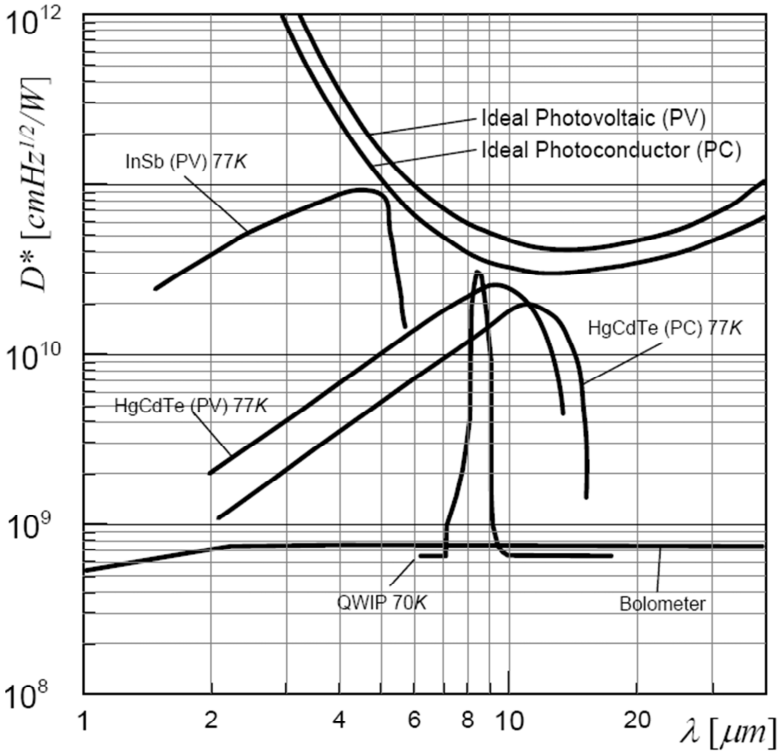

Fig. 2.2 Spectral responses of infrared detectors and relative detectivity D^* (from Carlomagno and Cardone 2007)

The scan speed represents the rate at which a complete image (frame) is updated and is expressed in terms of frame rate (Hz). FPA systems of the last generation are characterized by high standard frame rates (often greater than 100 Hz) and, by the reduction of the number of acquired pixels (i.e., by windowing the frame) and their integration time (i.e., detector sensitivity). Frame rates can currently go up to several ten thousands of Hz. The image resolution, that is the capability of a system to measure surface temperature of small objects, is usually defined as instantaneous field of view (IFOV), which is expressed in terms of mrad; theoretically, IFOV is the ratio of detector pixel width over lens focal length. However, this is only an ideal design parameter and does not fully describe the performance of the actual system. In fact, when a lens of

reduced total field of view (FOV) is used, IFOV decreases, but the number of IFOVs in the frame remains the same. Then, the number of IFOVs (pixels) that describes the complete FOV gives a better description of the image resolution. Modern systems are able to produce images composed of up to several hundreds of thousands of pixels at standard frame rates. More rigorously, the spatial resolution of the IR camera may be defined in terms of the Modulation Transfer Function (MTF_{IR}), which is the mathematical description of the detected signal modulation (also due to the pixel finiteness) as a function of the spatial frequency (de Luca and Cardone, 1991). The intensity resolution, or dynamic range, is expressed in terms of number of digital intensity levels the thermal image is composed of. The latest generation of cameras provides typically 14-bit A/D conversion, which allows measuring small temperature differences even in the presence of a large temperature range in the viewed scene.

The energy actually detected by an IR system depends not only on the emissivity coefficient of the surface under measurement, but also on environmental conditions. In fact, the total radiation I' detected by the camera can be written as:

$$I' = \tau_r \varepsilon I^b_{obj} + \tau_r (1-\varepsilon) I^b_{amb} + (1-\tau_r) I^b_{atm} \tag{2.8}$$

where: τ_r is the transmissivity of the atmosphere between the surface and the camera, I^b_{obj} is the radiation intensity corresponding to a black body at the object temperature T_{obj}, I^b_{amb} is the black body radiation intensity corresponding to the (effective) temperature of the object surroundings T_{amb}, called the reflected ambient (or background) temperature and I^b_{atm} is the radiation intensity corresponding to a black body at the temperature of the atmosphere $T_{atm.}$. In Eq. 2.8, the term $\tau_r \varepsilon I^b_{obj}$ is the emission from the surface captured by the radiometer, $\tau_r (1-\varepsilon) I^b_{amb}$ is the reflected emission from ambient sources, and $(1-\varepsilon)$ is the surface reflectivity (T_{amb} is assumed constant for all emitting surfaces of the half sphere seen from the object surface). The term $(1-\tau_r) I^b_{atm}$ is the emission from the atmosphere, with $(1-\tau_r)$ being the atmosphere emissivity. For the sake of simplicity in the Eq. 2.8, the dependence from T and wavelength is not indicated.

Generally, the transmissivity of the atmosphere τ_r is assumed to be equal to unity, which simplifies Eq. 2.8. Thus, by using Eq. 2.2 and Eq. 2.8, a semi-empirical adaptation of

the Planck's law with the parameters R, B, and F can be found. The typical calibration function of an IR camera can be put in the form:

$$U_D = \varepsilon \frac{R}{e^{B/T_{obj}} - F} + (1 - \varepsilon) \frac{R}{e^{B/T_{obj}} - F} \tag{2.9}$$

where: U_D is the detected signal, R is a function of integration time and wavelength, B is a function of wavelength alone, and F is a positive value very close to 1. If the object used for calibration is a black body, the calibration constants R, B and F, besides taking into account the sensed wavelength band and the radiation constants, consider only emission and absorption from atmosphere.

A simpler way to perform the calibration, which does not take in account T_{amb} variations, is the *in situ* calibration proposed by Sargent et al. (1998), which practically neglects the second term of the second member of Eq. 2.9.

Needless to say that, if a window (or a mirror) exists in the optical path between test section and IR camera the constants of Eq. 2.9 depend also on the transmissivity (reflectivity) through such a window (mirror).

2.2 Particle Image Velocimetry

Particle Image Velocimetry is a measurement technique, most commonly known as PIV (Adrian, 1991 and Rafael et al., 2007). PIV permits to obtain two components of the instantaneous displacement field in a plane. Such displacements are the movement of tracer particles which seed the flow. These particles are illuminated in a plane of the flow at least twice within a short time interval. Recording the light scattered by the particles, a single frame or a sequence of frames are obtained. Evaluating the particle displacements between the light pulses, the velocity field can be inferred.

In order to be able to handle the great amount of data which can be collected employing the PIV technique, sophisticated post-processing is required. A typical layout of a PIV configuration is depicted in Fig. 2.3.

The seeding particles are illuminated by a laser sheet in a plane of the flow. The time delay between the two pulses depends on the flow velocity and the magnification. The displacement is evaluated by means of scattered light of the seeding particles recorded on a single frame or on two separate frames. The camera output is then transferred to the

computer. The image is divided in small subareas called “interrogation areas” or “interrogation windows”. Using a statistical approach (such as auto-correlation or cross-correlation), the local displacement vector of the seeding particles for each interrogation window is obtained. Such a result is reached under the assumption that all the particles within one interrogation area have moved homogeneously between the two laser pulses.

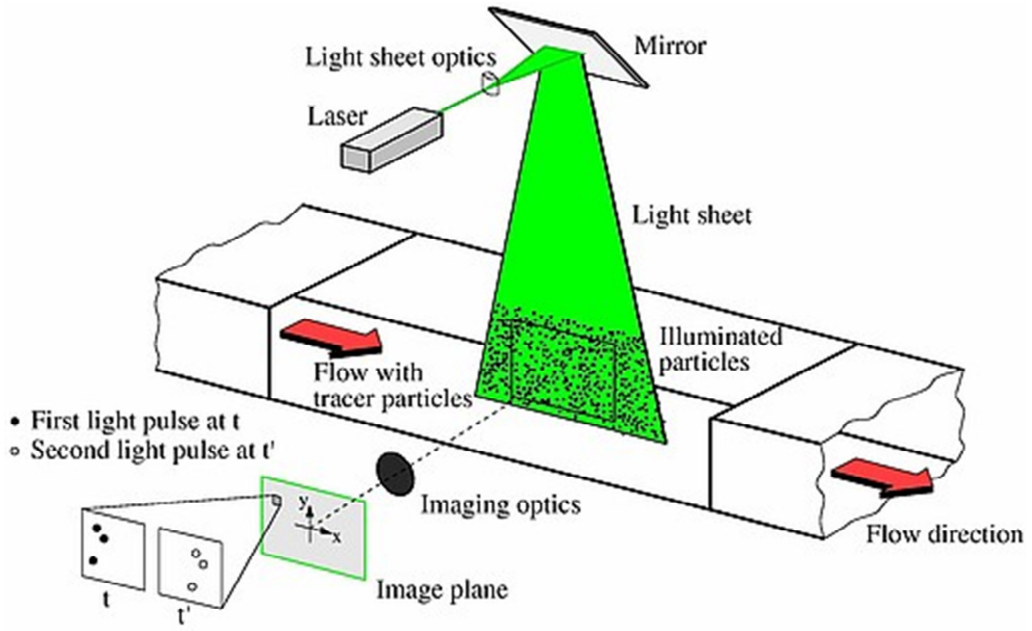

Fig. 2.3 PIV experimental apparatus sketch (from Rafael et al., 2007)

The local velocity vector, into the plane illuminated by the laser sheet, is obtained employing the time delay between the two laser pulses and the magnification.

The process of interrogation is repeated for all the interrogation windows of the PIV recording. PIV technique general aspects are reported in following:

Non-intrusive velocity measurement. PIV technique is an optical technique which has the advantage to be non-intrusive and it does not affect the flow field differently from other techniques as pressure tubes, hot wire or probes. This allows the application of PIV even in high-speed flows avoiding shocks or boundary layers perturbation caused by the probe presence.

Indirect velocity measurement. PIV technique infers the local fluid velocity indirectly by means of the measurement of the velocity of tracer particles which are added within the flow before the experiment starts.

Whole field technique. PIV is a technique which allows to record images of large part of flow fields. Several are the applications (in gaseous and liquid media) where it is possible to extract the velocity information out of these images. Such a characteristic is unique to the PIV technique. All other techniques allow only a velocity punctual measurement but with a high temporal resolution. Instead PIV temporal resolution is restricted due to the technological limitations (recording frame rate). Differently from its temporal resolution, PIV spatial resolution is very large. Instantaneous image capture and high spatial resolution of PIV allow the detection of spatial structures even in unsteady flow fields.

Temporal resolution. Usually the PIV systems are characterized by a high spatial resolution, but by a relative low frame rates. However, nowadays this technological limitation has been overcome by the development of high-speed lasers and cameras which permit to perform time resolved measurements.

Spatial resolution. The PIV spatial resolution is related to the interrogation areas. The interrogation areas have to be large enough to include at least a number of particles which permits to have reliable statistical values, but they have also to be small enough to avoid that velocity gradients affect the measurement. The interrogation area also determines the number of independent velocity vectors.

Velocity lag. As previously said PIV technique needs to use tracer particles to measure the fluid velocity. Such tracer particles have to faithfully follow the fluid elements motion. In order to check if such a condition is satisfied the relaxation time concept has to be introduced. The mismatch between the fluid velocity and tracer particles velocity is mainly influenced by the gravitational forces if the fluid density (ρ) and the tracer particles density (ρ_p) are different. Assuming spherical particles in a viscous fluid at very low Reynolds number, it is possible to derive the gravitationally induced velocity U_G from Stokes' drag law:

$$U_g = d_p^2 \frac{(\rho_p - \rho)}{18\mu} g \tag{2.10}$$

where g is the acceleration due to gravity, μ the dynamic viscosity of the fluid and d_P the particle diameter. For a continuously accelerating flow, the velocity lag can be derived using Eq. 2.10:

$$U_S = U_P - U_f = d_p^2 \frac{(\rho_p - \rho)}{18\mu} a \tag{2.11}$$

where U_p is the tracer particle velocity, U_f the fluid velocity and a the fluid acceleration. The step response of U_p usually has an exponential law if the particle density is much greater than the fluid density:

$$U_P(t) = U_f \left[1 - exp\left(-\frac{t}{\tau_S}\right)\right] \tag{2.12}$$

with the relaxation time τ_S:

$$\tau_S = d_p^2 \frac{\rho_p}{18\mu} \tag{2.13}$$

Such solution is not valid when the fluid acceleration is not constant or Stokes drag does not apply (e.g. at higher flow velocities). In these conditions the equation of the particle motion is more difficult, and the solution is no longer a simple exponential decay of the velocity. Nevertheless, τ_S is the best parameter to check the tendency of particles to faithfully follow the fluid velocity. The result of Eq. 2.12 is illustrated in figure 2.4, where the time response of particles with different diameters is shown for a strong deceleration in air flow.

Illumination. In order to well expose the camera sensor by particles scattered light, high power light source of illumination is necessary. The light scattering improves when larger particles are employed but such a condition is in contradiction to the need of having tiny particles which better follow the fluid flow. The light scattered by a particle depends on several parameters as: ratio between the particles refractive index and surrounding medium, particles' size, their shape and the observation angle. Mie's scattering theory (van de Hulst, 1957) can be applied to show the light scattering pattern of a spherical particle whose diameter (d_p) is larger than the incident light wavelength λ_l. The light scattering polar distributions for an oil particle, with different diameters in air illuminated by a light with a wavelength of 532 nm, are depicted in Figs. 2.5 a) and b).

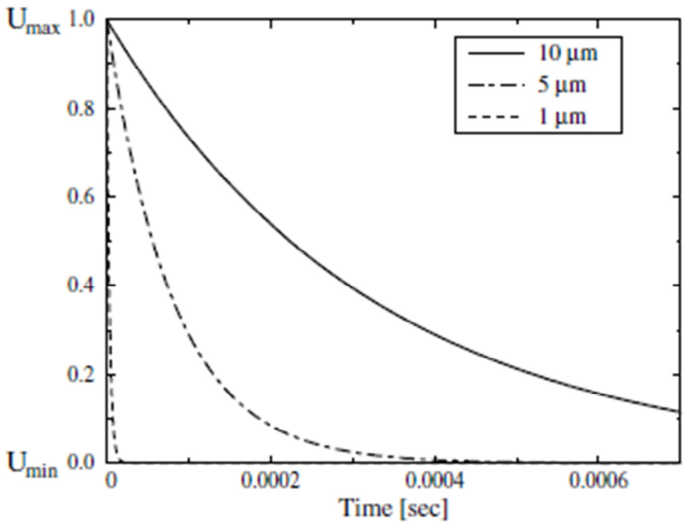

Fig. 2.4 Time response of oil particles with different diameters in a decelerating air flow (from Rafael et al., 2007)

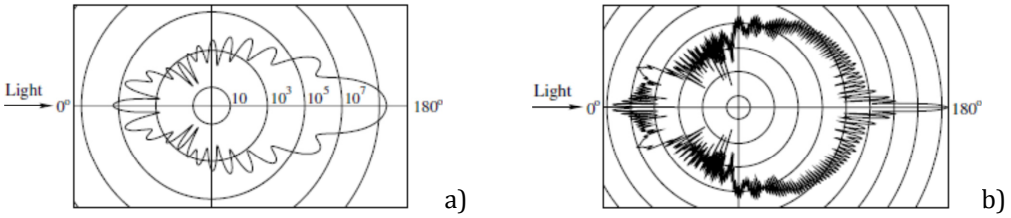

Fig. 2.5 Light scattering by a: a) 1 µm and b) 10 µm oil particle in air (from Rafael et al., 2007)

The Mie scattering can be characterized by the normalized diameter, q, defined as:

$$q = \frac{\pi d_p}{\lambda_l} \tag{2.14}$$

when q is larger than unity, its local maxima appear approximately in the angular distribution ranging between 0° and 180°. Higher is q greater is the ratio between forward and backward scattering intensity. Hence, it would be advantageous to record in forward scatter, but, due to the limited depth of field, recording at 90° is most often used.

In water experiments, usually, the tracer particles have a dimension that is one order of magnitude larger than those used for air experiments. This is due to the water

refractive index which is greater than air's one causing a less powerful light scattering of tracer particles. In water the light scattering pattern is different from that obtained in air. Indeed the light is not blocked but spread in all direction, as depicted in Fig. 2.6, causing a multiscattering phenomenon. Such a phenomenon can cause a considerably increase in the intensity of the light scattered by tracer particles.

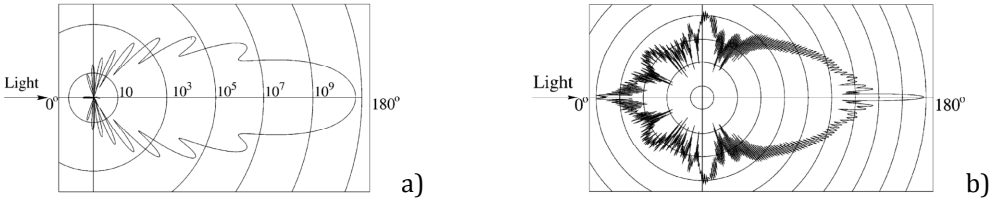

Fig. 2.6 Light scattering by a: a) 1 μm and b) 10 μm glass particle in water (from Rafael et al., 2007)

Duration of illumination pulse. The illumination light pulse has to be short enough to "freeze" the particles motion avoiding image blurring during the pulse exposure.

Time delay between illumination pulses. The delay time between the two illumination pulses is a function of magnification and mean fluid velocity. Such a delay time has to be set long enough to have a clear detectable tracer particles displacement but short enough to avoid out-of-plane tracer particles motion.

Density of tracer particle images. Fig. 2.7 shows three different kind of image density. Low image density is depicted in Fig. 2.7 a); each individual particle can be detected and images corresponding to the same particle originating from different illuminations can be identified. Such a type of image needs to be analysed by using a tracking methods. Therefore, this condition is stated as "Particle Tracking Velocimetry", abbreviated "PTV". The images of individual particles can be detected even in the case of medium image density (Fig. 2.7 b)).

However, it is no longer possible to identify image pairs by visual inspection of the recording. Hence for medium image density is required to apply the standard statistical PIV evaluation techniques. For the case of high image density (Fig. 2.7 c)), it is not possible to identify individual images as they overlap in most cases and form speckles. This situation is called "Laser Speckle Velocimetry" (LSV).

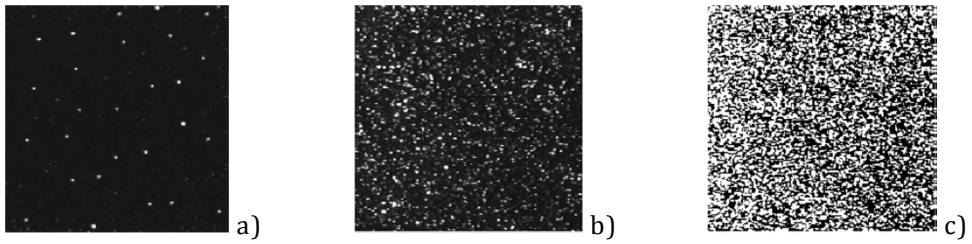

Fig. 2.7 The three types of particle image density: a) low, b) medium and c) high (from Rafael et al., 2007)

Chapter 3

Experimental Rigs

Two different experimental rigs have been used to study air and water synthetic jets in free and impinging configurations by using PIV technique and IR Thermography.

3.1 Air Jet Facility

Fig. 3.1 shows the schematic of the twin circular air synthetic jets device. The loudspeaker, whose diameter is 270 mm, splits the cavity in two sub-cavities with a volume *Vol* equal to 2 dm^3. The two nozzles, attached to both sub-cavities, have a length *L* of 210 mm, a thickness of 1 mm and an inner diameter *D* of 21 mm. The distance between the two nozzle axes *l* is varied during the tests (the distances *l* = 1.1 *D*, 3 *D* and 5 *D* are considered). The related dimensionless parameter $\sum$ is defined as the ratio between the jet-axes-distance (*l*) and the exit nozzle diameter (*D*). Such a jet-axes-distance is the parameter that differentiates this device with respect to that present in literature (Lasance and Aarts, 2008 and Lasance et al., 2008). The distance *l* = 1.1 *D* corresponds to the condition for which the two pipes are adjacent. The two sub-cavities are designed in order to have the same resonance frequency. Indeed the nozzle length and diameter are equal for both the synthetic jets and the same cavity volume is achieved by filling the upper and the bottom sub-cavity using particular geometrical items. The single jet configuration is obtained deflecting one of the two synthetic jets by using a bended tube at the exit of the orifice (checking through the pressure transducers that no pressure variations are induced in the sub-cavities).

The classical formula to evaluate the Helmholtz resonance frequency (Helmholtz, 1860) is:

$$f_H = \frac{c}{2\pi}\sqrt{\frac{\pi D^2/4}{Vol \cdot L'}} \tag{3.1}$$

where f_H is the Helmholtz resonance frequency, c is the air speed of sound, $\pi D^2/4$ is the nozzle cross section area, Vol is the cavity volume and L' is the effective nozzle length

(equal to 0.24 *m* and corresponding to the geometric nozzle length plus the edge corrections according to Persoons, 2012). Each cavity should have, according to Eq. 3.1, a Helmholtz resonance frequency of about 45.9 Hz.

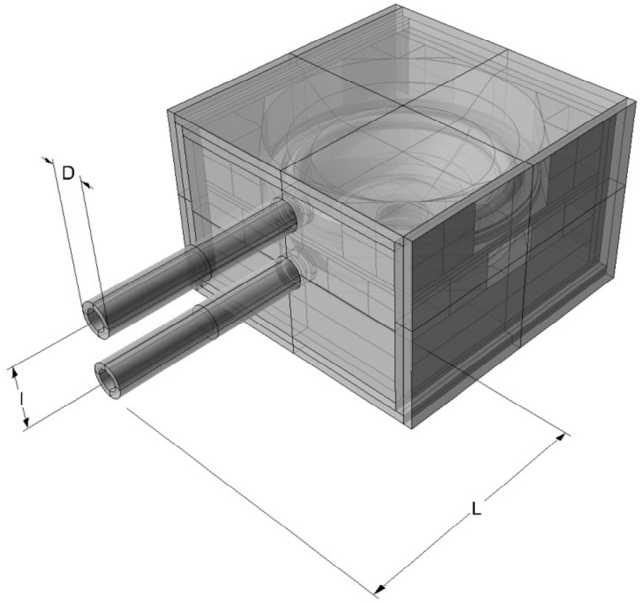

Fig. 3.1 Twin synthetic jets device

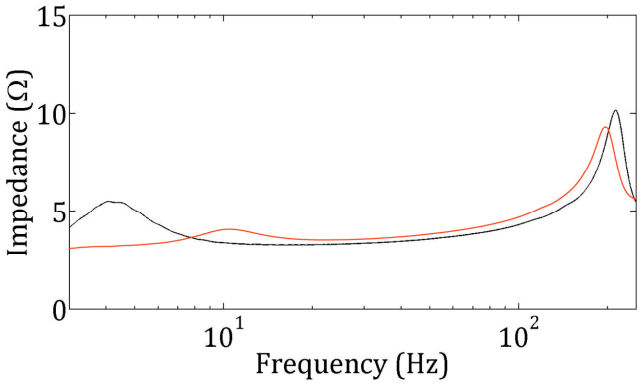

Fig. 3.2 Impedance versus the input frequency for free (red curve) and impinging synthetic jet configuration (black curve)

Both the gas dynamics (Helmholtz resonance) and the mechanical dynamics of the loudspeaker influence the overall system response of a synthetic jet. The complete system behaves like two degrees of freedom mass-spring-damper system (Gallas et al., 2003 and Persoons, 2012).

Two different loudspeakers (CIARE®HS250) are used in the experiments described in subchapters 3.1.1 and 3.1.2. The difference is only due to the diverse loudspeaker resonance frequency. In the free synthetic jets configuration (subchapter 3.1.1) the loudspeaker has a resonance frequency of 56 Hz, while in the impinging synthetic jets configuration (subchapter 3.1.2) the loudspeaker resonance frequency has a value of 25 Hz. The loudspeaker nominal diameter is 208 mm and its equivalent oscillating mass is 56 g. According to Persoons (2012), the overall system has two resonance frequencies equal to about 13 Hz and 200 Hz, in the first and 6 Hz and 194 Hz in the second case. In both configurations, the two complete system resonance frequencies are found experimentally by measuring the loudspeaker impedance. They were equal to about 10 Hz and 196 Hz, in the first case, and about 4 Hz and 210 Hz, in the second one, as shown in Fig. 3.2 (red and black curve respectively).

The small discrepancy between the resonance frequencies evaluated according to Persoons (2012) and those measured should be ascribed to the geometry of the sub-cavities that is highly irregular and three-dimensional and to the nozzle exits that are not located on the centre of the face opposite to the oscillating membrane (Chanaud, 1994 and 1997 and Alster, 1972).

3.1.1 Experimental apparatus for free synthetic jets

The single and twin air synthetic jets device (characterized by 10 Hz and 196 Hz resonance frequencies) has been employed to study the free flow field at Reynolds number equal to 6700, Strouhal number equal to 0.046 and jet-axes-distance of 1.1, 3 and 5 nozzle diameters.

Instantaneous velocity fields were measured using PIV as shown in the experimental setup (Fig. 3.3). Illumination sheets are generated with a double cavity Nd-YAG laser with a separation of 80 μs between the first and the second laser pulse. The energy output per pulse is approximately 150 mJ with a pulse duration of 5 ns. The thickness of the sheets is 0.5 mm and the illuminated region has a width of about 210 mm. The imaging system is synchronized with the synthetic jet in order to perform phase-average measurements. The same PC sound card that provides the sinusoidal signal with a frequency f of 10 Hz to the loudspeaker (passing by a CIARE® YSA 300 Hi-Fi amplifier) generates also a trigger signal for the PIV system. Hence the acquisition is performed at a frequency f_2 equal to:

$$f_2 = \frac{f}{\frac{1}{NDiv} + n} \tag{3.2}$$

The acquisition is carried out sampling the phenomenon every n = 10 periods of membrane oscillation with a phase shift of 360°/*NDiv* (where *NDiv* = 30 is the number of the phases which are sampled), in this way the synthetic jet is sampled at each 12°. The average of each phase is performed on 200 instantaneous flow fields. Air is seeded with olive oil droplets with a nominal diameter of about 1 μm. Particle images are acquired with a PCO SensiCam CCD camera lens with 50 mm focal length and with a relative aperture *f/#* equal to 8. The pixel array size is 1280 x 1024 pixels and each pixel depth is 12 bits. The resulting resolution for the digital images is 6 pixels/mm in the illumination plane. All the 6000 double frame images taken for each test are used to obtain reliable turbulent statistics.

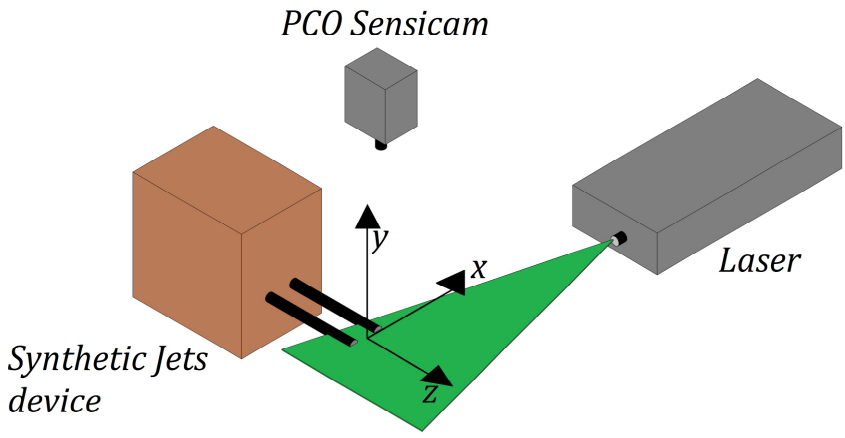

Fig. 3.3 Free synthetic jets experimental setup

The vector field has been obtained processing images with a multiple pass algorithm with window deformation by using the Blackman weighting windows according to Astarita and Cardone (2005) and Astarita (2006, 2007, 2008). The final interrogation window size is 24 x 24 pixels with an overlap of 75% thus producing a vector pitch of 1 mm (21 vectors/*D*). The uncertainty in displacement, related to the interrogation area size, is the main contribution to uncertainty in velocity. In this work according to the works describing the PIV software by Astarita (Astarita and Cardone 2005 and Astarita 2006, 2007, 2008), for the given particle size (approximately 2 pixel), noise level (signal to

noise ratio equal > 5) and displacement field the uncertainty was found to be almost everywhere smaller than 0.1 pixel providing a velocity uncertainty of 2% in the jet.

The data are presented by using a triple decomposition (Hussain and Reynolds, 1970 and Kitsios et al., 2010):

$$u_i(\underline{x},t) = U_i(\underline{x}) + \tilde{u}_i(\underline{x},t) + u_i(\underline{x},t) \tag{3.3}$$

where $u_1 = u$, $u_2 = v$, $u_3 = w$ and $\underline{x} = (x,y,z)$. U_i is the time-average, $\tilde{u}_i$ is the phase-correlated organised contribution to the velocity and u'_i is the turbulent velocity fluctuation. The time-average velocity is defined as:

$$U_i(\underline{x}) = \lim_{\tau\to\infty} \frac{1}{\tau} \int_0^{\tau} u_i(\underline{x},t)\, dt \tag{3.4}$$

while the phase-average velocity is:

$$< u_i(\underline{x},t) >= \lim_{N\to\infty} \frac{1}{N} \sum_{n=0}^{N-1} u_i(\underline{x}, t+n\tau) \tag{3.5}$$

where N is the number of flow fields of the same phase, τ is the period of the organised contribution, whose reciprocal coincides with the actuation frequency f. Hence the phase-average velocity is the average in any spatial point for a fixed phase φ in the synthetic jet generation cycle. The phase-correlated organised contribution to the velocity is then defined as:

$$\tilde{u}_i(\underline{x},t) =< u_i(\underline{x},t) > - U_i(\underline{x}) \tag{3.6}$$

while the turbulent velocity fluctuation is:

$$u'_i(\underline{x},t) = u_i(\underline{x},t) - < u_i(\underline{x},t) > \tag{3.7}$$

The time-average turbulent kinetic energy is defined as:

$$\overline{TKE} = \sum_{i=1}^{3} \overline{\left(u'_i(\underline{x},t)\right)^2} \Big/ U_0^2 \tag{3.8}$$

while the phase-average turbulent kinetic energy is calculated as:

$$< TKE >= \sum_{i=1}^{3} < \left(u'_i(\underline{x},t)\right)^2 > \Big/ U_0^2 \tag{3.9}$$

3.1.2 Experimental apparatus for impinging synthetic jets

The single and twin air synthetic jets device (characterized by 4 Hz and 210 Hz resonance frequencies) has been employed to study the flow field and heat transfer in an impinging configuration.

For the flow field measurements the experimental apparatus is sketched in Fig. 3.4. The operating conditions are: Reynolds number equal to 5100, Strouhal number equal to 0.024 and the jet-axes-distance of 1.1, and 3 nozzle diameter for five different values of dimensionless nozzle-to-plate distance *H/D* (2, 4, 6, 8 and 10).

Instantaneous velocity fields were measured using PIV as shown in the experimental setup (Fig. 3.4). Illumination is provided by a Quantel Evergreen laser (Nd-YAG, 200 mJ/pulse) with a separation of 65 μs between the first and the second laser pulse. The pulse duration is of 5 ns, the sheet thickness is of 0.5 mm and the illuminated region has a width of about 210 mm. The imaging system is synchronized with the synthetic jet in order to perform phase-average measurements as in subchapter 3.1.1.

The synthetic jets device is supplied with a sinusoidal input signal with a frequency *f* of 4 Hz by a Hi-Fi amplifier (CIARE® YSA 300) driven with a signal generator (DIGILENT Analog Discovery™). In order to perform phase-average PIV measurements, the same signal generator is used as external trigger with frequency f_2 equal to 3.87 Hz.

The acquisition is carried out sampling the phenomenon every period (n = 1) of membrane oscillation with a phase shift of 360°/*NDiv* (where *NDiv* = 30 is the number of the phases which are sampled), in this way the synthetic jet is sampled at each 12°. The average of each phase is performed on 400 instantaneous flow fields. Air is seeded with

olive oil droplets with a nominal diameter of about 1 μm. Particle images are acquired with a Zyla 5.5 sCMOS camera lens with 50 mm focal length and with a relative aperture *f/#* equal to 11. The pixel array size is 2560 x 2160 pixels and each pixel depth is 16 bits. The resulting resolution for the digital images is 10.84 pixels/mm in the illumination plane. All the 12000 double frame images taken for each test are used to obtain reliable turbulence statistics.

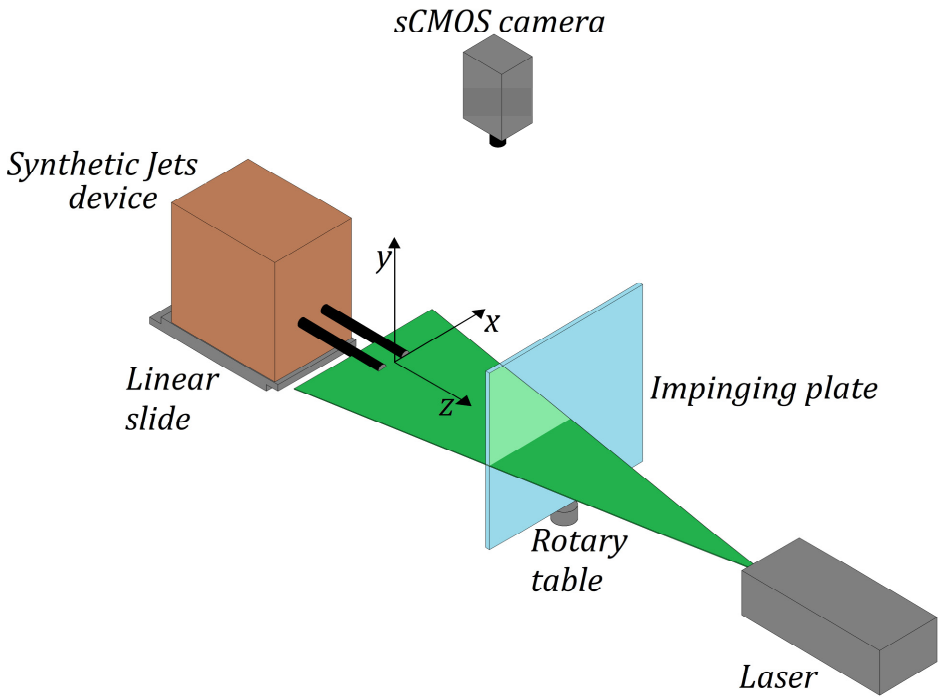

Fig. 3.4 Impinging synthetic jets experimental apparatus for PIV measurements

The vector field has been obtained processing images with a multiple pass algorithm with window deformation by using the Blackman weighting windows according to Astarita and Cardone (2005) and Astarita (2006, 2007, 2008). The final interrogation window size is 24x 24 pixels with an overlap of 75% thus producing a vector pitch of about 0.55 mm (38 vectors/D).

The uncertainty in displacement, related to the interrogation area size, is the main contribution to uncertainty in velocity. According to the works describing the PIV software by Astarita (Astarita and Cardone 2005 and Astarita 2006, 2007, 2008), for the given particle size (approximately 2 pixel), noise level (signal to noise ratio ≥ 5) and

displacement field the uncertainty was found to be almost everywhere smaller than 0.1 pixel providing a velocity uncertainty of 2% in the jet.

For the heat transfer measurements the experimental apparatus is sketched in Fig. 3.5. It includes a stainless steel foil (243 mm wide, 715 mm long and 40 μm thick), constituting the target plate, which is steadily and uniformly heated by Joule effect by passing an electric current through it and is cooled by the synthetic air jets impinging on it. Two couples of bus bars, made of copper, clamped at the shortest sides of the foil are maintained at constant potential difference by using a stabilized DC power supply. The electrical contact between bus bars and foil is enhanced by putting there an indium wire (about 1 mm in diameter). Furthermore, the foil thermal expansion is balanced by the spring-loaded bolts linked to the bus bars and by two spring-loaded insulators (Imbriale et al., 2012). The target plate is positioned horizontally with the synthetic jets impinging vertically above in order to minimize the effects of the natural convection on the foil.

Experiments are performed for five values of the nozzle-to-plate distance (namely 2, 4, 6, 8 and 10 D). All the experiments are performed, as previously said, at the same value of the Reynolds number (5,100) and Strouhal number (0.024). Such values of Reynolds number and Strouhal number are evaluated according to Persoons and O'Donovan (2007) from the measured cavity pressure (p_c) with respect to ambient pressure (p_{amb}) by integrating the unsteady Bernoulli equation for an incompressible flow between a location inside the cavity and a location outside the pipe:

$$\frac{dw}{dt} = \left(\frac{p_c - p_{amb}}{\rho} - \frac{k_{loss} w|w|}{2} \right) \frac{1}{L} \tag{3.10}$$

where the head losses k_{loss} are estimated using the PIV measurements performed on the free synthetic jets. The transducers used to measure the cavity pressure are two Honeywell HSCDRRN002NDAA5 with a response time of 0.46 ms and an accuracy of ±1.5% of the full scale (2 inches of water).

The loudspeaker is supplied with a sinusoidal input signal with a frequency f of 4 Hz by a Hi-Fi amplifier (CIARE® YSA 300) driven with a signal generator (DIGILENT Analog Discovery™). In order to perform phase-average heat transfer measurements, the same signal generator is used as external trigger with frequency f_2 equal to 120 Hz for the infrared camera (whose integration time is 590 μs), thus sampling the investigated

phenomenon each 12°. For each sampled phase, 200 thermal images are acquired for a total of 6000 images.

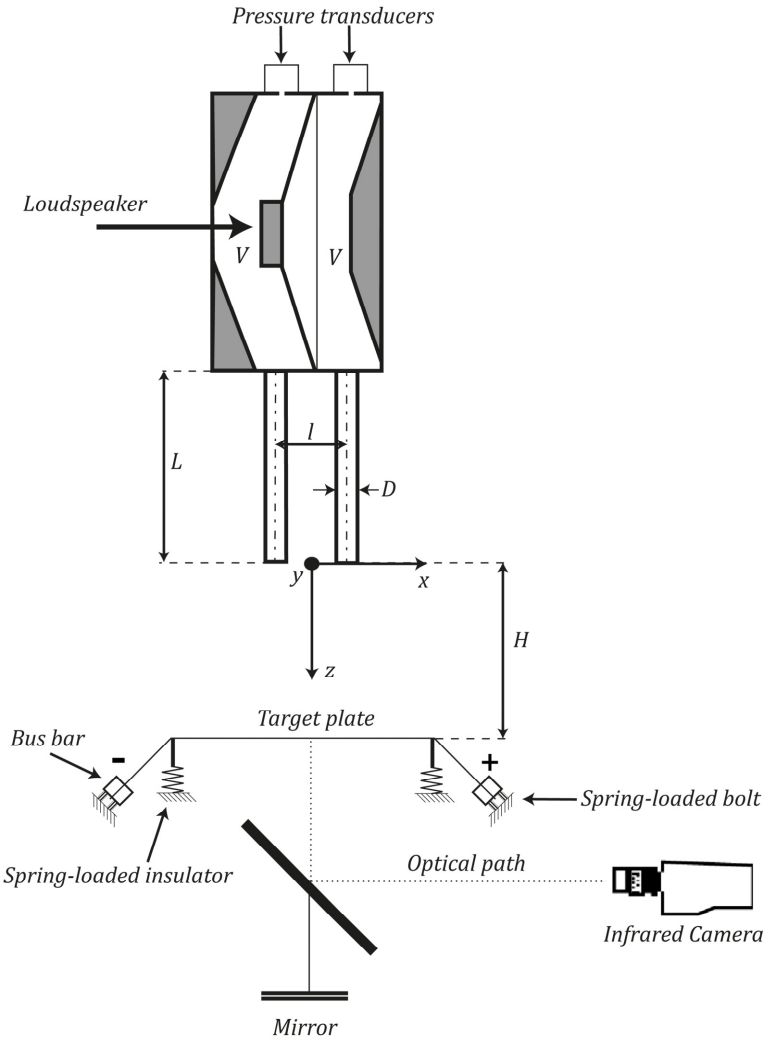

Fig. 3.5 Impinging synthetic jets experimental apparatus for heat transfer measurements

An infrared camera (CEPID JADE III 320 x 240 InSb focal plane array) measures the foil surface temperature with a spatial resolution of 1.17 pixels/mm (24.5 pixels/*D*). The IR camera is accurately calibrated with a blackbody (Carlomagno and Cardone, 2010) for the whole measurement range taking also in account the mirror presence in the optical path; the noise equivalent temperature level (NETD) of the camera is about 25 mK and the

rms error from the blackbody calibration is less than 0.1 K. The foil surface is coated with high emissivity paint (ε = 0.95) in order to increase accuracy of temperature measurements. In the present case, the IR camera is used in conjunction with the unsteady (Golobic et al., 2012) and steady (Carlomagno and Cardone, 2010) heated thin foil heat transfer sensor. According to the application of the local unsteady energy balance to the foil, the convective heat transfer coefficient h can be evaluated as:

$$h = \frac{q'_j - q'_r - q'_k - q'_n - \rho_{foil}\, c_p\, s\, {dT_w}/{dt}}{T_W - T_{aw}} \tag{3.11}$$

with q'_j the Joule heat flux, q'_r the radiation heat flux, q'_k the tangential conduction heat flux, q'_n the natural convection heat flux, ρ_{foil} the stainless steel density, c_p the stainless steel specific heat, s the foil thickness, dT_w/dt the time derivative of wall temperature, T_w the wall temperature and T_{aw} the adiabatic wall temperature.

On the other hand, by applying a steady state energy balance to a foil (Carlomagno and Cardone, 2010) the relationship obtained is:

$$\overline{h} = \frac{q'_j - \overline{q'_r} - \overline{q'_k} - q'_n}{\overline{T_W} - \overline{T_{aw}}} \tag{3.12}$$

where the upper bar indicates the time-average quantities in steady conditions (evaluated as the average of the whole 6000 acquired IR images).

The surface temperature distribution is measured by viewing the rear face of the foil (i.e. the side opposite to jet impingement) through a mirror, as shown in Fig. 3.5. In fact, since the Biot number ($Bi = \bar{h}s/\lambda_f$ where λ_f is the thermal conductivity of the foil) and the inverse of the modified Fourier number ($Fo_f = \pi/\alpha f s^2$ where α is the thermal diffusivity) are small with respect to unity, the time-average and phase-average temperature can be considered as uniform across the foil thickness (Astarita and Carlomagno, 2013). The unsteady heat transfer measurements can be performed not only if the inverse of the modified Fourier number is small but also if the IR camera has enough sensitivity to detect the temperature oscillation. Such a condition is satisfied only if:

$$\frac{q'_j - q'_r - q'_k - q'_n}{\rho_{foil}\, c_p\, s\, f_p\, NETD} \gg 1 \tag{3.13}$$

where f_p is the phenomenon frequency. For the described experiments, considering a loudspeaker frequency equal to 4 Hz, the condition in Eq. 3.13 is verified since the typical value of the ratio is equal to 25. Such a value was achieved with a typical Joule heating of about 830 W/m^2 which was limited by the temperature increase above the adiabatic wall temperature (i.e. T_w-T_{aw} equal to about 14 K in the stagnation point) chosen in order to afford to perform such measurements without affecting flow quality and system operability.

To reduce the effect of temperature measurement noise (NETD equal to 25 mK) the unsteady term dT_w/dt was evaluated over phase-average and filtered time sequences. The fields are averaged over the 200 samples for each phase. In order to further improve the accuracy of derivatives, a more smooth data is attained with a 7 points second order polynomial filter both in time and space.

Each test run consists of two parts: first, with electric current off, T_{aw} is measured and the so-called "cold images" are recorded; then, electric current on, T_w is measured and the "hot images" are recorded (Carlomagno and de Luca, 1989 and Meola et al., 1996).

The net rate of radiation heat loss is estimated as:

$$q'_r = \varepsilon\sigma(T_w^4 - T_{amb}^4) \tag{3.14}$$

with T_{amb} the ambient temperature (q'_r it is found being at worst 45% of q'_j at distances from the centre of impingement higher than 4 diameters).

A little more complex is the procedure to compute thermal losses for tangential conduction (that are found to be at worst equal to 2% of q'_j). In particular, considering the foil plane corresponding with axes x and y, thermal losses for tangential conduction for a metallic foil sensor can be expressed following Meola et al. (1996) and Carlomagno et al. (2011):

$$q'_k = s\, \lambda_f(x,y)\left(\frac{\partial^2 T}{\partial x^2}(x,y) + \frac{\partial^2 T}{\partial y^2}(x,y)\right) = s\, \lambda_f(x,y)\, \nabla^2 T \tag{3.15}$$

Losses due to natural convection are mostly related to those of a heated plate facing downward (McAdams, 1954). To calculate exactly these losses in our experimental facility, ad hoc experiments were performed to get an empirical correlation. By applying this correlation thermal losses were evaluated with an accuracy of ±10% of the total value of said losses. The natural convection losses are, at worst, equal to 7% of q'_j.

Parameter	Typical value	Typical error
T_{aw}	293 K	0.25 K
T_w	305 – 323 K	0.25 K
T_a	293 K	0.1 K
V	3 V	0.03 V
I	46 A	0.46 A
ε	0.95	0.01
q'_n	51 W/m^2	5.1 W/m^2
ρ_{foil}	79500 Kg/m^3	79.5 Kg/m^3
c_p	502 J/KgK	20 J/KgK
s	40 10^{-6} m	8 10^{-7} m
dT_w/dt	-3.9 – 2.5 K/s	0.21 K/s
ρ	1.225 Kg/m^3	1.225 10^{-2} Kg/m^3
p_c-p_{amb}	-100 – 100 Pa	7.5 Pa
D	0.021 m	0.1 10^{-3} m
μ	1.8 10^{-5} Pa s	1.8 10^{-7} Pa s
k_{loss}	0.47	0.047
L	0.21 m	0.1 10^{-3} m

Table 3.1 Control parameters and their uncertainty

The experimental data are reduced in dimensionless form in terms of time-average Nusselt number $\overline{Nu} = \bar{h}D/k$ (k is the thermal conductivity of air at film temperature defined as $(T_w+T_{aw})/2$), phase-average Nusselt number $Nu_\varphi=h(\varphi)D/k$ and standard deviation of Nusselt number phase-average fields Nu'.

The uncertainty for time and phase-average measurements are reported in Table 1. Such an uncertainty analysis is based on the method of Moffat (1998): the error in Re, considering Eqs. 1.1 and 3.10 and Table 3.1, is less than ±4%, the error for the $\overline{Nu}$,

considering Eq. 3.12 and Table 3.1, is less than ±3.5%, the error of Nu_{φ} considering Eq. 3.11 and Table 3.1, is less than ±12.5% and the error of Nu' is less than ±7.4%.

3.2 Water Jet Facility

The experimental measurements of the high Reynolds number impinging synthetic jets were undertaken in an acrylic tank 1000 mm long, 500 mm wide and 500 mm deep, filled with filtered water as shown in Fig. 3.6. Such a facility is located in the LTRAC laboratory of the Monash University and is the same used by Cater and Soria (2002). The tank was filled by water through the Perspex roof. In each experiment synthetic jets were generated by using a reciprocating piston within a cylinder which discharges water from a circular cylinder with inner diameter D_p = 50 mm through an orifice plate of a given diameter D = 10 mm and thickness of 2 mm, positioned in the centre of the tank wall at the exit of the jet. On the top was located a linear bearing which supported the impinging plate. The distance (H) between the orifice plate and the impinging plate was adjusted by using such a linear bearing. The piston was connected to an AC motor through a flexible coupling and an eccentric plate. The rotating speed of the AC motor was adjustable through a motor drive. Increasing the eccentric radius (which is equal to the half piston stroke l_p) and the driving frequency (or actuation frequency f), the desired synthetic jets, with known Reynolds number and Strouhal number, was obtained.

The water in the tank was seeded with hollow glass spheres (Potter spherical, with a density of 1100 kg/m^3) with a nominal diameter of 11 μm having a relaxation time of 7.39 μs and, hence, faithfully re-appearing the water velocity. Prior to the experiments the seeding particles were prepared following the process described in Soria and Parker (2005). A pump was used to homogenize the water and particles inside the tank to reach a high uniformity.

The particles were illuminated by a Quantronix Nd: YLF twin cavity laser system capable of supplying 30 mJ/pulse at a wavelength of 527 nm. The thickness of the laser sheet was adjusted to 1 mm and the laser sheet was aligned horizontally including the jet axis through using several optical lenses and mirrors (4 high energy mirrors, a convex lens with -25 mm focal length, a concave lens with 100 mm focal length and one cylindrical lens with -150 mm focal length). The time difference between two laser pulses was 40 us. The scattered light from the particles was recorded on a PCO-DIMAX high speed cameras with CMOS array size 2016 x 2016 pixel^2. The camera was mounted with

100 mm Zeiss lens and *f/#* number was set up to 2. The camera acquired at its maximum acquisition rate of 624 Hz (in a double frame configuration) and the field of view was approximately 6.3 *D* x 6.3 *D*.

The resulting resolution for the digital images is 31.33 pixels/mm in the illumination plane. Both camera and laser were synchronized by a delay generator (DG645) which started generating signals when the hall sensor detected the lowest piston position during its oscillation. The switch Trigger/Camera allowed to start acquiring images when the phenomenon was steady.

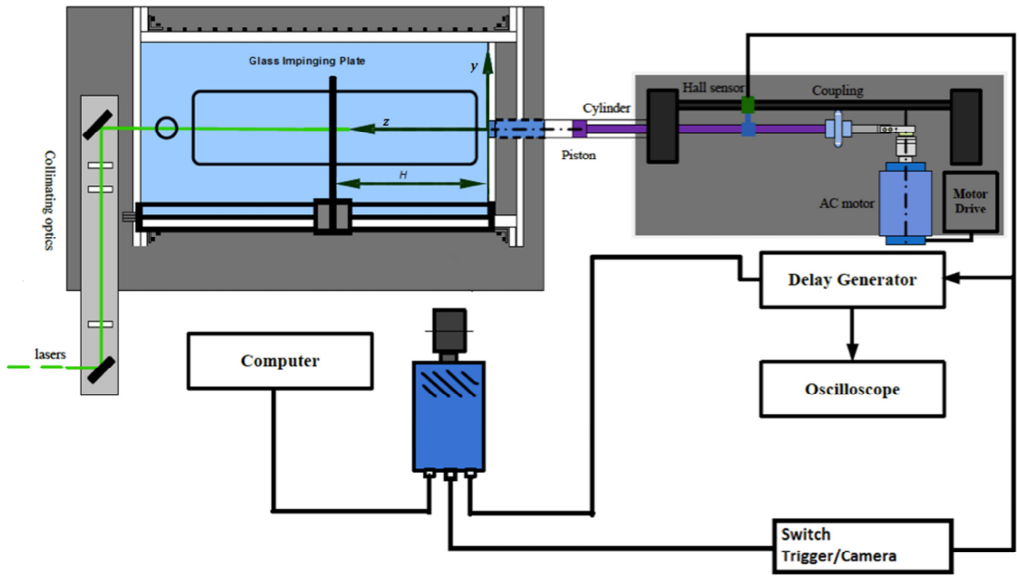

Fig. 3.6 High Reynolds impinging synthetic jets experimental apparatus for PIV measurements

The experiments parameters are reported in the following table:

Case	*Re*	*Sr*	*f* (Hz)	l_p (mm)	*H/D*
A	16000	0.025	4	8	2-4-6
B	16000	0.05	8	4	2-4-6
C	16000	0.1	16	2	2-4-6

Table 3.2 Experimental parameters

Each cycle was sampled with: A) 156, B) 78 and C) 39 fields, respectively. In order to obtain reliable turbulent statistics for each experiment 49920 double frame images were

acquired. Hence each phase-average snapshot, was obtaining through averaging: A) 320, B) 640 and C) 1280 snapshots, respectively.

The vector field was obtained processing images with a multigrid cross-correlation digital particle velocimetry (MCCD-PIV) analysis which is described in Soria (1996a,b and 1998) and Soria et al. (1999). The accuracy and uncertainty associated with multigrid cross-correlation PIV measurements were investigated and discussed in Soria (1996b and 1998). For the first pass the size of the interrogation window was 64 pixel, while for the second pass 32 pixel windows were used. The sample spacing between the centres of the interrogation windows was 16 pixels (50% of overlap). The vector fields were validated using a standard local median filter as described in Westerweel (1994), obtaining less than 5% of rejected vectors.

Chapter 4

Free Synthetic Jets

In this Chapter the free flow field for single and twin synthetic jets is analysed and discussed. The influence of the dimensionless jet-axes distance (Σ) on the flow field has been evaluated.

As reported in Chapter 3 and subchapter 3.1.1, experiments are carried out at Reynolds number equal to 6700, Strouhal number equal to 0.046 and non-dimensional spacing equal to 1.1, 3 and 5. The employed device and the experimental apparatus are sketched in Figs. 3.1 and 3.4.

In subchapter 4.1 the time-average measurements are reported for the single synthetic jet (subchapter 4.1.1) and the twin synthetic jets (subchapter 4.1.2). Then in subchapter 4.2 the phase-average measurements are described for the single (subchapter 4.2.1) and the twin configuration (subchapter 4.2.2).

4.1 Time-Average Flow Fields

4.1.1 Single synthetic jet (SSJ)

Fig. 4.1 presents the time-average axial velocity and the time-average turbulent kinetic energy ($\overline{TKE}$) obtained for a single jet configuration. Differently from what reported in Greco et al. (2013), here $\overline{TKE}$ has been evaluated considering (as defined in Eq. 3.8) only the w' and u' as the oscillation with respect to the phase-average velocity ($\langle u \rangle$ and $\langle w \rangle$) and not as the oscillation with respect to the time-average velocity (U and W). Hence, substantially, the phase-correlated organised contribution to the velocity ($\tilde{u}$ and $\tilde{w}$) has been removed from the $\overline{TKE}$ values shown in Greco et al. (2013). For the sake of clarity, the definition of the time-average turbulent kinetic energy is reported in Eq. 4.1:

$$\overline{TKE} = \left(\overline{u'^2} + \overline{w'^2}\right)/U_0^2 \tag{4.1}$$

The synthetic jet shows that near the nozzle exit the time-average turbulent kinetic energy acquires values different from zero only on the nozzle edge where turbulent

fluctuations mostly develop because of the shear layer (as occurs in continuous jet (Mi et al. 2007)). $\overline{TKE}$ values increase along the shear layer and penetrate in the jet axis at approximately z/D equal to 3.5, defining the existence of a region where the time-average turbulent kinetic energy level is very low as occurs in a potential core for continuous jets (Abravomich, 1963). Hence, such a region where the time-average turbulent kinetic energy is not penetrated is called, hereinafter, potential core-like region.

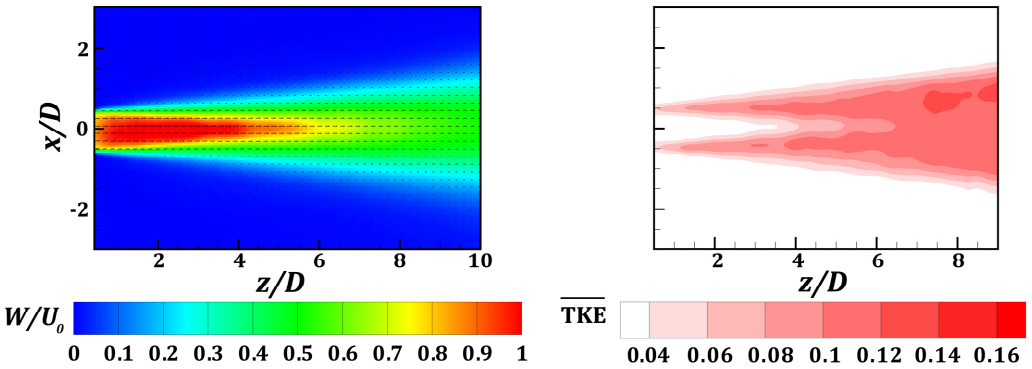

Fig. 4.1 Time-average flow field with velocity vector and contour (left) and time-average turbulent kinetic energy (right)

In addition to that, the time-average centreline axial velocity W_c for a SSJ has been evaluated and depicted in Fig. 4.2 a). Three different regions of the synthetic jet evolution can be observed. The first zone shows an abrupt slope and an increase of the time-average centreline axial velocity from the nozzle exit up to z/D = 1 (the time-average velocity at the nozzle exit should obviously be equal to zero). In the second region, 1 < z/D < 3.5, the time-average centreline axial velocity shows an approximately constant profile while in the last region the velocity decay is different from the typical 1/x law approached in the far field (Glezer and Amitay, 2002). Indeed, according to Cater and Soria (2002), the far field of the jets is defined from the axial location at which the Reynolds stresses show a self-similarity behaviour, which is further downstream at approximately z/D = 25. After the time-average centreline axial velocity peak, according to Shuster and Smith (2007), a region where the flow makes the transition from discrete vortex rings to a nominally steady turbulent jet exists and this region occurs over a greater streamwise extent when L_0/D > 3 (in the present experiments $L_0/D \cong 22$).

Fig. 4.2 b) shows the jet width b, which is defined, according to Shuster and Smith (2007), as the distance between two positions where the axial velocity is half of the local

maximum (or the centreline velocity as done in subchapter 5.1 and 5.2 because of the inlet velocity profile). According to the b streamwise profile two different regions can be observed. As a matter of fact the jet width shows a constant behaviour up to z/D = 3.5, which is ascribed to a cinematic motion of the vortex ring at the beginning of the blowing cycle. After this station, where the transition to a steady turbulent jet begins, the jet width behaviour is characterized by an almost linear growth, as shown by Cater and Soria (2002). This linear growth starts at z/D = 3.5 where the axial velocity assumes an almost bell-shaped profile (as visible in the phase-average flow fields) and the $\overline{TKE}$ penetrates to the jet axis. Moreover the spreading rate of the jet has been determined by fitting the data with a straight-line and the obtained value is 0.23, slightly higher than the empirical spreading rate (about 0.225) of Bremhorst and Hollis (1990), valid in the range 10 > z/D > 40.

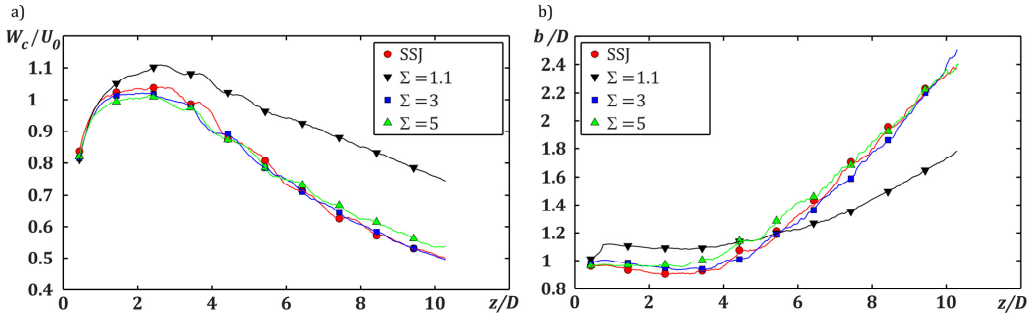

Fig. 4.2 a) Time-average centreline axial velocity for each configuration, b) jet width evolution for each configuration

4.1.2 Twin synthetic jets (TSJ)

Fig. 4.3 shows the time-average axial velocity (left) and $\overline{TKE}$ (right) for the twin jet configurations. For $\sum$ = 1.1, there is an abrupt interaction between the two averaged jets which leads to obtain an almost merged jet on the symmetry axis of the field close to the nozzle exit plane. It has to be highlighted that $\overline{TKE}$ shows a maximum on the axis x/D equal to 0. Such a maximum is due to the 180° phase shift between the two synthetic jets which causes a stronger shear layer. The $\overline{TKE}$ values acquired by the TSJ configuration with $\sum$ = 1.1 are definitely higher than that attained by other configurations.

In the twin jet configuration with a jet-axes-distance of 3 diameters the two averaged jets begin to merge at a distance, from the exit-tube-plane, of about 8 diameters while there is no merging, in the investigated region, for the twin jet configuration with $\sum$ = 5. Such a consideration is valid also for their $\overline{TKE}$ values. Moreover it is possible to see that

for these two configurations the $\overline{TKE}$ distribution for each synthetic jet is equal to the single synthetic jet one.

The time-average centreline axial velocity for the tested configurations are plotted in Fig. 4.2 a). All the curves collapse in the region $z/D < 1$ and tend to zero in agreement with the theory (Smith and Glezer, 1998). Moreover it is possible to highlight that the curves, related to single and twin jet configurations with $\sum = 3$ and $\sum = 5$, collapse in the entire investigated region. This result is obtained, according to Shuster and Smith (2007), because the flow conditions are relative to the same Reynolds number and Strouhal number. This finding leads to consider that the twin jet configurations with $\sum = 3$ and $\sum = 5$ show the same behaviour of the single jet configuration. Regarding to the twin jet configuration with $\sum = 1.1$, although it has the same stroke length of the other jet configurations, its jet centreline velocity values are higher and the linear decrease shows a lower slope because of the strong interaction between the two jets. As a matter of fact the suction cycle of one nozzle creates a depression, which accelerates the other jet in a stronger way than the other jet configurations, leading to an increase of the axial velocity field and, particularly, of the jet centreline velocity. In Fig. 4.2 b) also the jet width for all the twin jet configurations is plotted. In this figure one can highlight that also the twin jet configurations, as the single one, show an initial constant behaviour approximately up to $z/D = 3.5$. Furthermore single and twin jet configurations with $\sum = 3$ and $\sum = 5$ show the same jet width. Hence, also the beginning point of the jet width spread for the twin jet configurations is the same of the single jet one for the same reasons, related to the turbulent kinetic energy and the axial velocity profile, previously explained. The twin jet configuration with $\sum = 1.1$ shows the same beginning point of the jet width spread but a lower jet width rate because of two main reasons: on the symmetry axis, the two jets interact with each other, not being able to spread as a single jet and the presence of the double vortex ring structure (see subchapter 4.2.2) whose vortex rings are not aligned with the jet-axis. Hence the effect, on the jet width rate, is lower than the one provided by a single jet-axis aligned vortex ring and this explains the different behaviour of the twin jet configuration with $\sum = 1.1$.

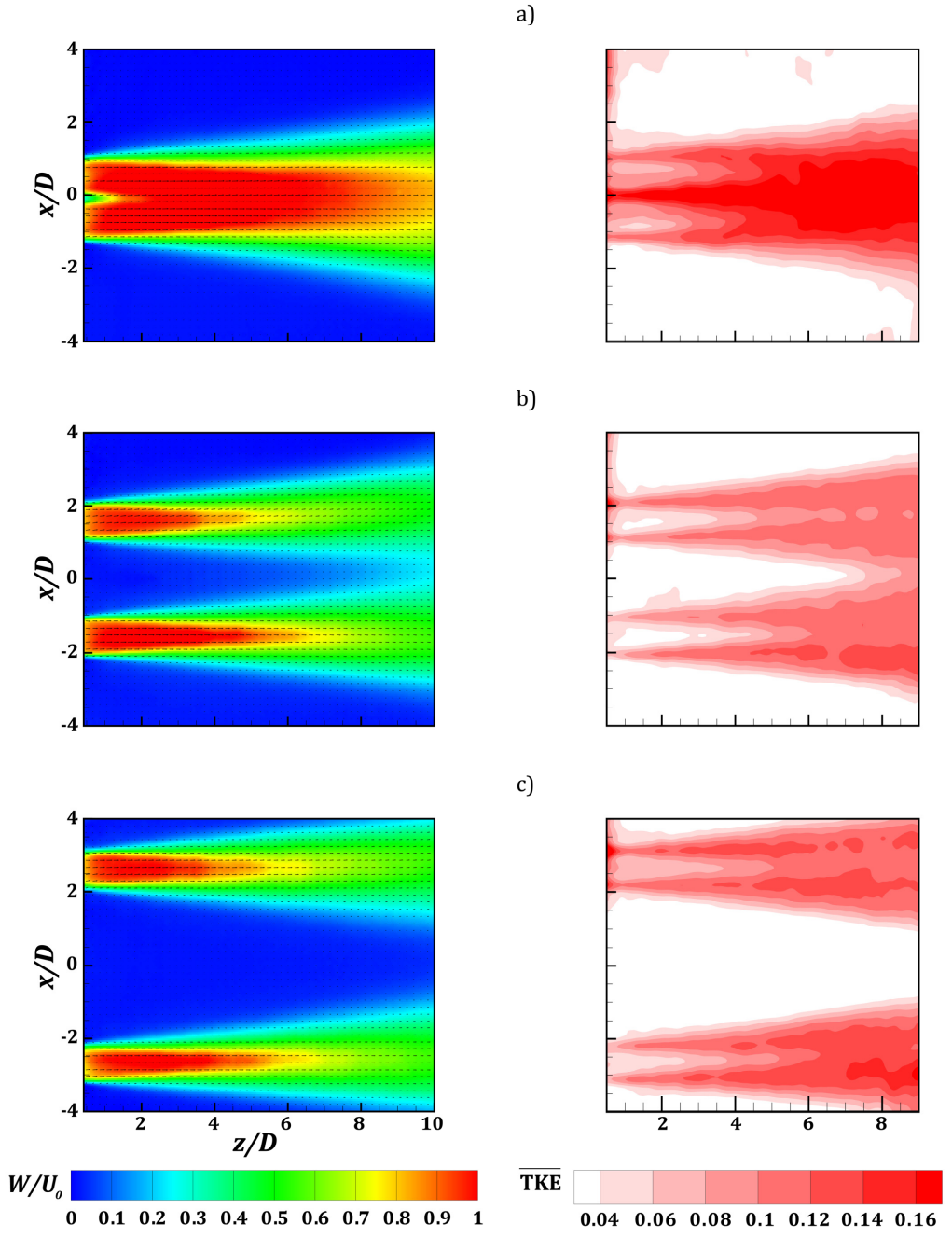

Fig. 4.3. Time-average flow field with vector arrows and contour (left) and time-average turbulent kinetic energy (right) for TSJ with a) $\sum$ = 1.1, b) $\sum$ = 3 and *c)* $\sum$ = 5

4.2 Phase-Average Flow Fields

4.2.1 Single synthetic jet (SSJ)

Fig. 4.4 shows eight phase-average flow fields for the single jet configuration, starting from φ = 0° (the beginning of the jet ejection is chosen as the reference starting point in agreement with Di Cicca and Iuso, 2007), up to φ = 168°. For each phase the velocity vector arrows, placed every 0.2 D in x and z direction, in the bottom half, and every 0.5 D in the z direction in the top half are plotted. The contour plots of the phase-average axial velocity and of the phase-average turbulent kinetic energy (considering only the turbulent in-plane components u' and w' as reported, for the sake of clarity, in Eq. 4.2) are superimposed to the vector plots in the bottom and top half respectively. Since the exit velocity begins to increase at φ = 0°, the shear layer starts to roll up and by φ = 48°, the vortex ring is completely formed and placed at about 2 diameters from the exit.

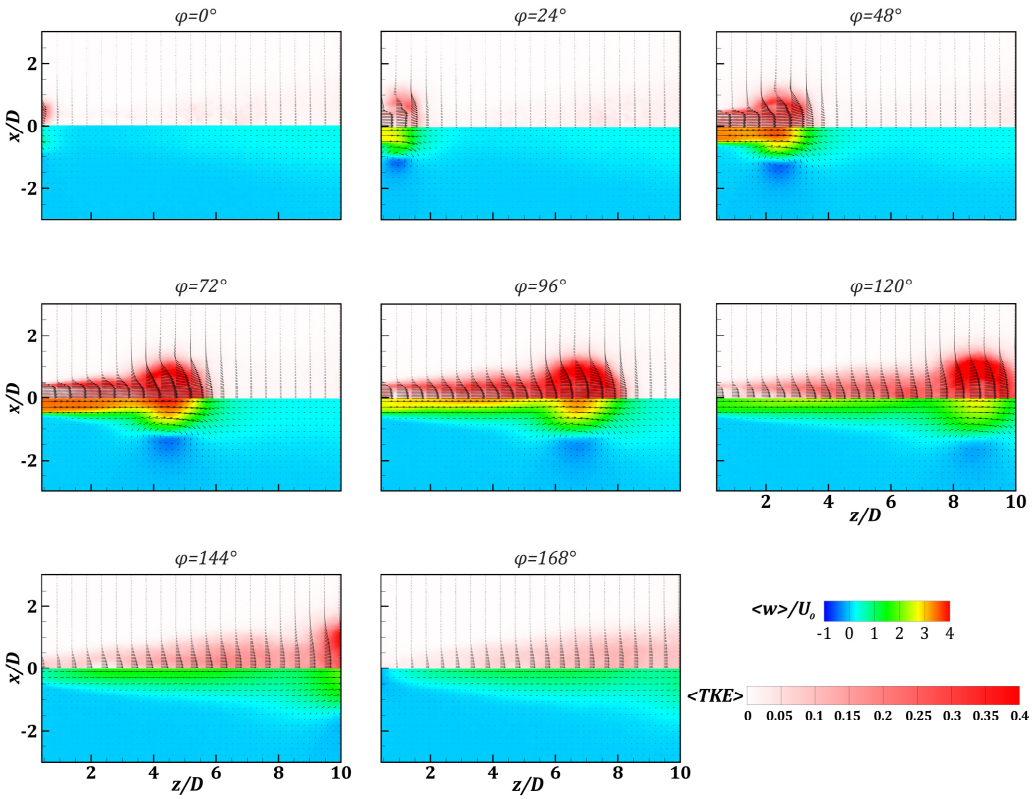

Fig. 4.4 Phase-average flow field (bottom) and phase-average turbulent kinetic energy (top) for the SSJ

From φ = 48° to φ = 144° the synthetic jet develops and the vortex ring weakens. At φ = 168° the ring has moved out of the measurement zone.

The in plane turbulent kinetic energy is computed as:

$$< TKE >= (< u'^2 > + < w'^2 >)/U_0^2 \tag{4.2}$$

It is interesting to focus on the development of the profile of the axial velocity and of the <*TKE*>. At φ = 24° the circular synthetic jet starts forming and a top hat profile of the axial velocity is visible near the exit nozzle. From φ = 24° to φ = 120° the circular synthetic jet develops and the axial velocity profiles, on the jet-axis, begins to vary from a top hat profile ($0 < z/D < 3.5$ at φ = 72°) to a bell-shaped one ($z/D > 3.5$). This aspect is in analogy with the potential core in conventional turbulent jets. Also the <*TKE*> penetrates inside the jet core for φ = 72° only after 3.5 diameters from the nozzle exit and a triangular core, where the <*TKE*> is not already penetrated, can be defined in analogy with turbulent jets (Abramovich, 1963).

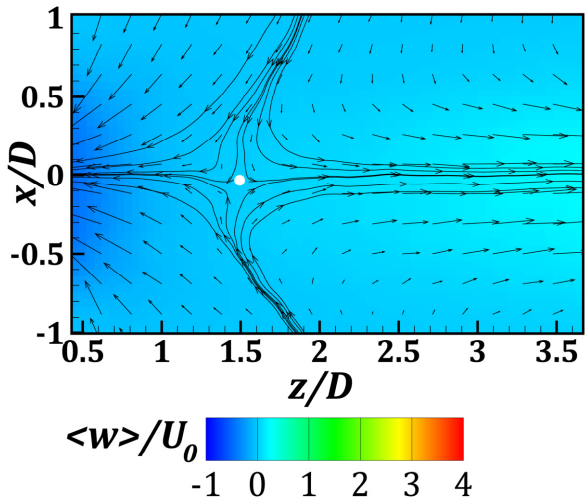

Fig. 4.5 Phase-average flow field with saddle point (white spot) for the SSJ at φ = 264°

As shown in Fig. 4.5 for φ = 264°, during the suction cycle, that starts at φ = 180°, the flow field is characterized by the presence of a saddle point (indicated in Fig. 4.5 with a white spot) that divides the flow field in two subparts, which show opposite sign of the

axial velocity. The saddle point has not always the same z/D station and reaches a maximum distance, from the tube exit, of about 1.5 diameters at φ = 264°.

4.2.2 Twin synthetic jets (TSJ)

Figs. 4.6, 4.7 and 4.8 show the contour plots of the phase-average axial velocity for the three twin jet configurations; the axis x/D = 0 coincides with the axis of the symmetry between the two jets. For the sake of brevity only eight phases representing a half cycle are included, thanks to the symmetry between the two jets.

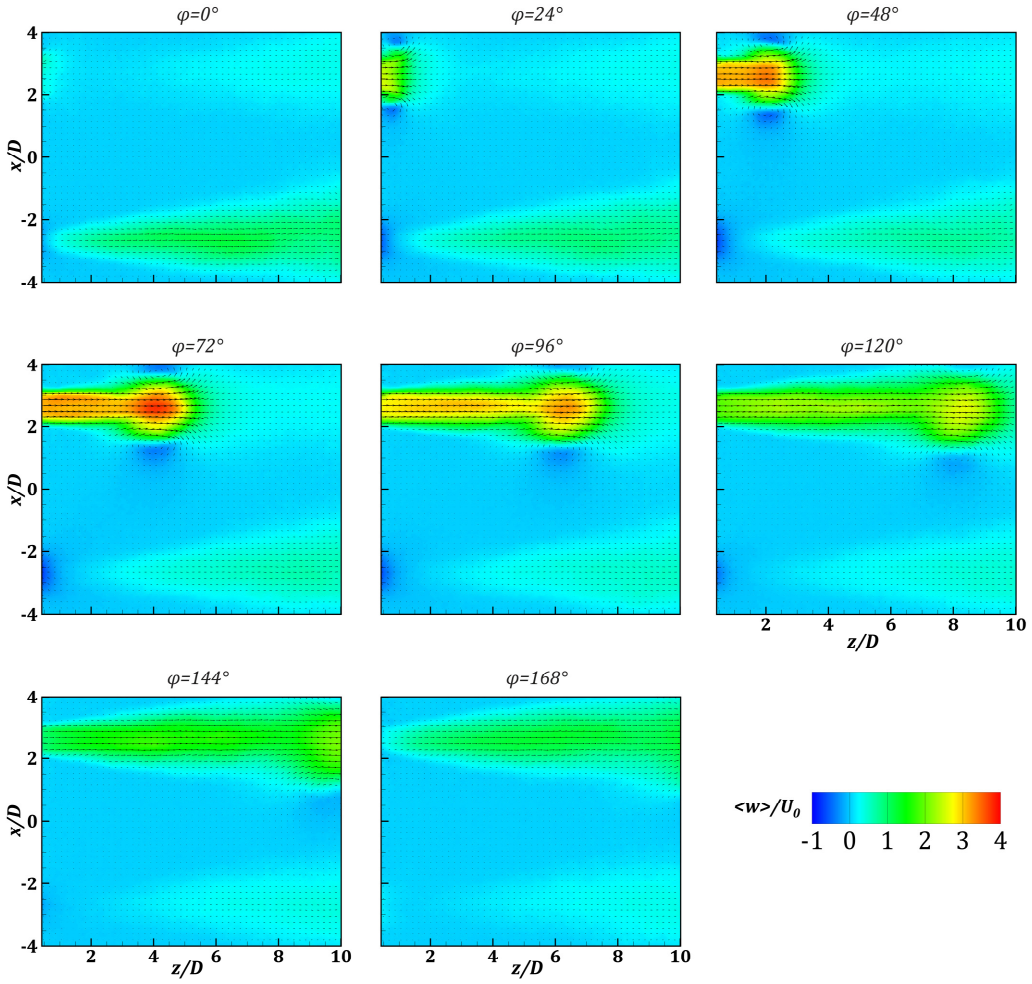

Fig. 4.6 Phase-average flow field for the twin jet configuration with ∑ = 5

For each configuration, the 180° phase shift existing between the two jets is clearly detectable. Indeed, in each figure it is possible to note that, while the top sub-cavity is

generating its synthetic jet, the bottom one is starting the suction cycle. Also in the TSJ configuration each jet shows, in the ejection cycle, a vortex ring surrounding it and the velocity maximum is again positioned in the centre of the vortex ring itself; a saddle point is again observed during its suction cycle.

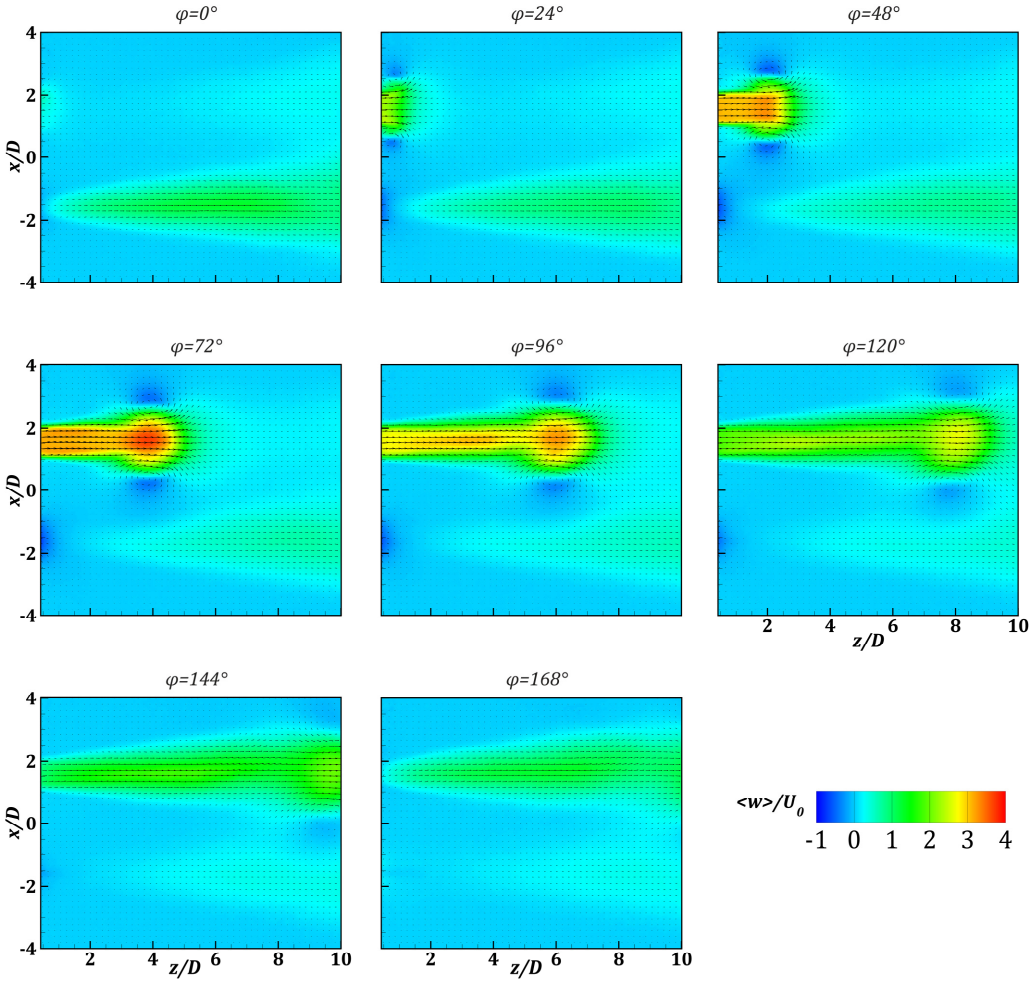

Fig. 4.7 Phase-average flow field for the twin jet configuration with $\sum = 3$

In Fig. 4.9 contour plots of the phase-average turbulent kinetic energy and axial velocity profiles are shown at $\varphi = 72°$. For the tested twin jet configurations it is possible to detect the triangular region where the *<TKE>* is very low, which has the same extension of the one already found in the single jet configuration ($0 < z/D < 3.5$ at $\varphi = 72°$). According to Smith and Glezer (1998) the trajectory of the vortex ring has been computed

by identifying the position of peak centreline velocity, which reflects the passage of the centre of a vortex ring. The trajectory, for the single jet configuration, shows a linear behaviour as the one found by Shuster and Smith (2007).

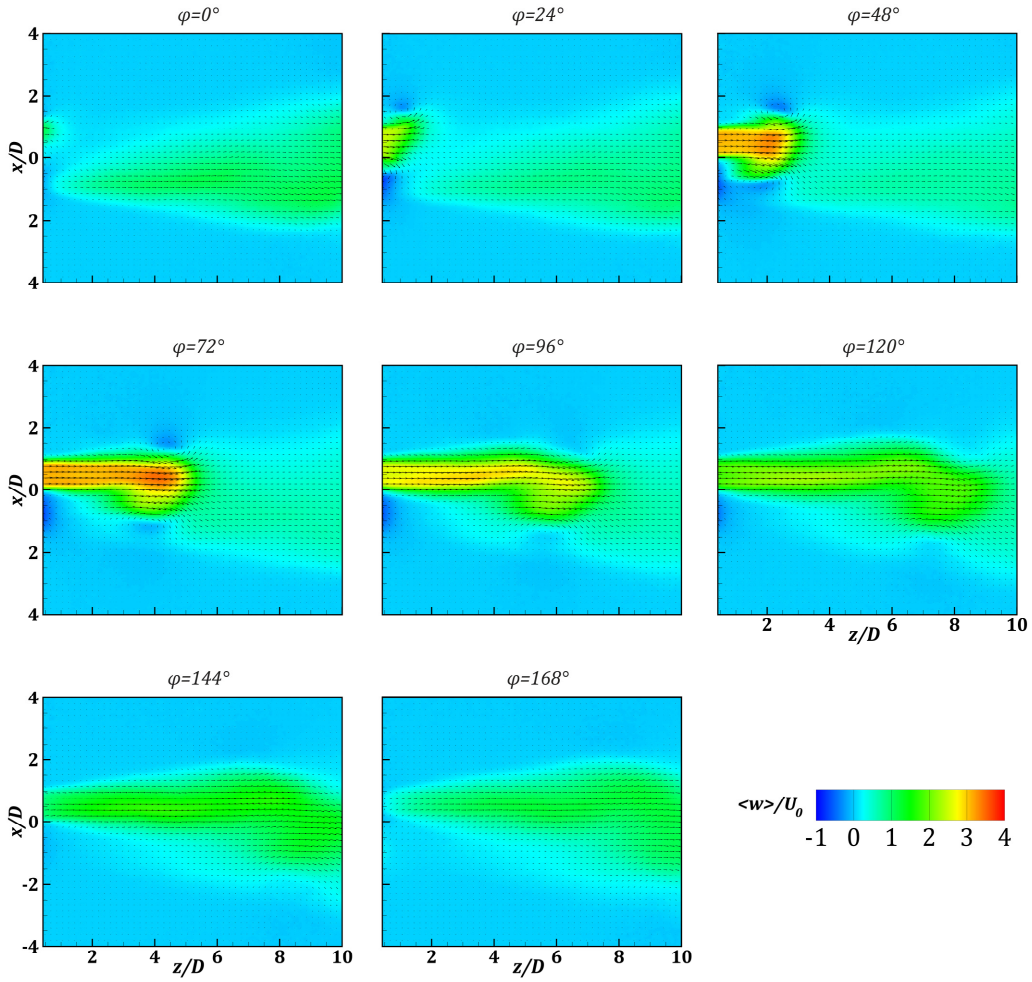

Fig. 4.8 Phase-average flow field for the twin jet configuration with $\sum$ = 1.1

By fitting the present experimental values with a linear regression, the following linear formula is obtained:

$$\frac{z}{L_0} = 1.3\frac{t}{\tau} - 0.08 \tag{4.3}$$

The comparison between the trajectory of the vortex ring for the single jet configuration and the one for the twin jet configurations with $\sum = 3$ and $\sum = 5$ is shown in Fig. 4.10. The curves show a linear growth very similar to the one of the single jet configuration. The correlation coefficient R^2 with respect to the regression line (Eq. 4.3), is estimated to be equal to 0.9931. These results lead to consider,again, that the twin jet configurations with $\sum = 3$ and $\sum = 5$ show the same behaviour of the single jet configuration.

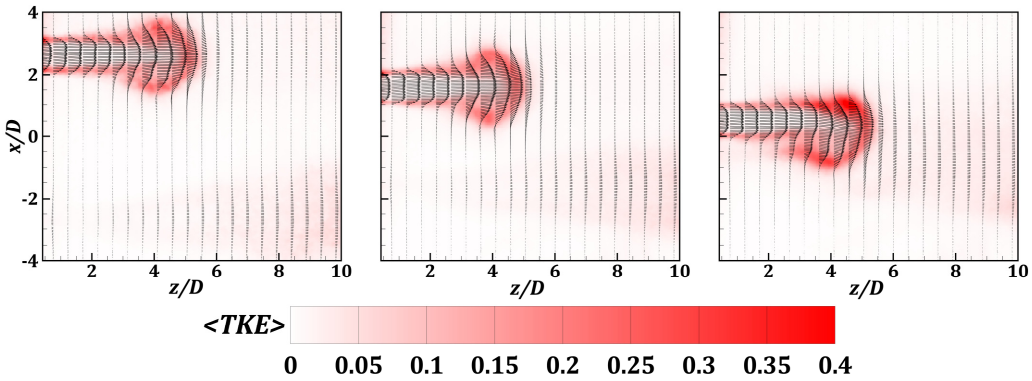

Fig. 4.9. Phase-average turbulent kinetic energy with axial velocity vectors for TSJ at $\varphi = 72°$ with $\sum = 5$ (left), $\sum = 3$ (centre) and $\sum = 1.1$ (right)

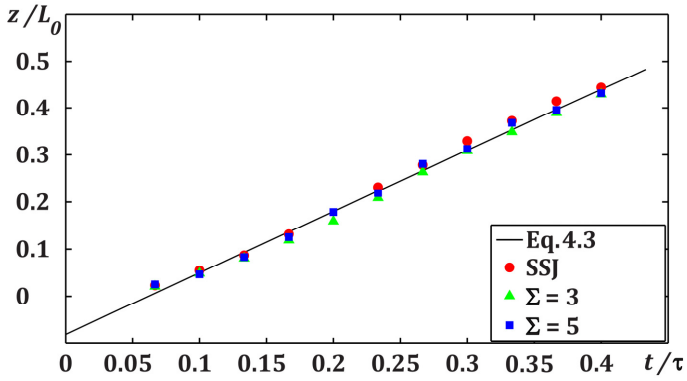

Fig. 4.10. Trajectory of the vortex ring fort the SSJ and the TSJ with $\sum$ equal to 3 and 5

For the twin jet configuration with $\sum = 1.1$ it is not possible to detect the vortex ring centre through knowing the position of the velocity peak because, as visualized in Fig. 4.11, a double vortex ring structure exists. Indeed one can notice that, at $\varphi = 36°$, when the

top jet is forming, only the top footprint of the vortex ring is visible while the bottom one is created at φ = 48°. This phenomenon is ascribed to the suction cycle of the bottom nozzle which delays the formation of the vortex ring and causes the presence of a double-core in the bottom vortex ring, (see Fig. 4.11 from φ = 60° to φ = 84°), which aggregate at φ = 96°. In Fig. 4.11 (φ = 96°) one can note that the top footprint starts splitting in two, as shown in φ = 96° and φ = 108°.

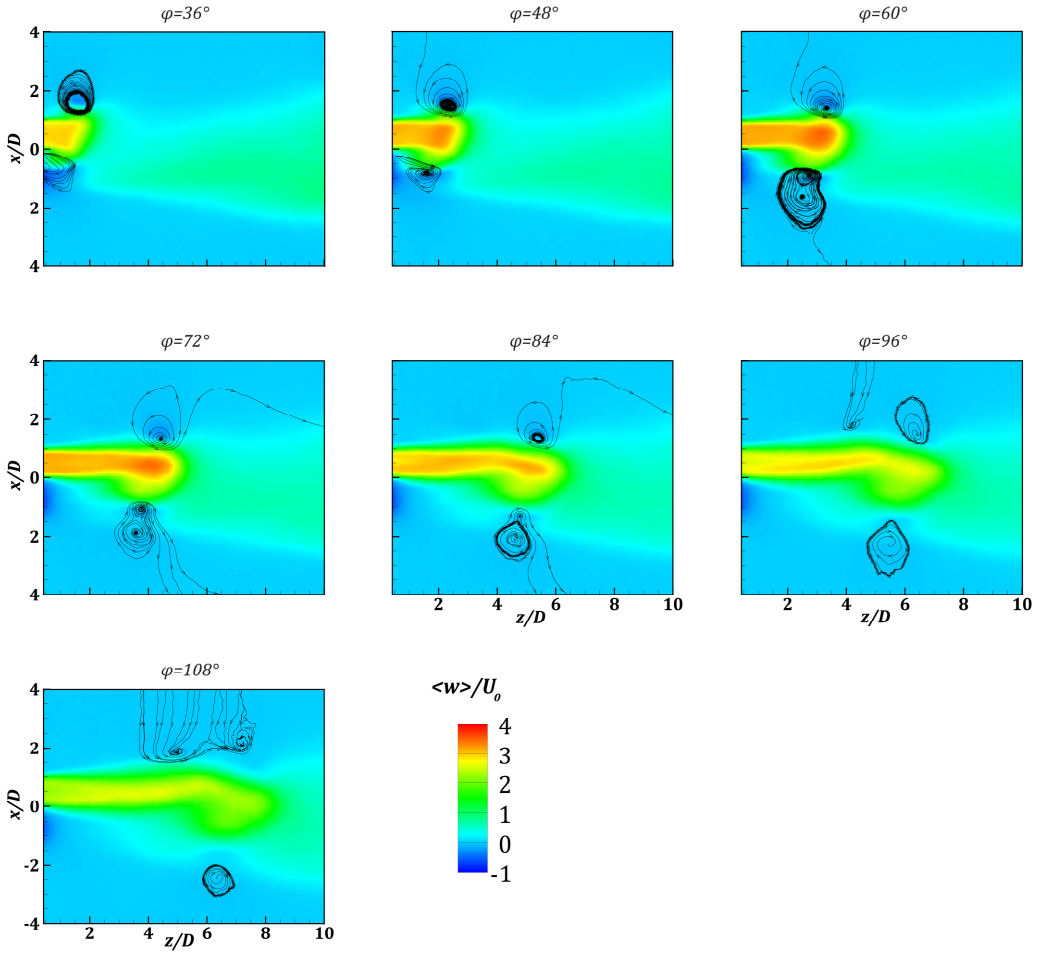

Fig. 4.11 Formation and evolution of the double vortex ring structure

Consequently at φ = 108° it is possible to detect three footprints, which are the evidence of the presence of a double vortex ring structure. The three footprint positions allow to figure out that the double ring vortex structure consists in two vortex rings whose axis is not parallel to the jet one, as shown in Fig. 4.12. The obtained double vortex

ring structure is analogue to that described by Webster and Longmire (1998) in their study of the evolution of vortex rings issued from cylindrical pipes with inclined exit. This structure is the reason why the axial velocity peak is located upstream with respect to the other twin jet configurations. Indeed in Fig. 4.11 at φ = 96° it is possible to see that the velocity peak is at station z/D = 4 instead of z/D = 6 as in the other twin jet configurations, as shown in Figs. 4.6 and 4.7 at the same phase φ = 96°.

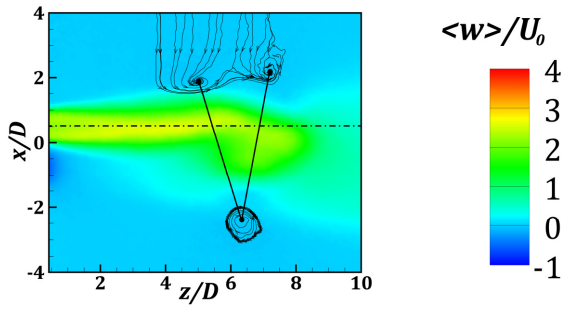

Fig. 4.12 Intersections formed by the double vortex ring structure and the top-jet-axis at phase φ = 108°

Chapter 5

Impinging Synthetic Jets

The present Chapter is divided in two main subchapters: low Reynolds number (subchapter 5.1) and high Reynolds number (subchapter 5.2) impinging synthetic jets.

The first subchapter deals with the analysis of the impinging flow field (subchapter 5.1.1) and heat transfer (subchapter 5.1.2) of a single synthetic jet compared to the twin one at the same operating condition (i.e Strouhal number equal to 0.024 and Reynolds number equal to 5100). The influence of the dimensionless jet-axes distance (Σ) on the flow field and the heat transfer has been evaluated.

In subchapters 5.1.1.1 and 5.1.1.2, the time-average features of the impinging flow field for single and twin synthetic jets (for Σ equal to 1.1 and 3), respectively, are analysed. In particular the entire flow field morphology and the behaviour over the impinging plate of the velocity components, according to the triple decomposition, are shown.

Then in subchapters 5.1.1.3 and 5.1.1.4, the evolution of the entire flow field and the behaviour of each velocity component, for single and twin synthetic jets (only for Σ equal to 1.1) respectively, is discussed through the phase-average measurements.

In subchapter 5.1.2 the heat transfer behaviour of single and twin impinging synthetic jets (for Σ equal to 1.1, 3 and 5) is shown. The time-average heat transfer features are discussed in subchapter 5.1.2.1 for both configurations and the phase-average heat transfer behaviour is described in subchapter 5.1.2.2.

In subchapter 5.2, the impinging flow field of a single synthetic jet at high Reynolds number (equal to 16000) has been analysed. The effect of the Strouhal number (equal to 0.025, 0.05 and 0.1) on the flow field has been studied. Such a study could be useful for several industrial applications where high Reynolds number impinging continuous jets are employed (i.e. blade cooling, paper drying, glass tempering etc.).

The time-average flow field of the single synthetic jet is discussed in subchapter 5.2.1. The flow field morphology and the behaviour over the impinging plate of the velocity components, according to the triple decomposition, are analysed.

In subchapter 5.2.2 the evolution of the synthetic jet and the behaviour of the velocity components are discussed by using the phase-average measurements.

5.1 Low Reynolds number Synthetic Jets

5.1.1 Flow field measurements

As stated in Chapter 3.1.1 the results are shown following the triple decomposition. In subchapter 5.1.1.1 the time-average flow fields and turbulent statistics are shown as maps. Only the maps for H/D equal to 2 and 6 are shown for the sake of brevity while the behaviour over the plate of all the quantities (mean and statistics) is plotted.

Then in subchapter 5.1.1.2 the time-average flow fields for the several values of jet-axes-distance are depicted (always only for H/D equal to 2 and 6). Even for these configurations the behaviour of flow field parameters near the wall is reported.

In subchapter 5.1.1.3 and 5.1.1.4 the phase-average behaviour of these two main configurations (H/D equal to 2 and 6) is described for SSJ and TSJ (only the $\sum$ equal to 1.1 case).

Since the time-average flow field velocity components are symmetric with respect to the z axis for all the velocity quantities an average between the $x < 0$ and $x > 0$ maps have been performed in order to reduce the measurement noise (for all the jet-axes-distance). The same approach has been used also for all the phase-average measurements of the single synthetic jet.

5.1.1.1 Time-average flow field for SSJ

The time-average axial and radial velocity maps are shown only for H/D equal to 2 and 6, in Fig. 5.1. (other maps are not reported for the sake of brevity). These two configurations are chosen because the flow field behaviour is different for $H/D < 4$ and $H/D > 4$. The mean-squared axial and radial phase-correlated organised contribution to the velocity, axial and radial turbulence and the time-average Reynolds stress (for phase-correlated and turbulent components) are depicted in Figs. 5.2-5.4. As it is possible to see the morphology of time-average velocity components (Fig. 5.1) is completely different between the two H/D configurations. For H/D equal to 2 the flow field is affected by the presence of the impinging plate which influences the flow field up to about 1 D upstream. For this reason in the configuration with H/D equal to 2 the centreline velocity does not attain its maximum velocity (approximately 1.05 U_0).

The time-average radial velocity over the plate is higher for the shortest configuration; moreover, their distributions are completely different. As a matter of fact for *H/D* equal to 2 the time-average radial velocity component shows a region (in the axial direction) of high velocity which increases from the stagnation point up to *x/D* equal to about 0.7. It has a minimum at *x*/D equal to 1.2 and then increases again. Differently, at *H/D* equal to 6, that minimum is located at *x/D* equal to 1.75 and the starting increase is not so sharply sloped.

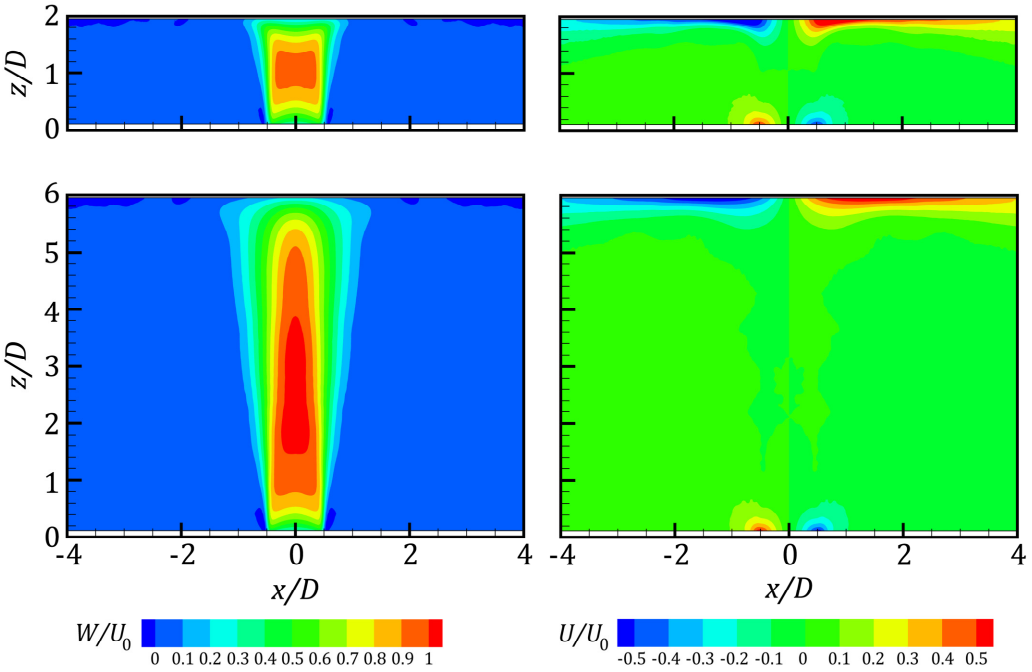

Fig. 5.1 Time-average axial (left) and radial (right) velocity maps for *H/D* equal to 2 (top) and 6 (bottom)

In Fig. 5.2 it is worth noting that the mean-squared axial and radial phase-organized velocity components resemble the time-average axial and radial velocity components, so, the same considerations can be drawn. Furthermore the mean-squared axial phase-correlated organized contribution to the velocity component attains values which are ten times greater than those in the radial direction (in the region not affected by the impinging plate).

This can be explained considering that these two variables are related to the sinusoidal external force which generates the flow field. This sinusoidal external force perturbs the flow field much more in the axial direction than the radial one and, also for this reason, the maximum value of the mean-squared axial phase-correlated organized contribution to the velocity component is located on the nozzle exit. It is important to highlight how the jet approaches the impinging plate. Indeed in the shortest H/D configuration, the axial profile (for both the variables W and $\overline{\widetilde{w}^2}$) presents a double peak profile (symmetric with respect to x/D equal to 0), with a minimum on the jet axis, differently from the H/D equal to 6 configuration where such a profile is bell-shaped.

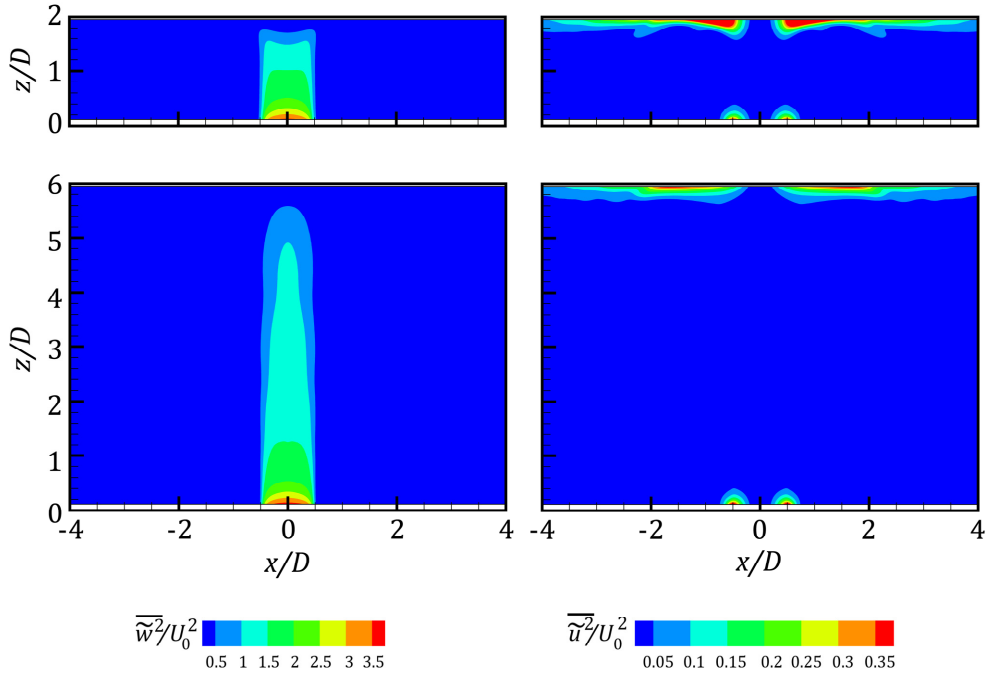

Fig. 5.2 Mean-squared axial (left) and radial (right) phase-correlated organised contribution to the velocity maps for H/D equal to 2 (top) and 6 (bottom)

This behaviour can be ascribed to the mean-squared turbulent component. Indeed in Fig. 5.3 a potential core-like region (where the turbulence is very low) has an extension of about 3.8 D. Furthermore the mean-squared turbulent axial component shows its greatest value along the shear layer. Such values are higher for the H/D equal to 6 configuration.

This fluctuation starts at the nozzle exit and then spreads until merging on the jet axis at $z/$D equal to about 3.8. Differently, the mean-squared radial turbulent component attains its maximum value near the wall for the shortest nozzle-to-plate distance. Moreover the mean-squared radial turbulent fluctuation starts at z/D equal to about 0.4 D because (as visible in subchapter 5.1.1.3) in this region the fully-formation of the vortex ring occurs.

These mean-squared turbulent velocity component maps are very similar to what presented in Narayanan et al. (2004) and Roux et al. (2011) for a turbulent slot and circular continuous impinging jet, respectively.

Moreover the value of the mean-squared axial turbulent velocity component, in the region which is not affected by the impinging plate presence, shows a value which has an intensity of about two times greater than the radial ones as also seen in Narayanan et al. (2004).

On the contrary the situation is completely different over the impinging plate. Indeed, the mean-squared axial turbulent velocity component has a value which is about 40% of the radial one differently from what found by Knowles et al (1998) for a turbulent circular continuous impinging jet where such a ratio was equal to 60%.

Regarding the time-average phase-correlated organized contribution to the velocity Reynolds stress (Fig. 5.4), it is possible to see that the maximum values are near the edge of the nozzle exit in both configurations but, in the shortest one (H/D equal to 2), similar values are also attained near the impinging plate.

Differently, the time-average turbulent velocity Reynolds stress shows the highest value along the shear layer and near the impinging plate. As matter of fact for H/D equal to 2 the values near the impinging wall and along the shear layer are approximately the same (slightly higher the one on the plate) as also reported in Narayanan et al. (2004). Instead as H/D increases the value near the impinging plate decreases.

It is whore noting that the time-average turbulent Reynolds stress near the impinging plate shows a value which is opposite to the shear layer one located on the same region (i.e. $x > 0$ or $x < 0$). The same time-average turbulent Reynolds stress behaviour has been detected by Narayanan et al. (2004).

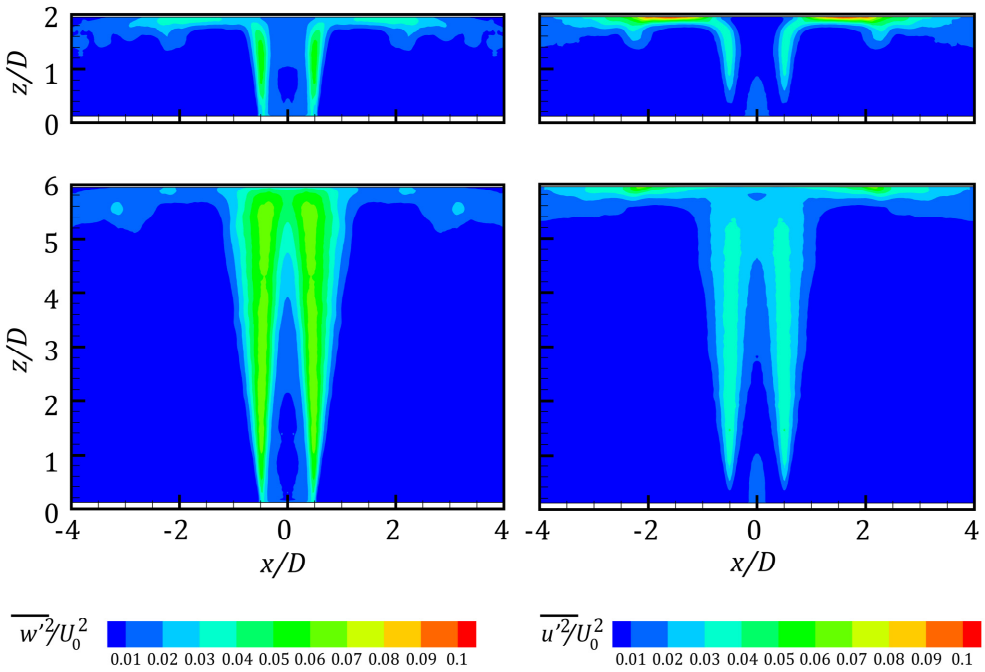

Fig. 5.3 Mean-squared axial (left) and radial (right) turbulent velocity maps for H/D equal to 2 (top) and 6 (bottom)

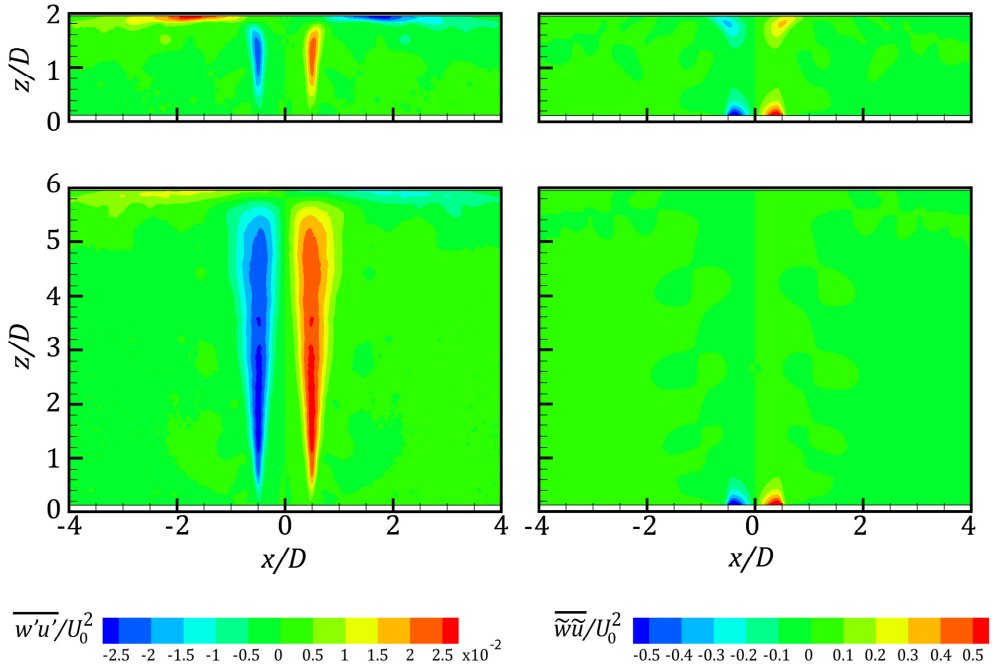

Fig. 5.4 Time-average turbulent (left) and phase-organized contribution to the velocity (right) Reynolds stress maps for H/D equal to 2 (top) and 6 (bottom)

In Figs. 5.5 and 5.6 the time-average centreline axial velocity and the jet width for all *H/D*'s configurations are depicted. It is possible to detect that, as reported by O'Donovan (2005) and Roux et al. (2011), the impinging plate influences the flow field up to approximately 1 *D* upstream. As told before the *H/D* equal to 2 and 4 configurations do not attain the maximum value which is reached by other configurations at approximately 3.5 *D*. For each configuration both W_c and *b* starts diverging from the other curves at about 1 *D* before the impinging plate. Obviously the decrease of the time-average centreline axial velocity component, as the jet width increases, is related to the impinging plate presence which affects the approaching synthetic jet causing a deceleration and a suddenly spreading of the jet itself. Such effects are much more visible at shorter *H/D* configurations because for high nozzle-to-plate distances the jet has already spread (accordingly to the jet width) and its velocity is already decreased enough.

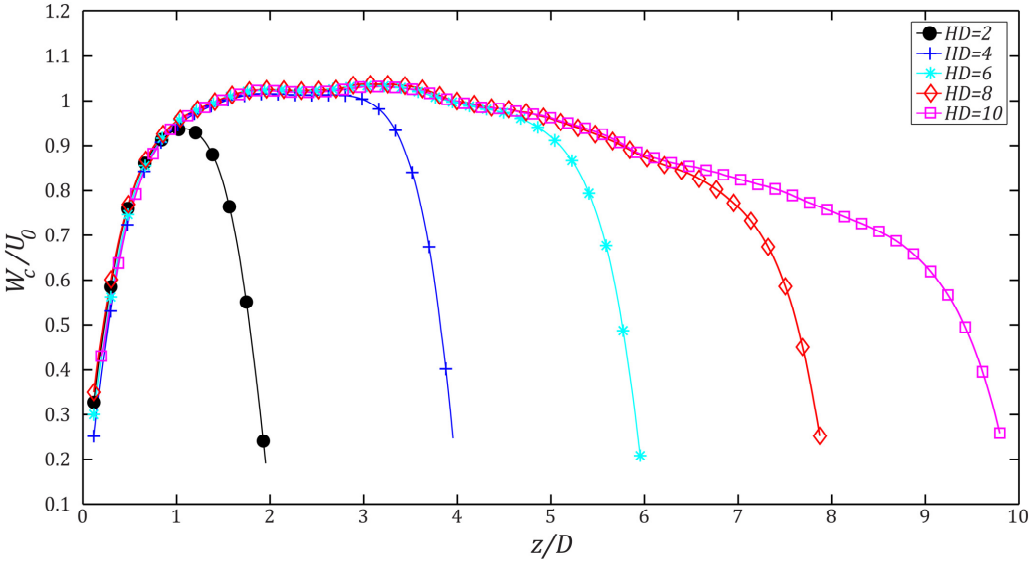

Fig. 5.5 Time-average centreline axial velocity for all *H/D*'s configurations

In Figs. 5.7-5.10 the profiles of these velocity components near the wall (approximately 0.05 *D* far from the impinging plate) are depicted.

In Fig. 5.7 the time-average radial and axial velocity components are depicted. The time-average axial velocity component at *H/D* equal to 2 shows a local minimum on the jet axis and then a maximum at *x/D* equal to -0.5 as also found by Rohlfs et al. (2012). This is the same position where the heat transfer maximum is located (see the discussion on the

inner-ring shaped region in subchapter 5.1.2). As the radial position increases the curve shows some lateral oscillations (around 2 diameters from the jet axis) characterized by low amplitude. Such a behaviour is ascribed to the generation of a counter rotating vortex ring on the impinging plate. At *H/D* equal to 4 the inner peak is barely visible at a radial location of 0.2 *D*. For this nozzle-to-plate distance the maximum value of the time-average axial velocity component on the jet axis is reached. For higher radial position the shape of this profile is similar to what obtained at *H/D* equal to 2. As *H/D* increases the peak (located on the jet axis) decreases and the later oscillations are barely visible at *H/D* equal to 6 and 8 or damped for higher *H/D* configurations.

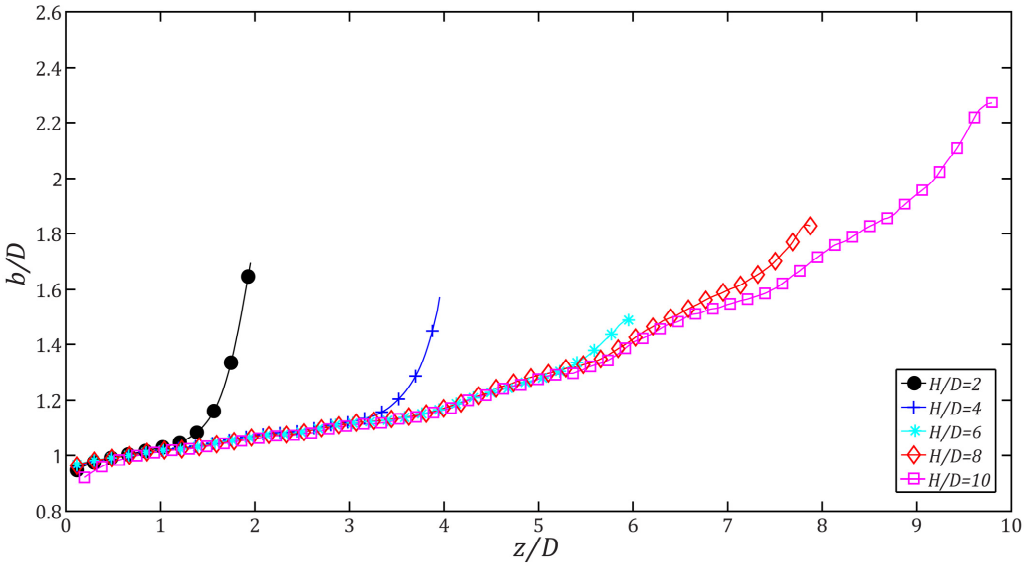

Fig. 5.6 Jet width for all *H/D*'s configurations

For the time-average radial velocity component, at *H/D* equal to 2, a maximum is found at *x/D* equal to about 0.75 and its value is about 0.8 U_0. Such a value is higher than that obtained by Roux et al. (2011) and O'Donovan (2005). Then lateral oscillations can be barely visible around *x/D* equal to 2. Such oscillations are located in the same position where the counter rotating ring vortex near the impinging plate is located (as shown and discussed in subchapter 5.1.1.3). At *H/D* equal to 4 the maximum has decreased and its radial location is at about 0.9 *D*. After that the curve shows the same shape of the *H/D* equal to 2 configuration. Indeed also for this configuration the very small lateral oscillations, caused by the counter rotating ring vortex generation near the impinging

plate, are barely observable. As *H/D* increases, the first maximum becomes less evident (and decreases for *H/D* higher than 6) and shifts towards higher *x/D* accordingly to the jet width behaviour and the lateral oscillations are damped (*H/D* equal to 6) or disappeared (*H/D* higher than 6).

For both components the high values (the ones included in the region where the synthetic jets impinges) are mainly originated by the column of fluid behind the vortex ring, while, the lateral oscillations are caused by the vortex ring that sweeps the impinging plate. Indeed for Strouhal number lower than 0.25 the synthetic jet (as describe also in McGuinn et al. (2013)) is composed by a leading vortex ring and a following column of fluid in the vortex ring rear.

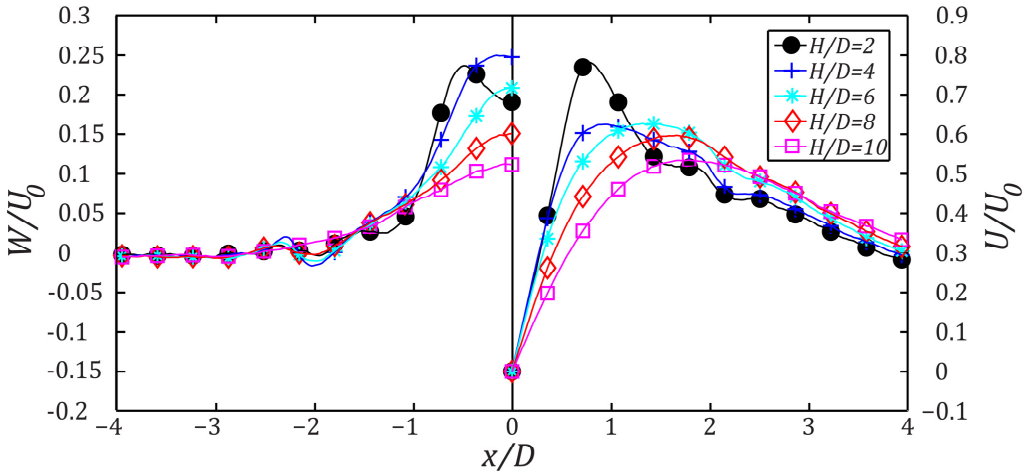

Fig. 5.7 Time-average axial (left) and radial (right) velocity components over the impinging plate for all *H/D*'s configurations

As stated before also the profile of the mean-squared phase-correlated organized contribution to the velocity (Fig. 5.8) over the plate resemble those of the time-average velocity components. The mean-squared axial phase-correlated organized contribution to the velocity component profile shows two peaks at *x/D* equal to 0.5 and about 2 at *H/D* equal to 2 (as occurs for *W*). For this configuration, a local minimum is present in the stagnation point. As *H/D* increases the first peak decreases and shifts towards the *x/D* equal to 0 position while the second one tends to *x/D* equal to 2. For *H/D* equal to 4 configuration the highest values are reached at *x/D* equal to 0 and 2 (the second peak). Such values decrease as *H/D* increases.

For the radial component, the first peak and the lateral oscillation are clearly detectable, for *H/D* equal to 2, at the same position of those of *U*. As *H/D* increases, the first peak decreases shifts towards greater *x/D* while the lateral oscillations damp.

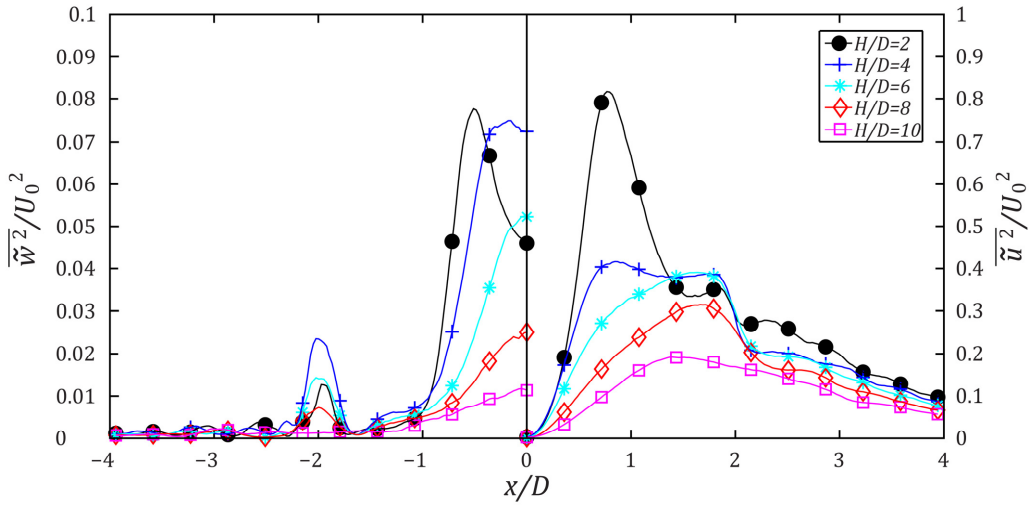

Fig. 5.8 Mean-squared axial (left) and radial (right) phase-correlated organised contribution to the velocity components over the impinging plate for all *H/D*'s configurations

Considering the mean-squared axial turbulent velocity component (Fig. 5.9) at *H/D* equal to 2, it is possible to highlight that a minimum is present on the jet axis because this value of nozzle-to-plate distance is lower than the potential core-like region extension. At *x/D* equal to -0.65 a first peak is located. Such a peak is caused by the shear layer influence. A second peak, higher than the first one, is at a radial position of -1.85 *D* from the jet axis This peak position and value is related to the presence of the counter rotating vortex ring near the impinging plate (as visible in subchapter 5.1.1.3). The same position, for the maximum axial fluctuation on the impinging plate, has been found also by O'Donovan (2005) and Roux et al. (2011). Also at *H/D* equal to 4 a minimum is found on the jet axis for the same reasons previously explained. The first peak, seen for the shortest configuration, has shifted toward the jet axis because it is related to the shear layer which is entering the jet axis (this nozzle-to-plate distance has approximately the same extension of the potential core-like region). The second peak has moved to *x/D* equal to -2.2 *D* and its value is decreased because is influenced by the counter rotating vortex ring which is less energetic. Its position is at higher radial position as reported in O'Donovan

(2005). For *H/D* equal to 6, the first peak has almost arrived to the stagnation point because the shear layer is completely inside the jet. The second peak (radial position equal to 2.2 *D*) value is a third lower than *H/D* equal to 4 case because the counter rotating vortex ring near the wall is partially generated. For this reason, as reported in subchapter 5.1.2, the second maximum of the heat transfer distribution is not detected (as also reported by Roux et al.(2011) for *H/D* equal to 5). Such a peak is not present for continuous impinging jet (Roux et al. (2011)) because the ring vortex, generated by the Kelvin-Helmholtz instability in continuous jet, is not so energetic to create a strong enough counter rotating vortex ring on the wall differently from the ring vortex generated by the synthetic jet ejection phase. Anyway this peak is located in a position where no more detection of the second heat transfer maximum is present but only a change in its slope (as also reported by Narayanan et al. (2004)). At *H/D* equal to 8 the maximum value in the stagnation point is reached because of the completely mixing of the shear layer while the second peak is disappeared. In the maximum nozzle-to-plate configuration the stagnation value starts decreasing. Differently from what reported by Roux et al. (2011) for a circular impinging continuous jet, the heat transfer distribution for an impinging synthetic jet at *H/D* greater than 4 does not resemble the mean-squared axial turbulent velocity component distribution.

Considering *H/D* equal to 2 it is possible to note that a plateau, for mean-squared radial turbulent velocity component (Fig. 5.9), is present from *x/D* equal to 0 to 0.5, then an abrupt increase is present with a peak at approximately 1.6 *D* (similar to what shown in O'Donovan (2005)). A second mild peak is present at *x/D* equal to 2 and then a monotonically decrease characterizes the curve. As *H/D* increases two main features can be inferred: the value on the jet axis increases because *H/D* becomes higher than the potential core-like region (the maximum is attained at *H/D* equal to 8) and the peak decreases shifting from a radial position of 2 *D* to 2.1 *D*. Differently from continuous impinging jet (O'Donovan (2005)) the location of the second peak is not so influenced by the *H/D*. Moreover, the position of the peak, at *H/D* equal to 2 and 4, is near the position where the second heat transfer maximum is present (subchapter 5.1.2).

Focusing our attention on the jet axis, the values of the axial turbulent component are lower than the corresponding phase-correlated one for *H/D*< 6. Such a difference is maximum at *H/D* equal to 4 and then decreases. For *H/D* >6 the behaviour is the opposite.

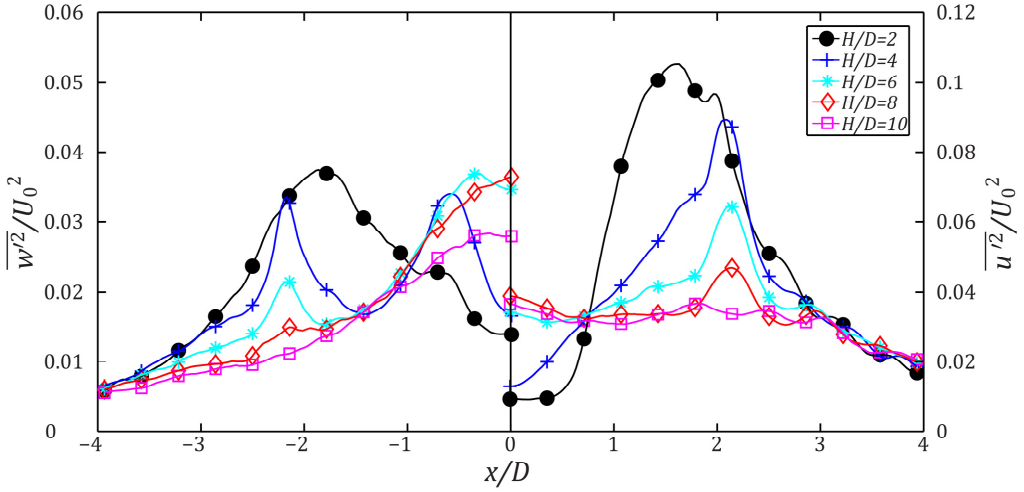

Fig. 5.9 Mean-squared axial (left) and radial (right) turbulent velocity components over the impinging plate for all H/D's configurations

In Fig. 5.10 the time-average turbulent and phase-correlated-organized contribution to the velocity Reynolds stress are depicted. The time-average turbulent Reynolds stress shows a peak at approximately x/D equal to about 1.7. As H/D increases, this peak decreases and for H/D higher than 4 disappears. The values attained by the mean-squared turbulent Reynolds stress are very similar to those found by Narayanan et al. (2004).

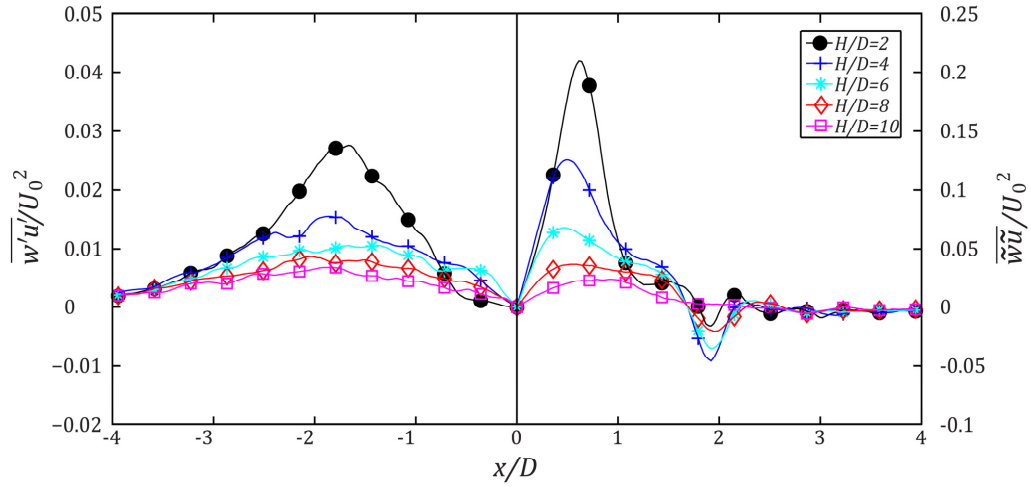

Fig. 5.10 Time-average turbulent (left) and phase-correlated organized contribution to the velocity (right) Reynolds stress over the impinging plate for all H/D's configurations

For the time-average phase-correlated organized contribution to the velocity Reynolds stress, a first peak is detected at *x/D* equal to 0.6 then lateral oscillations, with a minimum located at *x/D* equal to about 1.9, are observable. The maximum located at *x/D* equal to 0.6 decreases with *H/D* increases differently from the minimum located at *x/D* equal to 1.9 which attains its highest value for *H/D* equal to 4 and then decreases.

5.1.1.2 Time-average flow field for TSJ

In Fig. 5.11 the time-average axial and radial velocity maps for *H/D* equal to 2 and 6 are depicted. As it is possible to see the axial velocity component acquires its maximum at *x/D* equal to 0 where the two jets merge. Its value is higher than that attained by the SSJ configuration. As *H/D* increases the region where the velocity is higher than 1 is wider than the SSJ case. Even for the radial velocity component the values are higher because the wall jet is related of the contribution of two wall jets generated by both impinging synthetic jets. Furthermore, varying the nozzle-to-plate distance, the same considerations about the maps morphology, as for SSJ configuration, can be drawn.

The mean-squared axial and radial phase-correlated organized contribution to the velocity components (Fig. 5.12) are different from the SSJ case. The axial component shows a decreasing value, with respect to the SSJ case, near the region at *x/*D equal to 0 for both *H/D* configurations. This phenomenon is related to the 180° phase shift between the two sinusoidal external forces. Indeed such a 180° phase shift between the two external forces generates a destructive interference in the flow field (caused by the external forces) leading to a decrease of the flow field values in its axial direction. For the same reason the extension (in the axial direction) of value higher than 1 is lower (about 3 *D*) than the SSJ case (about 5 *D*) at *H/D* equal to 6. On the contrary in the radial direction such a phase shift generates, near the plate at *H/D* equal to 2, an higher value of the phase-correlated organized radial contribution to the velocity component which is located at *x/D* equal to 0 differently from SSJ case. This is due to the opposite direction attained by the two wall jet in that region. Differently, for *x/D* higher and lower than 0.55 the values are lower than SSJ case because of the same direction of the two wall jets. At *H/D* equal to 6 the radial component starts showing lower value, near the plate, than the SSJ case. This can be ascribed to the lower influence of the opposite direction of the two wall jets.

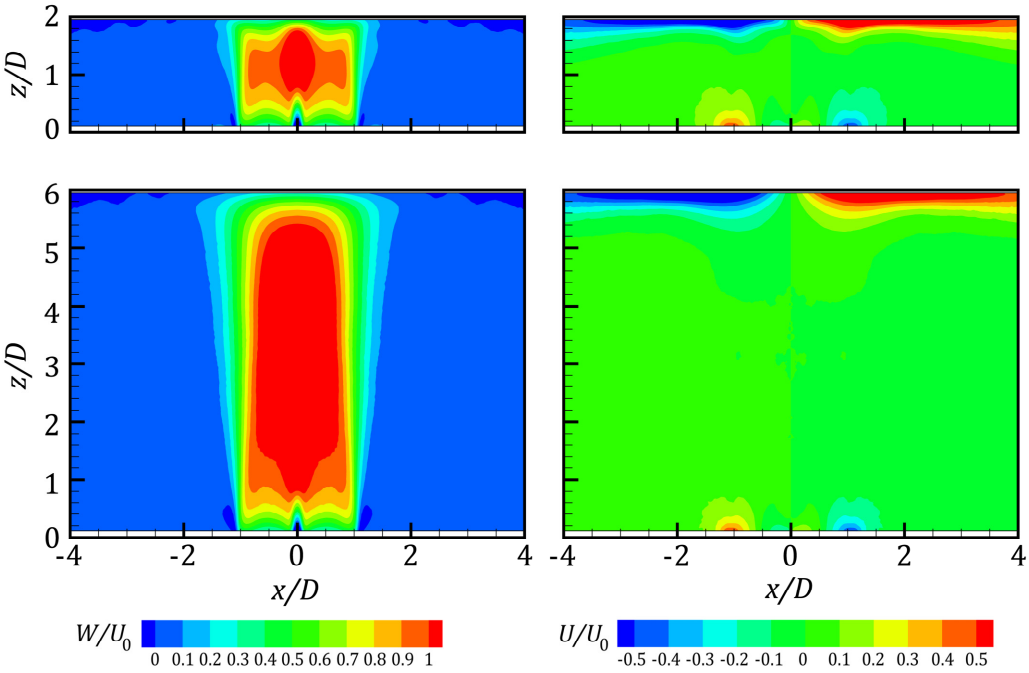

Fig. 5.11 Time-average axial (left) and radial (right) velocity maps for H/D equal to 2 (top) and 6 (bottom)

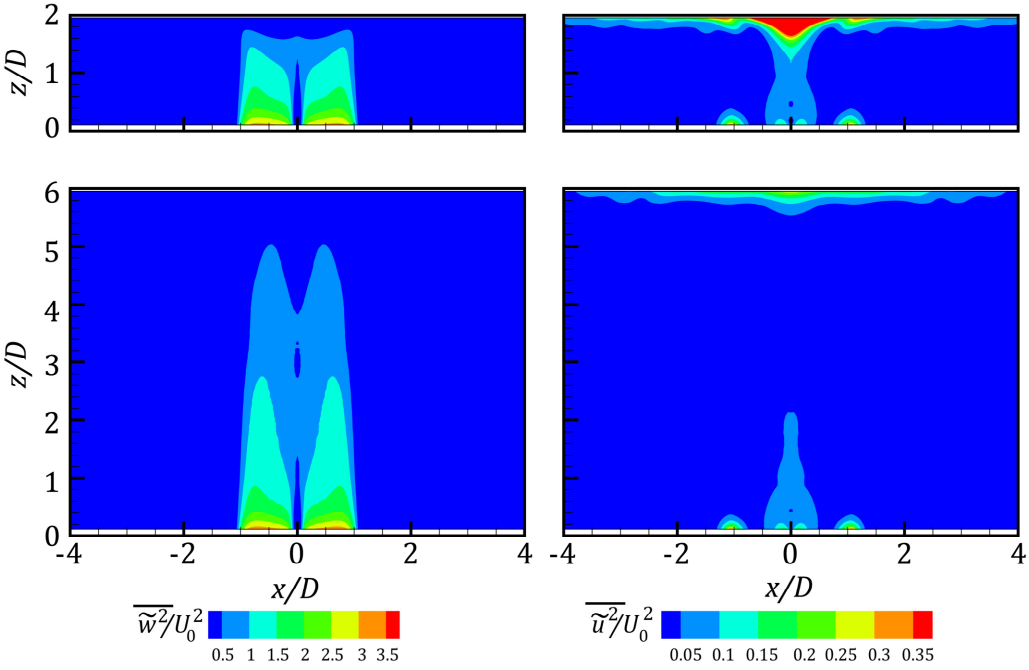

Fig. 5.12 Mean-squared axial (left) and radial (right) phase-correlated organised contribution to the velocity maps for H/D equal to 2 (top) and 6 (bottom)

In Fig. 5.13 the mean-squared axial and radial turbulent velocity components are shown. The axial component value is higher than that in SSJ case. At *x/D* equal to 0 such a value is more than twice of SSJ case one because, due to the 180° phase shift, the shear layer between the two synthetic jets is stronger and because it is given by the superimposition of the axial turbulence two impinging synthetic jets. Moreover it is possible to detect that a value of mean-squared axial turbulent velocity component, different from zero, on the jet axis (at *x/D* =± 0.55) occurs at *z/*D equal to about 2 differently from the SSJ case. This is not related to the potential core-like region extension (which is always the same of the SSJ case as visible in subchapter 5.1.1.4) but to the slight deflection of two synthetic jets toward the centre (*x/D* equal to 0) caused by their interaction The same consideration can be drawn for the radial component. Furthermore at *x/D* equal to 0 (where the two nozzles are adjacent) the radial value is not zero near the nozzles plane (*z/D* equal to 0) differently from what happens at the outer edges (at *x/D* =± 1.1) where, as for the SSJ case, the radial component different from zero starts later.

Regarding the time-average turbulent Reynolds stress (Fig. 5.14) it is possible to see that, at the *H/D* equal to 2, the values over the impinging plate are higher than ones along the external shear layers (at *x/D* = ± 1.1), differently from the SSJ configuration. Moreover along the *x/D* equal to 0 axis a switch of the turbulent component can be detected because this is the region of the overlap of the two inner shear layer. Indeed, considering the right synthetic jet, its left side passes from a negative value (as for the SSJ case) to a positive value which is caused by the right side of the left synthetic jet. As *H/D* increases, the inner contribution of the time-average turbulent Reynolds stress damps and disappears merging the outer contribution at *z/*D equal to about 3.8. After *z/*D higher than 4 such a distribution resembles that of the SSJ configuration. Differently from the SSJ case these region of high and low turbulent Reynolds stress are not parallel. Indeed, as reported in subchapter 5.1.1.4, synthetic jets are deflected towards *x/D* equal to 0 because of their interaction (as also reported in subchapter 4.2.2).

For the time-average phase-correlated organized contribution to the velocity Reynolds stress (Fig. 5.14) at *H/D* equal to 2 the region near the impinging plate shows lower values than the SSJ case. At higher *H/D* the map resembles the SSJ case one.

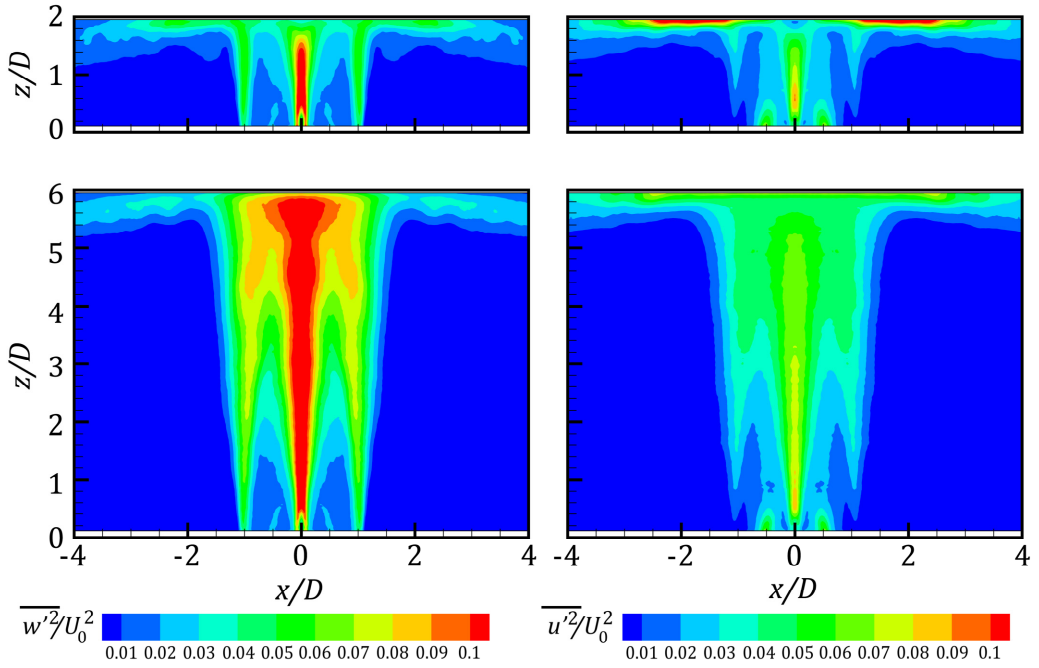

Fig. 5.13 Mean-squared axial (left) and radial (right) turbulent velocity maps for H/D equal to 2 (top) and 6 (bottom)

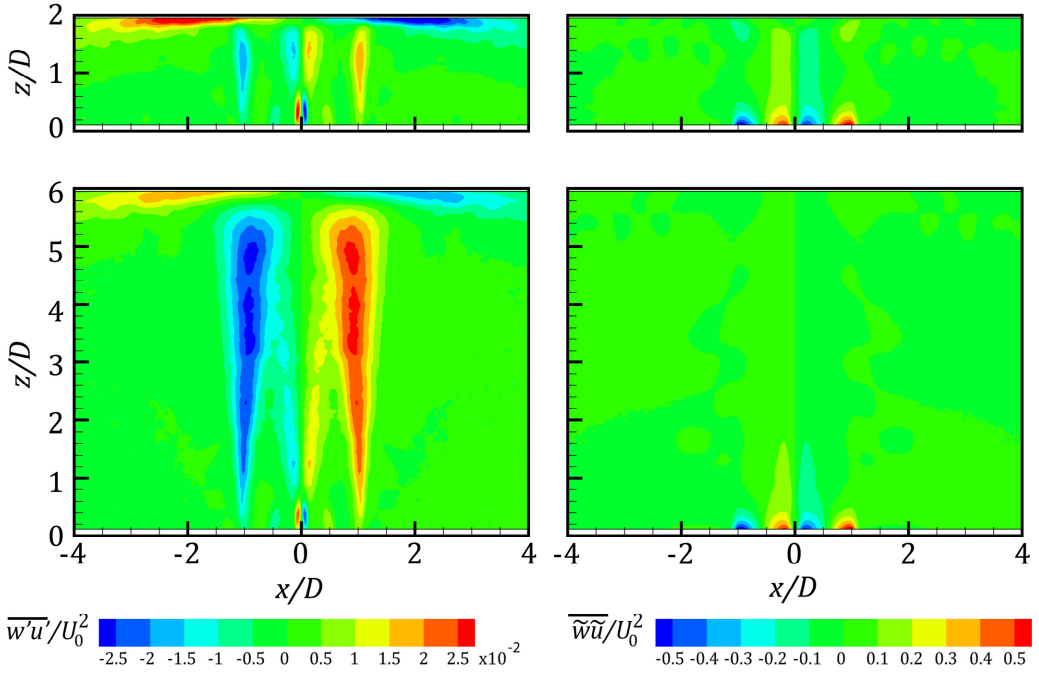

Fig. 5.14 Time-average turbulent (left) and phase-organized contribution to the velocity (right) Reynolds stress maps for H/D equal to 2 (top) and 6 (bottom)

In Figs. 5.15 and 5.16 the time-average centreline axial velocity and the jet width for all H/D's configurations are depicted. As for the SSJ configuration, the H/D equal to 2 and 4 configurations do not attain the maximum value which is reached by other configurations at approximately 3.8 D.

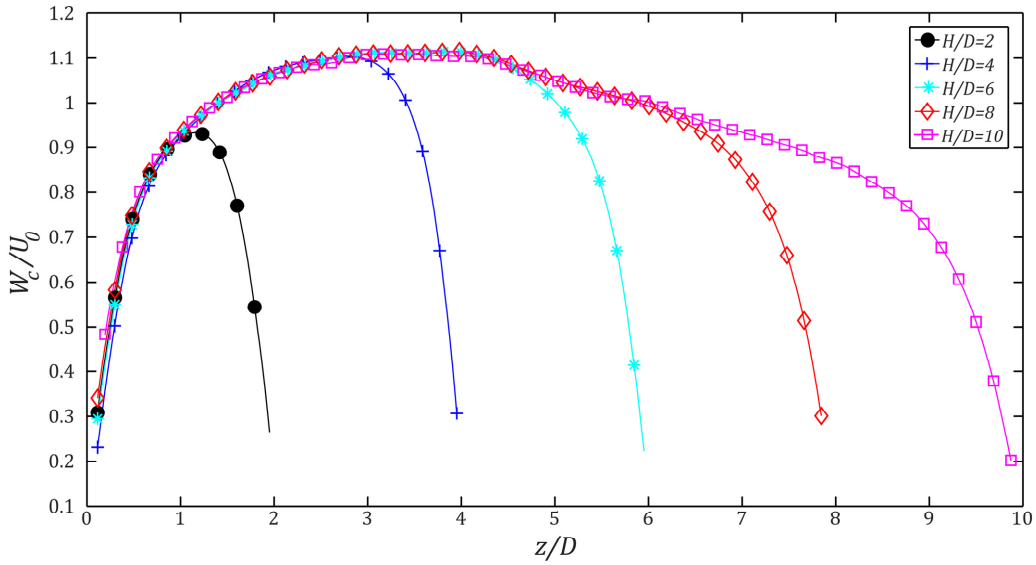

Fig. 5.15 Time-average centreline axial velocity for all H/D's configurations

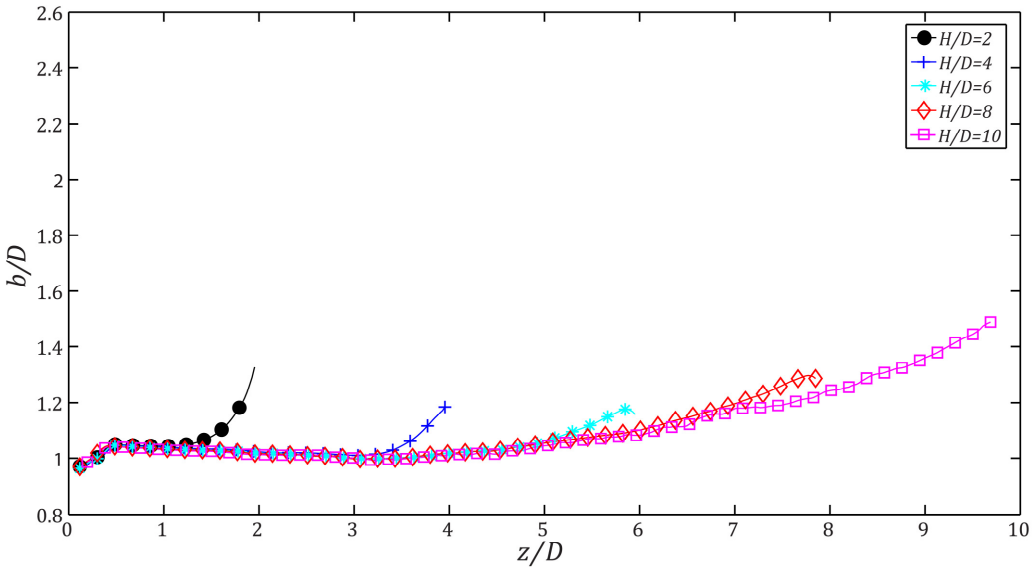

Fig. 5.16 Jet width for all H/D's configurations

Differently from the SSJ case the TSJ with Σ equal to 1.1 attains a higher centreline velocity but lower jet width (for the same reason reported in subchapter 4.1.2). Even for this configuration W_c starts decreasing in the same location where b starts increasing.

In Fig. 5.17 the time-average axial and radial velocity components over the impinging plate for all H/D's configurations are depicted. Considering that the exit centre of the two synthetic jets are located at $x/D = \pm 0.55$, it is possible to assert that, as for SSJ configuration, a minimum of the axial component is found near the jet axis (at x/D equal to -0.6) while two peaks are detectable at x/D equal to 0 and -0.9. If one considers the average of two SSJ profiles, shifted of 1.1 D with respect to each other, the minimum should be located at x/D -0.65 and the maxima at x/D equal to 0 and -1. This discrepancy between the actual TSJ profile and the one obtained by simply superimposing two shifted SSJ profiles is ascribed to the fact that the TSJ profile is not only the superimposition of the two shifted SSJ. Indeed the interaction of the two 180° phase-shifted synthetic jets causes also a deflection which is more evident for higher H/D (as visible in phase-average measurements – subchapter 5.1.1.4). For higher radial position (about 2.2 D) some oscillations are barely visible. As H/D increases these later oscillations damp and a unique peak is detected at x/D equal to 0, whose value decreases differently from the SSJ case where the maximum was attained at H/D equal to 4. As for the SSJ case, along the jet axis (i.e. x/D equal to -0.55) the maximum axial velocity is attained at the same nozzle-to-plate distance (H/D equal to 4).

Regarding the radial component a peak, for the shortest nozzle-to-plate configuration, is visible at a radial position of about 1.2 D. Even for this parameter this peak, differently from the SSJ case and the superimposition of the two SSJ shifted profiles, is not located at 0.75 from the jet axis but at 0.65 D. Moreover some oscillations, as those present in the SSJ case but with lower amplitude, are barely visible. As H/D increases, as for the single configuration, the peak shifts towards higher radial position and the oscillations are damped.

These oscillations (barely detectable in both components) are related, as previously said, to the generation of the counter rotating vortex ring near the impinging plate. Such oscillations are damped not because the counter rotating vortex ring is not generated, but because a second wall jet sweeps the impinging plate reducing the oscillations amplitude.

The mean-squared axial phase-correlated organized contribution to the velocity component (Fig. 5.18) shows, at H/D equal to 2, two peaks at x/D equal to 0 and -1. A local

minimum is detected at *x/D* equal to -0.45. At a radial position higher than 1 some oscillations with a decreasing amplitude can be detected as for the SSJ case.

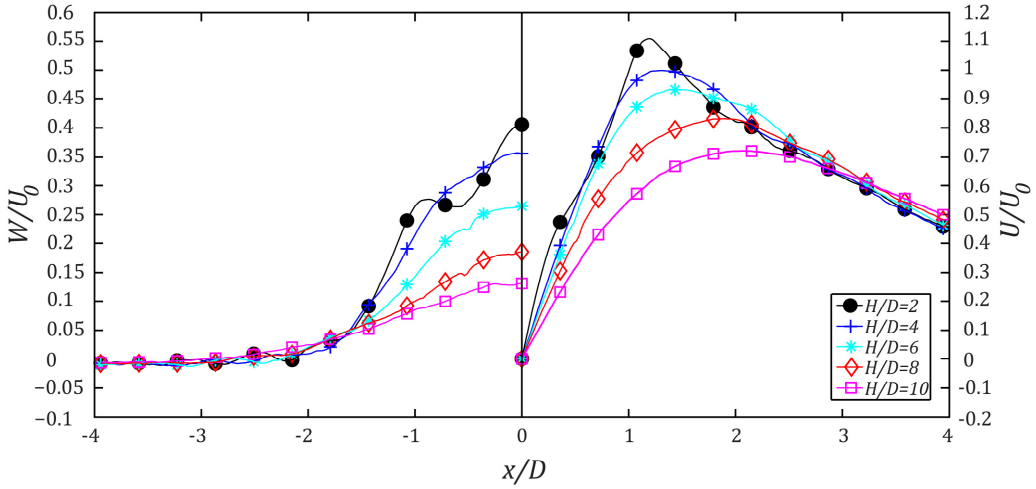

Fig. 5.17 Time-average axial (left) and radial (right) velocity components over the impinging plate for all *H/D*'s configurations

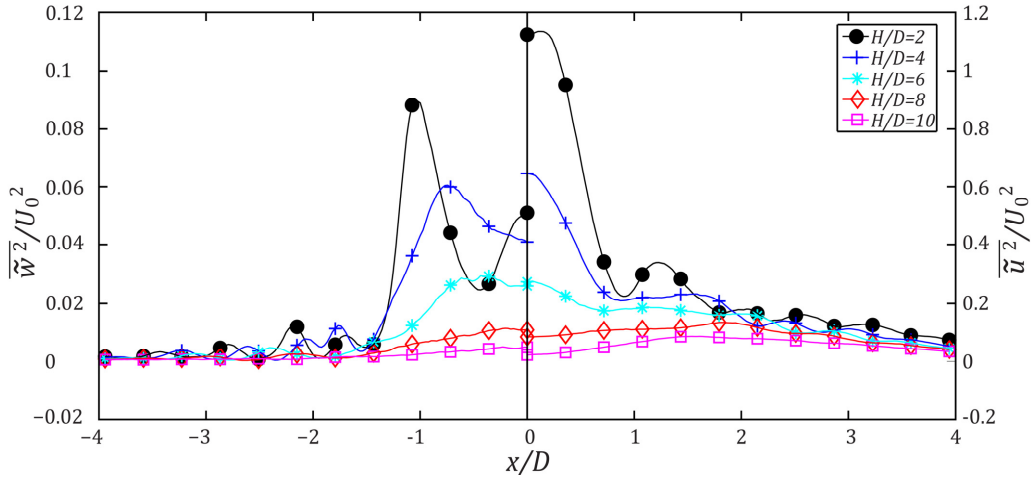

Fig. 5.18 Mean-squared axial (left) and radial (right) phase-correlated organised contribution to the velocity components over the impinging plate for all *H/D*'s configurations

The first peak is lower than the second one because, as previously said, the two 180° phase shift sinusoidal external forces generates a destructive interference near *x/D* equal to 0 region. As *H/D* increases the two peaks decrease and, in particular, the second one

shifts toward the first peak. Moreover the lateral oscillations are damped. Regarding the radial component, at *H/D* equal to 2, a local minimum is attained at *x/D* equal to 0 and a local maximum is located at *x/D* equal to about 0.1. A minimum is detectable at *x/D* equal to 0.9 and then, again, a maximum is observable at *x/D* equal to 1.2. For higher radial position (*x/D* > 1.5) lateral oscillations are present. AS *H/D* increases the first peak decreases and the lateral oscillations are damped. For both components, as stated before, the destructive interference of the two sinusoidal external forces leads to an abrupt decrease of values for nozzle-to-plate distances higher than 2.

The mean-squared axial and radial turbulent velocity components are shown in Fig. 5.19. The axial component, in the shortest configuration, shows three peaks at *x/D* equal to -0.3, -1.2 and -2.3. These second and third peaks are caused by the external peak of the two impinging single synthetic jets. Furthermore the first peak of the TSJ case is related to the first inner peak of the second impinging synthetic jet (see the SSJ case). Then for *x/D* higher than 2.3 the curve shows a monotonically decreasing with the same shape and law of the SSJ case. The values are much higher than those attained by the SSJ case. As *H/D* increases the third peak decreases while the second one increases (as for the SSJ case) and shifts towards the *x/D* equal to 0. The maximum value at *x/*D equal to 0 is attained at *H/D* equal to 6 and it is almost twice that in the SSJ case. In this configuration the second peak is disappeared differently from the SSJ case. For *H/D* greater than 6, the values start decreasing. Differently from the SSJ case, the value of the turbulent axial on the *x/D* equal to zero is always greater than the corresponding phase-correlated one for every *H/D* configuration.

Regarding the radial component its shape at *H/D* equal to 2 is very similar to the SSJ case profile. The difference is related to the higher values and the peaks position. Indeed two maxima are observable at *x/D* equal to 1.8 and 2.2 whose relative distance is the same observable in the SSJ configuration. As *H/D* increases the two peaks merge in one at *x/D* equal to about 2 (for *H/D* equal to 4) and then such a peak shifts at *x/D* equal to about 2.3 (for *H/D* equal to 6) decreasing its value. For *H/D* equal to 8 this peak is very weak and then disappears at *H/D* equal to 10. The value at *x/D* equal to 0 increases up to *H/D* equal to 8 and then starts decreasing as occurs also in SSJ case.

In Fig. 5.20 the turbulent and mean-squared phase-organized contribution to the velocity Reynolds stress are shown. For the time-average turbulent Reynolds stress a maximum can be detected at *x/D* equal to 2. As *H/D* increases this maximum decreases

and shifts towards lower radial position disappearing at H/D equal to 6. The values are higher than the SSJ configuration.

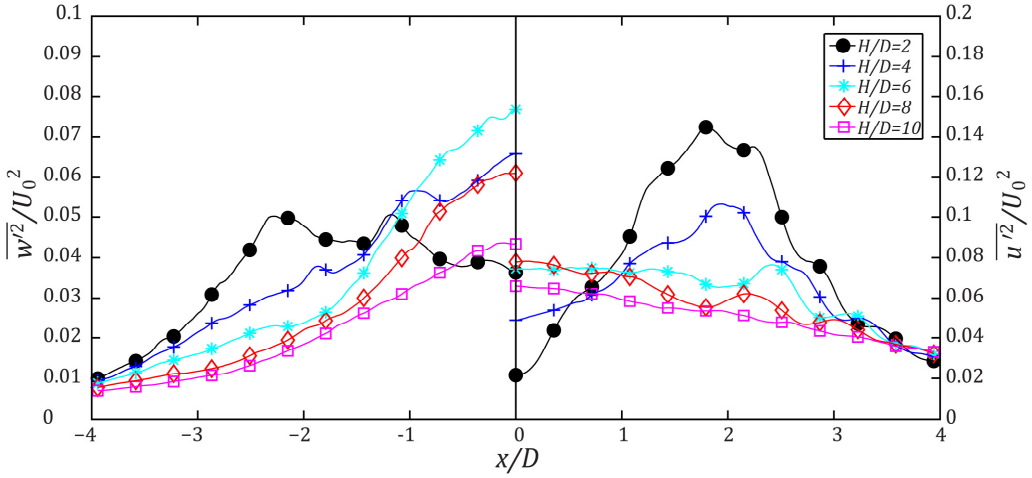

Fig. 5.19 Mean-squared axial (left) and radial (right) turbulent velocity components over the impinging plate for all H/D's configurations

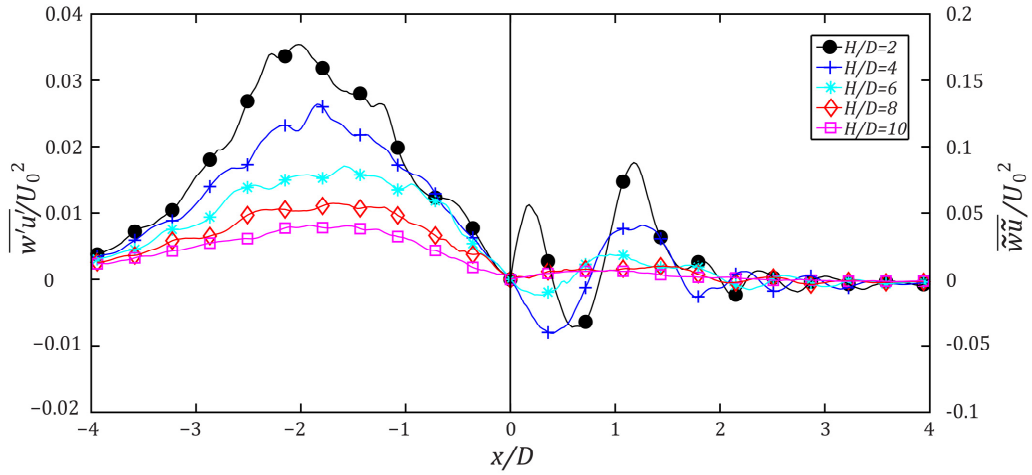

Fig. 5.20 Time-average turbulent (left) and phase-organized contribution to the velocity (right) Reynolds stress over the impinging plate for all H/D's configurations

For the phase-correlated organised contribution to the velocity parameter, at H/D equal to 2, a local minimum is situated at x/D equal to 0 then two peaks (at x/D equal to 0.2 and 1.2) and one tough (at x/D equal to 0.45) are detectable. At H/D equal to 4 the first

peak disappears while the first minimum shifts towards x/D equal to 0 and the second maximum decreases. As H/D increases the peak and the tough decrease and disappear (at H/D higher than 6). These values are lower than the SSJ case for the destructive interference generated by the two 180° phase shift impinging synthetic jets.

The time-average and mean-squared quantities characterizing the TWJ case with Σ equal to 3 are shown in Figs. 5.21-5.24.

In Fig. 5.21 the time-average axial and radial velocity components are depicted. Comparing these maps to the SSJ case and the other TWS case it is easily noticeable that a very weak interaction is present between these two impinging synthetic jets (as also reported in the free synthetic jets – Chapter 4). Indeed for the axial component it is possible to see that the distribution of the axial velocity (in the x direction) with respect to jet axes (located at $x/D = \pm 1.5$) is not completely symmetric for both values of H/D. This is related to the slightly interaction during the starting part of the ejection phase. Differently from the other TSJ configuration the merge between the two synthetic jets occurs only after H/D greater than 8.

The radial component shows, near the impinging plate at H/D equal to 2, alternating behaviour which is not visible at higher H/D. This is due to the strong wall jets generated at shorter nozzle-to-plate distance.

The same considerations, done for W, can be drawn also for the mean-squared axial phase-correlated organised contribution to the velocity component (Fig. 5.22). The mean-squared radial phase-correlated organised contribution to the velocity component shows the highest value near the impinging plate in the overlap region between the two impinging synthetic jets ($-1.5 < x/D < 1.5$). Such a region is more extended than the previous TSJ case. Furthermore this high value, differently from the other TSJ case, is still very high at H/D equal to 6. This can be explained by the fact that in this configuration the opposite direction of the two wall jets is still influent. For the same reason the external values (x/D higher and lower than 1.5) are higher than the previous TSJ case.

The mean-squared turbulent velocity components are shown in Fig. 5.23. For both components the maps are the equivalent of the superimposition of two SSJ located at $x/D = \pm 1.5$. At H/D equal to 2 the maximum values are included in $1.5 < x/D < 1.5$ which is the overlap region between the two impinging synthetic jets. At higher nozzle-to-plate distance the radial turbulent velocity maximum is still located in the overlap region while the axial attains a maximum along the internal shear layer close to the plate.

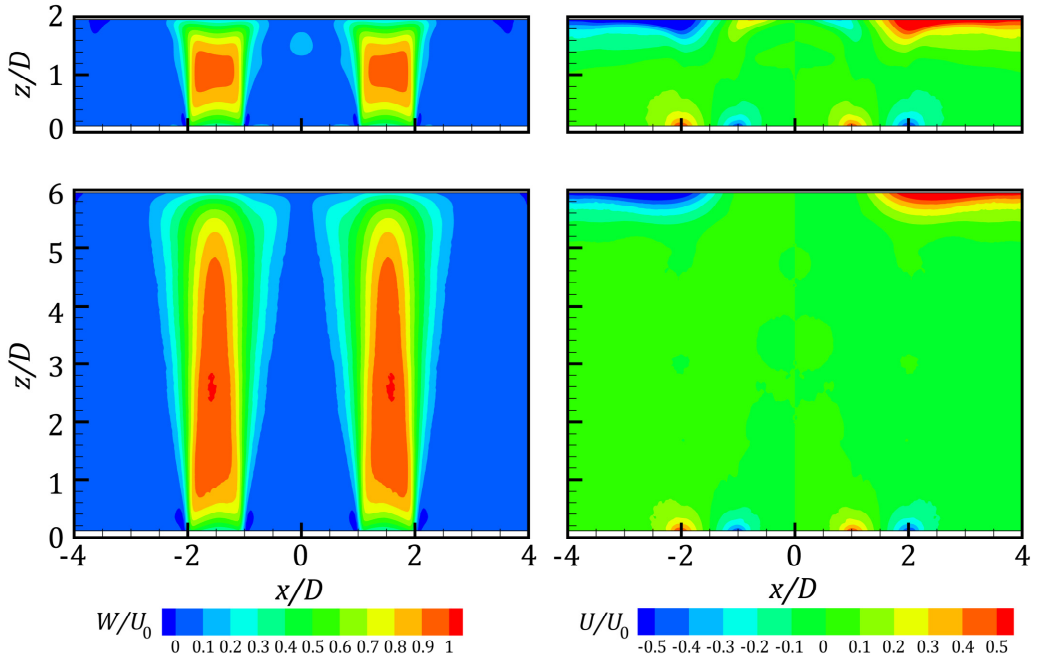

Fig. 5.21 Time-average axial (left) and radial (right) velocity maps for H/D equal to 2 (top) and 6 (bottom)

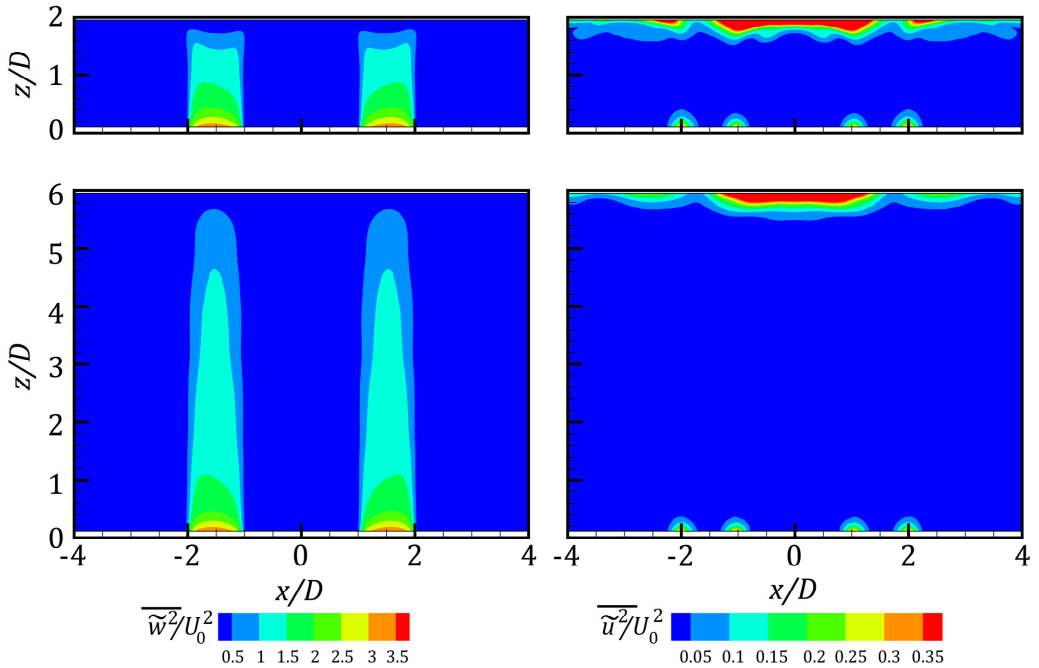

Fig. 5.22 Mean-squared axial (left) and radial (right) phase-correlated organised contribution to the velocity maps for H/D equal to 2 (top) and 6 (bottom)

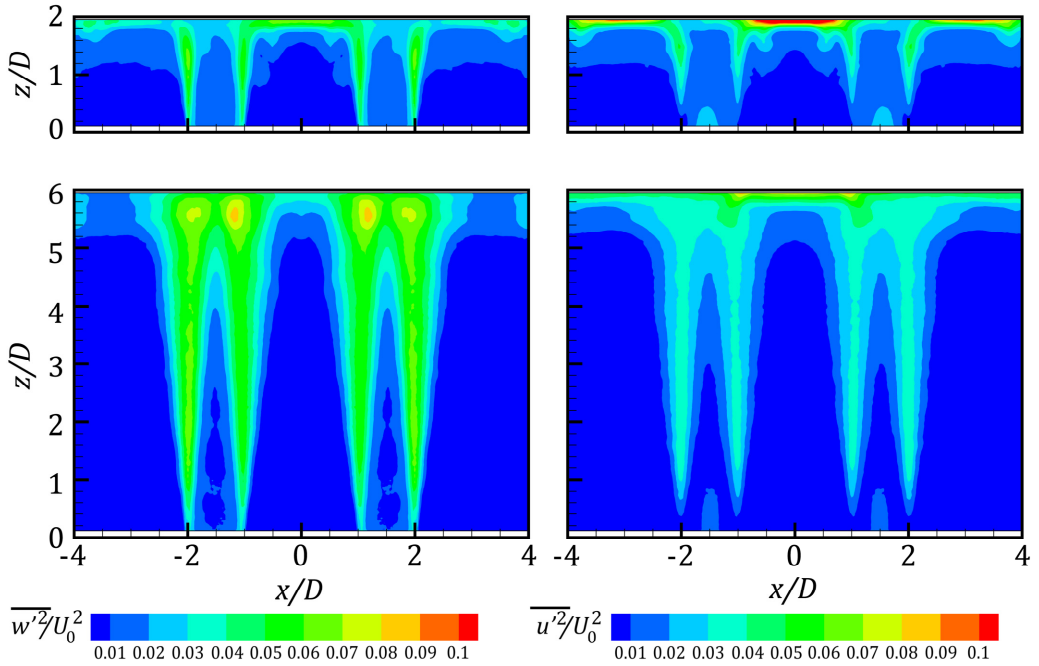

Fig. 5.23 Mean-squared axial (left) and radial (right) turbulent velocity maps for H/D equal to 2 (top) and 6 (bottom)

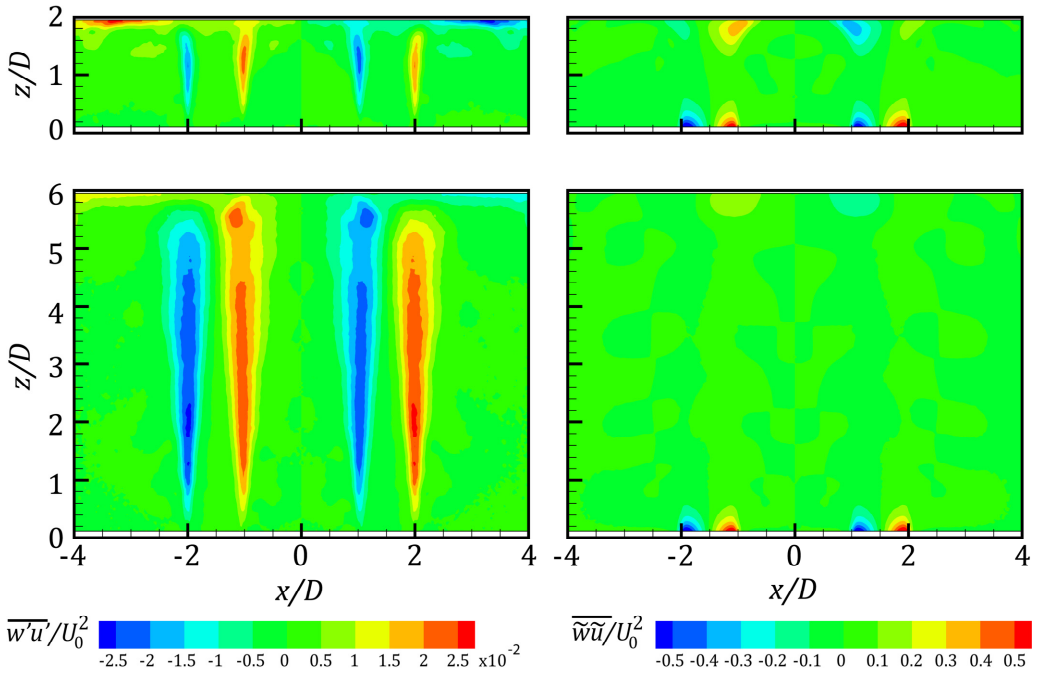

Fig. 5.24 Time-average turbulent (left) and phase-organized contribution to the velocity (right) Reynolds stress maps for H/D equal to 2 (top) and 6 (bottom)

Such a behaviour is due to the fact that the shear layer is superimposed to the wall jet of the other impinging synthetic jet, hence, two are the axial turbulence contributions. Moreover the internal one is higher than the external one because the axial turbulence related to the wall jet tends to decreases for a radial position, from the jet axis, higher than 2 (see Fig. 5.9).

In Fig. 5.24 the time-average turbulent and phase-organized contribution to the velocity Reynolds stress are reported. The main difference with the SSJ case is that the time-average turbulent Reynolds stress, at H/D equal to 2, does not show high values in the overlap region ($-1.5 < x/D < 1.5$). Indeed, near the impinging plate, the right negative turbulent Reynolds stress (related to the left impinging SSJ) and the left positive turbulent Reynolds stress value (related to the right impinging SSJ) balance. Differently from the SSJ case the internal turbulent Reynolds stress arrives very close to the impinging plate (easily detectable for the H/D equal to 6 configuration). The time-average phase-organized contribution to the velocity Reynolds stress shows, at H/D equal to 2, internal values, near the impinging plate, which are slightly greater than the SSJ case, and such values are still barely visible at H/D equal to 6.

In Fig. 5.25 the time-average centreline axial velocity is depicted. The behaviour is completely similar to the SSJ case. Some differences can be detected through the jet width, reported in Fig. 5.26. These differences are visible only for high nozzle-to-plate distance. At H/D equal to 10 a steep slope (starting at z/D equal to about 9.5) is visible near the impinging plate due to the interaction and merging of the two synthetic jets.

Time-average axial and radial velocity components near the impinging plate are depicted in Fig. 5.27. The axial component at H/D equal to 2 is similar to the SSJ configuration. Indeed the minimum of this profile is located at x/D equal to -1.5 and then two lateral local maxima are located at $\pm$ 0.5 D from the jet axis. As H/D increases the profile changes showing a maximum near the jet axis. Such a maximum has the same value for H/D equal to 4 and 6 (differently from the SSJ case where the highest value was for the H/D equal to 4 configuration). Then this peak decreases its value as H/D increases.

Regarding to the radial profile, at H/D equal to 2, it is possible to note that a maximum is located at x/D equal to about 2.25 while a minimum (which is lower than the maximum) has a radial position of 0.75 D. This is in agreement to the SSJ behaviour.

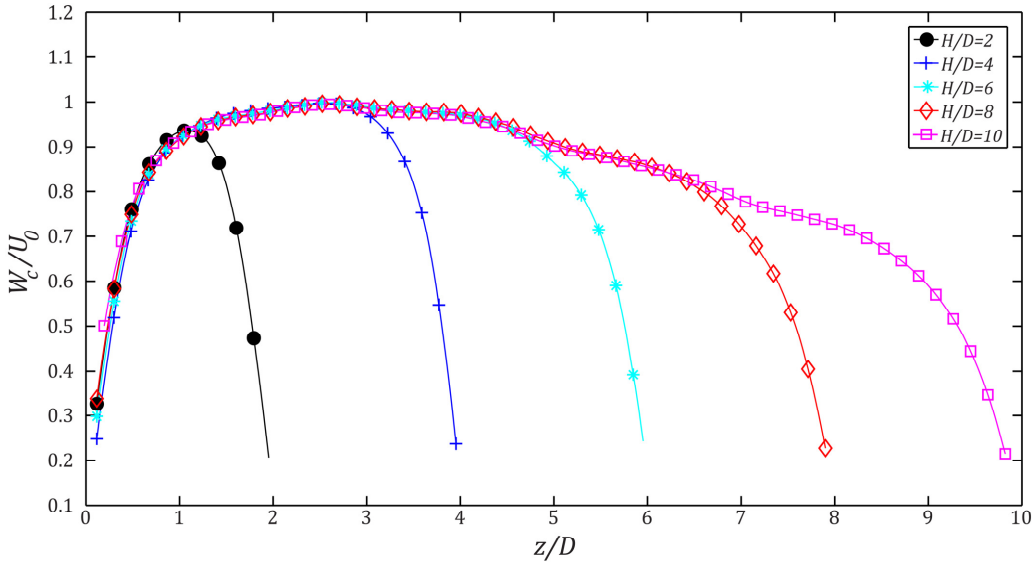

Fig. 5.25 Time-average centreline axial velocity for all H/D's configurations

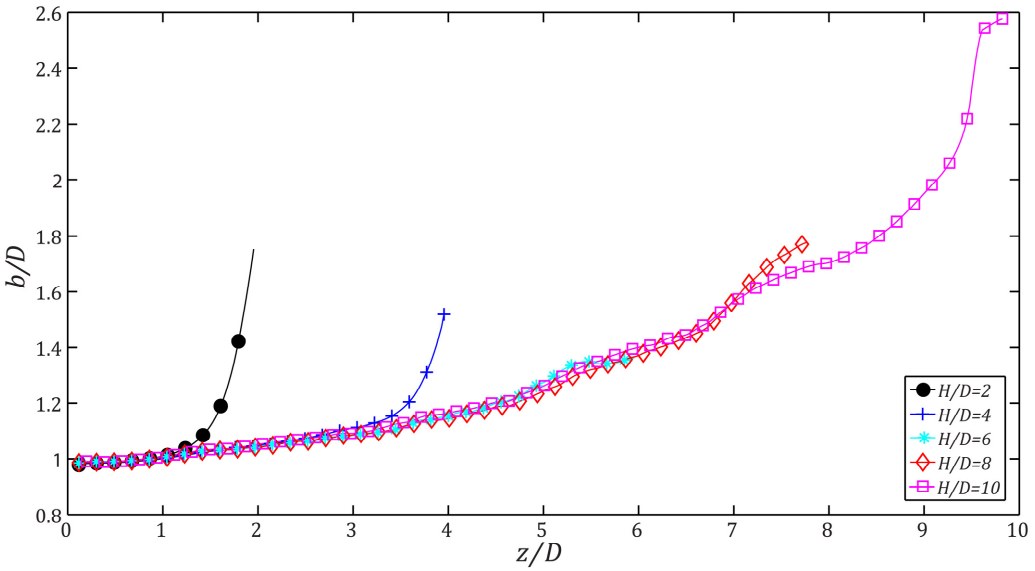

Fig. 5.26 Jet width for all H/D's configurations

The difference between the maximum and minimum value is related to the second synthetic jets impinging on the opposite side which increases the maximum and decreases the minimum. As H/D increases, as for the SSJ configuration, the peak decreases and shifts towards higher radial position while the minimum increases. For both components, differently from the SSJ case, the lateral oscillations are not so evident because, as for the

other TSJ configuration, they are damped by the second wall jet generated by the other impinging synthetic jet.

Mean-squared axial and radial phase-correlated organised contribution to the velocity components profile near the impinging wall are reported in Fig. 5.28.

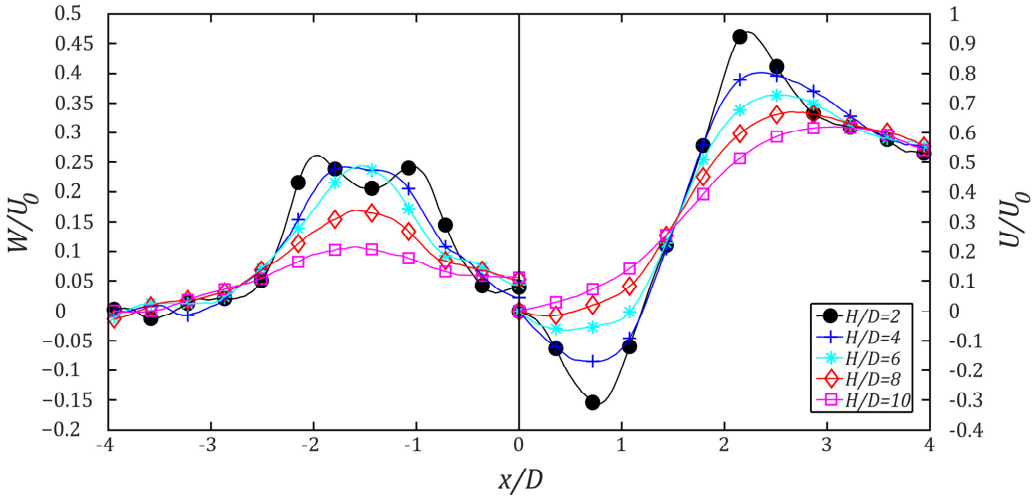

Fig. 5.27 Time-average axial (left) and radial (right) velocity components over the impinging plate for all H/D's configurations

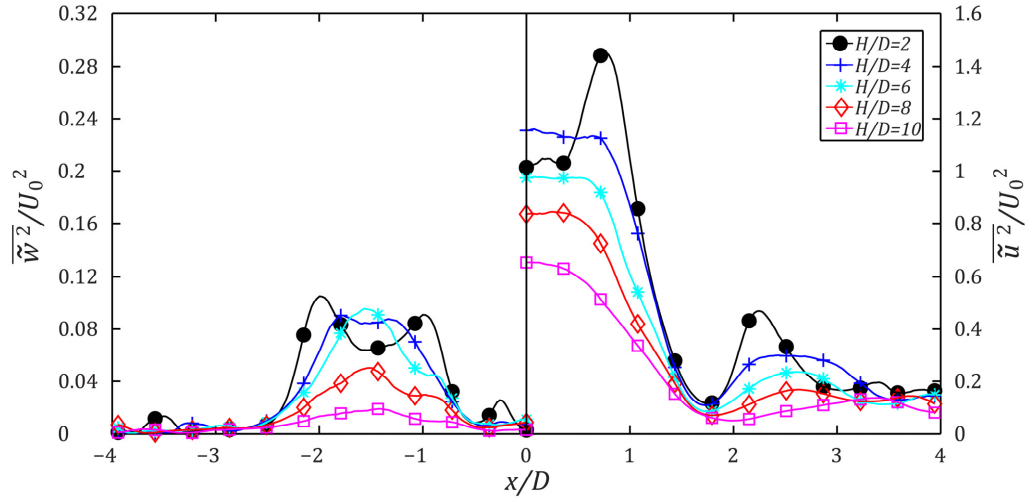

Fig. 5.28 Mean-squared axial (left) and radial (right) phase-correlated organised contribution to the velocity components over the impinging plate for all H/D's configurations

As for the SSJ configuration the axial component resemble the time-average velocity axial component. As matter of fact the behaviour is the same but, differently from the SSJ case, the maximum value on the jet axis is attained at H/D equal to 6 instead of 4. Moreover at H/D equal to 2 it is possible to see that the external peak is slightly higher than the internal one because the destructive interference (which is much lower than the TSJ with Σ equal to 1.1) between the two sinusoidal external forces is stronger near the overlap region ($-1.5 < x/D < 1.5$).

The radial component, differently from the SSJ case, shows a minimum which is not on the jet axis (x/D equal to 1.5) but, accordingly to the SSJ case, the two maxima which are located at ± 0.75 D from the jet axis. Near the $x/$D equal to 0 region a plateau, generated by the two wall jets which sweep the impinging wall, is visible. The inner peak is higher than the external one because of the two wall jet are opposite in direction (when sweep the impinging plate) and such a different direction is stronger near the region at x/D equal to 0. As H/D increases the inner peak reduces creating, firstly, a more extended region (H/D equal to 4) which reduces for higher H/D. The second peaks decreases (for H/D equal to 4, 6 and 8) and then disappears (H/D equal to 10).

In Fig. 5.29 the mean-squared axial and radial turbulent components are shown. The axial component at H/D equal to 2 shows, mainly, two peaks: one near the x/D equal to 0 axis and the other one at x/D equal to -3.3. The first peak is higher because it is due to the inner peaks of two impinging synthetic jets (see Fig. 5.8) while the outer one is related to the SSJ outer peak. The third peak, at x/D equal to about -2.2 is generated by the peak located at x/D equal to -0.65 of the SSJ configuration. At H/D equal to 4 three peaks are detectable at x/D equal to approximately -0.9, -2.1 and -3.3. These three peaks are generated by the two peaks present in the SSJ case. Indeed the first two peaks are located at about 0.6 D from the jet axis as occurs in the SSJ configuration. As H/D increases the third peak disappears while the other two are still barely visible at H/D equal to 6 (with a minimum on the jet axis). Then a unique peak, as for the SSJ case, is detectable (H/D equal to 8) which decreases for H/D higher than 8. As for the SSJ configuration, on the jet axis, the maximum is attained at H/D equal to 8 but near the x/D equal to 0 the maximum values is obtained in the shortest configuration.

The radial component shows a peak at x/D equal to 0 and then a second and third one at a radial position of about 3.2 and 3.5 D. At H/D equal to 4 the first peak decreases and shifts towards higher radial position and the second and the third one merge in a unique

peak at *x*/D equal to about 3.3 (differently from the SSJ configuration) with a decreased value. As *H/D* increases the first peak continues decreasing and shifting far from *x/D* equal to 0 and the second one disappears.

The time-average turbulent and phase-organized contribution to the velocity Reynolds stress near the impinging plate are depicted in Fig. 5.30.

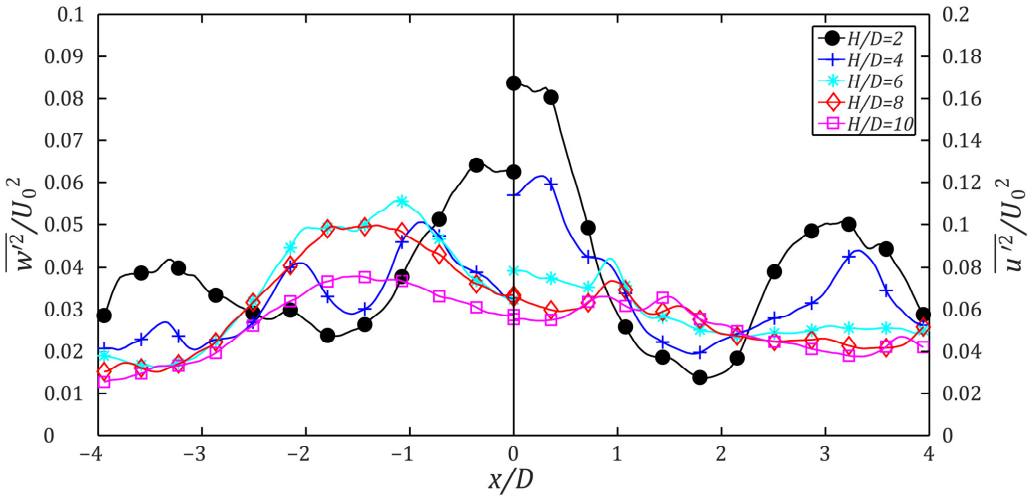

Fig. 5.29 Mean-squared axial (left) and radial (right) turbulent velocity components over the impinging plate for all *H/D*'s configurations

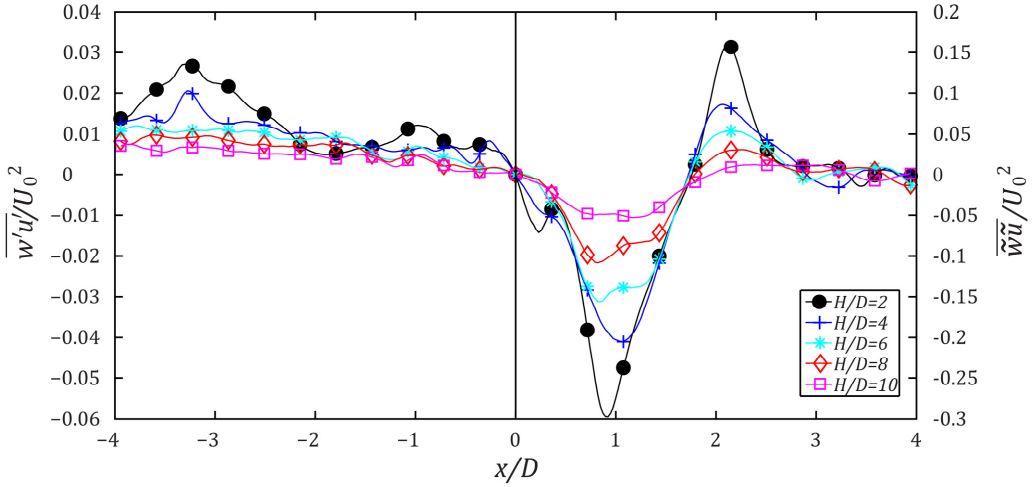

Fig. 5.30 Time-average turbulent (left) and phase-organized contribution to the velocity (right) Reynolds stress over the impinging plate for all *H/D*'s configurations

The turbulent Reynolds stress, at *H/D* equal to 2, two peaks are detected at -0.9 and -3.2 *D*. The external peak is located from the jet axis at the same position that occurs in the SSJ configuration. As *H/D* increases these two peaks decrease (*H/D* equal to 4) and then disappear (*H/D* higher than 6) as occurs in the SSJ case.

The phase-correlated organized contribution to the velocity Reynolds stress shows two peaks at 0.9 and 2.1 *D* which are located a radial position from the jet axis of .0.5 *D*. These two peaks, at *H/D* equal to 4, are shifted towards the jet axis of about 0.1 *D* and decreased. Then, as *H/D* increases, the minimum is split in two local minima, which decrease, and the maximum continues decreasing.

5.1.1.3 Phase-average flow field for SSJ

In Figs. 5.31 – 5.33 all the velocity components are depicted for *H/D* equal to 2. For the sake of brevity, only eight phase-average flow fields (representing the ejection phase) are reported. The phases range from $\varphi = 0°$ (the beginning of the jet ejection is chosen as the reference starting point in agreement with Chapter 4), up to $\varphi = 168°$. For each phase the velocity vector arrows are placed every 0.08 *D* in x and *z* direction.

In Fig. 5.31 the phase-average axial and radial velocity maps are shown. At $\varphi = 0°$ the synthetic jet starts being issued by the nozzle and at $\varphi = 24°$ the vortex ring is formed. Then the synthetic jet impinges and spreads over the plate as observable at $\varphi = 48°$. For this phase, it is possible to detect the formation of a counter rotating vortex ring near the impinging plate (as better visible in Fig. 5.37) and also two regions of high radial velocity at *x/D* equal to about 0.75 (where the complete rotation of the impinging synthetic jet occurs) and at the position of the convective primary vortex ring. From this phase to $\varphi = 120°$ the effect of the impinging plate on the impinging synthetic jet is clearly observable. Indeed the morphology of the axial velocity is characterized by a hemispherical axial velocity decreasing, near the plate, caused by the strong adverse pressure gradient. For $48° \leq \varphi \leq 96°$, the vortex ring continues sweeping the impinging plate and the position of high radial velocity is always located at *x/D* equal to 0.75 (while the second region shifts towards higher radial position with the vortex ring and its value decreases). For this range of phases the axial velocity attains the maximum value. For $\varphi > 96°$ the vortex ring is out of the measurement zone and the values of axial and radial velocity start decreasing.

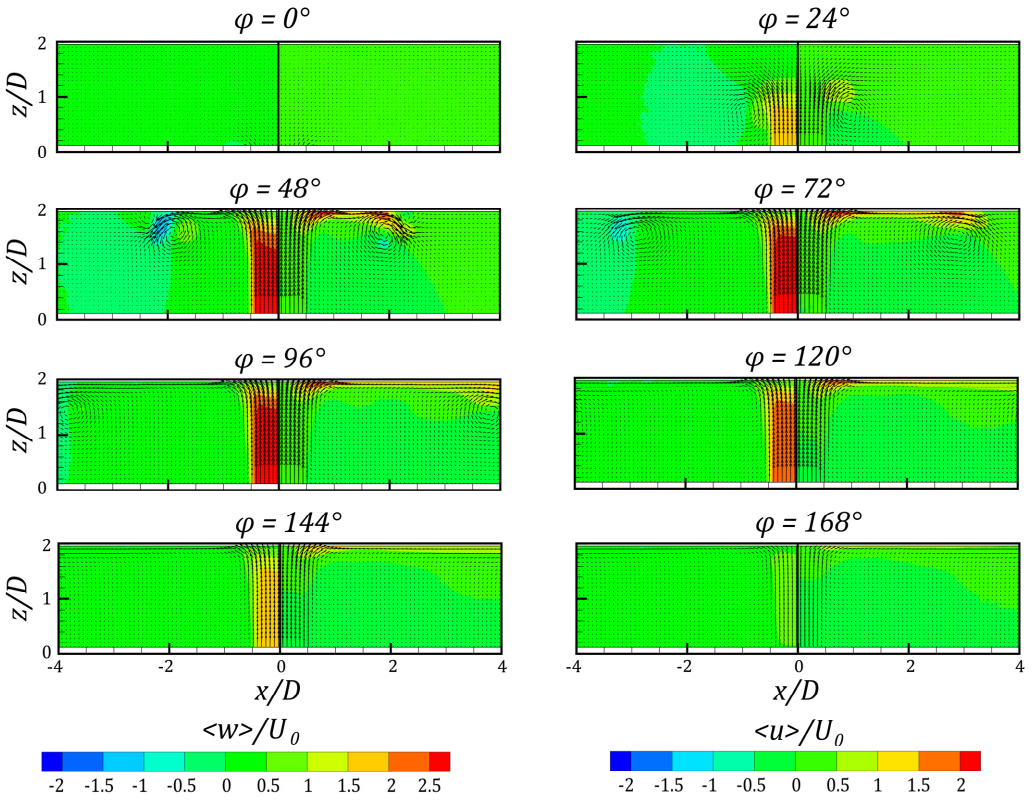

Fig. 5.31 Phase-average axial (left) and radial (right) velocity maps at H/D equal to 2

In Fig. 5.32 the phase-average mean-squared axial and radial turbulent velocity maps are depicted. At φ = 0° the axial values are zero because, obviously, the synthetic jet is coming out. At φ = 24° the axial turbulent velocity acquires non-zero values on the front boundary of the vortex ring while the radial one attains its maximum near the vortex ring core. At φ = 48° the maximum value for both components is located in the middle between the vortex ring and the counter rotating one. Moreover, for the axial turbulent velocity a value different from zero is also detected at x/D equal to -0.5 and along the shear layer (only for z/D > 1). The radial turbulent velocity shows high values also along the last zone (z/D > 1) of the shear layer. At φ = 72° the axial component has maxima located in the vortex ring core, near the impinging wall at x/D between 1.5 and 2 and along all the shear layer up to the nozzle exit. Differently, the radial component shows a zero turbulent value near the nozzle (0 < z/D < 0.4) and maxima along the wall (1 < x/D < 2.25) and ahead of the vortex ring (near the wall) at a radial position equal to approximately 3.3 D. At φ = 96° the vortex ring is completely detached from the impinging plate (as visible from the peak

of axial and radial turbulence) but near the plate still high value of axial ($1.5 < x/D < 2.5$) and radial ($1 < x/D < 2.5$) are observable. For $\varphi > 96°$ the two maxima, located in vortex ring core, are out of the measurement zone and the other high values start decreasing (still visible is the maximum of axial turbulence near the impinging plate at x/D equal to approximately 2). It is important to highlight that for this nozzle-to-plate configuration, from φ equal to 48° until φ equal to 120° the zone between $-0.5 < x/D < 0.5$ is characterized by no turbulence and a constant value of the velocity, resembling the potential core behaviour of a continuous jet (defined as a potential core-like region).

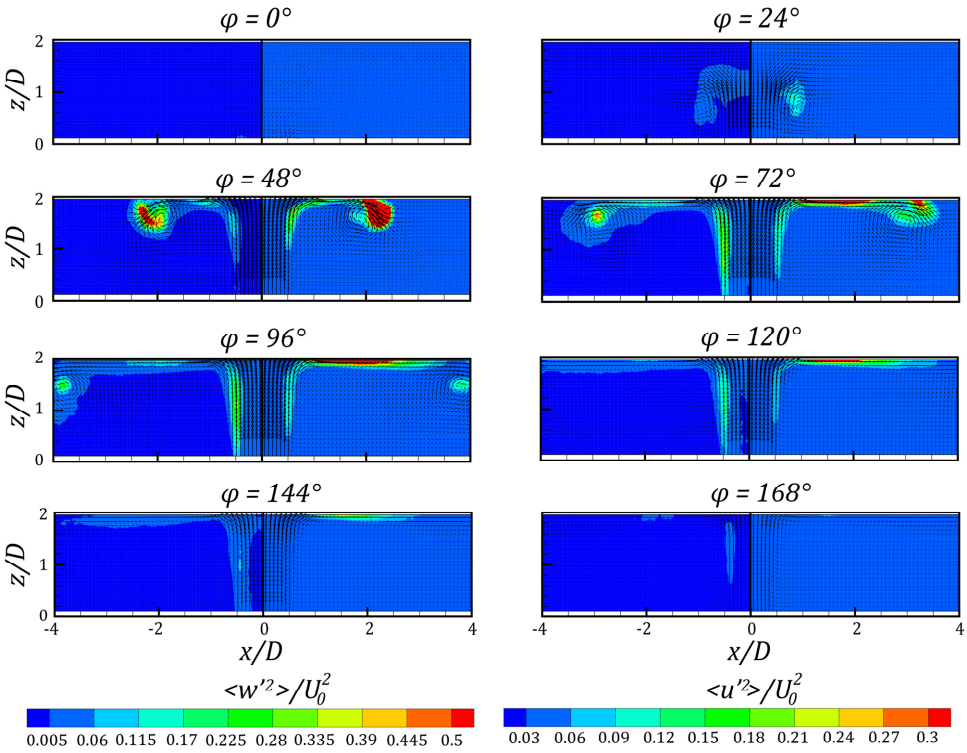

Fig. 5.32 Phase-average mean–squared axial (left) and radial (right) turbulent velocity maps at H/D equal to 2

In Fig. 5.33 the phase-average turbulent Reynolds stress is shown. Seen this variable shows a symmetric opposite behaviour only the evolution in the left region (i.e. $x < 0$) is described. The turbulent Reynolds stress begins showing values different from zero after the synthetic jet generation (φ = 0°). Indeed at φ = 24° near the vortex ring core the turbulent Reynolds stress attains its maximum, while ahead of the vortex ring core a

minimum is located. At φ = 48°, negative values are detectable in the last zone of the shear layer (as also occurs for the mean-squared axial turbulent component) and in the core of the counter rotating vortex ring (near the impinging plate). High values are observable between the two vortex rings and near the impinging plate in the zone included between the primary vortex ring and the shear layer. As φ increases the turbulent Reynolds stress along the shear layer increases in value (more negative) and width (see φ = 72° and 96°) and extends until the nozzle exit while the zone of high turbulent Reynolds increases because follows the vortex ring convection. At φ = 96° the turbulent Reynolds stress maps strongly resemble that of a continuous impinging jet (Narayanan et al., 2004). For φ > 96° the values start decreasing.

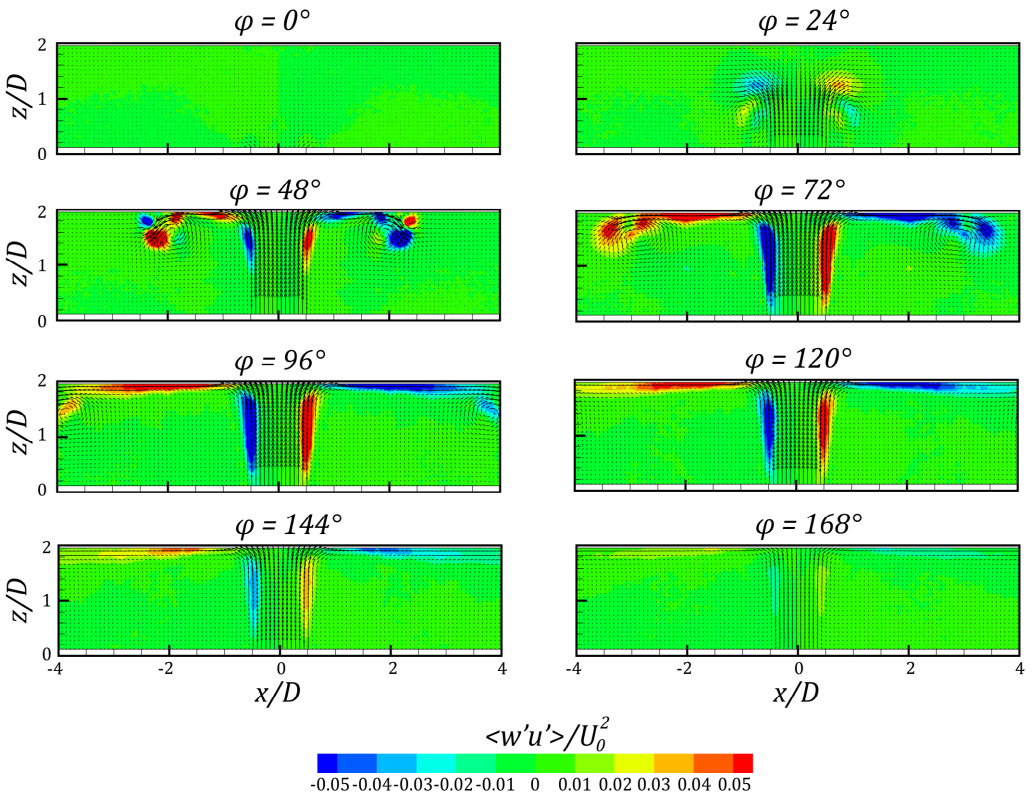

Fig. 5.33 Phase-average turbulent Reynolds stress maps at H/D equal to 2

In Figs. 5.34 – 5.36 all the velocity components are depicted for H/D equal to 6. In Fig. 5.34 the phase-average axial and radial velocity maps are reported. It is possible to see how the vortex ring is generated (by the roll-up of the shear layer sheet) and convects

downstream (first three phases). Then (at φ = 72°) it impinges on the plate and still generates a smaller counter rotating vortex ring (than that generated in the shortest nozzle-to-distance configuration, as also visible in Fig. 5.37). For this latter phase it is possible to highlight that a maximum in the radial velocity, near the impinging plate, is detectable at a radial position of about 1.3 *D* from the jet axis. The axial velocity, approaching the impinging plate, shows a bell-shape distribution that is completely different from the behaviour detected for the shortest configuration. At φ = 96° the vortex is sweeping the plate and a local radial maximum is located between the vortex ring and the impinging plate. Differently from the shortest case, the second radial velocity peak has approximately the same value of the first one. At this phase, the axial component shows a region of high value that has the greatest extension (toward the impinging plate). As φ increases, the radial and axial values decrease.

In Fig. 5.35 the phase-average mean-squared axial and radial turbulent velocity maps are shown. The behaviour, in the first two phases, is similar to what shown for the case at *H/D* equal to 2. Then, at φ = 48°, high value of the axial turbulence is located mainly along the shear layer and near the front boundary of the vortex ring. The radial turbulence shows its maximum along the shear layer, as well, and near the vortex ring core. At φ = 72° it is possible to point out that the mean-squared axial turbulent velocity has high value all along the shear layer (until the nozzle exit) and in the counter rotating vortex ring. The radial turbulence shows, basically, the same characteristics of the axial one. Differently from the shortest nozzle-to-plate configuration, the axial and radial turbulence start merging on the jet axis at *z/D* equal to about 3.8. That zone, featured by a zero turbulence value, is the so-called potential core-like region. At φ = 96° the axial turbulence has its maximum along the shear layer and in the vortex ring core but, differently from *H/D* equal to 2, the zone of high turbulence near the wall at *x/D* equal to about 2 shows lower values. The radial turbulence still shows (as for *H/D* equal to 2) a high value region near the plate (which covers the zone between the shear layer and the vortex ring) apart from the maxima present along the shear layer and inside the vortex ring core. At $\varphi \geq 120°$ the turbulence values start decreasing and the vortex ring is moved out of the measurement region.

In Fig. 5.36 the phase-average turbulent Reynolds stress is depicted. At φ = 24° it is possible to see the Reynolds stress value, different from zero, re located in the same position previously seen for the shortest nozzle-to-plate case.

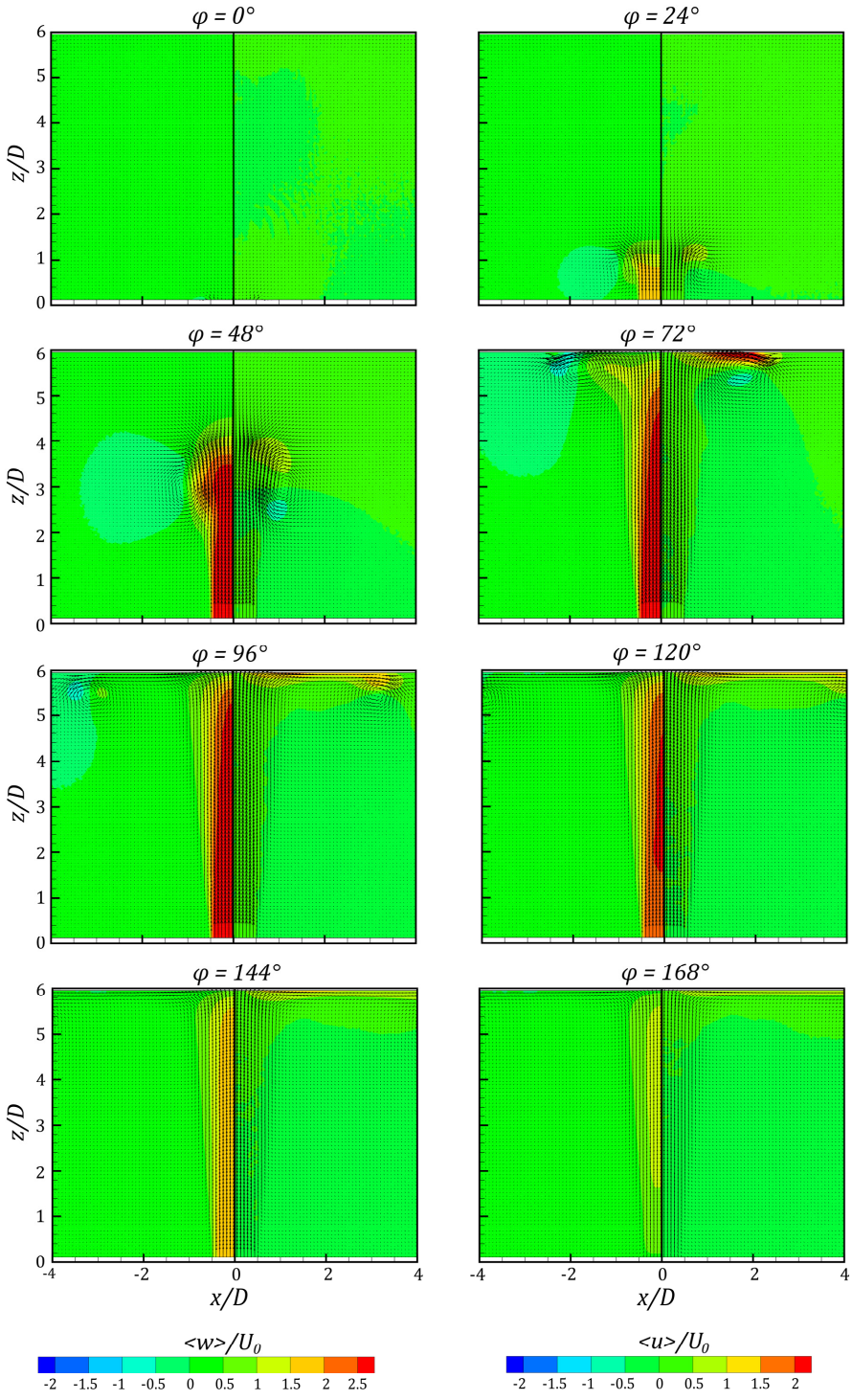

Fig. 5.34 Phase-average axial (left) and radial (right) velocity maps at H/D equal to 6

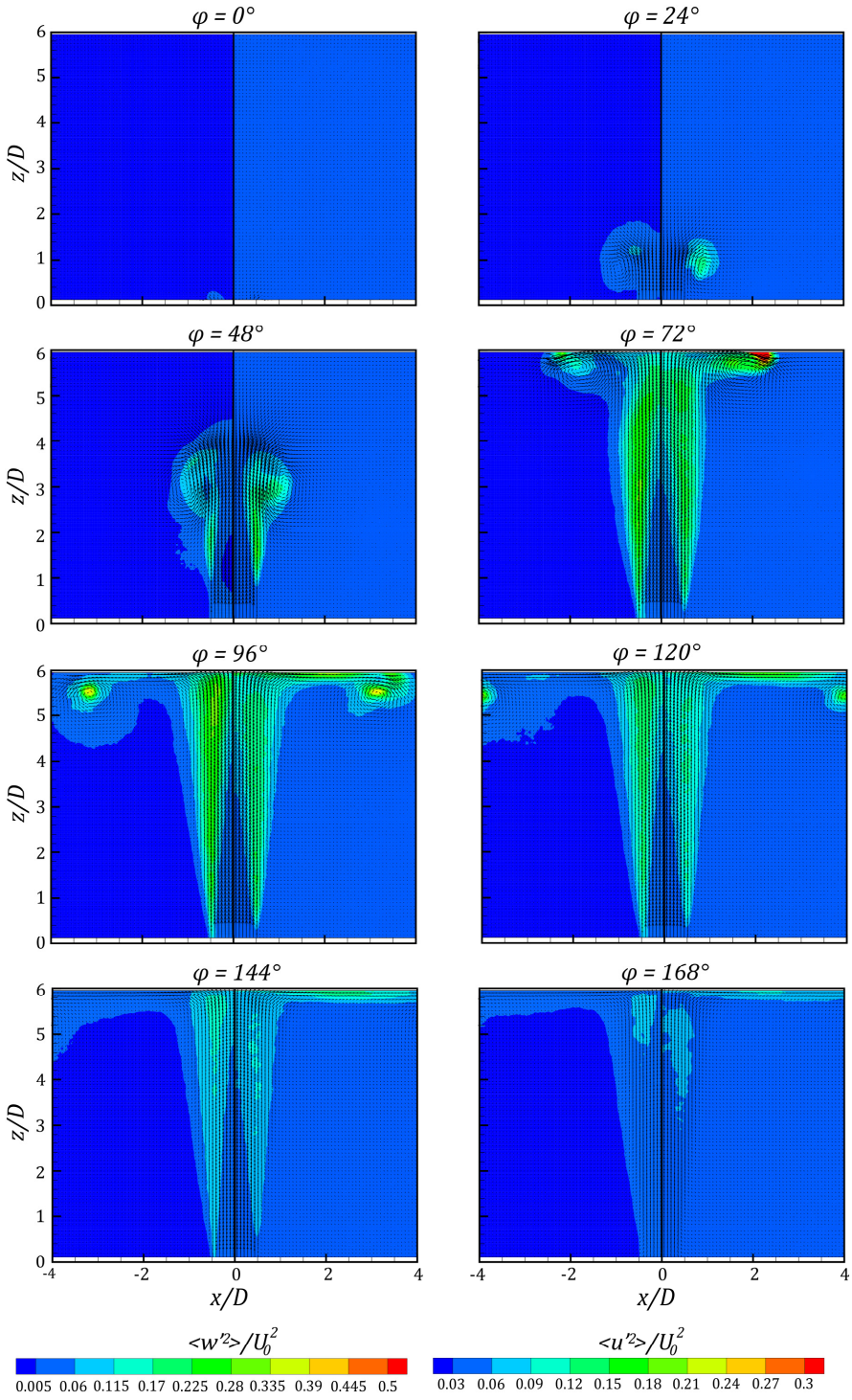

Fig. 5.35 Phase-average mean–squared axial (left) and radial (right) turbulent velocity maps at H/D equal to 6

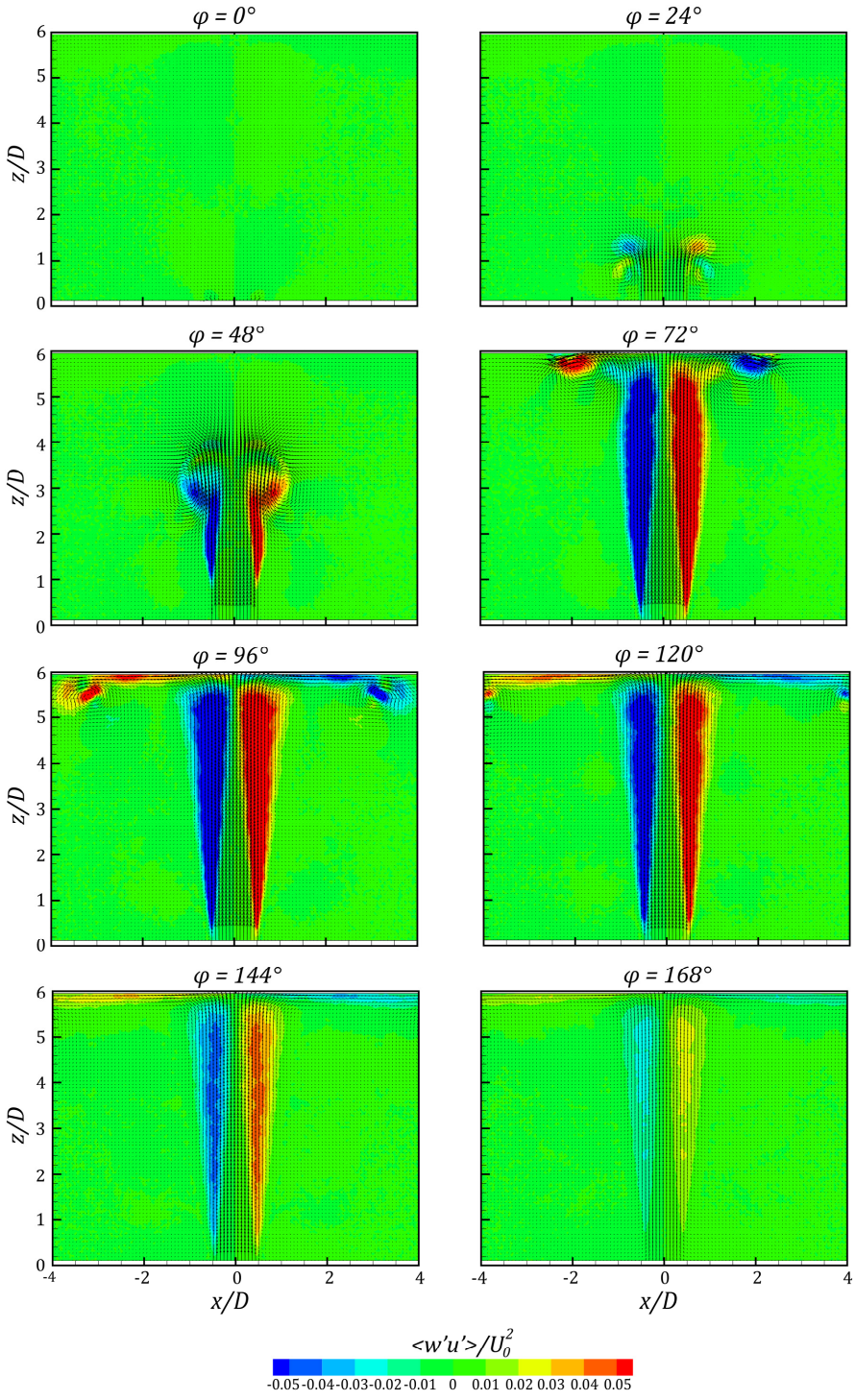

Fig. 5.36 Phase-average turbulent Reynolds stress maps at H/D equal to 6

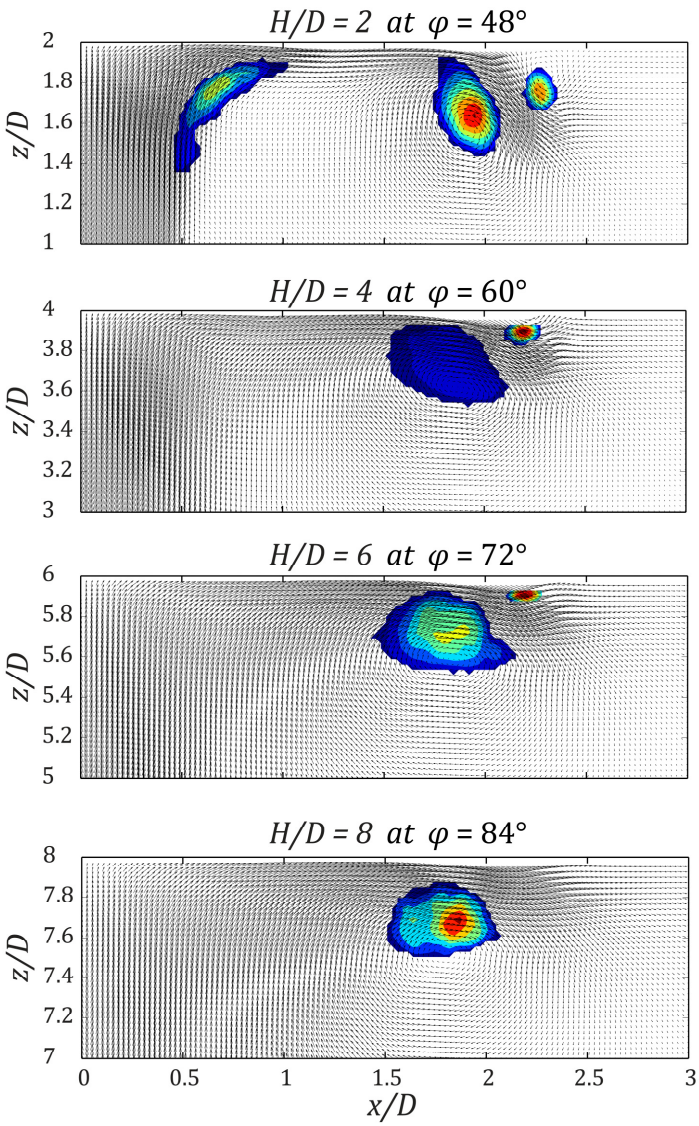

Fig. 5.37 Counter rotating vortex ring generation for different nozzle-to-plate distances, highlighted by the Q-criterion contour (Q_c>0)

At φ = 48° the high value are located mainly along the shear layer and near the vortex ring core. Also at φ = 72° the maximum values are located along the shear layer and near the vortex ring. As the vortex ring sweeps the plate (φ = 96°) also a zone of high value of the Reynolds stress is detectable near the plate (between the end of the shear layer and the vortex ring). For φ > 96° the values start decreasing.

In Fig. 5.37 the generation of the counter rotating vortex ring on the impinging plate is shown for several nozzle-to-plate distances. The positive values of the Q-criterion contour

(Jeong and Hussain, 1995) are superimposed to the velocity vector map. Firstly it is possible to point out that for *H/D* equal to 2 the Q-criterion detects not only the primary (generated by the synthetic jet ejection phase) and the counter rotating vortex rings but also the zone at *x/D* equal to 0.5 because a strong deflection of the impinging synthetic jet occurs. At *H/D* equal to 2 the counter rotating vortex ring is easily detectable and its centre is quite far from the impinging plate. As *H/D* increases, the counter rotating vortex ring becomes less wide and more attached to the impinging plate until it disappears (*H/D* equal to 8). Such a behaviour is related to the fact that higher is the nozzle-to-plate distance, lower is the primary vortex ring vorticity. This phenomenon allows to detect the position (about *x/D* equal to 2) where usually the counter rotating vortex ring arises. The formation of this counter rotating vortex is the cause of a heat transfer increase (as visible in subchapter 5.1.2) as also reported in literature (Hadžiabdić and Hanjalić, 2008, Rholfs et al., 2012, Ianiro and Carlomagno, 2014).

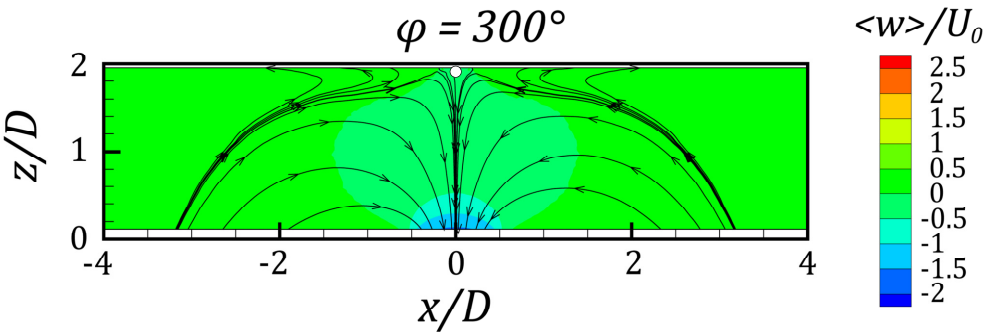

Fig. 5.38 Saddle point (white spot) position with streamlines for SSJ at *H/D* equal to 2

In Fig. 5.38 the saddle point position is shown. For this value of φ (equal to 300°) the saddle point reaches the maximum excursion just touching the impinging plate. In general, such a behaviour is very relevant for a device, which is supposed to work as an electronic cooler. Indeed in this condition, during the suction phase, the device could ingest air coming from the hot plate which has to be cooled. This behaviour could deteriorate the heat transfer performance of the electronic cooling device.

5.1.1.4 Phase-average flow field for TSJ

For the twin synthetic jets, only the Σ equal to 1.1 configuration is analysed. The phase-average axial and radial velocity are shown in Figs. 5.39 and 5.40, respectively. At φ

= 0° the right synthetic jet starts coming out but, differently from the SSJ case, at φ = 24° the vortex ring is not fully formed because the starting suction phase of the left synthetic jet delays such a formation (only the right vortex ring footprint is observable). At φ = 48° the right synthetic jet impinges but it is slightly deflected towards *x/D* equal to 0. Indeed near the plate the negative radial velocity is higher and more extended (in the axial direction) than the positive one. At φ = 72° the axial distribution is not symmetric with respect to the right synthetic jet centreline (located at *x/D* equal to 0.55) but the maximum is attained along *x/D* equal to 0. This is due to the interaction of the two jet which is stronger near the *x/D* equal to 0 axis. The radial velocity still presents two maxima: the first near the plate where the jet has its complete rotation and the second between the plate and the sweeping vortex ring. At φ = 96° the right synthetic jet seems to be less stretched by the left one because the interaction starts decreasing. For $\varphi \geq$ 120° the values become lower.

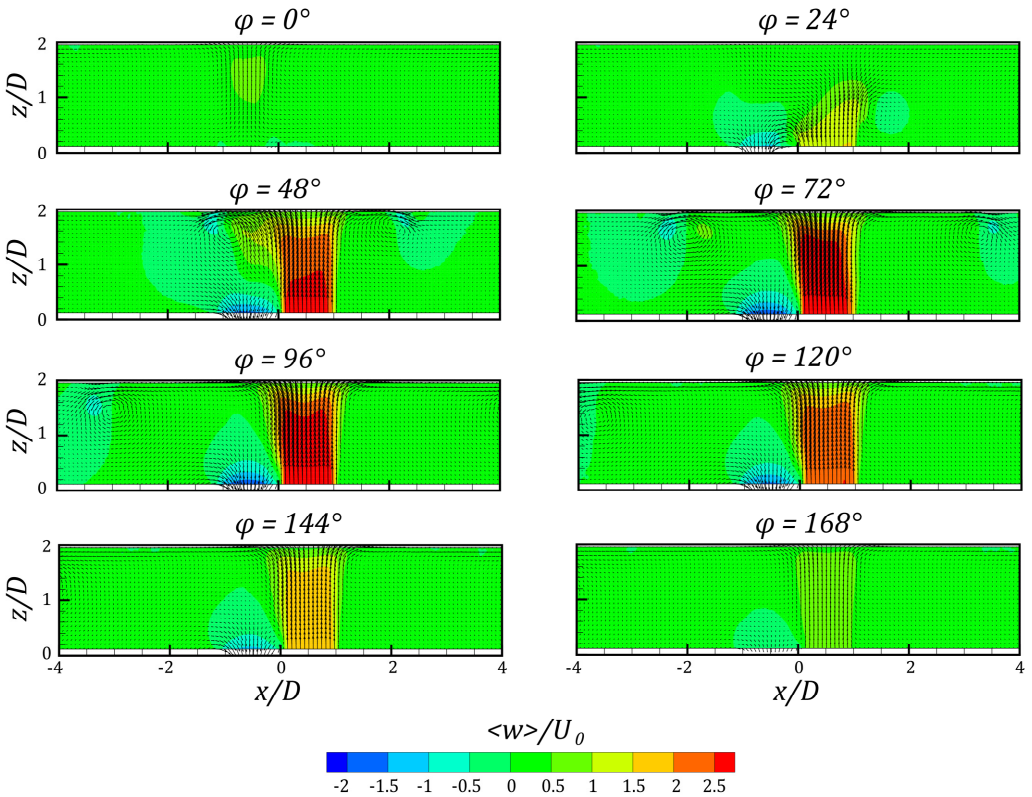

Fig. 5.39 Phase-average axial velocity maps at *H/D* equal to 2

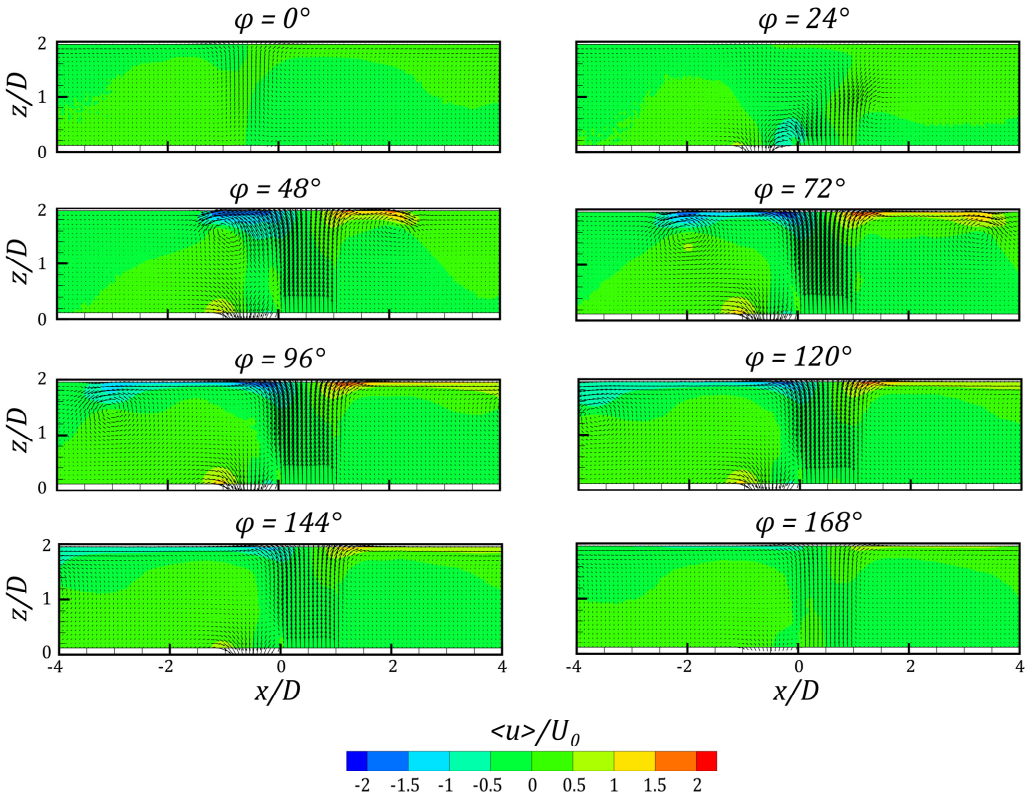

Fig. 5.40 Phase-average radial velocity maps at H/D equal to 2

In Figs. 5.41 and 5.42 the phase-average mean-squared axial and radial turbulent velocity are shown respectively. At φ = 0° no zero values of axial and radial turbulence are still present due to the trailing part of the left synthetic jet. At φ = 24° the axial turbulence attains high value on the front of the vortex ring while the radial one is located in the vortex ring core and between the two jets. At φ = 48° the axial turbulence shows high values along the internal shear layer which are higher than the external one. This is due to the interaction of the two 180° phase-shift jets. Indeed the extension of the turbulence of the internal shear layer arrives until the nozzle exit, differently from the external one. Moreover the axial turbulence of the left vortex ring footprint is lower than the right one because of the suction phase of the left synthetic jet. The same considerations can be drawn for the radial turbulence. Moreover a region of high turbulence , connecting the left nozzle exit and the internal shear layer, is present (above all for the radial component). At φ = 72° the turbulence along the internal shear layer increases and is still higher than the external one. The axial turbulence attains also high value in the vortex core and in the

zone near the plate between the vortex ring and the shear layer. The radial component acts as the axial one apart from the region near the vortex ring. Indeed here the maximum is attained near the plate where the counter rotating vortex is located. At φ = 96° the behaviour of turbulence is the same, indeed, maxima are located along the shear layer, in the ring vortex centre (on the vortex ring left side near the impinging plate for the radial component) and near the impinging plate. For φ > 96° the values start decreasing. In all the phases it is possible to see that, as previously described, the right synthetic jet is deflected towards the *x/D* equal to 0 axis. Furthermore even in this TSJ configuration a potential core-like region is detectable.

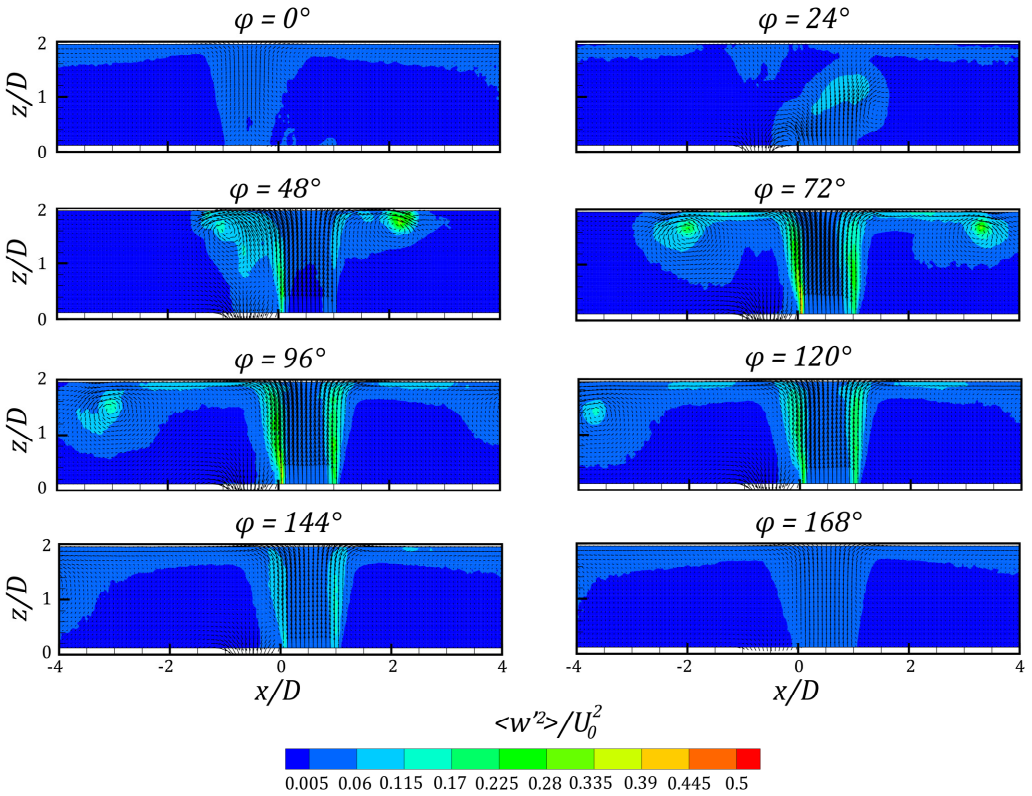

Fig. 5.41 Phase-average mean–squared axial turbulent velocity maps at *H/D* equal to 2

In Fig. 5.43 the phase-average turbulent Reynolds stress are depicted. The Reynolds stress behaves like the turbulent components previously described. Indeed the main features are: maximum value along the shear layer (higher at the internal shear layer), in

the ring vortex core and on its front side and near the plate in the zone between the shear layer and the convecting vortex ring.

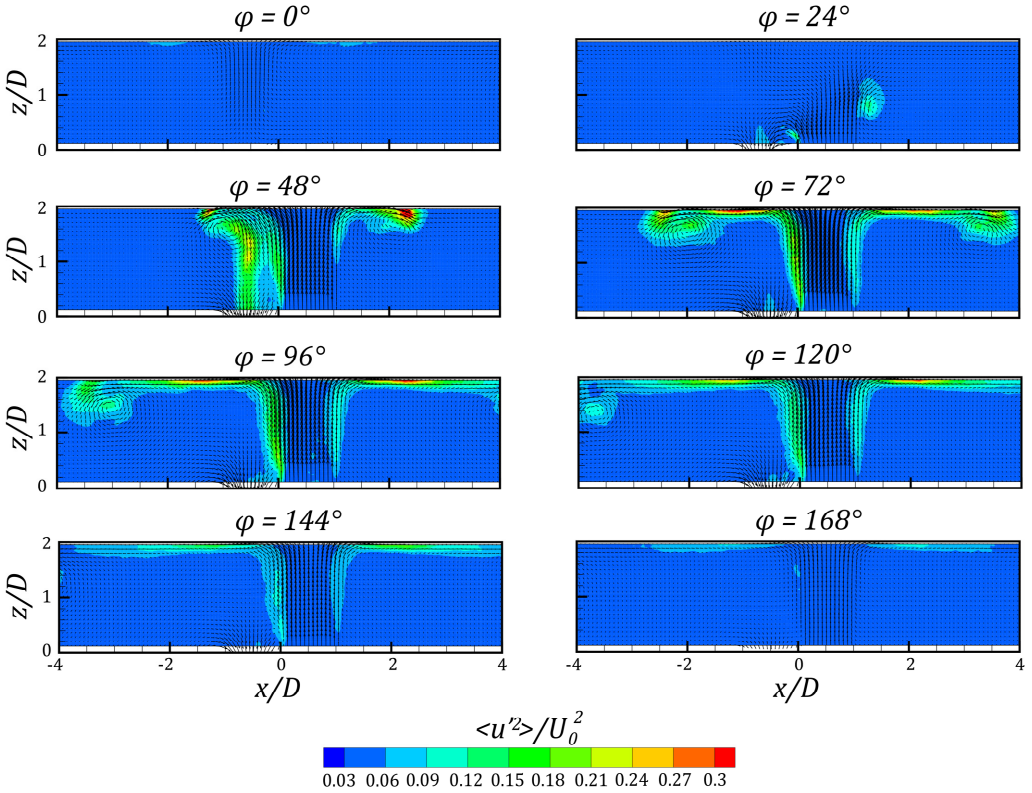

Fig. 5.42 Phase-average mean–squared radial turbulent velocity maps at H/D equal to 2

In Fig. 5.44 the saddle point during the right synthetic jet ejection phase is depicted. At φ = 24° a first saddle point (white spot) is observable near the left synthetic jet nozzle exit. The saddle point is not located along the left synthetic jet axis but on its left side because the right synthetic jet is starting its ejection. At φ = 48° two saddle points can be detected. The first one continues moving towards higher radial position (because of the formation and convection of the right ring vortex) and a second one created between the left vortex ring footprint and the suction of the left synthetic jet. At φ = 72° the first saddle point is almost on the edge of the measurement region while the second one is slightly moving towards the impinging plate. For φ = 96° the first saddle point is out of the field of view, while the second one attains its maximum excursion distance from the nozzle exit. For φ > 96° the latter saddle point returns to the nozzle exit. Differently from the SSJ case, this configuration creates a fluid dynamic condition that does not allow having suction of

air coming from the hot plate. This is due to the right impinging synthetic jet that confines the field affected by the suction phase of the left synthetic jet, which can ingest air (during its suction phase) only from its left side and from the right nozzle (in this plane). Such a condition, differently from the SSJ case, should not deteriorate the heat transfer rate.

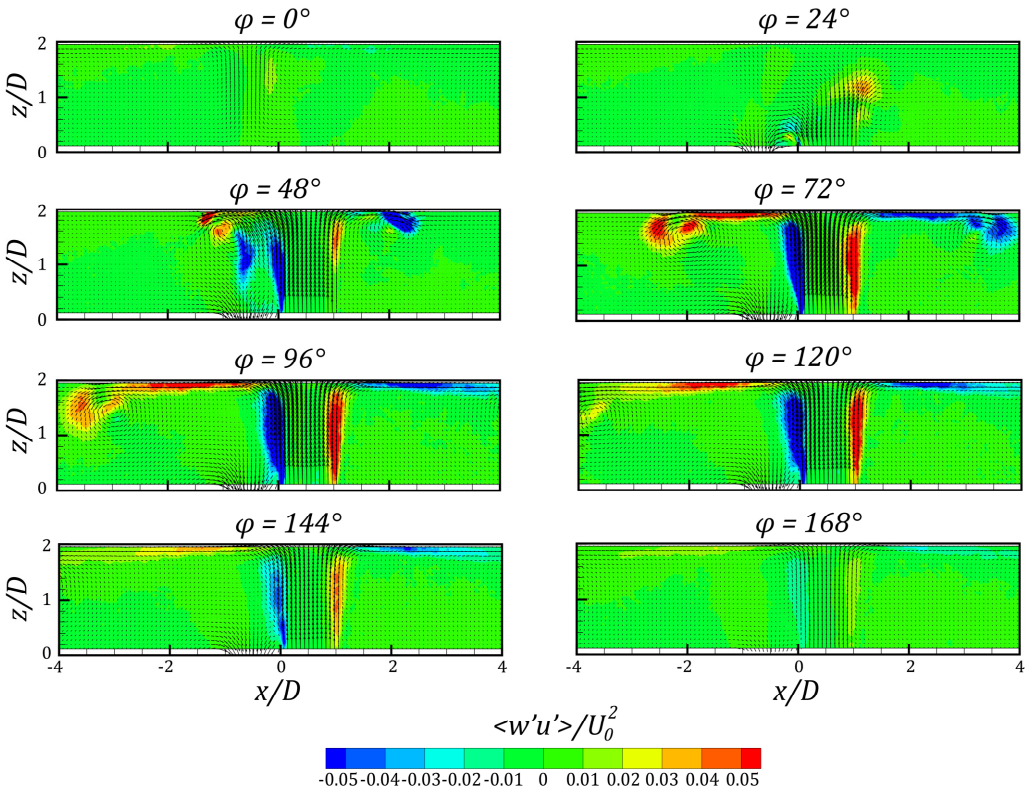

Fig. 5.43 Phase-average turbulent Reynolds stress maps at H/D equal to 2

In Figs. 5.45 and 5.46 the phase-average axial and radial velocity components are depicted. At φ = 0° the footprint of the trailing part of the left synthetic jet is still present. At φ = 24° the right synthetic jet is issued and the behaviour is similar to what shown in the shortest nozzle-to-plate case. At φ = 48° the jet is going to approach the impinging plate but, as it is possible to observe, the ring vortex is deflected because of the interaction with the left synthetic jet which is acting like a sink. At φ = 72° the jet is impinging and the axial profile is bell-shaped, differently from the H/D equal to 2 case. Moreover the jet is considerably deflected toward the x/D equal to 0 axis. Focusing our attention to the radial component it is possible to see that the negative velocity is higher than the positive one

because of the previously described deflection. For φ = 96° the left radial value does not show an high peak (as in the previous phase) because the vortex ring is sweeping and for $\varphi \geq 120°$ the velocity values decrease and the vortex ring goes out of the measurement zone. Furthermore the radial velocity over the plate, for these phases, does not show a peak where the impinging jet rotates. Indeed this value has the magnitude of the one created between the sweeping vortex ring and the impinging plate (differently from the *H/D* equal to 2 configuration).

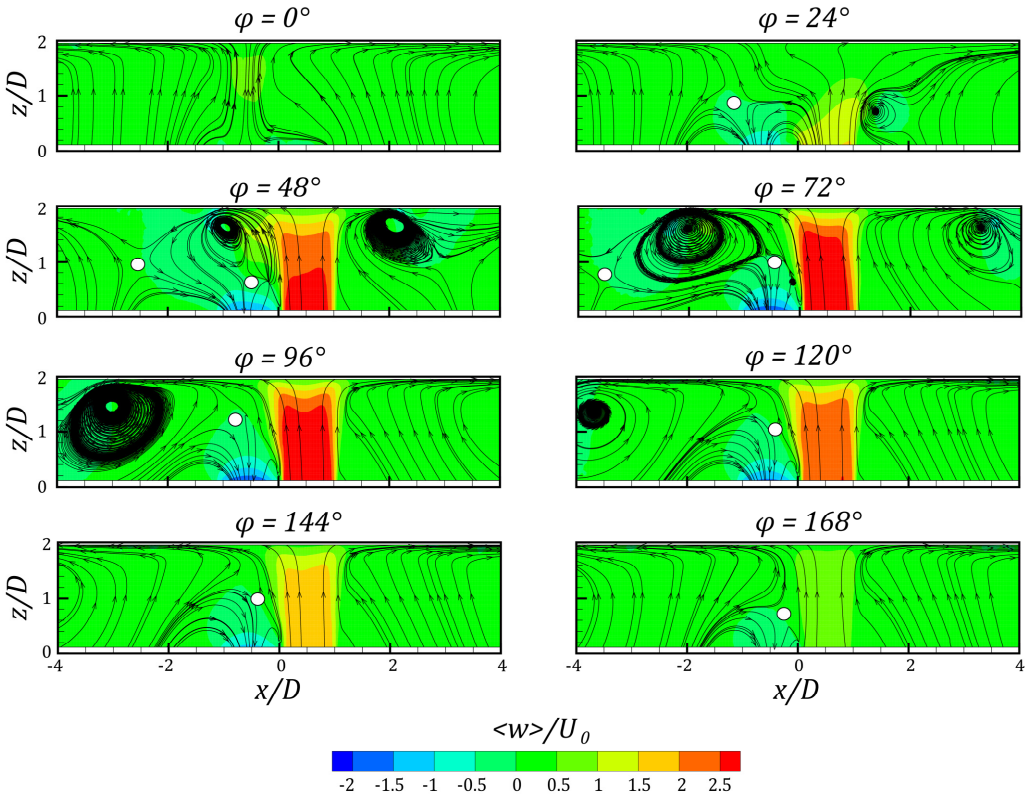

Fig. 5.44 Saddle points (white spots) position with streamlines for TSJ at *H/D* equal to 2

In Figs. 5.47 and 5.48 the phase-average mean-squared axial and radial turbulent velocity, respectively, are shown. At φ = 0° no-zero values of turbulence are still present because of the trailing part of the impinging left synthetic jet. At φ = 24° the axial turbulence shows values different from zero along the shear layer and on the front boundary of the jet. The radial turbulence has a peak in the vortex ring core.

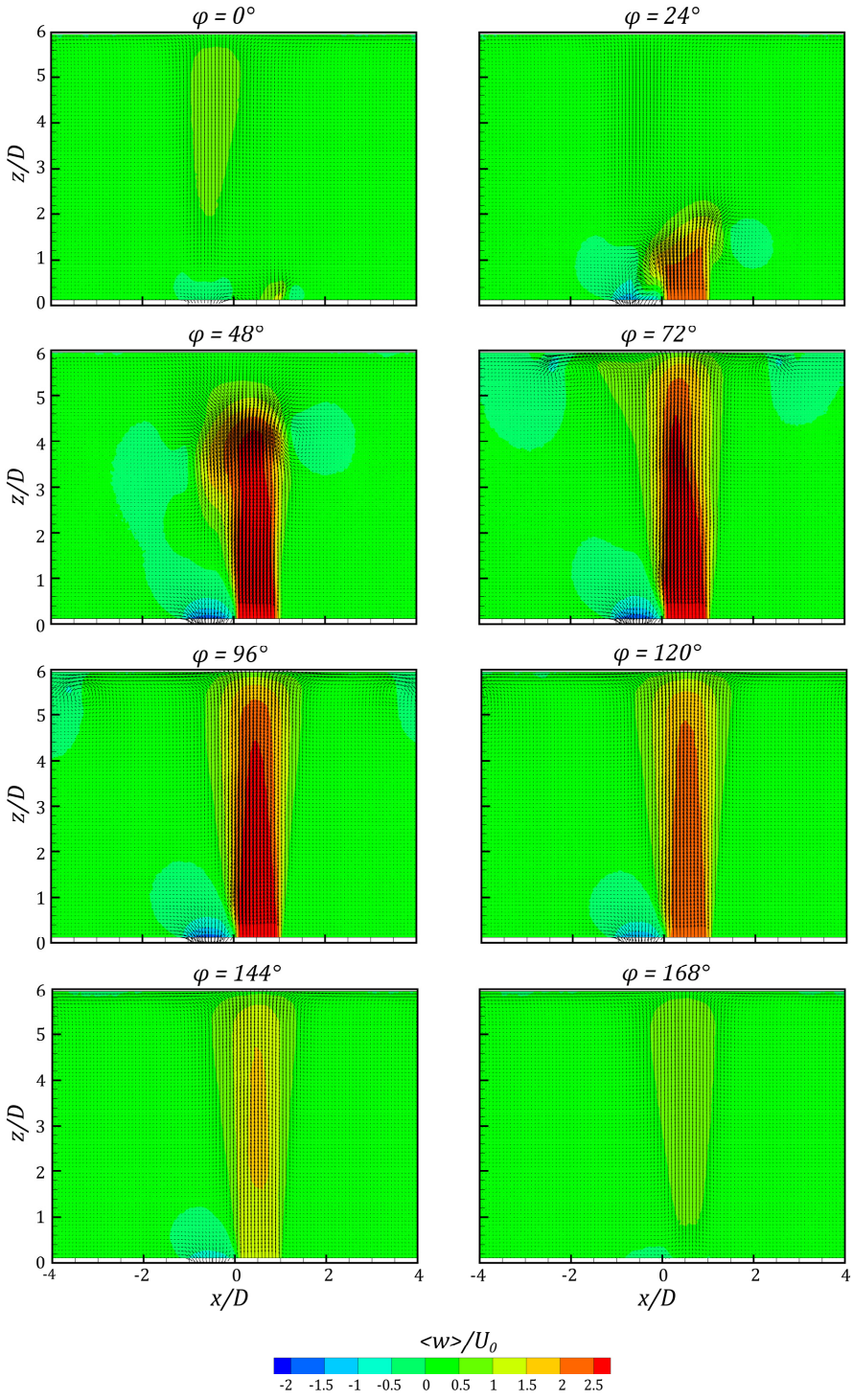

Fig. 5.45 Phase-average axial velocity maps at H/D equal to 6

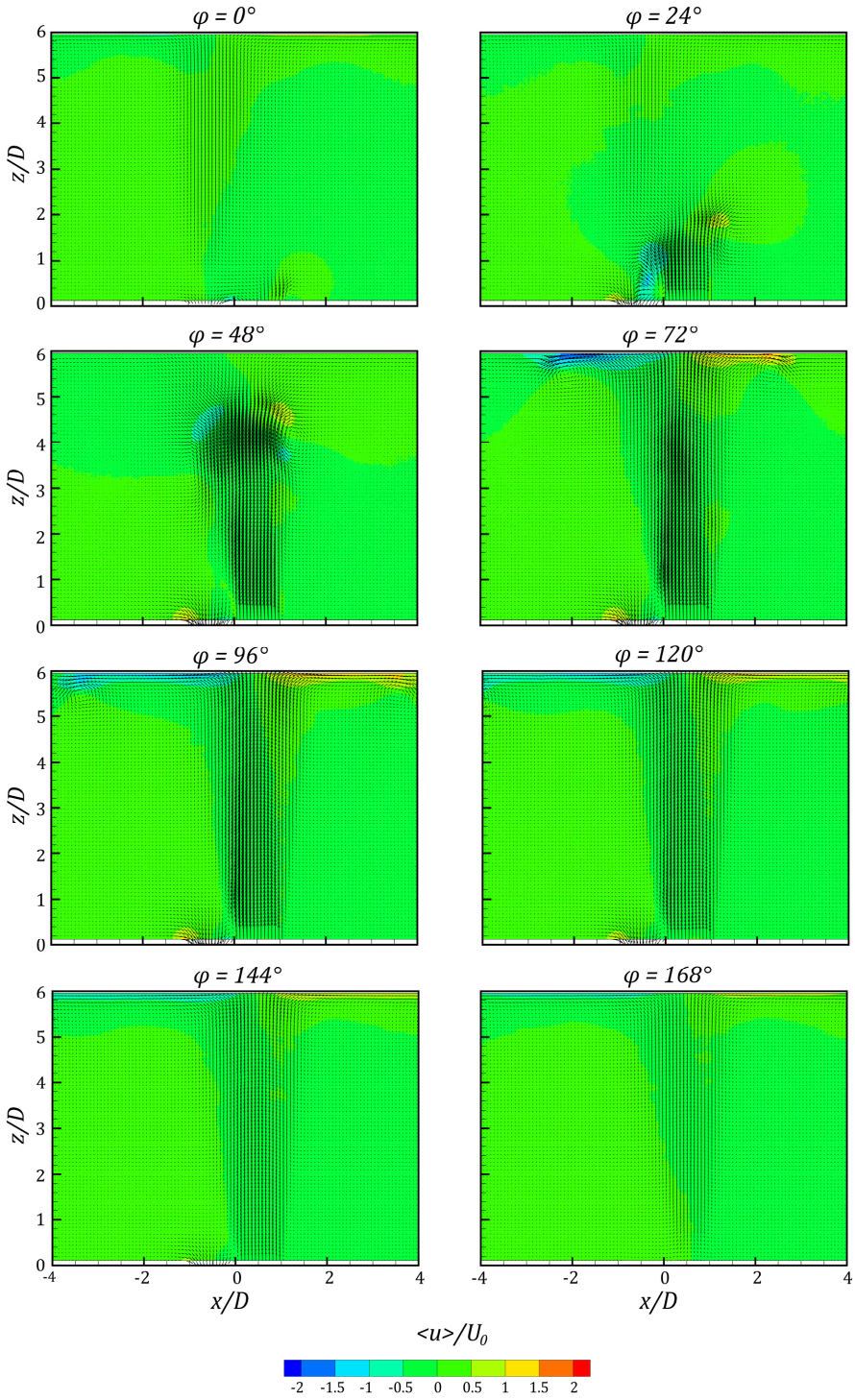

Fig. 5.46 Phase-average radial velocity maps at H/D equal to 6

At φ = 48° the axial turbulence along the internal shear layer has increased and is thicker than the external one. Furthermore the two shear layers start merging at z/D equal to about 3.8 and coalesce with the axial turbulent developed on the front boundary of the convecting vortex ring. Also the radial turbulence seems to start merging but still shows its peak in the vortex ring core. It is necessary to point out that the axial value, as the radial one, of the right vortex ring footprint is higher than the left one. This could be related to the fact that the left part of the vortex ring is affected by the suction phase of the left synthetic jet which damps partially the oscillations. At φ = 72° the turbulent axial component shows higher value along the internal shear (than the external one) and also a maximum located in the vortex ring core (with a greater value in the right footprint). The turbulent radial component acts as the axial one along the shear layer but, near the impinging plate, shows a maximum between the plate itself and the convecting vortex ring (where the counter rotating is placed). Furthermore both components start merging at a axial position of about 3.8 diameters from the nozzle exit. Such a zone is the so-called potential core-like region. At φ = 96° the vortex ring continues sweeping the impinging plate, featured by a decreased axial turbulence maximum in the core. Moreover a high value zone of radial turbulence, which spans from the vortex ring core until the impinging shear layer, is observable. For $\varphi \geq 120°$ the values start decreasing. The deflection and the wider internal shear layer (with high values) presented in these turbulent components is the reason why in the time-average measurement the extension of the potential core-like region seems to be lower (up to 2 diameters).

In Fig. 5.49 the phase-average turbulent Reynolds stress is depicted. After the beginning of the ejection phase for the right synthetic jet (at φ = 0°) the zones of high Reynolds stress (at φ = 24°) are located along the shear layer and near the vortex ring (front side). At φ = 48° the shear layer is developing and the Reynolds stress attains higher absolute values along the inner shear layer than the outer one. Furthermore the vortex ring core zone shows high values as well. At φ = 72° regions of high values are observed along the shear layer and near the zone between the vortex ring and the counter rotating one. At φ = 96° the values near the vortex ring are decreased while the ones along the shear layer are still high. For φ >96° the vortex ring is moved out of the measurement zone and the values along the shear layer start decreasing.

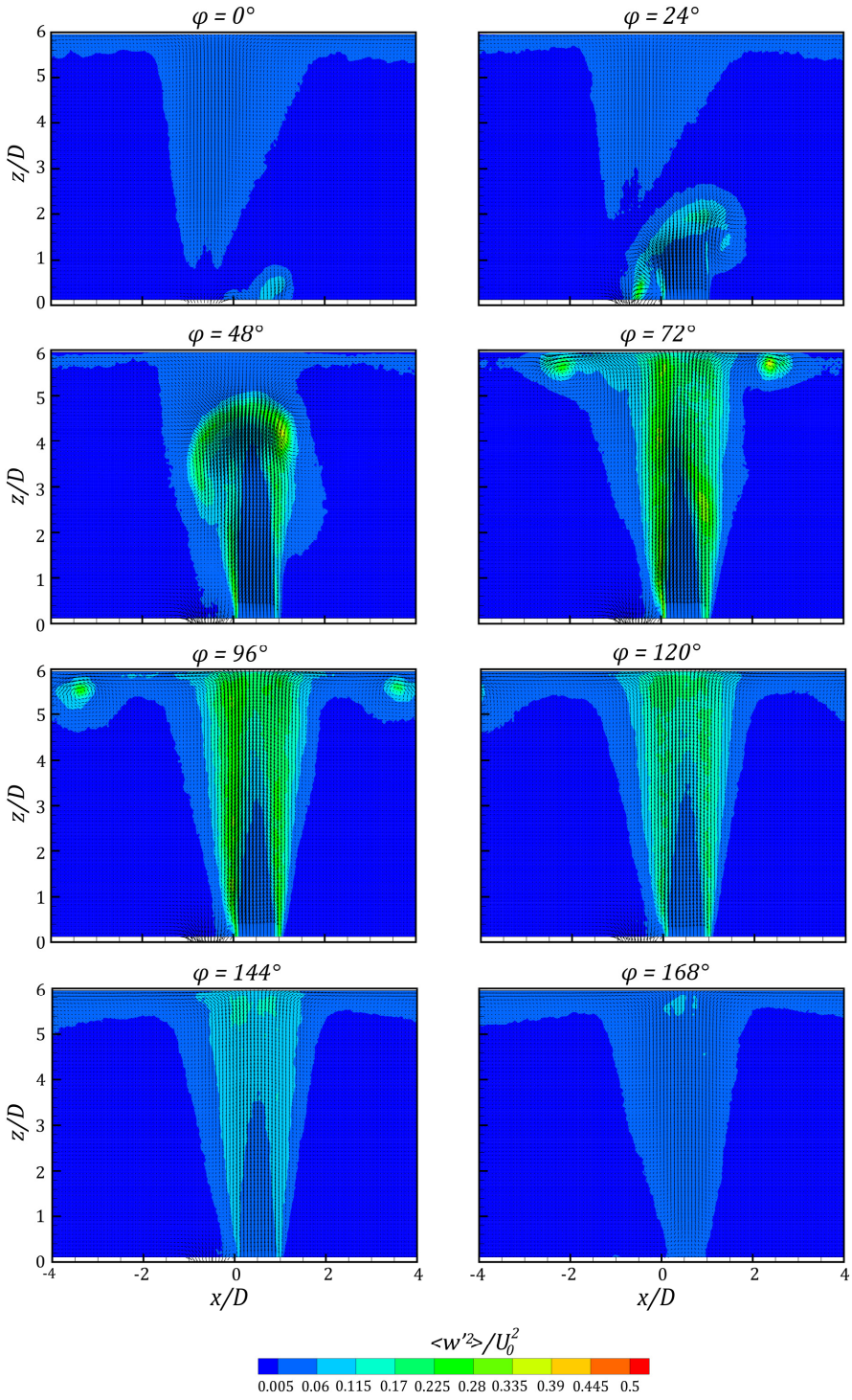

Fig. 5.47 Phase-average mean–squared axial turbulent velocity maps at H/D equal to 6

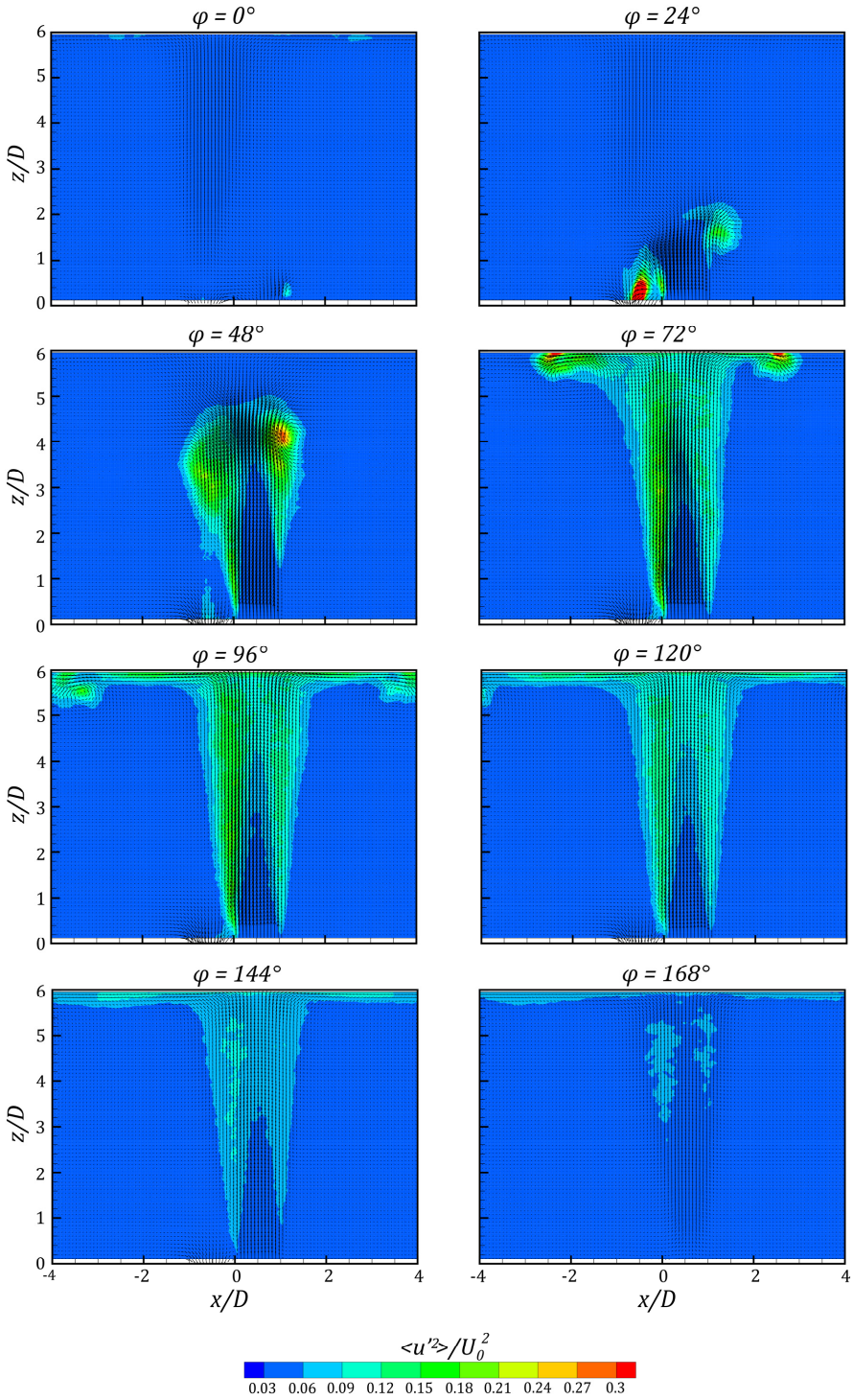

Fig. 5.48 Phase-average mean–squared radial turbulent velocity maps at H/D equal to 6

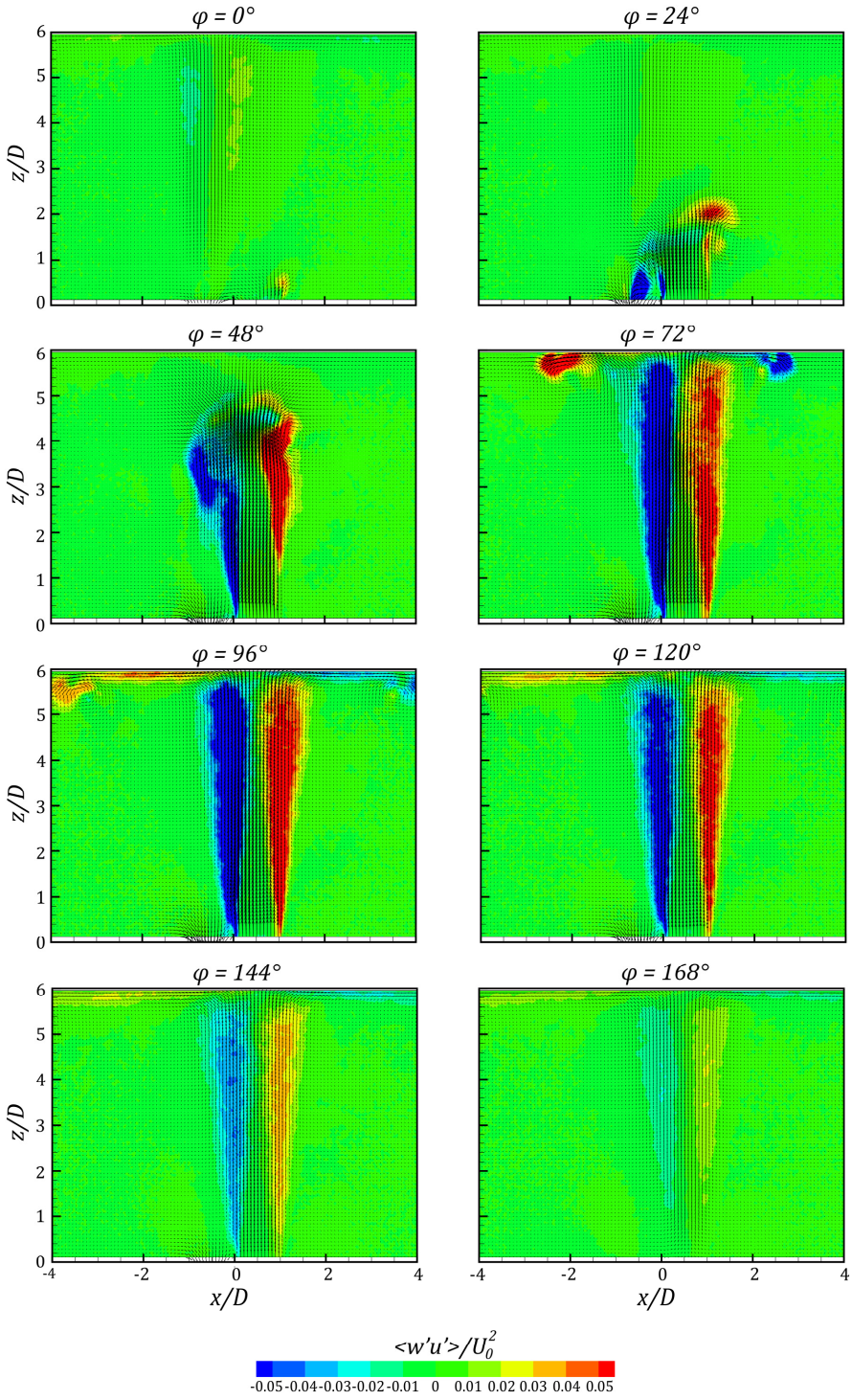

Fig. 5.49 Phase-average turbulent Reynolds stress maps at H/D equal to 6

5.1.2 Heat transfer measurements

$\overline{Nu}$ and *Nu'* maps and profiles (time-average) for single and twin circular impinging synthetic air jets with $\sum$ equal to 1.1, 3 and 5 are shown in Figs. 5.50-5.54. Since the time-average flow field of all tested configurations is symmetric with respect to *x* and *y* axes, $\overline{Nu}$ and *Nu'* maps are obtained by averaging the four quadrants in order to reduce the measurement noise. For the sake of brevity, owing to the symmetry with respect to *y* axis, only half map of $\overline{Nu}$ (on the left) and *Nu'* (on the right) are presented.

In Figs. 5.55 – 5.60 Nu_{φ} maps (phase-average) for single and twin circular impinging synthetic air jets with $\sum$ equal to 1.1, 3 and 5 are depicted. In order to reduce the measurement noise, owing to the fact that phase-average flow field is symmetric with respect to the *x* axis, Nu_{φ} maps are obtained averaging the positive *y* region with negative one. With the objective to compare heat transfer distribution at different phases and different value of *H/D*, it is necessary to set a reference phase zero. The reference phase zero is set to correspond with the phase in which the heat transfer time derivative in the stagnation point changes its sign and becomes positive (for the TSJ the reference stagnation point is the right one). For the sake of brevity, only the impingement half cycle is presented with 8 heat transfer phase maps with a step of 24°, for both single and twin synthetic jet configurations.

5.1.2.1 Time-average measurements

At short distance from the nozzle (inside the potential core-like region), many physical features can be considered as in analogy with continuous jets (Jambunathan et al., 1992) impinging within the length of their potential core (i.e. *H/D* = 2 and 4). At *H/D* = 2 an inner ring shaped region with local $\overline{Nu}$ maximum appears at *x/D* ≈ 0.5 and an outer region with local $\overline{Nu}$ maximum appears at *x/D* ≈ 1.9 (see Fig. 5.50). Such a phenomenon is even more evident in Fig. 5.54 where the $\overline{Nu}$ and *Nu'* profiles at *y/D* = 0 are presented for H/D = 2, 4, 6 and 10. Maximum values of *Nu'* are also obtained approximately in the same regions where inner and outer ring shaped structures are located as easily detectable in *Nu'* map.

The $\overline{Nu}$ values, measured in the first ring shaped region, are slightly higher than the values obtained in the stagnation region. This can be related to the behaviour of the time-average axial velocity component and the mean-squared phase-correlated organized contribution to the velocity component (Figs. 5.7-5.8). Indeed a peak of these parameters,

for this nozzle-to-plate configuration, is observable at *x/D* equal to 0.5. This ring shaped region is not present for nozzle-to-plate distances higher than 4 (after the end of the potential core-like region), as detectable from $\overline{Nu}$ and *Nu'* profiles in Fig. 5.54. This behaviour is also detectable in the axial velocity components profiles (W, $\overline{\widetilde{w}^2}$ and $\overline{w'^2}$) which, for a nozzle-to-plate distance higher than 4, show a bell-shaped profile in the region near the jet axis (almost bell-shaped for $\overline{w'^2}$).

The second peak (outer ring shaped region) is present for *H/D* lower than 4 while for *H/D* equal to 6 only a change in the $\overline{Nu}$ slope is visible. For *H/D* greater than 6 such a peak disappear. The presence of this peak can been ascribed to unsteady separation and later reattachment as shown by Hadziabdic and Hanjalic (2008) and Rohlfs et al. (2012). According to Rohlfs et al. (2012) the unsteady separation is due to the formation of the secondary counter rotating vortex on the wall which is generated by the passage of the ring vortex (as seen in subchapter 5.1.1.3). In these experiments the formation of the counter rotating vortex is visible until *H/D* equal to 6. The size and vorticity of this counter rotating vortex decreases as *H/D* increases. This behaviour agrees with the heat transfer profiles. Furthermore the presence of such a counter rotating vortex is even detectable from the velocity profile over the plate. Indeed the second peak present in Figs. 5.8 ($\overline{\widetilde{w}^2}$ and $\overline{\widetilde{u}^2}$) and 5.9 ($\overline{w'^2}$ and $\overline{u'^2}$) are related to the counter rotating vortex generation. It has to be point out that such a second heat transfer peak is not only related to the phase-average measured counter rotating vortex caused by the primary vortex ring. Indeed others counter rotating vortex are generated by the vortex ring caused by the Kelvin-Helmholtz instabilities of the column of the fluid following the primary ring vortex (because the Strouhal number is equal to 0.024).

At a nozzle-to-plate distance equal to 6 diameters the maximum heat transfer in the stagnation point is detected, in agreement with what happens for continuous jets. Seen that the stagnation heat transfer is influenced by all the velocity components, such a result could be ascribed to two main features: firstly high turbulent ($\overline{w'^2}$ and $\overline{u'^2}$) values are attained (at this *H/*D equal to 6) which are, at least, more than twice those of the shorter ones; secondly the values of W and $\overline{\widetilde{w}^2}$ are slightly lower than previous cases (similar to *H/*D =2 case and about 0.8 of *H/D* = 4 case).

Nu' resembles the $\overline{Nu}$ profile and is strictly related to the axial fluctuating velocity profile (phase-correlated and turbulent components). Indeed the peaks location and the profiles of *Nu'* are very similar to what shown in Figs. 5.8 and 5.9 for the fluctuating

velocity components. Moreover the value of *Nu'* map becomes more uniform and its maximum value decreases at high *H/D* because, as the distance from the nozzle increases (Shuster and Smith, 2007), synthetic jets act like turbulent continuous jets. As matter of fact all the fluctuating velocity values decrease for *H/D* higher than 6.

The $\overline{Nu}$ maps for twin synthetic jets with $\sum$ = 1.1 (Fig. 5.51) show two distinct stagnation points only for *H/D* = 2. As a matter of fact, considering Fig. 5.54, the relative $\overline{Nu}$ profile shows a first peak at *x/D* = 0 and a symmetric second peak at approximately *x/D* ≈ 1.05. The first and the second peak are related to the existence of the inner ring shaped region. Such a ring occurs around the two stagnation points, located at *x/D* ≈ 0.55, and shows a diameter equal to 1 *D*. The superimposition of the two inner ring shaped regions at *x/D* = 0 is the reason why the first peak is higher than the second one. This can be related to the behaviour of the time-average axial velocity component and the time-average phase-correlated organized contribution to the velocity axial component (Figs. 5.17-5.18). Indeed a peak of these parameters, for this nozzle-to-plate configuration, is observable at about the same radial locations. Moreover for this value of *H/D* also the outer ring shaped region can be detected at about *x/D* ≈ 2.5 (see Fig. 5.54). Near this radial location, the peak of the time-average axial (at *x/D* equal to 2.3) and radial (*x/D* equal to 2.2) turbulence is located (see Fig. 5.19).

The *Nu'* maps and profile clearly show the effect of the unsteady passage of the vortex ring. Due to the superimposition of the two inner ring shaped regions, the value of *Nu'* acquired at *x/D* = 0 is not equal to the one attained at *x/D* ≈ 1.05 (see also Fig. 5.54) as also occurs for the axial velocity fluctuation behaviour (Figs. 5.18-5.19). As *H/D* increases the strong interaction between the two adjacent jets produces a different heat transfer behaviour characterized by a maximum $\overline{Nu}$ value at *H/D* = 4 as visible in Fig. 5.54. As previously said for the single synthetic jet, such a maximum could be explained focusing on the attained values of the velocity component on the jet axis. The *H/D* equal to 4 configuration shows turbulence values which are almost twice those attained by the shortest configuration but only about half or more (0.65 and 0.85 times for the radial and axial turbulent component, respectively) of *H/D* equal to 6. On the contrary, considering *W*, $\overline{\widetilde{w}^2}$ and $\overline{\widetilde{u}^2}$, the ratio is lower than 1 (with respect to *H/D* equal to 2) and higher than 1 (with respect to *H/D* equal to 6). Hence, in conclusion, such a nozzle-to-plate configuration can be assumed as the best compromise between the velocity component values that leads to a maximum heat transfer in the stagnation point.

For $\sum$ = 1.1 and 4 ≤ *H/D* ≤ 8 *Nu'* presents a different behaviour from the $\overline{Nu}$ profile. In fact at *H/D* equal to 4 the *Nu'* profile shows the peak relative to the inner ring shaped region but the second peak is strongly reduced. Such a second peak disappears for *H/D* higher than 4 differently from the first one. Such a behaviour can be observed for the mean-squared axial turbulent velocity components (Fig. 5.19) but it is not so easily detectable for the other fluctuating variables. This could be related to the presence of the second wall jet which passes over the same zone of the plate (already swept by the vortex ring) causing a change in the variables value, differently form the SSJ configuration. Indeed in Fig. 5.18 only small later oscillations, approximately in the same radial position, can be barely seen. The first *Nu'* peak shifts toward the centre (as occurs for $\overline{\widetilde{w}^2}$) as *H/D* increases because the jet, as previously explained, starts acting as a turbulent continuous jet. At *H/D* equal to 10 the *Nu'* profile is very similar to the one of a single synthetic jet. At all the nozzle-to-plate-distances the values of $\overline{Nu}$ measured are higher than the SSJ case. Moreover it is worth nothing that the values attained by *Nu'* for such a twin synthetic jets configuration are lower than the one acquired by the single synthetic jet (Figs. 5.51, 5.52 and 5.54). This is related to the presence of two impinging synthetic jets. Indeed, in this configuration there is always an heat transfer caused by the impingement. This condition leads to a decreasing variation of the Nusselt number (*Nu'*) as also occurs for the phase-correlated velocity contributions in the TSJ case (with respect to SSJ case).

Regarding the twin synthetic jets with $\sum$ = 3 (Fig. 5.52) the Nusselt number maps show two clearly distinct stagnation regions, approximately at *x/D* ≈ 1.5 with its inner and outer ring shaped regions. In this configuration, for *H/D* = 2, the peak located approximately at *x/D* ≈ 1 is higher than the peak at *x/D* ≈ 2. This effect is related to the fact that the peak which is closer to the centre is more affected by the presence of the other jet and a beneficial effect is attained. Such a phenomenon decreases with *H/D* increase, disappearing already for *H/D* = 4. Also in this case *Nu'* and $\overline{Nu}$ maps and profiles present a similar behavior. As matter of fact at *H/D* = 2 the *Nu'* profile shows two peaks at approximately *x/D* ≈ 2.1 and *x/D* ≈ 3.5 showing the presence of the inner and outer shaped regions, as also visible in the velocity components (Figs. 5.27-5.29). The relationship between the velocity component and the heat transfer behaviour is the same previously explained for the SSJ case. As *H/D* increases, the inner and outer structures disappear as visible in Figs. 5.52 and 5.54 (and also all the velocity component). Moreover the maxima in *Nu'* profile merge in a unique maximum located at approximately *x/D* ≈ 1.5,

where the synthetic jet impinges (as occurs for $\overline{\tilde{w}^2}$ and $\overline{w'^2}$ in Figs. 5.28 and 5.29, respectively). The behaviour of twin synthetic circular air jets with $\sum$ = 5 (Fig. 5.53) is very similar to the one shown for $\sum$ = 3.

Nusselt number maps show two distinct stagnation regions, approximately at *x/D* equal to 2.5, which are present for all *H/Ds*. Also in this case, as for the single synthetic jet, for *H/D* = 2 a ring-shaped region is visible around each stagnation region, as shown in Fig. 5.53. Indeed the *Nu'* profile shows two peaks at about *x/D* ≈ 2.2 and *x/D* ≈ 3.2.

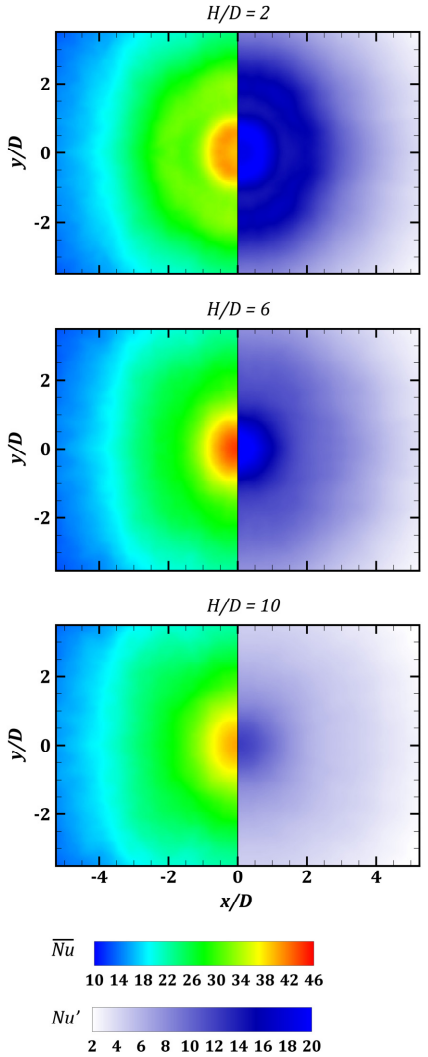

Fig. 5.50 $\overline{Nu}$ (left) and *Nu'* (right) maps for single synthetic jet

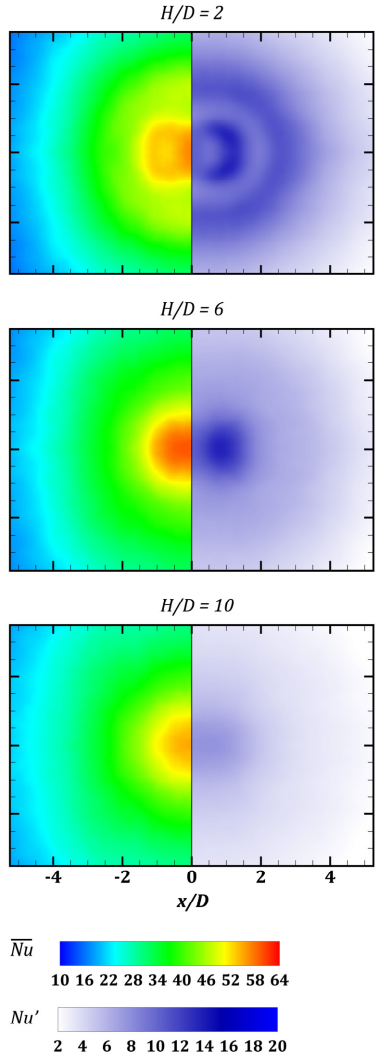

Fig. 5.51 $\overline{Nu}$ (left) and *Nu'* (right) maps for twin synthetic jet ($\sum$ = 1.1)

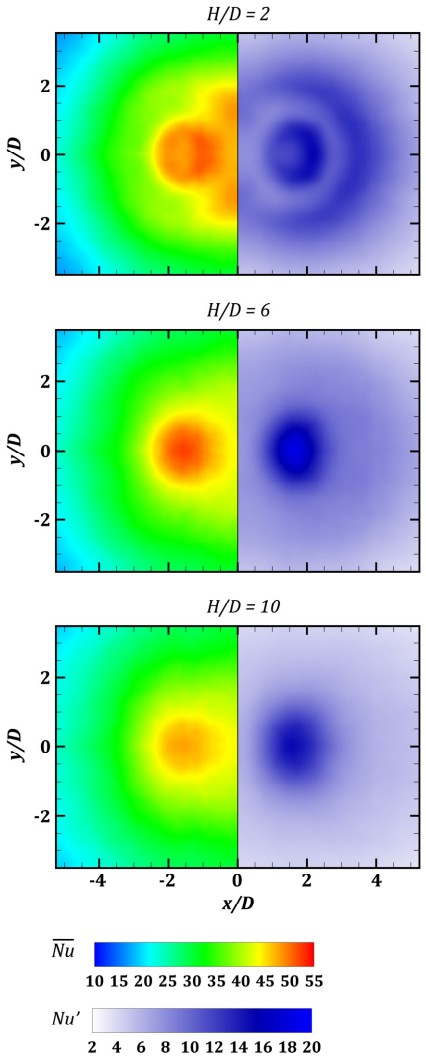

Fig. 5.52 $\overline{Nu}$ (left) and Nu' (right) maps for twin synthetic jet ($\sum$ = 3)

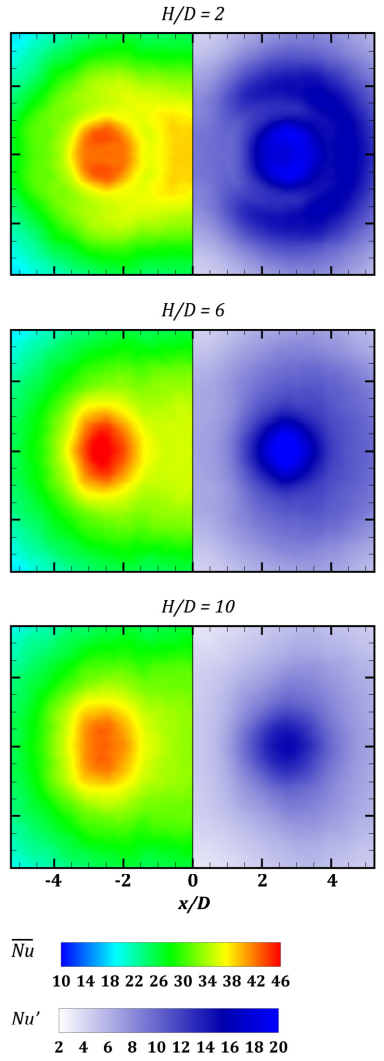

Fig. 5.53 $\overline{Nu}$ (left) and Nu' (right) maps for twin synthetic jet ($\sum$ = 5)

The inner peak is lower because is more affected by the other impinging synthetic jet, as occurs for the twin configuration at $\sum$ = 3. In this figure a mild plateau at x/D = 0 is detectable for values of H/D equal to 2, 4 and, barely, 6. Such a plateau decreases with increasing the nozzle-to-plate-distance disappearing already for H/D equal to 8. This phenomenon is ascribed to the interaction of the two outer ring shaped regions related to the two existing stagnation regions. The behaviour of $\overline{Nu}$ and Nu' profile at higher H/D is similar to one of twin synthetic jets with $\sum$ = 3.

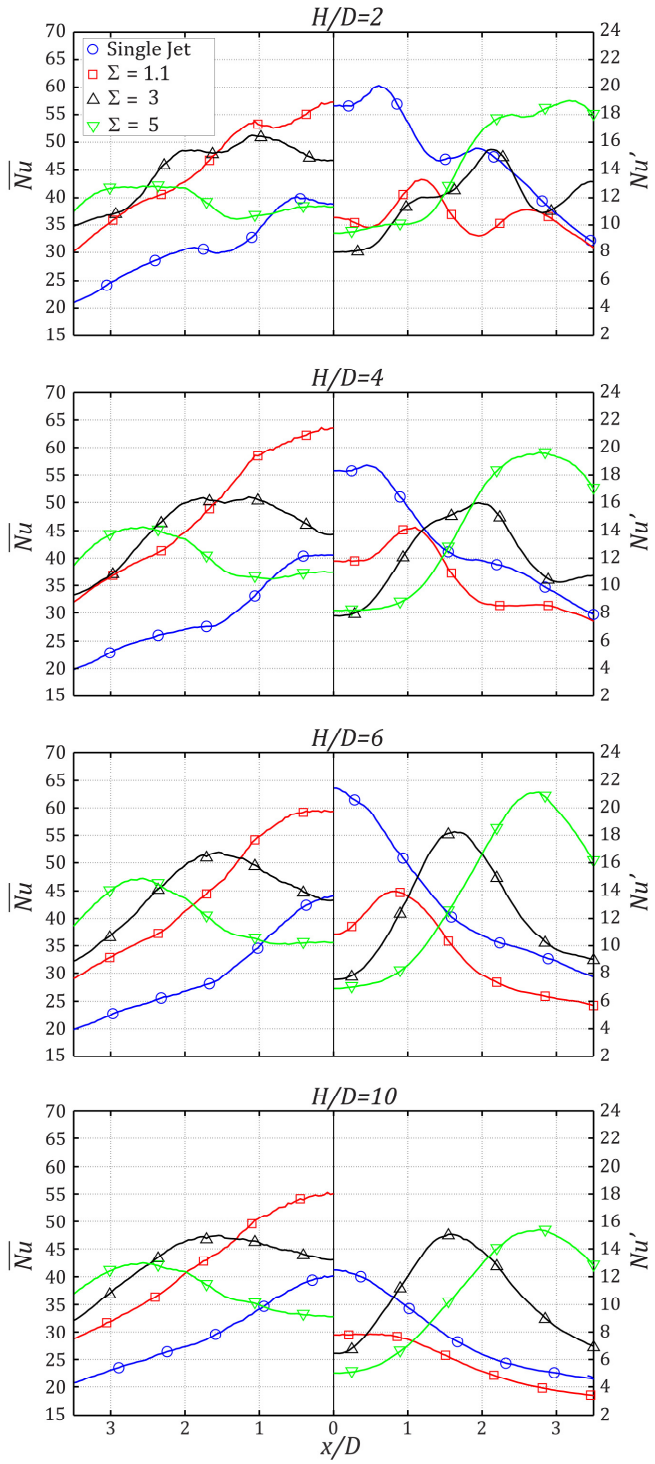

Fig. 5.54 $\overline{Nu}$ (left) and Nu' (right) profile for y/D = 0

5.1.2.2 Phase-average measurements

Fig. 5.55 shows Nusselt number maps for the SSJ at H/D = 2, starting from φ = 0° up to φ = 168°. As previously assumed, at φ = 0° the jet reaches the target plate and starts spreading over the foil, as visible at φ = 24°. At φ = 48° the jet is sweeping the surface and the inner ring shaped region arises at radial distance (r) from the stagnation point of 0.5 D from the centre of impingement. This result is in agreement with DNS simulation of a continuous circular impinging jet by Rohlfs et al. (2012).

This inner ring shaped region is caused by the radial wall acceleration (see Rohlfs et al., 2012 and Gardon and Akfirat, 1965). According to Rohlfs et al. (2012) this radial acceleration generates an increase of the spatial gradient of axial velocity near the impinging plate (for the continuity equation) which leads fresh air near the plate itself. This agrees with the no bell-shaped profile of the axial velocity near the impinging plate which can be observed in Fig. 5.7. At φ = 72° the Nu_{φ} value at inner ring location increases its value, likely because synthetic jet continues impinging over the foil causing an increase of the wall radial acceleration, and an outer ring shaped region can be detected at a radial distance of 1.9 D. The outer ring shaped region can been ascribed to unsteady separation and later reattachment due to the formation of the secondary counter rotating vortex on the wall, generated by the passage of the primary vortex ring and subsequently vortex rings caused by the Kelvin-Helmholtz instability. Hence the delay between the appearances of the two ring shaped regions can be ascribed to the travelling time necessary to the primary vortex ring to assume the requested vorticity in order to generate, for the first time, the secondary counter rotating vortex. Indeed, such ring structures is already present at φ = 24° but is not so clearly visible as in the next phases. At φ = 24° the outer ring is the one formed by the passage of the sweeping vortex ring which creates the counter rotating one (as seen in subchapter 5.1.1.3). After the ring vortex is passed (indeed the zone featured by high heat transfer is widening) the outer ring shaped region is still present. This one could be ascribed to the column of fluid which follows the ring vortex (as described for a L_0/D higher than 4 in McGuinn et al., 2014). Higher is the dimensionless stroke length (L_0/D) longer is the following column of fluid. Hence in this case ($L_0/D \approx 42$) this column of fluid acts like a turbulent continuous jet generating vortex rings, because of the Kelvin-Helmholtz instability. Such vortex rings are the cause of the counter rotating vortex rings near the wall and, consequently, the cause of the continuous presence of the outer ring shaped region of Nusselt number maxima.

The outer ring shaped region moves from *r/D* equal to about 1.8 to *r/D* equal to approximately 2. Such a motion is caused because the synthetic jet is still impinging, indeed vortex ring is still travelling, so the location of the secondary vortex ring separation is moved towards higher radial position At φ = 96° the Nusselt number acquires its maximum value. After φ = 96°, phase-average Nusselt number values in this region decrease and the two ring shaped regions weaken probably because the biggest part of the incoming flow (for the cycle) has already impinged. The map for *H/D* equal to 4 (not shown herein for the sake of brevity but present in the attached movie to Greco et al., 2014) presents result similar to those at *H/D*=2. The case of *H/D* equal to 6 is presented in Fig. 5.56. In agreement with what seen in the $\overline{Nu}$ map at *H/D* = 6, the two ring shaped regions are not present. The absence of the inner ring shaped region is caused by two main features: the value of *H/D* which is greater than the synthetic jet potential core-like region (as reported in subchapters 5.1.1.1 and 5.1.1.3); the ring vortex does not have enough vorticity to generate a strong enough secondary counter rotating vortex (as depicted in Fig. 5.36). It is possible also to note that the maximum value of Nu_φ is attained around φ = 72° for *H/D* equal to 6 while it is attained at around φ = 96° for *H/D* equal to 2. Moreover the heat transfer rate is more spatially concentrated near the stagnation point for *H/D* = 6 than the case with *H/D* = 2 where such a cooling occurs inside the area enclosed by the outer ring shaped region.

For all the *H/D* values, the phase-average Nusselt number maps for φ > 168° (not shown herein for the sake of brevity but present in the attached movie 1 to Greco et al. (2014)) present a decreasing value of the heat transfer, with respect to the map at φ = 168° and have all a similar spatial distribution.

The phase-average Nusselt number maps for the TSJ with $\sum$ equal to 1.1 and 5 at *H/D* equal to 2 and 6 are reported in Figs. 5.57 - 5.60. The phase-average Nusselt number maps for the configuration with $\sum$ =3 have not been reported because their behaviour is very similar to that of the twin synthetic jets with $\sum$ =5. (All phase-average Nusselt number maps are attached to Greco et al. (2014) as video sequences in movie 2, 3 and 4 for $\sum$ = 1.1, 3 and 5, respectively). The phase-average Nu_φ maps (Fig. 5.56) of TSJ for $\sum$ =1.1 at *H/D* equal to 2 show a different behaviour with respect to SSJ (Fig. 5.53). During the ejection phase, at φ = 0°, a higher heat transfer (Nu_φ in the stagnation point is about double with respect to the single synthetic jet), is shown mainly due to the strong jet interaction (as shown in subchapters 5.1.1.2 and 5.1.1.4). At φ = 24° the phase-average

Nu_φ map of TSJ already shows, with respect to SSJ, the inner ring shaped region; at φ = 48° such a map shows an higher value of Nu_φ at the inner ring shaped region and the presence of the outer ring shaped region differently from SSJ. These phenomena are caused by the higher centreline velocity of the TSJ with respect to SSJ (as reported in Chapter 4 and subchapter 5.1.1). In fact such a higher velocity generates a faster spreading of the impinging synthetic jet over the foil, hence a greater wall radial acceleration. Furthermore at φ = 72° the TSJ Nu_φ map shows a higher value at inner and outer ring regions with respect to SSJ. In the following phases the value acquired by the phase-average Nusselt number for TSJ are comparable (at φ = 96°) or slightly lower (at φ = 120°) than those of SSJ in the same phase. Finally the inner and outer ring shaped regions disappear approximately at the same phase for both configurations. For *H/D* equal to 6 the outer and inner ring shaped regions for both configurations (Figs. 5.56 and 5.58) are not detected because, as in the case of the single synthetic jet, the nozzle-to-plate distance is much higher than the potential core-like region of the synthetic jet. Moreover it is possible to highlight that also for this value of *H/D* the phase-average Nusselt number map of TSJ, for the first four phases, attain a higher value with respect to the SSJ due to the higher impinging axial velocity and axial fluctuations. On the other hand, the behaviour, in the last four phases, is the same for both configurations.

TSJ for $\sum$ =5, differently to the SSJ and to $\sum$ =1.1, present at phase zero two heat transfer maxima in the stagnation points (see figs.5.59 and 5.60). One maximum is due to the right jet generated from the right TSJ that is reaching the target plate (in the right part of map), while on the left the maximum is due to the extinguishing left TSJ. All these TSJ configurations show a behaviour close to SSJ one during the ejection phase but with a different position of stagnation point. For all the *H/D* values, in each twin synthetic jet configuration, the phase-average Nusselt number maps for φ > 168° (not shown herein) present a symmetric distribution respect 180° phase delay and the *y* axis (as visible in movie 2, 3 and 4 attached to Greco et al., 2014).

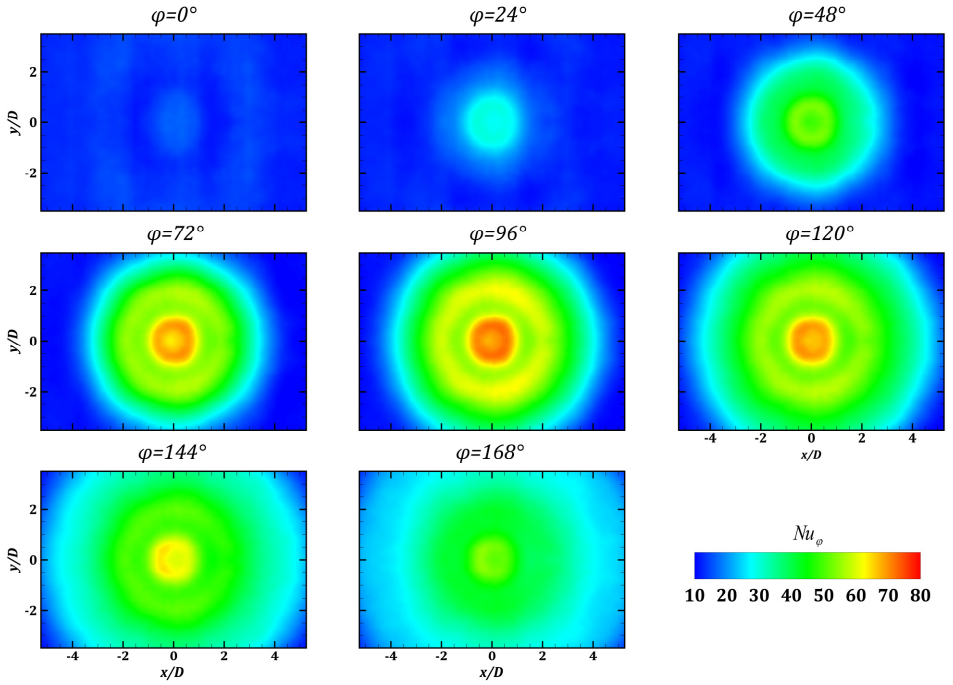

Fig. 5.55 Phase-average Nusselt number maps for SSJ at H/D = 2

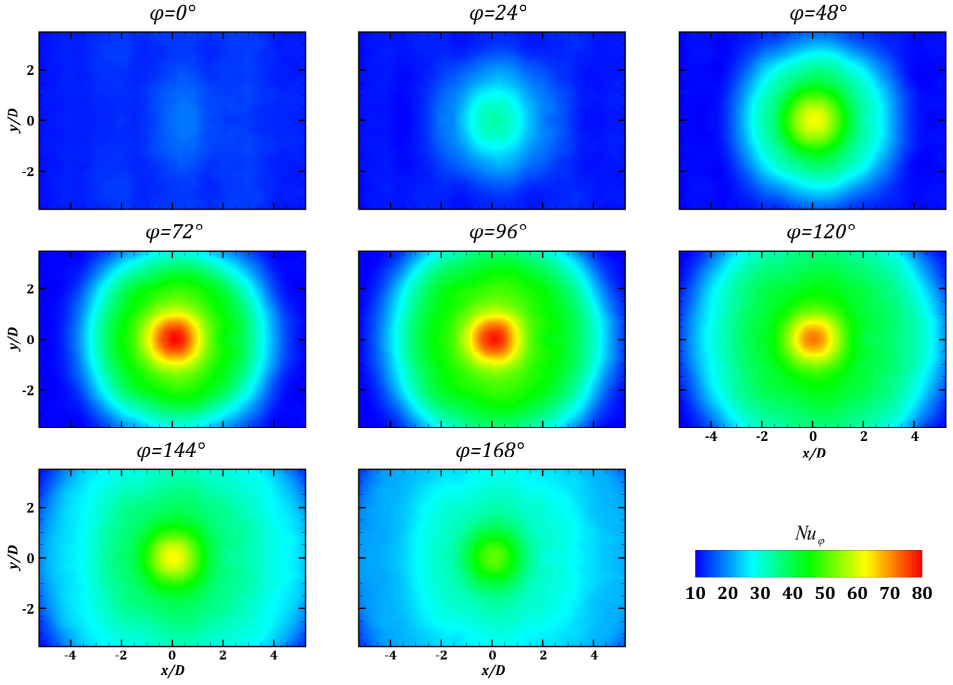

Fig. 5.56 Phase-average Nusselt number maps for SSJ at H/D = 6

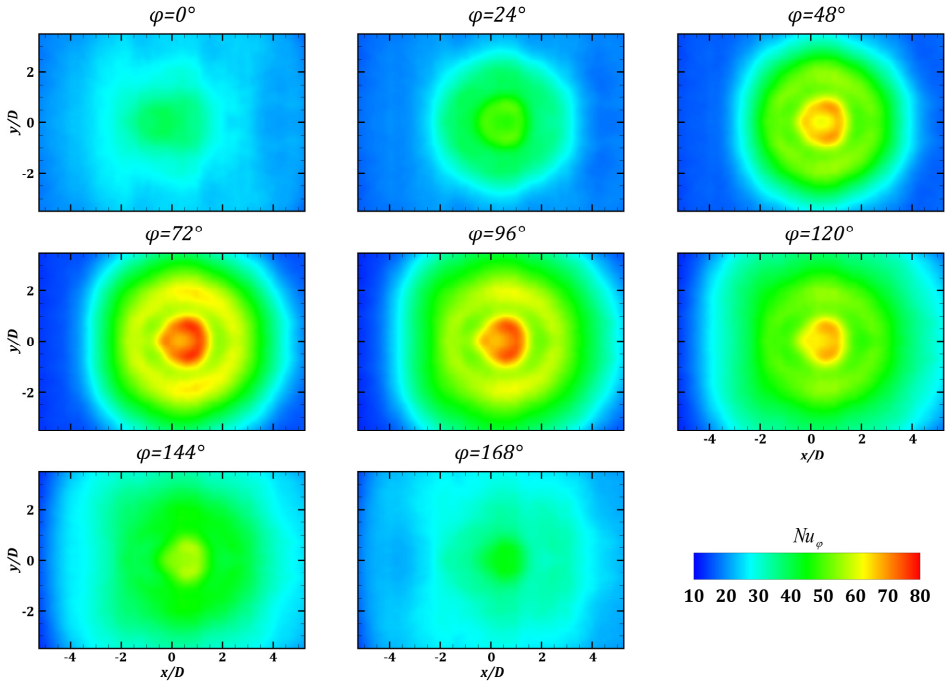

Fig. 5.57 Phase-average Nusselt number maps TSJ ($\sum$ = 1.1) at H/D = 2

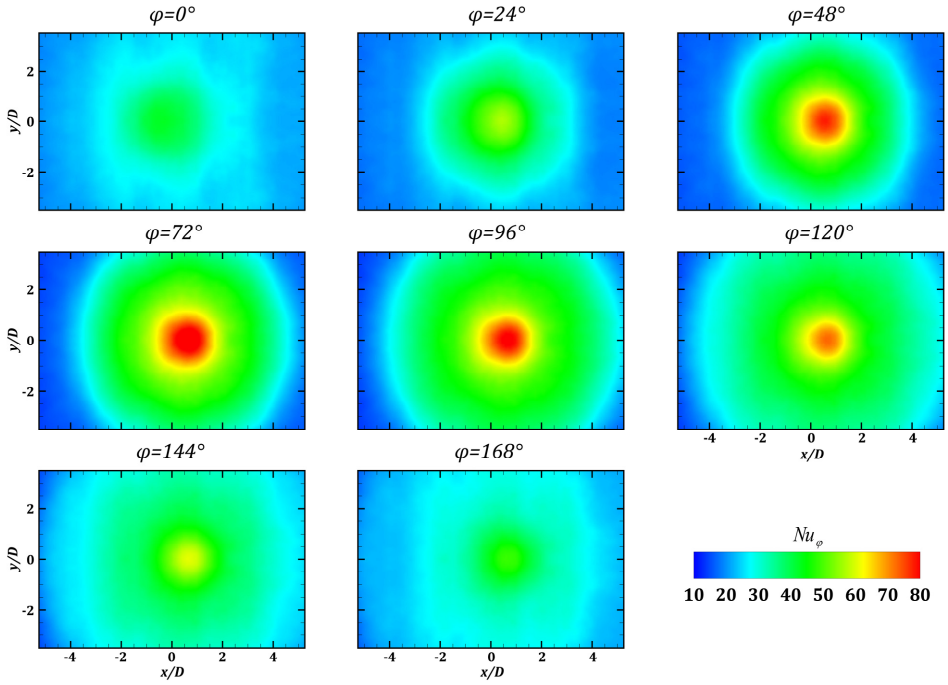

Fig. 5.58 Phase-average Nusselt number maps TSJ ($\sum$ = 1.1) at H/D = 6

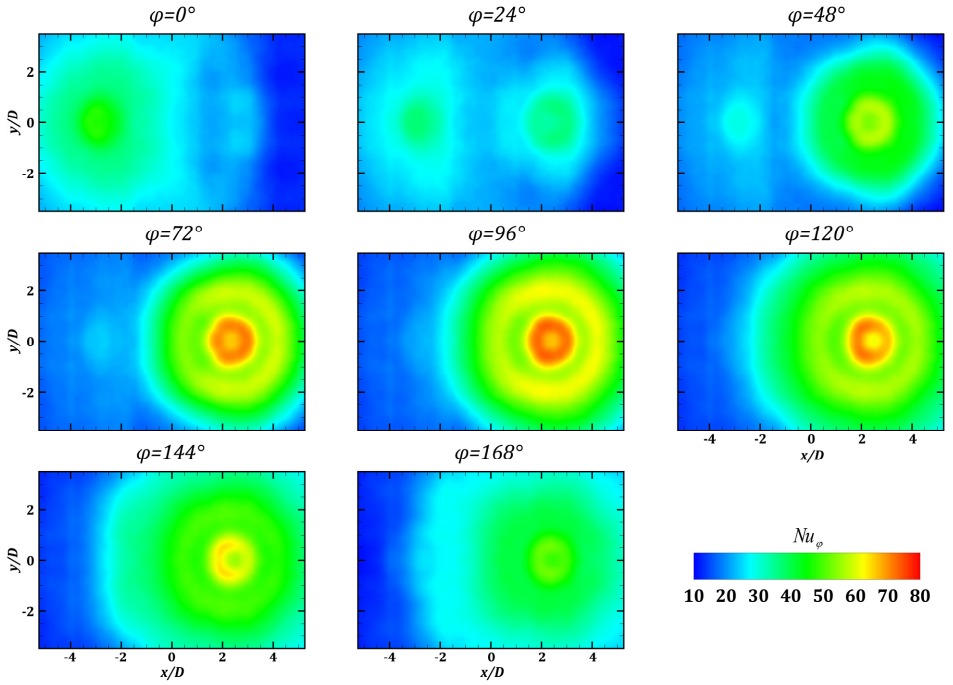

Fig. 5.59 Phase-average Nusselt number maps TSJ (∑ = 5) at H/D = 2

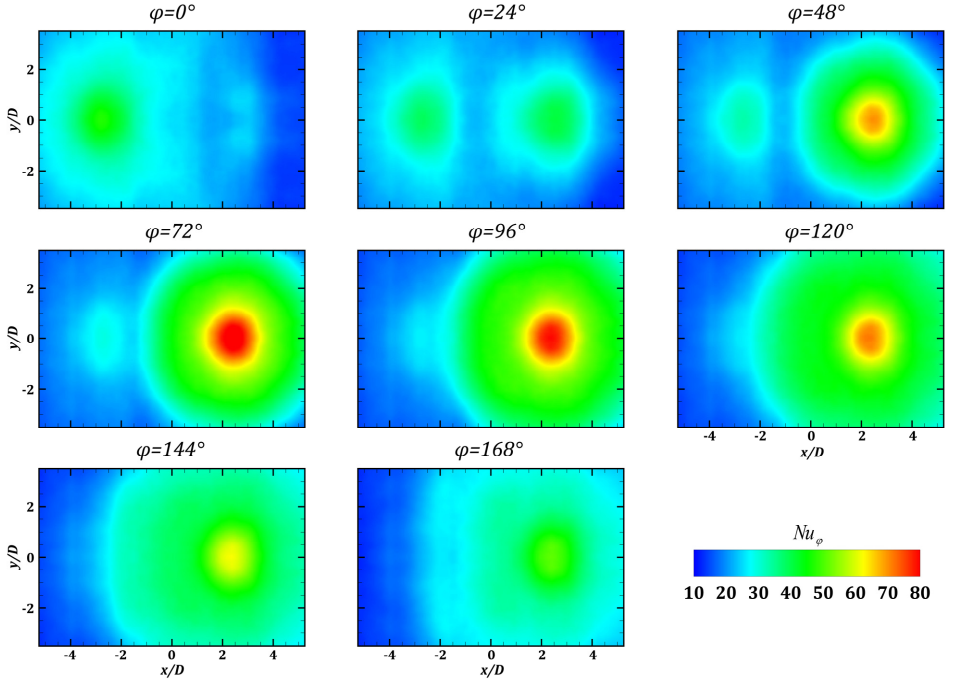

Fig. 5.60 Phase-average Nusselt number maps TSJ (∑ = 5) at H/D = 6

5.2 High Reynolds number Synthetic Jets

In this chapter the investigation of an high Reynolds number (16000) impinging synthetic jet is undertaken. Three different values of Strouhal number (0.025, 0.05 and 0.1) and of orifice-to-plate distance (2, 4 and 6) are employed. As stated in Chapter 3.2 the results are shown following the triple decomposition. In subchapter 5.2.1 the time-average flow fields and their turbulent statistics are shown as maps. Only the maps for H/D equal to 2 and 6 are shown while the behaviour over the plate of all the quantities, at all the orifice-to-plate distances, is plotted. Then in subchapter 5.2.2 the phase-average measurements for the lowest and highest Strouhal number configurations at orifice-to-plate distance equal to 2 and 6 are analysed.

5.2.1 Time-average measurements

In Fig. 5.61 the time-average axial velocity maps are shown. As it is possible to see the region of high velocity is more extended (in the axial direction) as Strouhal number decreases. As matter of fact, according to McGuinn et al. (2013), the Strouhal number affects the synthetic jet flow field. For high Strouhal number the synthetic jet flow field is more similar to a simply vortex ring which convects downstream while, for low Strouhal number, it starts acting more like a continuous jet. For this reason, when the Strouhal number increases, the column of fluid which follows the starting vortex ring (formed during the beginning of the ejection phase) decreases. This can also explain the time-average centreline axial velocity (Fig. 5.62) and the jet width (Fig. 5.63) behaviour. Indeed the time-average centreline axial velocity values increase as the Strouhal number decreases. On the contrary, the jet width has higher values for lower Strouhal number.

It is worth noting that the value of the time-average centreline axial velocity is higher than the low Reynolds case while the jet width near the orifice exit is 0.8 differently from the low Reynolds number configuration. This can be ascribed to the recirculation flow and the vena contracta phenomena which develops along the orifice edge when the ratio between the plate thickness and the orifice diameter is lower than 0.75 (Gomes et al., 2006). In our experiments, this ratio is 0.2.

In Fig. 5.64 the time-average radial velocity component maps are shown. Focusing on near the impinging plate, it is possible to point out that, starting from the stagnation point (x/D equal to 0), a different behaviour is visible.

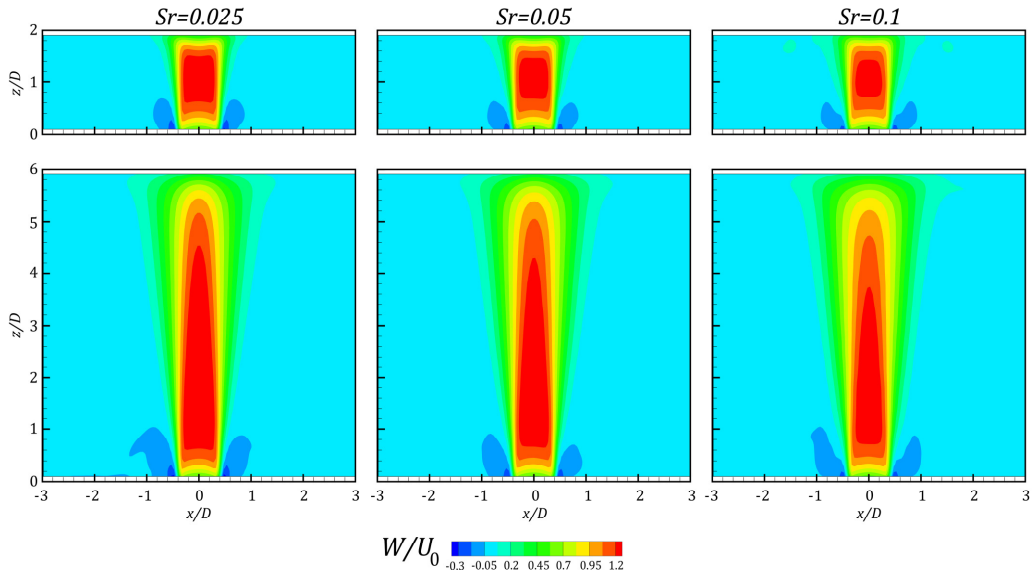

Fig. 5.61 Time-average axial velocity maps for H/D equal to 2 (top) and 6 (bottom)

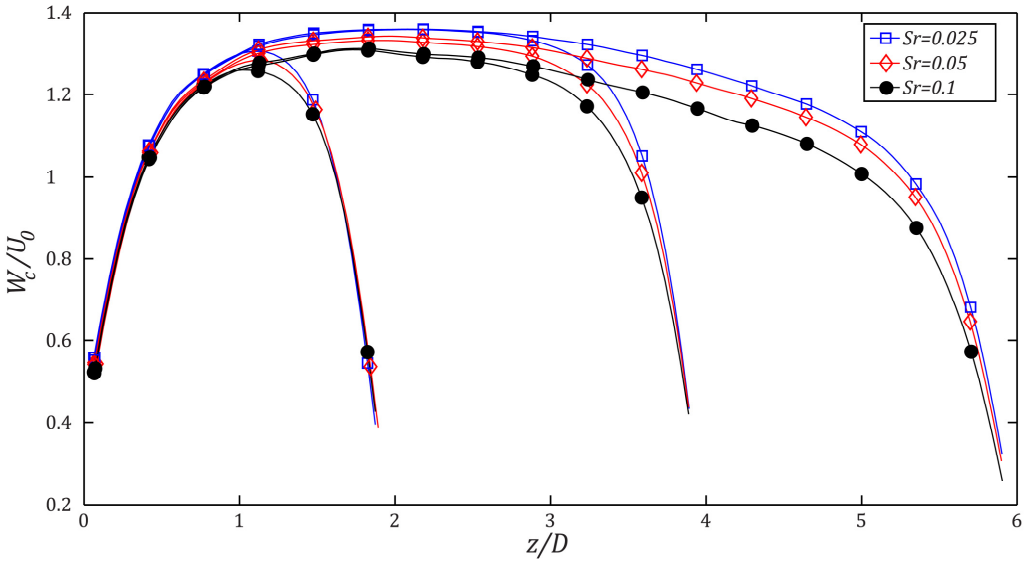

Fig. 5.62 Time-average centreline axial velocity for all Strouhal number and H/D's configurations

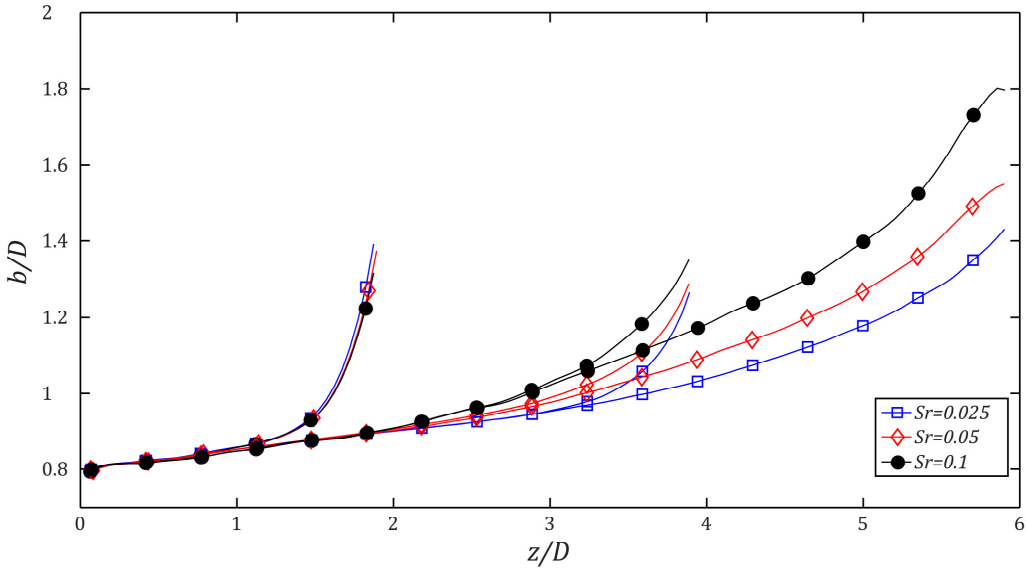

Fig. 5.63 Jet width for all Strouhal number and H/D's configurations

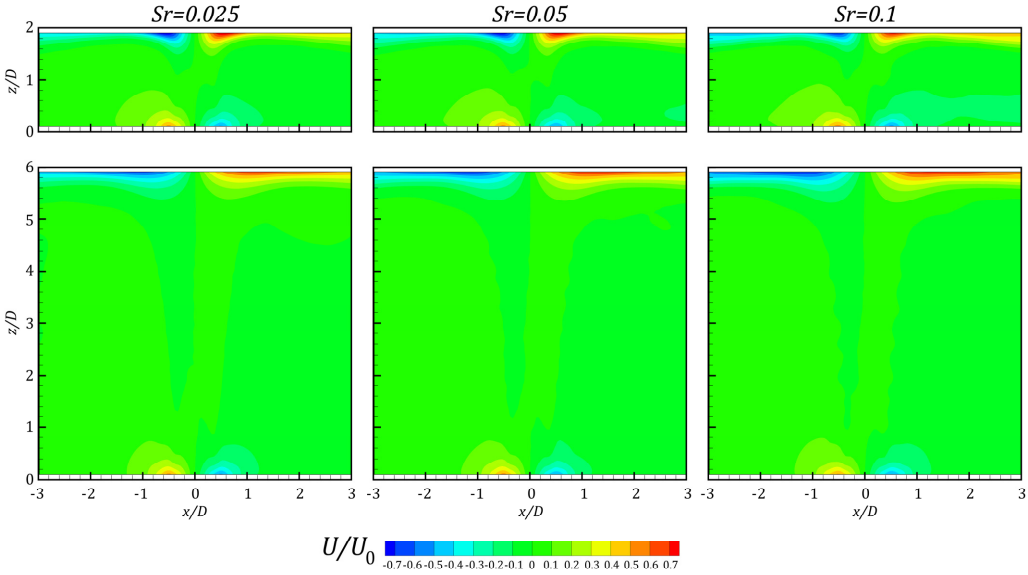

Fig. 5.64 Time-average radial velocity maps for H/D equal to 2 (top) and 6 (bottom)

For a lower Strouhal number, a zone ($0.2 < x/D < 0.8$ at H/D equal to 2) of high radial velocity is more extended in the axial direction. This could be ascribed to two main reasons: the vortex ring trajectory (in such a region, is closer to the impinging plate lower is the Strouhal number, as shown in subchapter 5.2.2) and the synthetic jet behaviour resembling more a continuous one at lower Strouhal number. Furthermore when the orifice-to-plate distance increases such a region decreases. This can be related to jet width (Fig. 5.63) and to the vortex ring trajectory. As matter of fact the jet width increases, as H/D increases, so the radial component grows more (differently from the axial component, as visible in the following profile on the impinging wall).

The mean-squared axial phase-correlated organised contribution to the velocity maps are depicted in Fig. 5.65. It is possible to highlight that the maximum value, attained on the orifice exit, increases as the Strouhal number decreases and is not influenced by the orifice-to-plate distance. Furthermore at high orifice-to-plate distance (i.e. H/D equal to 6) one can notice that the region influenced by high values of such a parameter decreases its extension as Strouhal number increases. The explanation is related to the half piston stroke l_p. As matter of fact this value influences the amplitude of the oscillating external force which perturbs the flow field. Higher is the half stroke piston length (lower is the Strouhal number), greater is the perturbation. Such a behaviour can be detected also near the impinging wall for the mean-squared radial phase-correlated organised contribution to the velocity (Fig. 5.66). Indeed the maximum value is attained near the plate from the configuration characterized by the lowest Strouhal number. Furthermore this maximum value decreases as the orifice-to-plate distance increases.

Time-average phase-organized contribution to the velocity Reynolds stress shows (in Fig. 5.67) its maximum value, near the orifice and the impinging plate, at a radial position equal to about 0.5 D, corresponding to the orifice edge. As the Strouhal number increases the value near the impinging plate decreases. Also the orifice-to-plate distance has the same effect: as H/D increases, the values, near the impinging plate, decrease and also shift towards higher radial position.

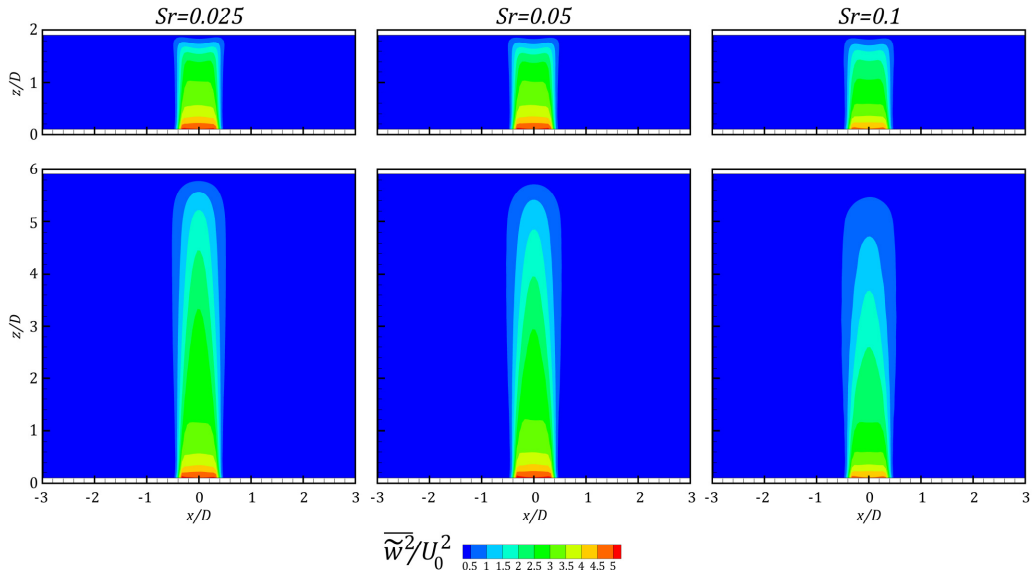

Fig. 5.65 Mean-squared axial phase-correlated organised contribution to the velocity maps for H/D equal to 2 (top) and 6 (bottom)

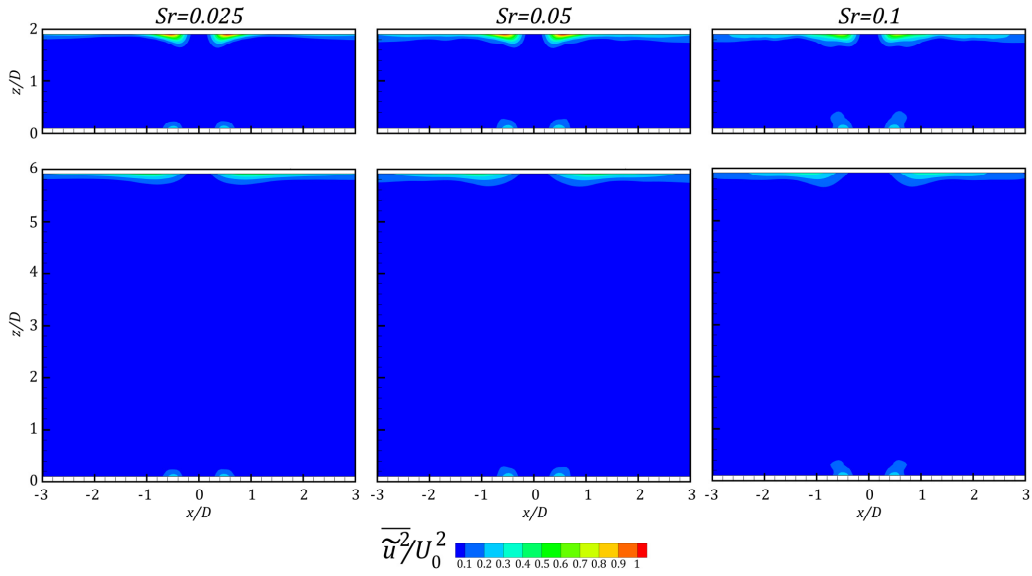

Fig. 5.66 Mean-squared radial phase-correlated organised contribution to the velocity maps for H/D equal to 2 (top) and 6 (bottom)

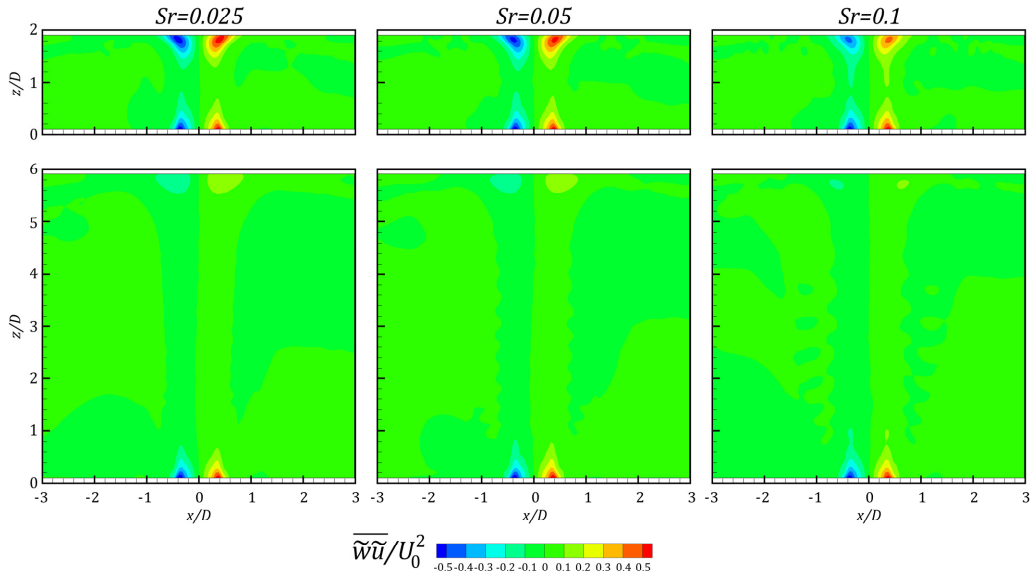

Fig. 5.67 Time-average phase-organized contribution to the velocity Reynolds stress maps for H/D equal to 2 (top) and 6 (bottom)

In Fig. 5.68 the mean-squared axial turbulent velocity maps are reported. For each configuration the maximum values are attained along the shear layer emanated by the orifice edge. At *H/*D equal to 2, the unique difference between these maps can be detected only near the impinging plate far from the stagnation point (*x/D* greater than about 1). The value, in this region, is higher for lower Strouhal number. This is ascribed to the vortex ring dynamics. As matter of fact, higher is the Strouhal number slower is the vortex ring convection velocity (Shuster and Smith, 2007), so the vortex ring stays more time near the impinging plate (for one actuation cycle) considering our field of view. Seen that the maximum of the mean-squared axial turbulent velocity component is in the vortex ring centre (as shown in subchapter 5.2.2) this leads to higher value near the plate for higher Strouhal number configurations. At *H/D* equal to 6 the same consideration can be drawn near the impinging plate but other differences can be highlighted. Indeed, the region interested by high value (along the shear layer), decreases its extension as the Strouhal number increases. As matter of fact the synthetic jet starts impinging on the plate while the actuator is still in its ejection phase (i.e. the first part of the ejection phase, as visible in subchapter 5.2.2) for lower Strouhal number (*Sr* equal to 0.025). Differently, in the highest Strouhal number configuration the synthetic jet starts approaching the plate when the actuator is decelerating (i.e. the last part of the ejection phase, as visible in

subchapter 5.2.2). For these reasons the shear layer (featured by high mean-squared axial turbulent velocity value, as visible in subchapter 5.2.2) reaches and stay more time near the plate for the lower Strouhal number case as visible in subchapter 5.2.2). Furthermore it is possible to point out that the extension of the region interested by a low axial turbulence level increases as the Strouhal number decreases. This is ascribed to a main presence, during the ejection phase, of the fluid column with respect to the vortex ring (which convects quicker for lower Strouhal number).

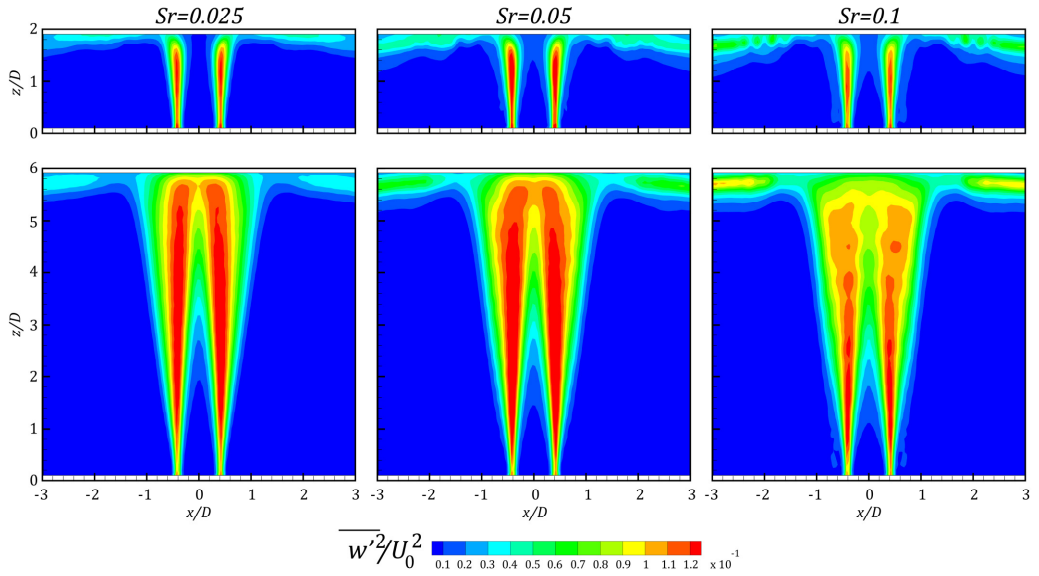

Fig. 5.68 Mean-squared axial turbulent velocity maps for H/D equal to 2 (top) and 6 (bottom)

In Fig. 5.69 the mean-squared radial turbulent velocity maps are depicted. This parameter shows its maximum value near the plate but, far from it, the local maximum is attained along the shear layer. This value, in the field far from the impinging plate, is about 40% of the corresponding axial component. Moreover also an axial peak, issued from the orifice plate, with higher extension, for greater value of the Strouhal number, is detectable for both orifice-to-plate configurations. As H/D increases the values near the wall decreases. Furthermore it is possible to see some waves along the shear layer boundary as Strouhal number increases. Such waves are related to the presence of the vortex ring in the field of view, during the ejection phase, that is greater as the Strouhal number increases.

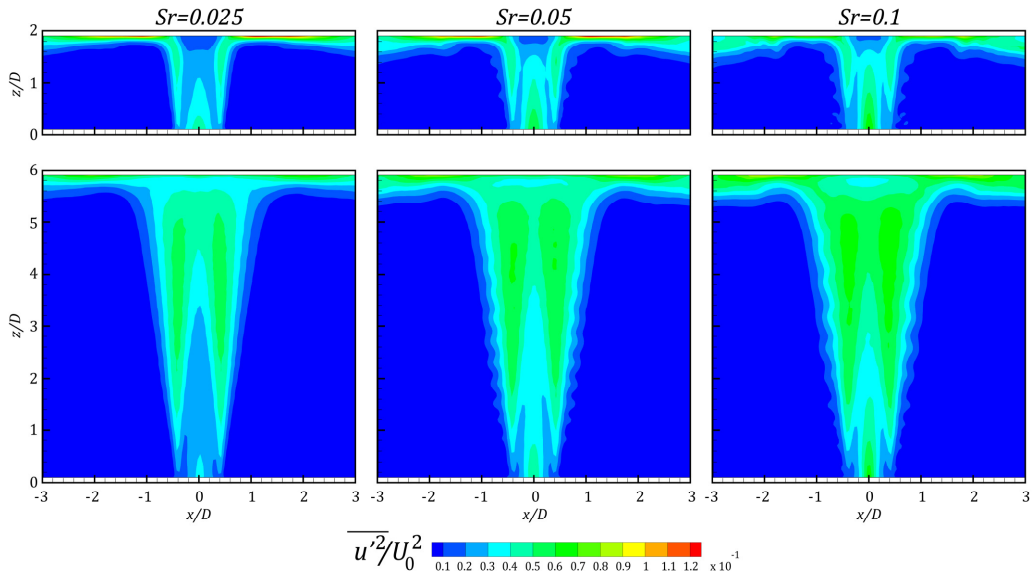

Fig. 5.69 Mean-squared radial turbulent velocity maps for *H/D* equal to 2 (top) and 6 (bottom)

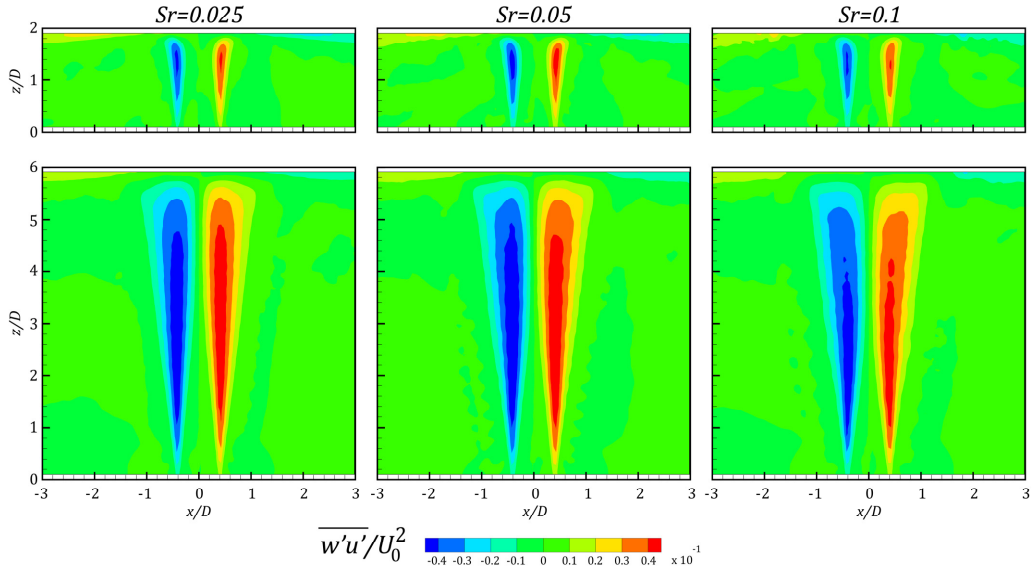

Fig. 5.70 Time-average turbulent Reynolds stress maps for H/D equal to 2 (top) and 6 (bottom)

Hence, the vortex ring influences on the mean-squared radial turbulent velocity is greater for higher Strouhal number. Moreover, it has to be taken into account that the number of samples in the case with the lowest Strouhal number is double of the second configuration (*Sr* equal to 0.05) and four times the third configuration samples number (*Sr* equal to 0.1), as reported in subchapter 3.2. This difference in the samples number contributes to promote this effect without corrupting the values.

The time-average turbulent Reynolds stress maps are shown in Fig. 5.70. They show the same general behaviour, far from the impinging plate, previously described for the mean-square turbulent axial velocity. Indeed no substantial difference are observable for *H/D* equal to 2 while in the highest configuration some differences between the extension of the high value region along the shear layer can be noticed (as for the mean-square axial turbulent velocity).

In Figs. 5.71-5.74 all the variables profile near the impinging plate (0.1 *D* from the impinging plate) for the three Strouhal numbers and orifice-to-plate distances are depicted.

The time-average axial velocity component (Fig 5.71) at *H/D* equal to 2 shows a profile with a local minimum on the jet axis. Such minimum attains its maximum value for the highest Strouhal number configuration. Then, at *x/D* equal to 0.35, a local maximum is detected. After that, the value starts decreasing. At *x/D* equal to about 1.75 a very small oscillation can be observed. The amplitude of this oscillation is damped as the Strouhal number decreases because such an oscillation is caused by the vortex ring sweeping on the plate which is more influencing for higher Strouhal number. As *H/D* increases the profile becomes bell-shaped and near the jet axis a switch in the maximum is observable. Indeed in the highest orifice-to-plate distance the maximum value is attained by the lowest Strouhal number configuration. This agrees with the centreline velocity and jet width behaviour, as shown in Figs. 5.62 and 5.63 respectively. As matter of fact, as *H/D* increases, a substantial difference is detected related to the Strouhal number. In the highest Strouhal number configuration the jet width becomes higher and the centreline decreases, as occurs on the jet axis in Fig. 5.71.

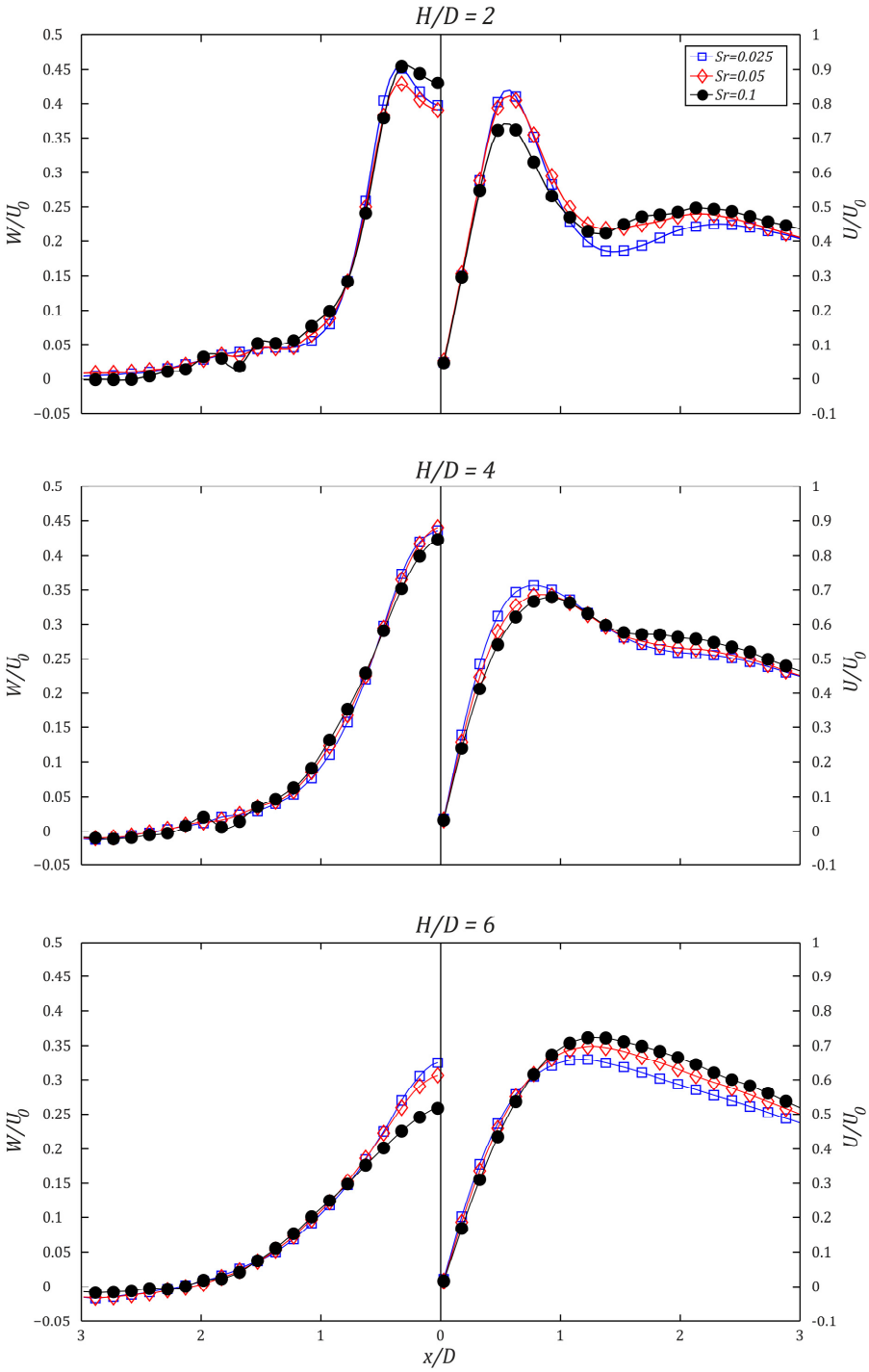

Fig. 5.71 Time-average axial (left) and radial (right) velocity components over the impinging plate for all Strouhal number and *H/D*'s configurations

Regarding to the radial velocity, a peak is located at *x/D* equal to 0.55 at *H/D* equal to 2. The highest Strouhal number configuration shows the minimum value at this radial position but, after *x/D* equal to about 1.5, it attains the highest value. This behaviour is completely opposite to the lowest Strouhal number case. This could be ascribed to two main reasons: the vortex ring (which influences more the flow field, higher is the Strouhal number) causes a radial velocity which is higher than the wall jet velocity and the vortex ring trajectory (shown in subchapter 5.2.2) is closer to the wall higher is the Strouhal number for a radial position higher than about 1.5 diameters.

Moreover all the curves show another local maximum at approximately 2.2 diameters from the jet axis. At *H/D* equal to 4 the first peak decreases and shifts towards a higher radial position, according to the jet width behaviour, while the second one is barely visible. The highest Strouhal number case still presents the highest value for a radial position higher than about 1.5 diameters according to the vortex ring trajectory. For *H/D* equal to 6 the highest Strouhal number case shows the maximum time-average radial velocity with a peak located at about 1.3. Furthermore the peak is closer to the jet axis and decreases as the Strouhal number decreases.

In Fig. 5.72 the mean-squared axial and radial phase-correlated organized contribution to the velocity components are depicted. The axial component shows a shape similar to the time-average axial velocity component. As previously said, these parameters are related to the external force, so, higher is the Strouhal number lower are the attained values. These axial values decrease as *H/D* increases. At *x/D* equal to -1.4 and -1.7 two peaks are detected. These peaks decrease as the Strouhal number reduces and the orifice-to-plate distance increases. The axial values are 30% of the radial one. Even the radial component shape is similar to the time-average radial velocity component. At *H/D* equal to 2 the switch between the curves, present at *x/D* equal to 1.5 for the time-average radial velocity component, is only present for the radial position included between 1.5 and 2 diameters. As *H/D* increases this switch is not present and higher is the Strouhal number, lower are the attained values. Moreover as *H/D* increases the first peak shifts towards higher radial position. Such a shifting is higher for greater Strouhal number.

The mean-squared turbulent velocity components are shown in Fig. 5.73. The axial component is not influenced by the Strouhal number at the shortest orifice-to-plate distance. The curves are characterized by local minimum on the jet axis and by two peaks located at *x/D* equal to -0.5 and -1.8.

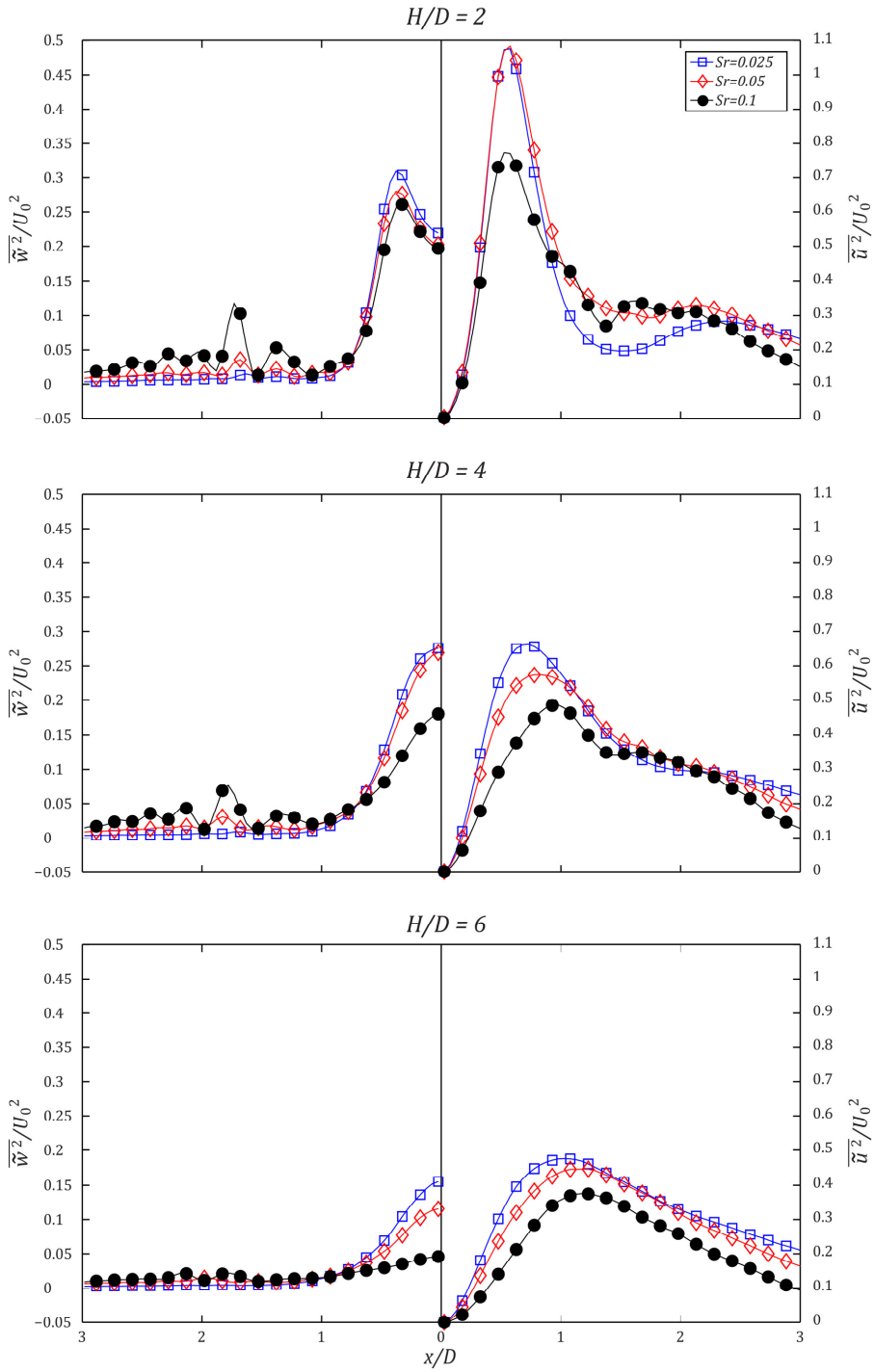

Fig. 5.72 Mean-squared axial (left) and radial (right) phase-correlated organised contribution to the velocity components over the impinging plate for all Strouhal number and H/D's configurations

The first peak is related to the shear layer which impinges on the plate. Indeed this peak shifts towards the jet axis as *H/D* increases. At *H/D* equal to 4 higher is the Strouhal number, greater is the value on the jet axis. This is related to the extension region seen in Fig. 5.68 which is influenced by the Strouhal number. For this orifice-to-plate distance higher is the Strouhal number higher is the value of the second peak. Such a condition is the same also for *H/*D equal to 6, where the values are also damped. For this value of the orifice-to-plate distance the value attained on the jet axis is decreased for *Sr* equal to 0.1 while is increased for the other two Strouhal numbers, accordingly with the extension region shown in Fig. 5.68.

The mean-squared radial velocity component shows, for the shortest orifice-to-plate configuration, two peaks located at *x/D* equal to 1.1 and 1.7 for *Sr* equal to 0.025 and 0.05 while at *x/*D equal to 1.25 and 1.8 for *Sr* equal to 0.1. Moreover the first two curves collapse and shows higher values. As *H/D* increases this difference decreases and for *H/D* equal to 6 the maximum value is attained by the highest Strouhal number. Regarding to the double peak it is still present for the highest Strouhal number configurations (barely visible at *H/D* equal to 6) while only one peak is detectable for *Sr* equal to 0.025 and 0.05.

In Fig. 5.74 the phase-correlated organized contribution to the velocity and turbulent Reynolds stress are shown. The turbulent Reynolds stress at *H/D* equal to 2 shows a first peak at around *x/D* equal to -0.7 and then a second one located at approximately at 2 diameters from the jet axis for the *Sr* equal to 0.025 configuration. For the highest Strouhal number case, the first peak is in the same position (barely visible for the highest Strouhal number case) but the second one is detected at position closer to the jet axis (*x/D* equal to about -1.8). The highest Strouhal number case shows the lowest values. As *H/D* increases, the first peak decreases and shifts towards the jet axis while the second one slightly (the lowest Strouhal number cases) or not (the highest Strouhal number case) decreases maintaining its position.

The phase-correlated organized contribution to the velocity Reynolds stress shows a peak at about 0.5 diameters from the jet axis. This peak has lower value as the Strouhal number increases. Such a peak decreases as the orifice-to-plate distance increases and only for the highest Strouhal number configuration a shift towards higher radial position is observable.

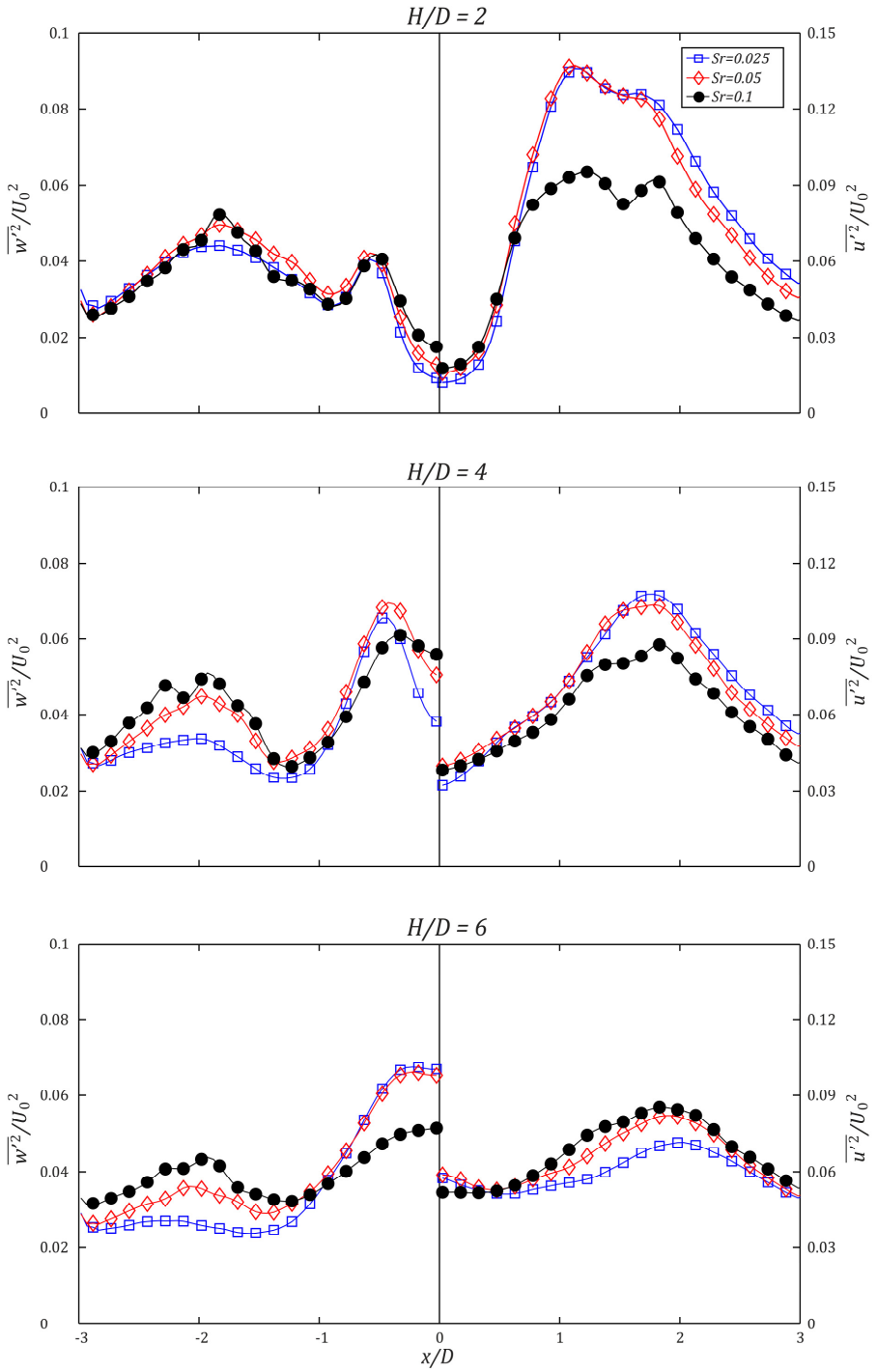

Fig. 5.73 Mean-squared axial (left) and radial (right) turbulent velocity components over the impinging plate for all Strouhal number and H/D's configurations

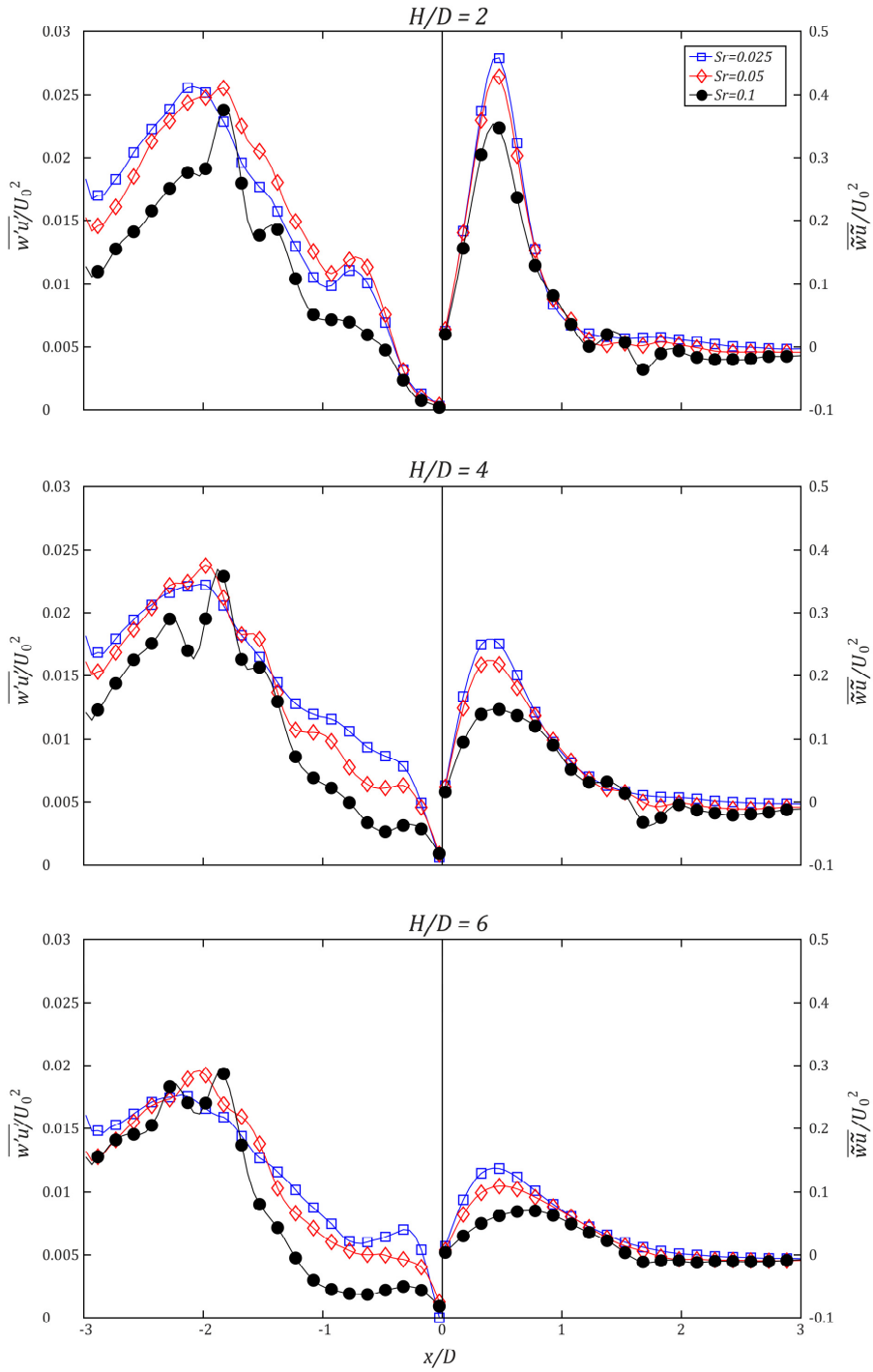

Fig. 5.74 Time-average phase-correlated organized contribution to the velocity (left) and turbulent (right) Reynolds stress over the impinging plate for all Strouhal number and *H/D*'s configurations

5.2.2 Phase-average measurements

In Figs. 5.75 - 5.86 the phase-average velocity components maps at *H/D* equal to 2 and 6 for *Sr* equal to 0.025 and 0.1 are shown. The same phases are reported for the two Strouhal number cases. Only 10 phases (for the *H/D* equal to 2) and 9 phases (for the *H/D* equal to 6), with a step of 18.46°,are chosen in order to represent the ejection cycle.

In Fig. 5.75 the phase-average axial and radial velocity maps at *H/D* equal to 2, for *Sr* equal to 0.025, are depicted. At φ = 0° the ejection phase starts while at φ = 18.46° the vortex ring is completely formed and the following column of fluid is easily detectable on its behind. Then the synthetic jet impinges and at φ = 36.92° it is sweeping the impinging plate. At this phase, it is possible to see that the axial velocity profile is not bell-shaped near the impinging plate because of the presence of the plate itself. Indeed a minimum of the local axial velocity is observable on the jet axis (*x/D* equal to 0) near the stagnation zone. The radial velocity component shows two maxima: the first one where the complete jet rotation is detectable (near the impinging plate at *x/D* equal to about 0.5) and the second one that is placed between the sweeping vortex ring and the plate. At φ = 55.38° the region of high axial velocity is more extended (in the axial direction) and the vortex ring is moved out of the measurement zone. For 55.38° < φ < 92.30° the behaviour of the synthetic jet does not shown any substantial differences and resembles the continuous one. For $\varphi \geq$ 92.30° the axial and radial velocity starts decreasing.

In Fig. 5.76 the phase-average mean-squared axial and radial turbulent velocity maps at *H/D* equal to 2, for *Sr* equal to 0.025, are shown. The synthetic jet starts being issued at φ = 0° and at φ = 18.46° is featured by a peak of axial turbulent near the vortex core. Also a value different from zero is observable along the shear layer. The radial component attains its maximum in the vortex ring core as well. Also a value different from zero is present on the nozzle exit centre. At φ = 36.92° high values of radial and axial turbulence are present along the shear layer but their maxima are still located in the vortex ring core. Furthermore, regarding to the radial component, another two maxima are barely visible: the first one is located where the complete rotation of the jet occurs and the second one is between the vortex ring and the impinging plate (where the counter rotating vortex should be). At φ = 55.38° the axial turbulent velocity component still shows its maximum along the shear layer while the radial one has its maximum in the region near the plate which spans from the impinging shear layer to the vortex ring (*x/D* ranging between 0.6 and 2.2). Furthermore the radial component shows high values along the shear layer and

in a zone near the jet axis (which starts from the nozzle exit). Considering the phases ranging from 55.38° to 92.30° no sensitive differences are observable, while for $\varphi \geq 92.30°$ the turbulence starts decreasing. It is possible to point out that during this ejection phase no merging of the shear layer can be observable. This leads to have a zone, along the jet axis, featured by zero axial turbulence level and low radial one.

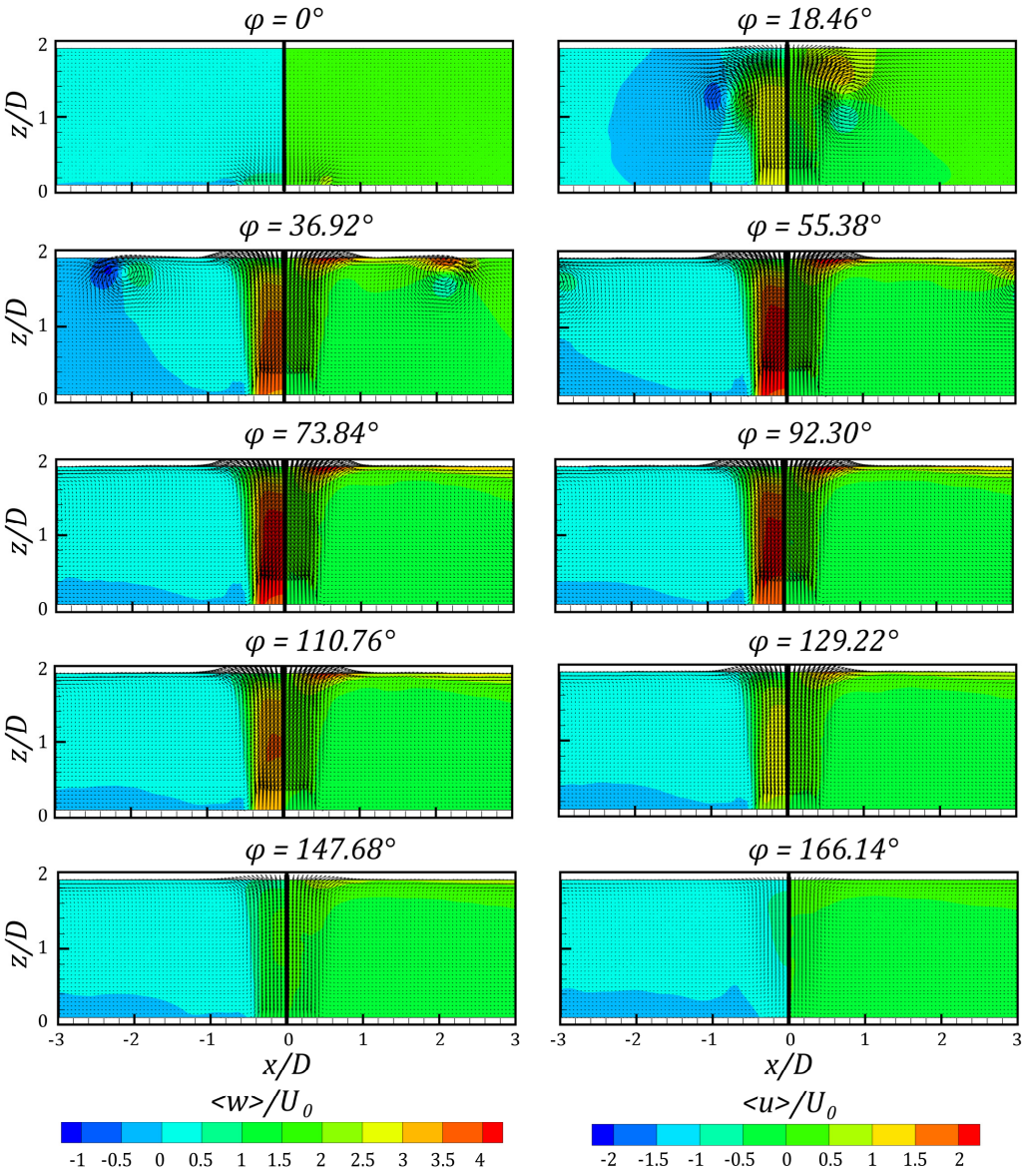

Fig. 5.75 Phase-average axial (left) and radial (right) velocity maps at H/D equal to 2 for Sr=0.025

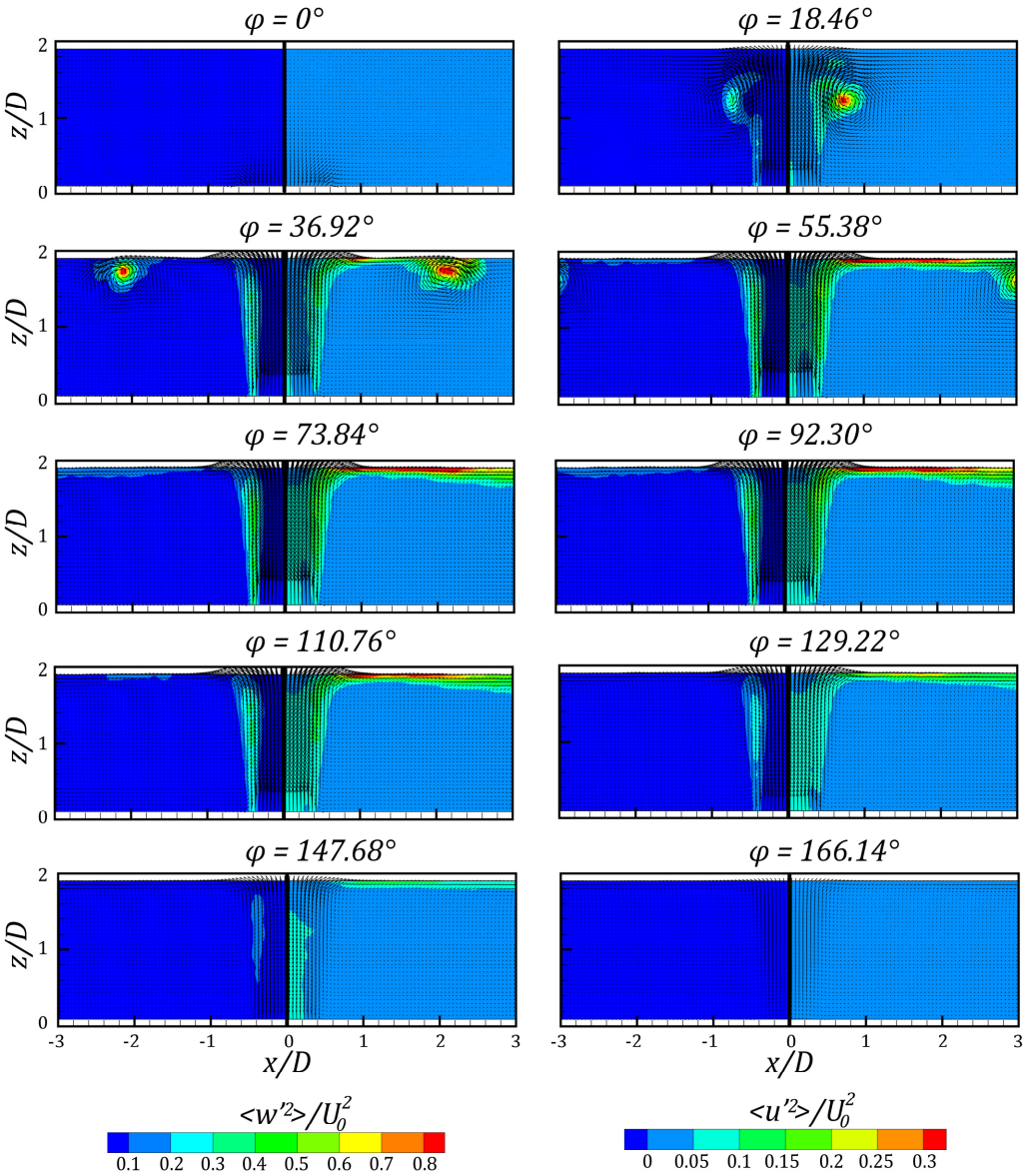

Fig. 5.76 Phase-average mean–squared axial (left) and radial (right) turbulent velocity maps at H/D equal to 2 for Sr=0.025

In Fig. 5.77 the phase-average turbulent Reynolds stress maps at H/D equal to 2, for Sr equal to 0.025, are depicted. The first no-zero values are detected at φ = 18.46° near the vortex ring core and in the last zone of the shear layer (which extends from the nozzle exit to the vortex ring position). At φ = 36.92° the Reynolds stress, different from zero, extends over the entire shear layer and is placed near the vortex ring core. Focusing on the distribution near the vortex ring core, four regions (in a cross distribution) characterized

by alternating value of the Reynolds stress region are observable. Furthermore an external peak located near the wall (ahead of the vortex ring itself), where the counter rotating vortex should be placed, is observable.

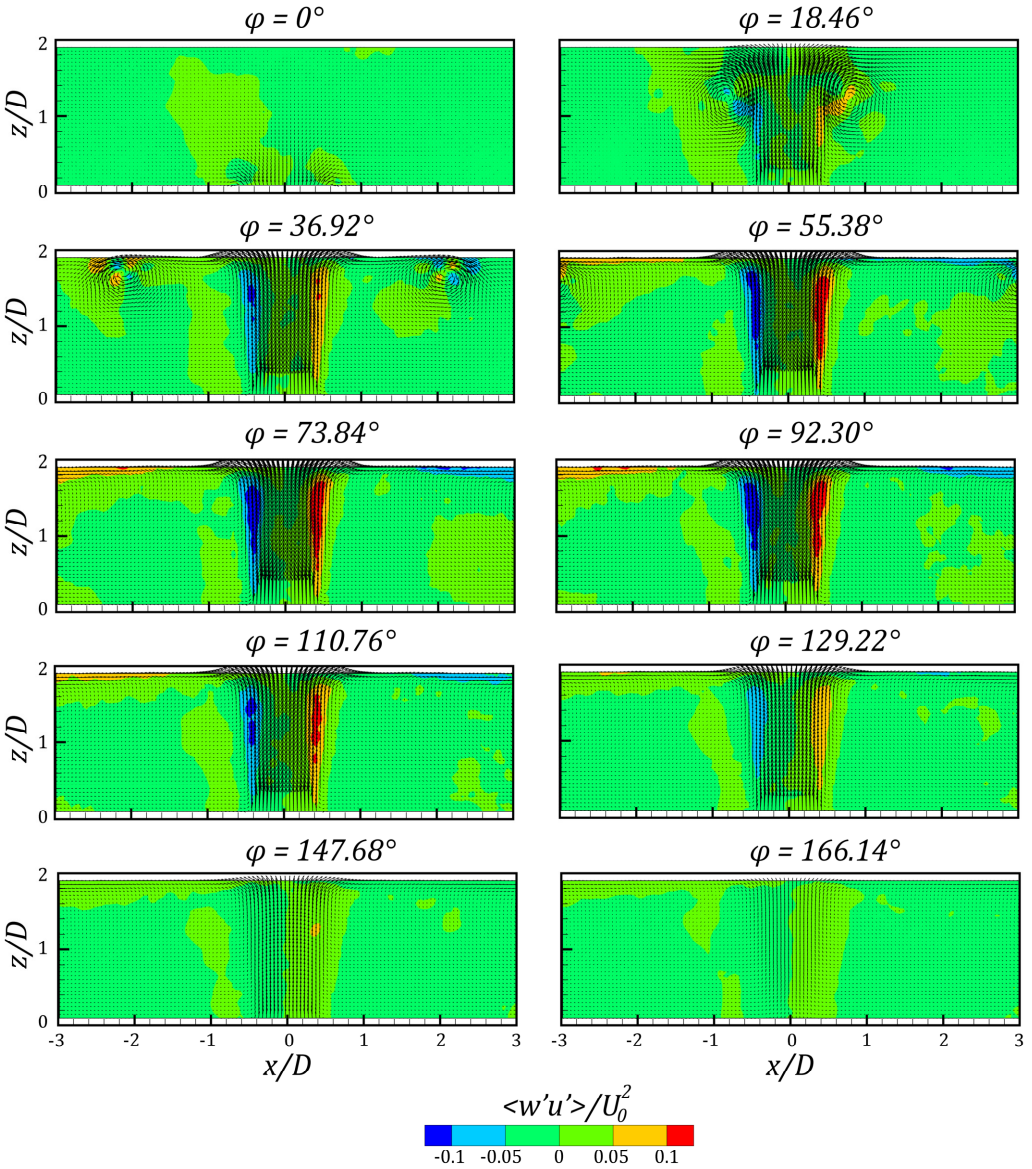

Fig. 5.77 Phase-average turbulent Reynolds stress maps at H/D equal to 2 for Sr=0.025

At φ = 55.38° the vortex ring is out of the field of measurement and the values along the shear layer increases. Moreover also high values are observable near the plate from $x/$D equal to approximately 1.5 to the end of the measurements region. At φ = 73.84° the

Reynolds stress distribution is similar to the impinging continuous jet one (Narayanan et al. 2004). For $\varphi \geq 92.30°$ the values start decreasing.

In Fig. 5.78 the phase-average axial and radial velocity components distributions are depicted for a *Sr* equal to 0.1 at *H/D* equal to 2. As for the previous case, at $\varphi = 0°$ the generation of the synthetic jet starts. At $\varphi = 18.46°$ the vortex ring is fully formed and starts its convection (see also $\varphi = 36.92°$) until it reaches the impinging plate ($\varphi = 55.38°$). Then ($\varphi = 73.84°$) the "sweeping phase" starts and two regions of high radial velocity can be detected. These two regions are, as usual, located near the maximum deflection zone of the impinging synthetic jet (at *x/D* equal to 0.5) and between the sweeping vortex ring and the impinging plate. The axial velocity component near the plate exhibits the usual profile with a local minimum on the jet axis (*x/D* equal to 0). At $\varphi \geq 92.30$ the axial velocity starts decreasing while the vortex ring is still in the measurement zone. At $\varphi = 110.76°$ the first peak of radial velocity at *x/D* equal to about 0.5 is decreasing because the jet axial velocity is reducing while the second peak is still clearly visible and high. As matter of fact at $\varphi = 129.22°$ the second radial peak is much higher than the first one which is almost disappeared. Only for $\varphi \geq 147.68°$ the vortex ring is moved completely out of the region of measurement. Such a behaviour is strictly related to the Strouhal number. As stated before, for high Strouhal number the column of fluid, following the vortex ring, decreases. Such a phenomenon leads to have a flow field much more influenced by the vortex ring presence.

In Fig. 5.79 the phase-average mean-squared axial and radial turbulent velocity maps at *H/D* equal to 2, for *Sr* equal to 0.1, are shown. From $\varphi = 0°$ to $\varphi = 55.38°$ the synthetic jet is formed and convects until the impinging plate. During these phases, the high radial and axial turbulent velocity values are mainly located in the vortex ring core and along the shear layer. Even for this Strouhal number case, it is possible to highlight that a no zero value of radial turbulence is observable on the nozzle exit and it extends until the impinging plate. At $\varphi = 73.84°$ the vortex ring starts sweeping the plate and the maxima, for the axial turbulent component, are detected in the vortex core and in the region near the plate (ahead of the vortex ring) where the counter rotating vortex should be arisen by the primary vortex ring passage. A similar behaviour characterizes also the radial turbulent component that also has another high value in the jet rotation zone (near the plate). For both components, high values are still observable along the shear layer. At $\varphi = 92.30°$ the maximum of the radial turbulent component, detected near the rotation jet

region, has moved near the plate in the region between 0.8 and 1.4 diameters from the jet axis. The axial turbulent component still shows the same maximum in the vortex ring core but the second one (near the plate) is decreased.

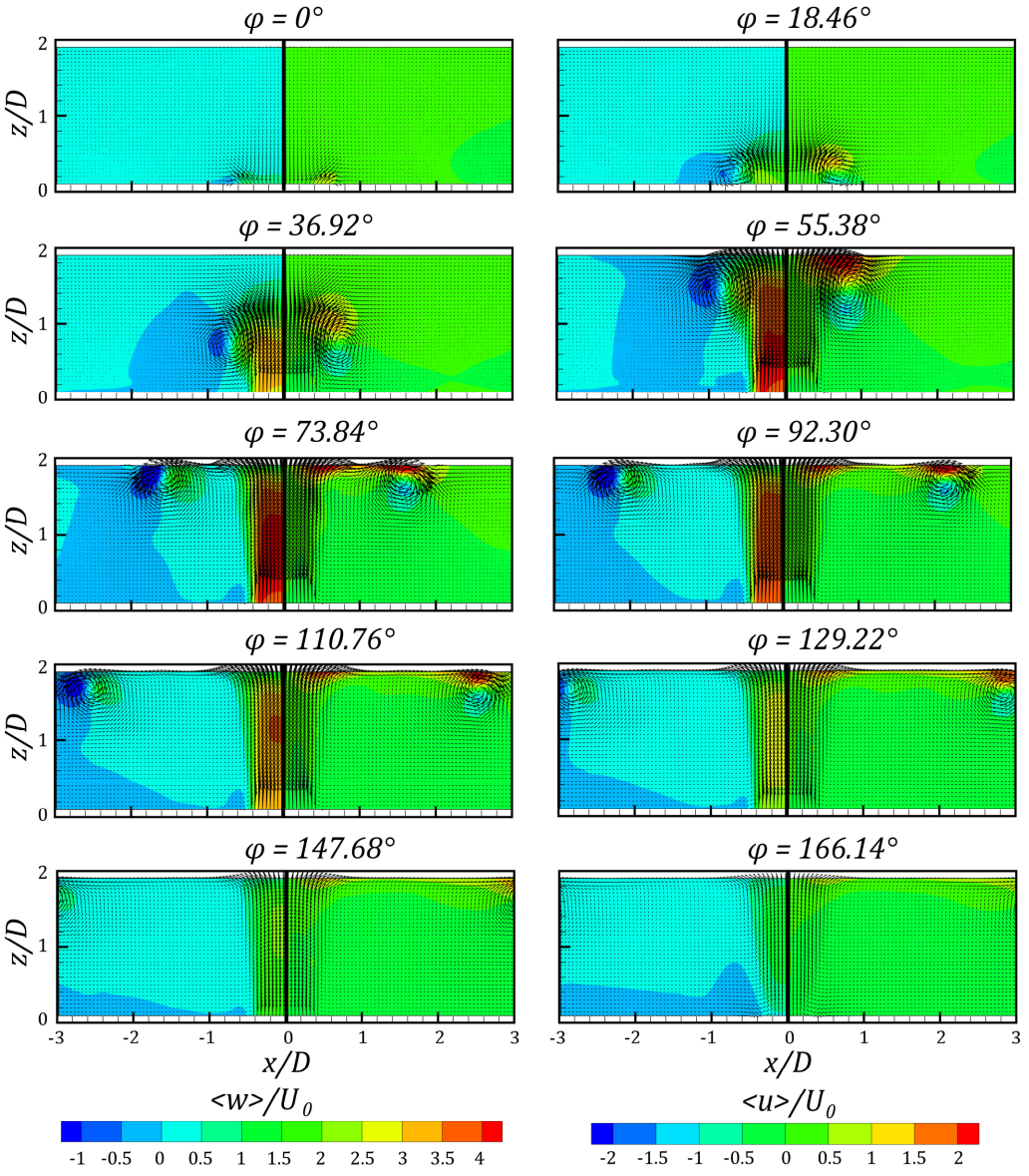

Fig. 5.78 Phase-average axial (left) and radial (right) velocity maps at H/D equal to 2 for Sr=0.1

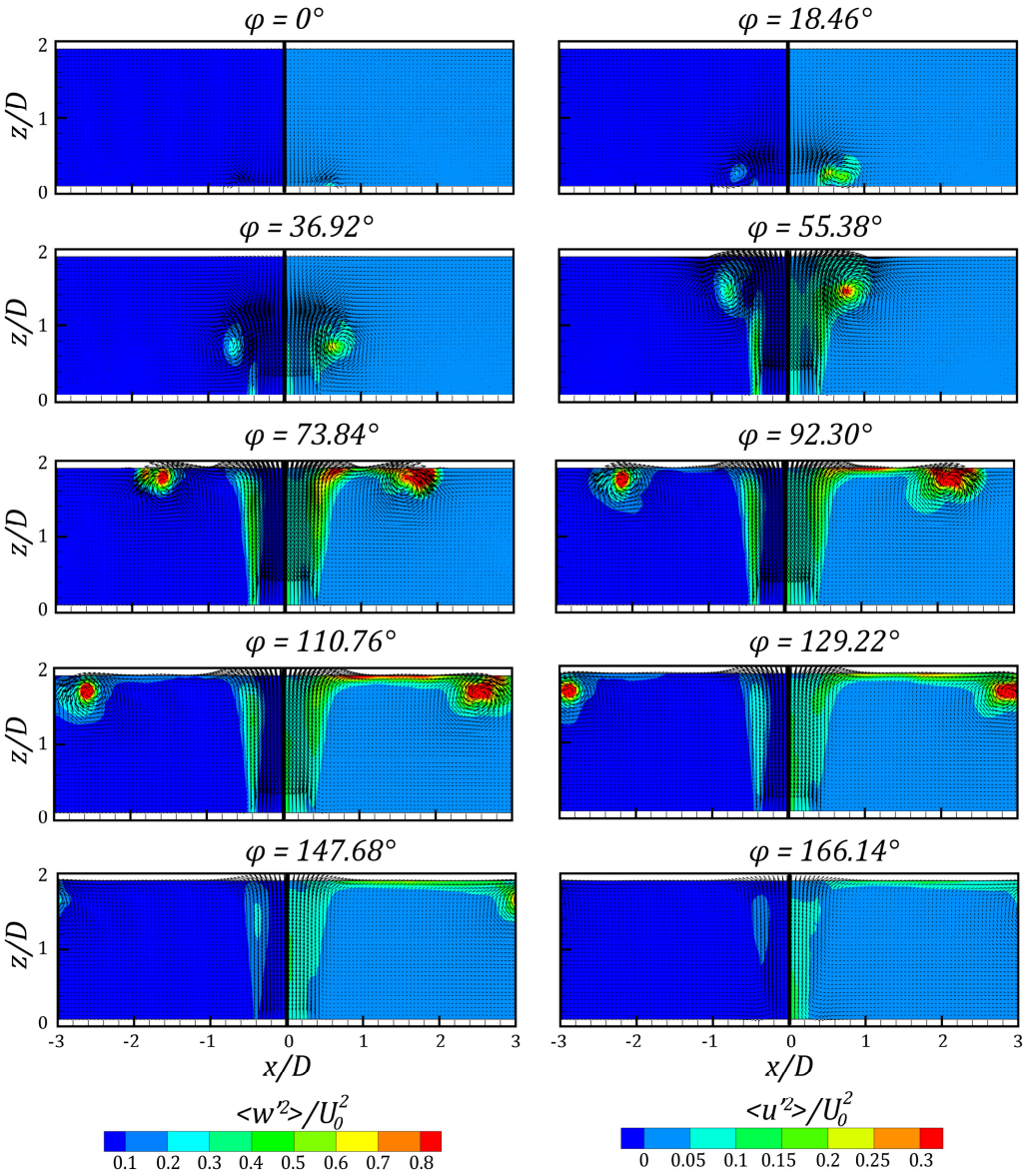

Fig. 5.79 Phase-average mean –squared axial (left) and radial (right) turbulent velocity maps at H/D equal to 2 for Sr=0.1

At φ = 110.76° the values along the shear layer are slightly decreased while the maxima near the vortex ring core are still visible. Furthermore the region near the impinging plate, featured by high radial turbulent value, extends more. For $\varphi \geq$ 129.22° the values near the plate and along the shear layer decreased while the values in the vortex ring core seems to be stable. Even for this configuration, as occurs for the shortest

orifice-to-plate case, no merging of the shear layer can be observed and a zone, featured by zero axial turbulence and low radial one, is observable near the jet axis.

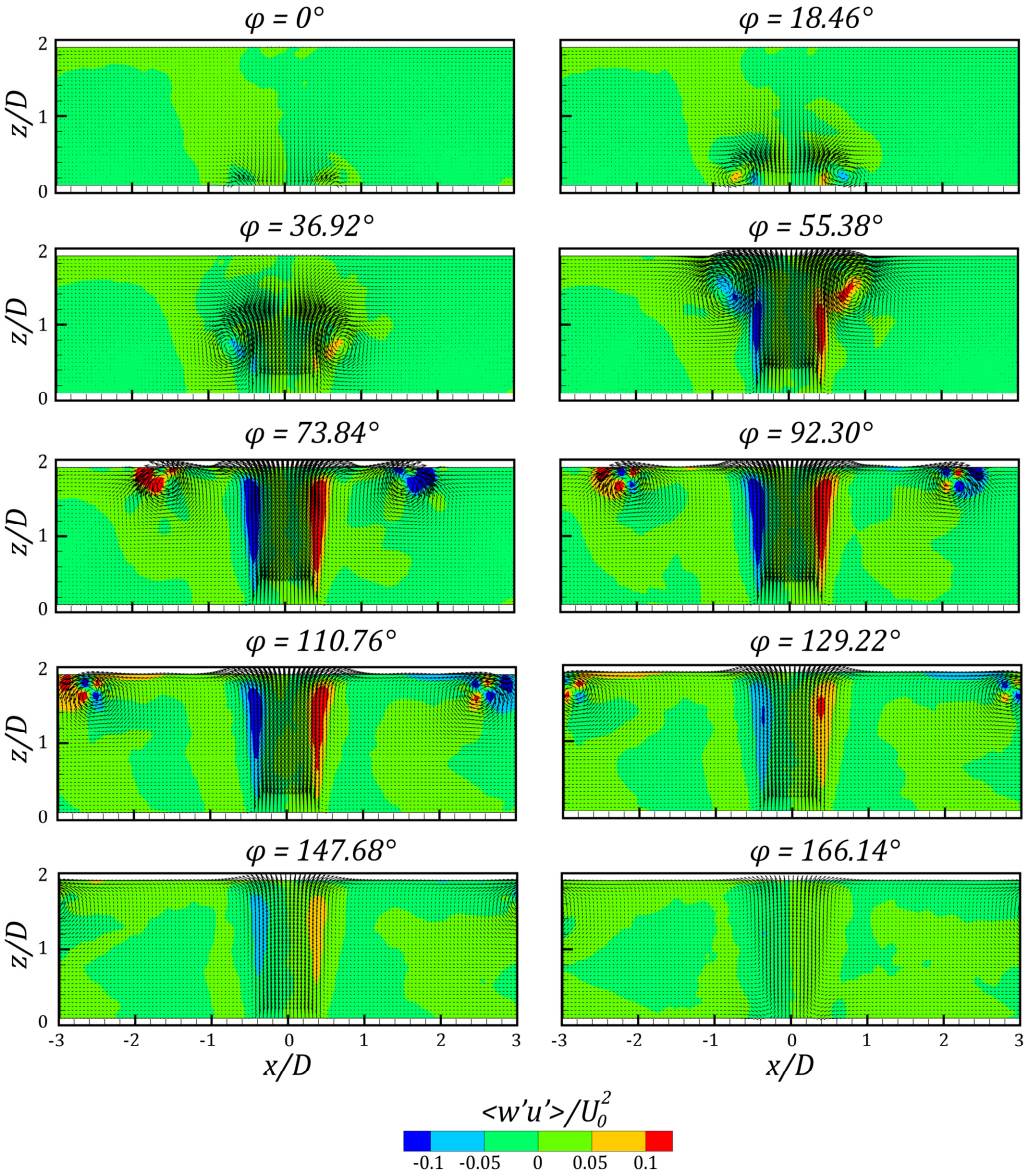

Fig. 5.80 Phase-average turbulent Reynolds stress maps at H/D equal to 2 for Sr=0.1

In Fig. 5.80 the phase-average Reynolds stress maps at H/D equal to 2, for Sr equal to 0.1, are reported. The high values are, as also seen before, located along the shear layer and in the vortex ring core ($0° \leq \varphi \leq 55.38°$). The turbulent Reynolds stress values

increase as φ growths (up to φ = 55.38°). Then high values of turbulent Reynolds stress are always observed along the shear layer (73.84° ≤ φ ≤ 92.30°) while they change their own distribution around the vortex ring. Indeed at φ = 73.84° a coherent value can be detected near the vortex ring (negative for x/D >0 and positive for x/D <0) while at φ = 92.30° an alternating distribution is observable with a presence of an external peak as also seen in Fig. 5.77. Such a distribution characterizes the zone near the vortex ring core until φ = 129.22° (last phase where the vortex is detectable). At φ = 110.76° the values near the vortex ring core and the ones along the shear layer start decreasing.

In Fig. 5.81 the phase-average axial and radial velocity distributions, for St equal to 0.025 at H/D equal to 6, are shown. The synthetic jet is issued (at φ = 0°) then convects (at φ equal to 18.46° and 36.92°) until it reaches the impinging plate. During these phases it is possible to see that the maximum of axial velocity is in the centre of the vortex ring (at φ = 18.46°) but at φ = 36.92° this maximum is located on the jet axis (in the following fluid column) but not in the vortex ring centre. This agrees with McGuinn et al. (2013) who found that the maximum velocity of a synthetic jet was not detected in the vortex ring centre but in the following trailing jet for high L_0/D values. At φ = 55.38° the synthetic jet has already spread over the plate. In this phase the radial velocity shows a maximum between the plate and the vortex ring which is higher than the one located in the maximum rotation of the impinging synthetic jet. This is also related to the axial velocity profile which approaches the impinging plate. Indeed in this case (H/D equal to 6) the profile is bell-shaped not causing a great peak of radial velocity as occurs for the shortest case (Fig. 5.71). At φ equal to 73.84° and 92.30° the vortex ring is out of the measurement zone and the flow field resembles the impinging continuous one. Furthermore a mild peak of high radial velocity is still located near the plate where the impinging jet rotates. For φ > 92.30° the axial and radial velocity values decrease.

In Fig. 5.82 the phase-average mean-squared axial and radial turbulent velocity component, for St equal to 0.025 at H/D equal to 6, are depicted. At φ = 18.46° the first values, different from zero, are observable. As usual, the high turbulent values are located near the vortex core and along the all shear layer (axial turbulence) or a part of it (radial turbulence). At φ = 36.92° the values are increasing near the vortex ring core while the shear layer is wider and more extended.

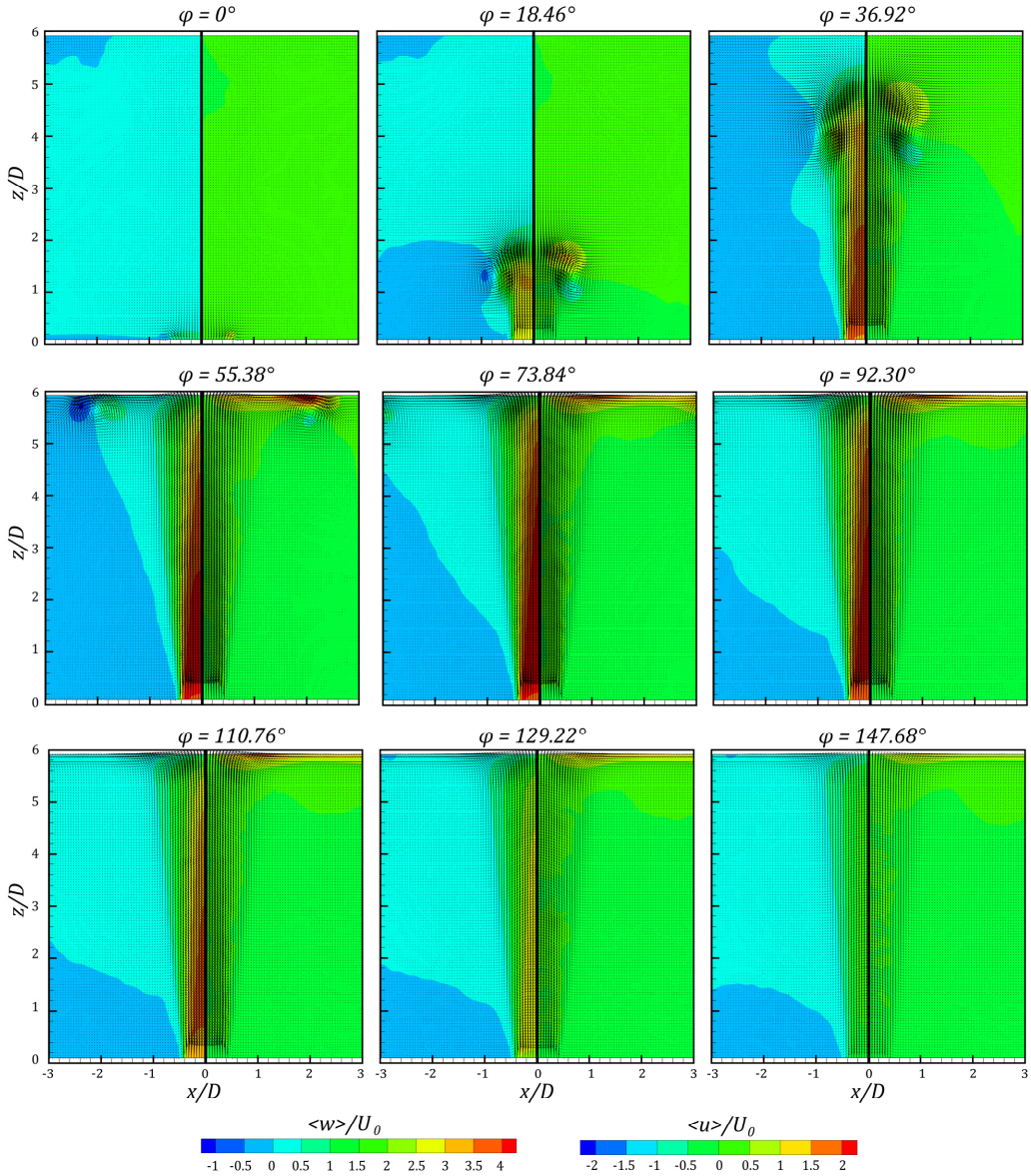

Fig. 5.81 Phase-average axial (left) and radial (right) velocity maps at H/D equal to 6 for Sr=0.025

It has to be highlighted that the axial turbulent velocity component shows high values also on the front boundary of the vortex ring but not in its centre, differently from the radial component. At φ = 55.38° the peak of axial turbulence is always near the vortex ring while the radial one is near the plate, where the counter rotating vortex ring should be located. Moreover the shear layer, characterized by high turbulent values, arrives until the impinging plate.

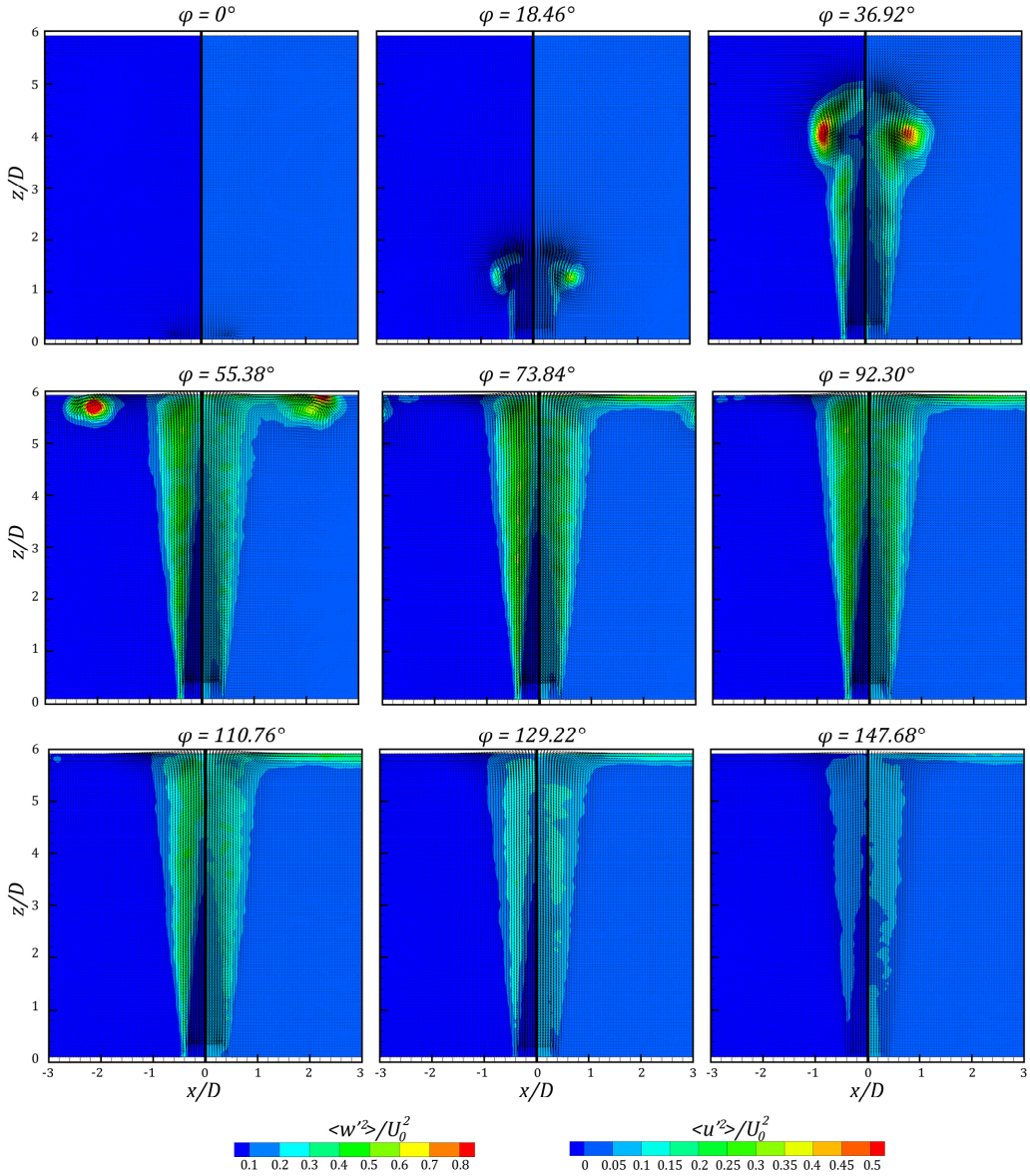

Fig. 5.82 Phase-average mean-squared axial (left) and radial (right) turbulent velocity maps at H/D equal to 6 for Sr=0.025

At φ = 73.84° the vortex ring is out of measurement zone while the high turbulent values are located along the shear layer and, only for the radial component, near the impinging plate. It has to be point out that from φ = 55.38° to φ = 92.30° the high turbulent values of the shear layer arrive on the impinging plate and the two shear layers merge on the jet axis far from the orifice plate. Such a triangular region is characterized by

zero axial turbulence and very low radial one. For φ > 92.30° these values start decreasing.

In Fig. 5.83 the phase-average turbulent Reynolds stress maps, for *St* equal to 0.025 at *H/D* equal to 6, are shown. The first no zero values are observed at φ = 18.46° near the vortex ring. At φ = 36.92° the high values are also along the shear layer.

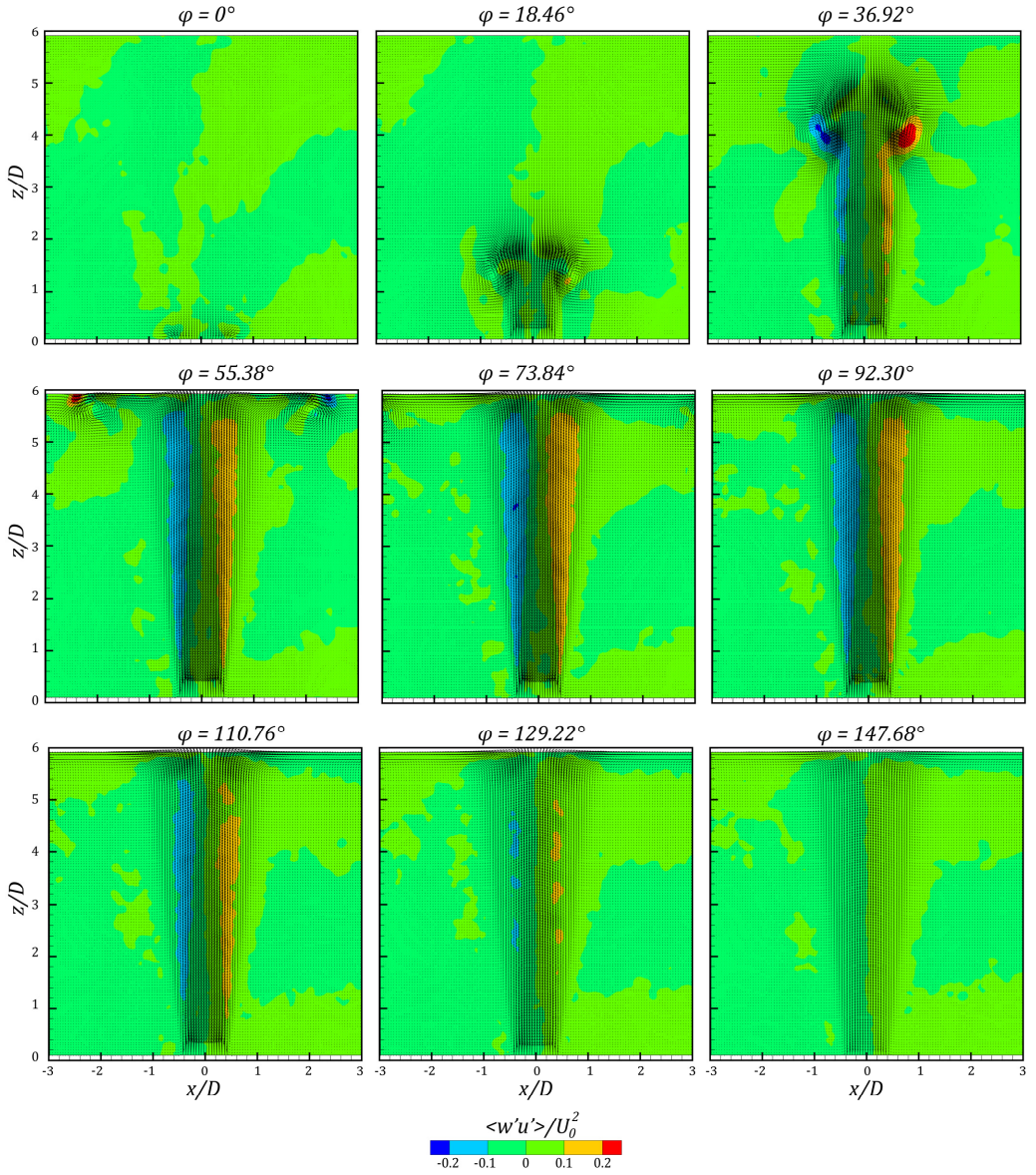

Fig. 5.83 Phase-average turbulent Reynolds stress maps at *H/D* equal to 6 for *Sr*=0.025

At φ = 55.38° the peak is detectable near the plate, ahead of the vortex ring, where the counter rotating vortex should be placed. From φ = 73.84° to φ = 92.30° the field is featured by high values along only the shear layer. For φ > 92.30° the values decrease.

In Fig. 5.84 the phase-average axial and radial velocity maps, for *St* equal to 0.1 at *H/D* equal to 6, are shown.

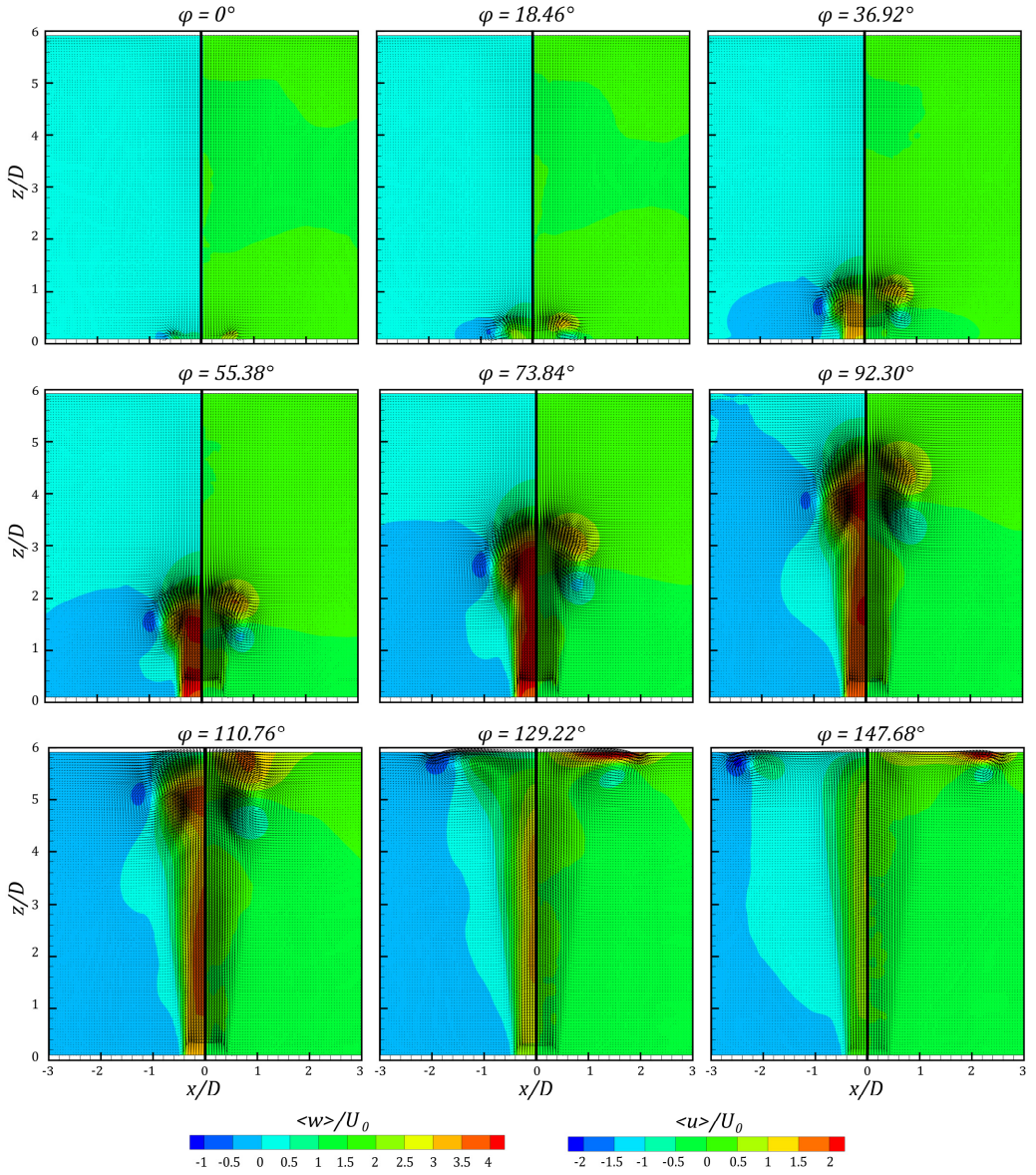

Fig. 5.84 Phase-average axial (left) and radial (right) velocity maps at *H/D* equal to 6 for *Sr*=0.1

At φ = 0° the synthetic jet start coming out and at φ = 18.46° the vortex ring is fully formed. From φ = 36.92° to φ = 92.30° the vortex ring convects downstream. During this period of the cycle the maximum of the axial velocity can be detected in the vortex ring centre. At φ = 92.30° the axial velocity values start slightly decreasing. For this reasons, differently from the lowest Strouhal number case (Fig. 5.81), the difference between the axial velocity of the vortex ring and the following column of fluid is not observable. Indeed the vortex ring starts decelerating for the impinging plate presence (as in the previous case – Fig. 5.81) but also the axial velocity of the following column of fluid decreases because the decelerating part of the ejection phase begins. Then, at φ = 110.76°, when the synthetic jet starts impinging, the axial values are definitely decreasing.

The radial component, at this phase, starts increasing near the plate. At φ = 129.22° high values of the radial component can be detected near the wall at a radial location where the vortex ring is placed. Then (φ = 147.68°), when the axial velocity is still decreasing, the high radial velocity region is still moving with the sweeping vortex ring.

The next phase is not reported because the vortex ring is out of the measurement zone and no relevant features are present in the field (because the ejection cycle is almost finished).

In Fig. 5.85 the phase-average mean-squared axial and radial turbulent velocity maps, for St equal to 0.1 at H/D equal to 6, are shown. During the formation and convection of the vortex ring (0° ≤ φ ≤ 92.30°) the high values of the turbulence are located near the vortex ring and along the shear layer. Furthermore, as in the previous case, high values of axial turbulence can be observed on the front boundary of the vortex ring but not in its centre, differently from the radial one. In this configuration, the region characterized by zero axial turbulence and very low radial one extends, in the axial direction, lower than the previous case. At φ = 110.76° the synthetic jet is impinging and the region of high turbulent values increases for both component. Then (φ = 129.22°) the high value of axial turbulence is still located near the vortex ring while the radial one shows high values near the vortex ring and also in the region, near the impinging plate, where the counter rotating vortex should be. In this phase the shear layer, with its high turbulent values, has not arrived near the impinging plate yet and the synthetic jet starts decelerating. As matter of fact it is possible to see that near the orifice plate, along the orifice edge, the turbulent values start decreasing. At φ = 147.68° the high turbulent values are still

detected moving with the sweeping vortex ring while the shear layer, that has just touched the impinging plate, shows drastically decreased values.

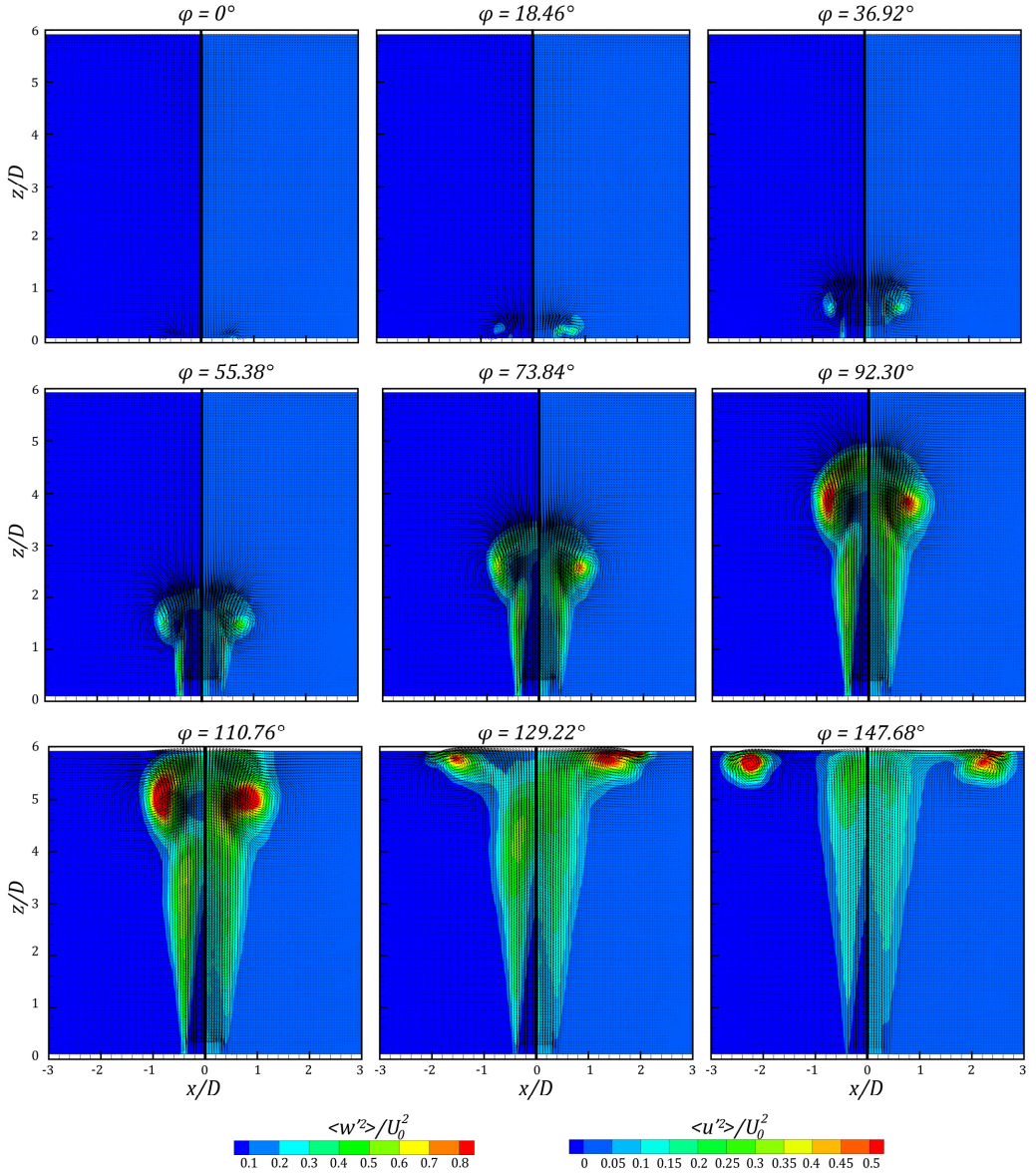

Fig. 5.85 Phase-average mean-squared axial (left) and radial (right) turbulent velocity maps at H/D equal to 6 for Sr=0.1

In Fig. 5.86 the phase-average Reynolds stress, for St equal to 0.1 at H/D equal to 6, are depicted. The Reynolds stress values are equal to zero until φ = 36.92°. At φ = 55.38°

values different from zero are observed along the shear layer and near the vortex ring core.

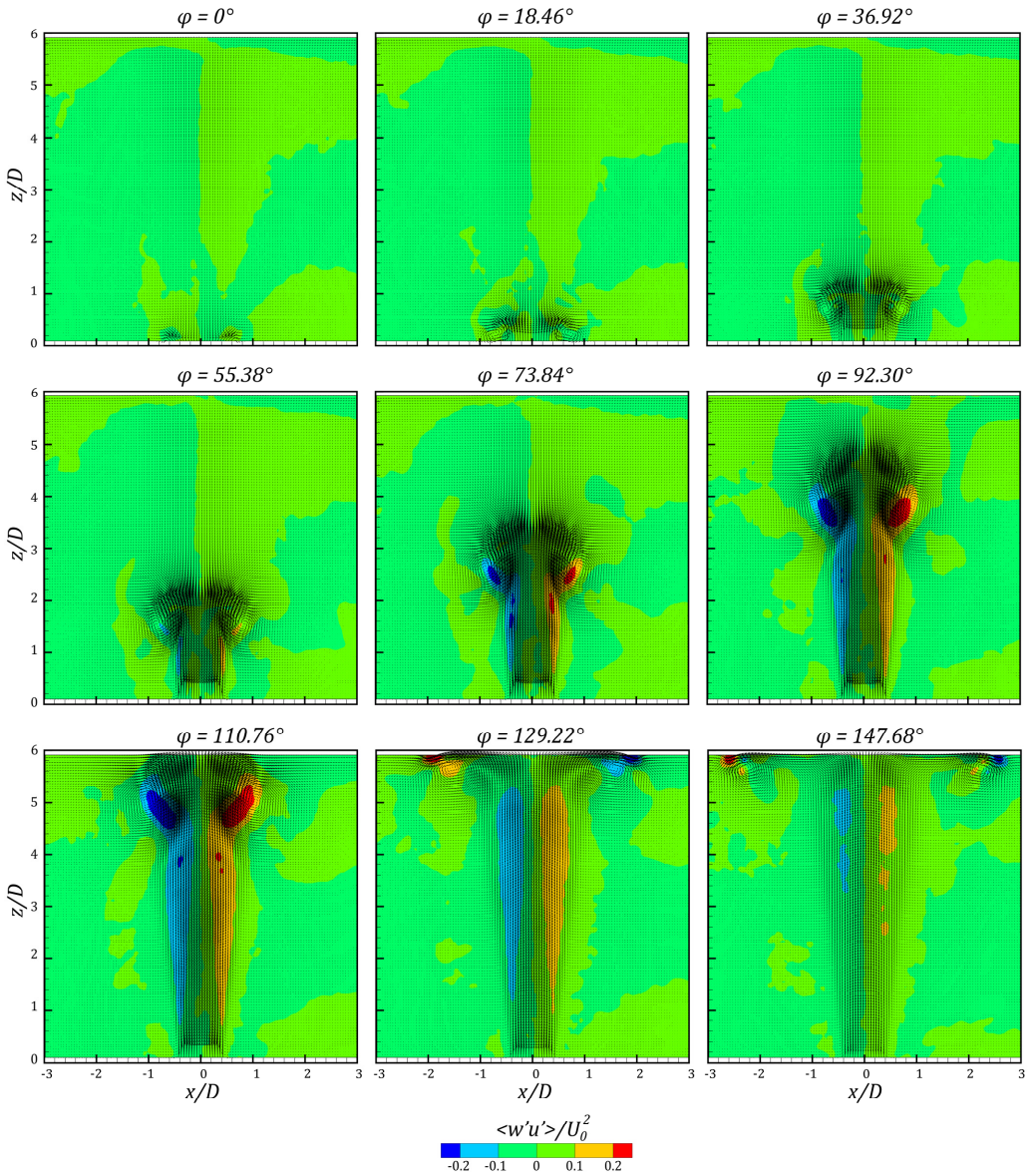

Fig. 5.86 Phase-average turbulent Reynolds stress maps at H/D equal to 6 for Sr=0.1

As φ increases (until φ = 110.76°) the Reynolds stress increases near the vortex ring core. At φ = 129.22° high values of Reynolds stress are visible along the shear layer and, above all, near the impinging plate. Indeed a maximum can be detected near the impinging plate, ahead of the vortex ring, where the counter rotating should be arisen. In this phase

the values along the shear layer start decreasing. At φ = 147.68° the high value near the vortex ring is still visible differently from the ones along the shear layer that are disappeared.

In Fig. 5.87 the vortex ring trajectory (in the last diameter upstream the impinging plate) for the three different Strouhal numbers at any orifice-to-plate distances are shown. The location of the vortex ring centre has been detected by using the maximum value attains by the Q-criterion (as defined in Jeong and Hussain, 1995) applied to the velocity maps for each phase. For *H/D* equal to 2 it is possible to highlight that the trajectories start from the same point (*x/D* equal to about 0.7) but then (at higher axial position) the highest Strouhal number trajectory shows a wider path. For *x/D* between 1.5 and 2 the highest Strouhal number vortex ring path shows the closest position to the plate. Then the three curves seem to collapse. The same behaviour can be observed at *H/D* equal to 4. The unique difference is that for *x/D* higher than 2 the difference between the vortex ring location is still present. Indeed it is possible to detect that higher is the Strouhal number, closer to the impinging plate is the vortex ring position. At *H/D* equal to 6 the curves at *Sr* equal to 0.05 and 0.1 collapse from *x/D* equal to 1.5 up to 2, then the same behaviour, previously described, can be detected.

In Fig. 5.88 the saddle point behaviour for the three different Strouhal number values at *H/D* equal to 2 (for φ = 295.38°) is shown. It is whore nothing that the distance of the saddle point form the orifice exit increases as the Strouhal number decreases. This is related to the half piston stroke (l_p) because higher is l_p (lower is the Strouhal number) higher is the volume of fluid which is injected in and drawn from the ambient. Hence, during the suction phase the saddle point moves towards higher axial position to let the higher requested volume to enter inside the device. Such a behaviour is more evident in this configuration (than in a nozzle configuration) because the ambient is constrained by two plate (the impinging and the orifice ones) so the fluid can not be drawn from the upstream space (as occurs in a nozzle configuration, see Fig. 5.38).

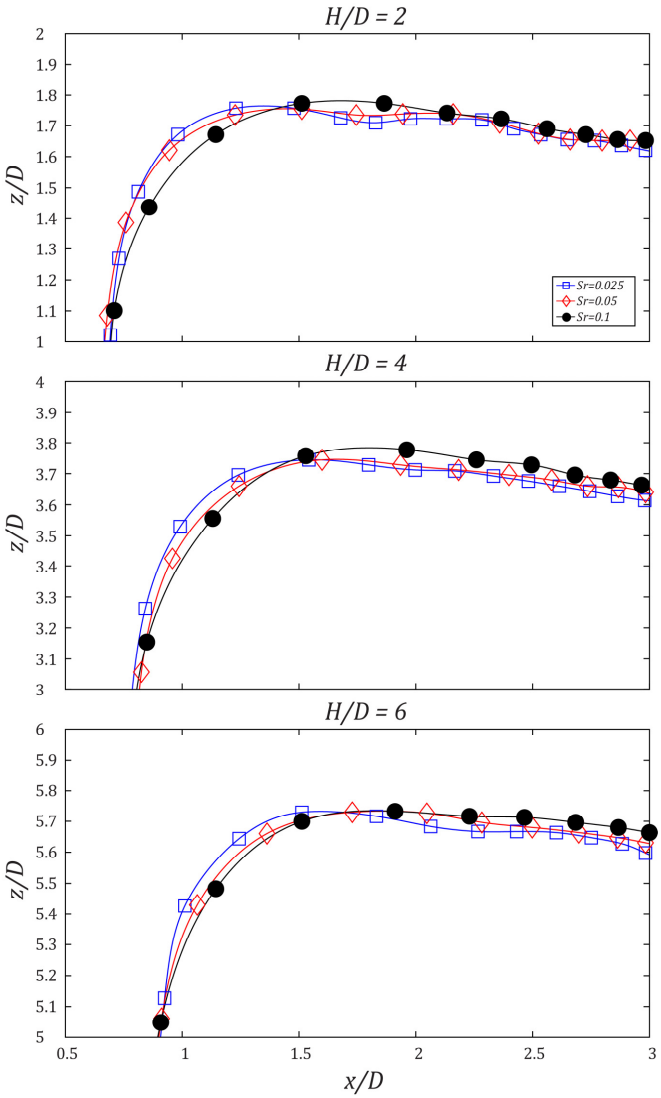

Fig. 5.87 Vortex ring trajectory for all the configurations

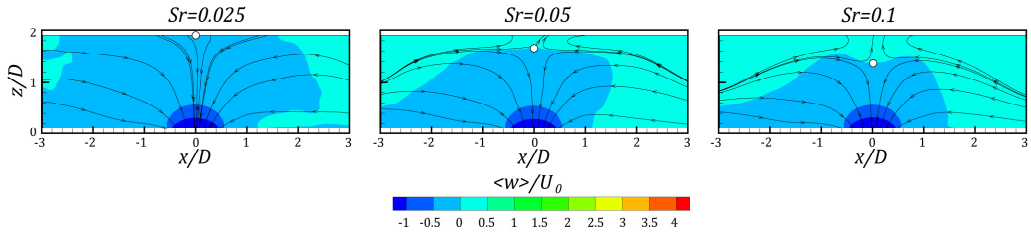

Fig. 5.88 Saddle point location for the three different values of Strouhal number at H/D equal to 2 for φ = 295.38°

Chapter 6

Conclusions

The present study has experimentally investigated the behaviour of a twin synthetic jet compared to a single synthetic jet. Firstly this device has been designed and characterized. The feature of the device is the possibility to vary the jet-axes-distance. This parameter has been varied to understand how it can influence the flow field and the heat transfer performance.

First of all the characterization of the free flow field, generated by the device, has been undertaken. The jet-axes-distances of 1.1 (side-by-side condition), 3 and 5 diameters have been tested. The results have been compared to the free flow field of a single synthetic jet in the same operating condition.

The side-by-side condition has led to a higher value of the time-average centreline axial velocity and turbulent kinetic energy than the single classical configuration. The other two cases (jet-axes-distances equal to 3 and 5) have shown a behaviour similar to the single case. Moreover a potential core-like region of low turbulence has been defined and the evolution of the synthetic jet flow field has been described through the phase-average measurements.

Seen these results, the investigation of the impinging flow field of both twin and single synthetic jet has been carried out. The study has been performed only for the jet-axes-distances of 1.1 and 3. As obtained for the free configuration, the turbulence level and the axial velocity for the side-by-side case are definitely higher than the single case. Moreover the jet-axes-distance equal to 3 configuration, again, resembles the single configuration behaviour. For the first time a deeply investigation on the impinging flow field of a classical single synthetic jet has been performed providing a careful insight on its behaviour. All the mean velocities and their statistics have been quantified and characterized. Moreover the time-average and phase-average behaviours of such quantities have been discussed. Other differences have been found during the suction phase. The single synthetic jet, operating at fixed Strouhal and Reynolds numbers (i.e 0.024 and 5100) has a saddle point that touches the impinging plate differently from the twin configuration. Indeed in this latter case the interaction between the two 180° phase

shift synthetic jets causes a generation of two saddle points which do not touch the impinging plate. This is a relevant observation for a device which is supposed to be used as an electronic cooling system.

Under these results the heat transfer behaviour of this device, always compared to the single case, has been evaluated. The twin synthetic jet device (in its side-by-side configuration) has shown a heat transfer enhancement for all the nozzle-to-plate distances. Its heat transfer rate has been compared to the single one. The time-average heat transfer behaviour of the single and twin synthetic jets has been explained through the results obtained in the impinging flow field study. A strong correlation between the axial velocity components and the heat transfer distribution has been found. Some aspects of the heat transfer behaviour (as the inner and outer region shaped of heat transfer maxima) have been explained through the potential core-like region and the vortex ring behaviour near the plate. The evolution of the heat transfer over the impinging plate has been described through the phase-average measurements.

Finally a fundamental study on the influence of the Strouhal number on the impinging synthetic jet flow field at high Reynolds number has been carried out. Any sensitive differences have been detected between low (5100) and high (16000) Reynolds number for a similar Strouhal number (0.024 for the low case and 0.025 for the high case). Differently the Strouhal number deeply affects the flow field of a single synthetic jet. It influences the jet centreline velocity (higher for lower *Sr*). the jet width (higher for greater *Sr* number) and also the vortex ring trajectory (wider and closer to the plate, at higher radial position, for higher *Sr* number). Moreover the extension of a region, featured by low turbulence, decreases as the Strouhal number increases because at high Strouhal number the influence of the vortex ring is greater. The evolution of the all velocity components (mean and statistics) have been described through the phase-average measurements. In this study it has been pointed out that the turbulence is located, above all, in the vortex ring core and along the shear layer. Such shear layer has a lower contribution than the vortex ring as the Strouhal number increases. Furthermore an important consideration has been drawn for the suction phase. The saddle point is located farther from the plate as the Strouhal number decreases. This result is important for the choice of an operating condition in order to avoid the injection of the hot air of the impinging plate which can cause a decrease of the device heat transfer performance.

Chapter 7

Future Works

The results obtained by this research have led to a better knowledge about the behaviour of a single and twin synthetic jet device. These results on the impinging flow field are among the few data sets, which show and try to explain the fluid dynamic behaviour of an impinging synthetic jet.

Nevertheless, many other aspects of the synthetic jets in the heat transfer, impinging fluid dynamic and acoustic field are still not very clear. Considering these results and the obtained conclusions several future works, on single and twin synthetic jets, should be addressed:

- a fundamental study on the impinging single synthetic jet to deeply understand how the Strouhal number can affect (through its impinging flow field) the heat transfer behaviour in order to optimize the electronic cooling performance;
- a comparison between the 180° phase shift twin synthetic jets and a 0°shift phase twin synthetic jets in order to finally understand if this device can be defined as a definite improvement in the heat transfer field;
- an acoustic study of this device to quantify the actual noise reduction;
- try to combine synthetic jets with passive method for heat transfer enhancement.

References

- Abramovich G.N., 1963, *The Theory of Turbulent Jets*, The M.I.T. Press, Cambridge, MA.
- Adrian R.J., 1991, *Particle-imaging techniques for experimental fluid mechanics*, Ann. Rev. Fluid Mech., 23, 261–304
- Allen M.G., Glezer A., 1995, *Jet vectoring using zero mass flux control jets*, AFOSR contractor and grantee meeting on turbulence and internal flows
- Alster M., 1972, *Improved Calculation of Resonant Frequencies of Helmholtz Resonators,* J. Sound Vib., 24, 63-85.
- Arik M., Icoz T., 2012, *Predicting heat transfer from unsteady synthetic jets*, J. Heat Transfer, 134, 1-8.
- Astarita T., 2006, *Analysis of interpolation schemes for image deformation methods in PIV: effect of noise on the accuracy and spatial resolution*, Exp. Fluids, 40, 977-987.
- Astarita T., 2007, *Analysis of weighting windows for image deformation methods in PIV*. Exp. Fluids, 43, 859-872.
- Astarita T., 2008, *Analysis of velocity interpolation schemes for image deformation methods in PIV*, Exp. Fluids, 45, 257-266.
- Astarita T., Cardone G., 2005, *Analysis of interpolation schemes for image deformation methods in PIV*, Exp. Fluids, 38, 233-243.
- Astarita T., Carlomagno G. M., 2013, *Infrared thermography for thermo-fluid-dynamics*, Springer
- Behera R.C., Dutta P., Srinivasan K., 2007, *Numerical study of interrupted impinging jets for cooling of electronics*, IEEE T. Compon. Pack. T, 30(2), 275-284.
- Beratlis N., Smith M.K,. 2003, *Optimization of synthetic jet cooling for microelectronics applications [VCSEL array example],*. P IEEE Semicond. Ther., 9th IEEE, 66-73.
- Bhapkar U.S., Srivastava A., Agrawal A., 2014, *Acoustic and heat transfer characteristics of an impinging elliptical synthetic jet generated by acoustic actuator*, Int. J. Heat Mass Tran., 79, 12-23.

- Bremhorst K., Hollis P., 1990, *Velocity field of an axisymmetric pulsed, subsonic air jet*, AIAA J., 28, 2043-2049.
- Cardone G., 2007, *IR heat transfer measurements in hypersonic plasma flows*, QIRT J., 4, 233-251.
- Carlomagno G.M., Cardone G., 2010, *Infrared thermography for convective heat transfer measurements*, Exp. Fluids, 49, 1187-1218.
- Carlomagno G.M., de Luca L., 1989, *Infrared thermography in heat transfer*, In: Yang W.J., editor, Handbook of flow visualization, London, Hemisphere Publishing Corporation, Chapter 32, 531-553.
- Carlomagno G.M., Discetti S., Astarita T., 2011, *Experimental assessment of a new heat flux sensor for measuring convective heat transfer coefficients*, QIRT J., 8(1), 37-49.
- Carlomagno G.M., Ianiro A., 2014, *Thermo-fluid-dynamics of submerged jets impinging at short nozzle-to-plate distance: A review*, Exp. Therm. Fluid Sci,, 58, 15-35.
- Cater J. E., Soria J., 2002,. *The evolution of round zero-net-mass-flux jets*, J. Fluid Mech., 472, 167-200.
- Chanaud R.C., 1994, *Effects of Geometry on the Resonance Frequency of Helmholtz Resonators,* J. Sound Vib., 178, 337-348.
- Chanaud R.C., 1997, *Effects of Geometry on the Resonance Frequency of Helmholtz Resonators, part II*, J. Sound Vib., 204, 829-834.
- Chandratilleke T.T., Jagannatha D., Narayanaswamy R., 2009, *Performance analysis of a synthetic jet-microchannel hybrid heat sink for electronic cooling*, In El. Packag. Tech. Conf. 11th IEEE, (630-635).
- Chaudhari M., Puranik B., Agrawal A., 2010a, *Heat transfer characteristics of synthetic jet impingement cooling*, Int. J. Heat Mass Tran., 53, 1057-1069.
- Chaudhari M., Puranik B., Agrawal A., 2010b, *Effect of orifice shape in synthetic jet based impingement cooling*, Exp. Therm. Fluid Sci., 34, 246-256.
- Chaudhari M., Puranik B., Agrawal A., 2011, *Multiple orifice synthetic jet for improvememnt in impingement heat transfer*, Int. J. Heat Mass Tran., 54, 2056-2065.

- Coe D.J., Allen M.G., Trautman M.A., Glezer A., 1994, *Micromachined jets for manipulation of macro flows*, Solid-State Sensor and Actuator Workshop, pp. 243–247.
- Compton D.L., 1972, *Use of an infrared-imaging camera to obtain convective heating distributions*, AIAA J., 10, 1130-2.
- de Luca L., Cardone G., 1991, *Modulation transfer-function cascade model for a sampled IR imaging-system*, App. Opt., 30, 1659-1664.
- Di Cicca G.M., Iuso G., 2007, *On the near field of an axisymmetric synthetic jet,* Fluid Dyn. Res., 39, 673-693.
- Eckart C., 1948, *Vortices and streams caused by sound waves*, Phys. Rev., 73, 68-76.
- Ervas N., Baysal O., 2009, *Micron-level actuators for thermal management of microelectronic devices*, Heat Transfer Eng., 30(1-2), 138-147.
- Gallas Q., Holman R., Nishida T., Carroll B., Sheplak M., Cattafesta L., 2003, *Lumped Element Modeling of Piezoelectric-Driven Synthetic Jet Actuators,* AIAA J., 41, 240-247.
- Gardon R., Akfirat J., 1965, *The role of turbulence in determining the heat-transfer characteristics of impinging jets*, Int. J. Heat Mass Tran., 8 (10), 1261–1272.
- Gartenberg E., Roberts A.S., 1992, *Twenty-five years of aerodynamic research with infrared imaging*, J. Aircraft, 29, 161-171.
- Gharib M., Rambod E., Shariff K., 1998, *A universal time scale for vortex ring formation*, J. Fluid Mech., 360, 121–140.
- Glezer A., Amitay M., 2002, *Synthetic Jets*, Annu. Rev. Fluid Mech, 34, 503-529.
- Golobic I., Petkovsek J., Kenning D.B.R., 2012, *Bubble growth and horizontal coalescence in saturated pool boiling on a titanium foil, investigated by high-speed IR thermography*, Int. J. Heat Mass Tran., 55(4), 1385-1402.
- Gomes L.D., Crowther W.J., Wood N.J., 2006, *Towards a practical piezoceramic diaphragm based synthetic jet actuator for high subsonic applications-effect of chamber and orifice depth on actuator peak velocity*, 3rd AIAA Flow Control Conference, 5(8), 267-283.
- Greco C.S., Ianiro A., Astarita T., Cardone G., 2013, *On the near field of single and twin circular synthetic air jets*, Int. J. Heat Fluid Fl., 44, 41-55.

- Greco C.S., Ianiro A., Cardone G., 2014, *Time and phase average heat transfer in single and twin circular synthetic impinging air jets*, Int. J. Heat Mass Tran., 73, 776-788.
- Gutmark E., Yassour Y., Wolfshtein M., 1982, *Acoustic enhancement of heat transfer in plane channels*, Proceedings of Seventh International Heat Transfer Conference, 441–445, Munich, Germany.
- Hadžiabdić M., Hanjalić K., 2008, *Vortical structures and heat transfer in a round impinging jet*, J. Fluid Mech, 596, 221-260.
- Helmholtz H., 1860, *Theorie der Luftschwingungen in röhren mit offenen enden*. Crelle Jl. Math., 57, 1-72.
- Holman R., Utturkar Y., Mittal R., Smith B.L., Cattafesta L., 2005, *Formation criterion for synthetic jets*, AIAA J., 43(10), 2110-2116.
- Hoogendorn C. J., 1977, *The effect of turbulence on heat transfer at a stagnation point*, Int. J. Heat Mass Tran. 20, 1333–1338.
- Hussain A.K.M.F., Reynolds W.C., 1970, *The mechanics of an organized wave in turbulent shear flow*, J. Fluid Mech., 41(02), 241-258.
- Imbriale M., Panelli M, Cardone G., 2012, *Heat transfer enhancement of natural convection with ribs*, QIRT J., 9(1), 55-67.
- Ingard U., Labate S., 1950, *Acoustic effects and nonlinear impedance of orifices*, J. Acoust. Soc. Am., 22, 211-218.
- Jagannatha D., Narayanaswamy R., Chandratilleke T.T., 2009, *Analysis of a synthetic jet-based electronic cooling module*, Numer. Heat Tr. A-App., 56(3), 211-229.
- Jambunathan K., Lai E., Mossand M.A., Button B.L., 1992, *A review of heat transfer data for single circular jet impingement*, Int. J. Heat Fluid Fl., 13, 106-115.
- James R.D., Jacobs J.W., Glezer A., 1996, *A round turbulent jet produced by an oscillating diaphragm*, Phys. Fluids, 8(9), p. 2484-2495.
- Jeong J., Hussain F., 1995, On the identification of a vortex, J. Fluid Mech., 285, 69-94.
- Kitsios V., Cordier L., Bonnet J. P., Ooi A., Soria J., 2010, *Development of a nonlinear eddy-viscosity closure for the triple-decomposition stability analysis of a turbulent channel*, J. Fluid Mech., 664, 74-107.

- Knowles K., Myszko, M., 1998, *Turbulence measurements in radial wall-jets,* Exp. Therm Fluid Sci., 17(1), 71-78.
- Kral L., Donovan J.F., Cain A.B., Cary A.W., 1997, *Numerical simulation of synthetic jet actuators*, In: Proceeding of the 4th AIAA Shear Flow Control Conference, AIAA p., 97, 1824.
- Lasance C.J.M., Aarts R.M., 2008, *Synthetic Jet Cooling Part I:Overview of Heat Transfer and Acoustic*, 24th Annual IEEE Semiconductor Thermal Measurement and Management Symposium, 20-35. IEEE.
- Lasance C.J.M., Aarts R.M., Ouweltjes O., 2008, *Synthetic jet cooling part II: experimental results of an acoustic dipole cooler*, 24th Annual IEEE Semiconductor Thermal Measurement and Management Symposium, 26-31. IEEE.
- Laxmikant M.D., Chaudhari M.B., 2015, *Heat transfer and acoustic study of impinging synthetic jet using diamond and oval shape orifice,* Int. J. Therm. Sci., 89 (2015), 100-109.
- Lebedeva I.V., 1980, *Experimental study of acoustic streaming in the vicinity of orifices,* Sov. Phys. Acoust., 26, 331-333.
- Lighthill S.J., 1978, *Acoustic streaming*, J. Sound Vib, 61, 391-418.
- Livingood J. N. B., Hrycak P., 1973, *Impingement Heat Transfer from Turbulent Air Stream Jets to Flat Plates*-A Literature Survey, NASA TM X-2778.
- Luo Z.B., Deng X., Wang L., Xia Z.X., 2011, *Experimental technique based on delay phase angle and PIV measurements of a dual synthetic jets actuator*, Proceedings of the 2011 Symposium on Piezoelectricity, Acoustic Waves and Device Applications, 1-5, Shenzhen, China.
- Luo Z.B., Xia Z.X., Bing L., 2006, *New generation of synthetic jet actuators*, AIAA J., 44 (10), 2418-2419.
- Mahalingam R., Glezer A., 2005, *Design and thermal characteristic of a synthetic jet ejector heat sink*, J. Electron. Packaging, 127, 172-177.
- Mallinson S.G., Hong G., Reizes J.A., 1999, *Some characteristics of synthetic jets*, In the Proceeding of the 30th AIAA Fluid Dynamics Conference, AIAA p., 99, 365.
- Martin H., 1977, *Heat and mass transfer between impinging gas jets and solid surfaces*, Adv. Heat Tran., 13, 1-60.
- McAdams W.H., 1954, *Heat Transmission*, 3rd Ed. McGraw-Hill, New York, NY

- McGuinn A., Farrelly R., Persoons T., Murray D.B., 2013, *Flow regime characterization of an impinging axisymmetric synthetic jet*, Exp. Therm. Fluid Sci., 47, 241–251.
- Medinkov E.P., Novitskii B.G., 1975, *Experimental study of intense acoustic streaming*, Sov. Phys. Acoust., 21, 152.
- Meola C., de Luca L., Carlomagno G.M., 1996, *Influence of shear layer dynamics on impingment heat transfer*, Exp. Therm. Fluid Sci., 13(1), 29-37.
- Mi J., Kalt P., Nathan G.J., Wong C.Y., 2007, *PIV measurements of a turbulent jet issuing from round sharp-edged plate*, Exp. Fluids, 42, 625-637.
- Moffat R.J., *Describing the uncertainties in experimental results*, Exp. Therm. Fluid Sci., 1988, 1, 3-17.
- Moore G.E., 1965, *Cramming more components onto integrated circuits*, Proceedings of the IEEE, 86(1), 114-117.
- Narayanan V., Seyed-Yagoobi J., Page, R. H., 2004, *An experimental study of fluid mechanics and heat transfer in an impinging slot jet flow,* Int. J. Heat Mass Tran., 47(8), 1827-1845.
- O'Donovan T.S., 2005, *Fluid flow and heat transfer of an impinging air jet*, Ph.D. Thesis.
- Peake D.J., Bowker A.J., Lockyear S.J., Ellis F.A., 1977, *Non obtrusive detection of transition region using an infrared camera*, AGARD-CP-224
- Persoons T., 2012, *General Reduced-Order Model to Design and Operate Synthetic Jet Actuators*, AIAA J, 50, 916-927.
- Persoons T., McGuinn A., Murray D.B., 2011, *A general correlation for the stagnation point Nusselt number of an axisymmetric impinging synthetic jet*, Int. J. Heat Mass Tran., 54, 3900-3908.
- Persoons T., O'Donovan T.S., Murray D.B., 2009, *Heat transfer in adjacent interacting impinging synthetic jets*, Proceedings of 2009 ASME summer heat transfer conference, 1-8, San Francisco, California.
- Persoons T., O'Donovan T.S., 2007, *A pressure-based estimate of synthetic jet velocity*, Phys. Fluids, 19, 12, art. no. 128104

- Raffel M., Willert C.E., Wereley S.T., Kompenhans J., 2007, *Particle Image Velocimetry, A Practical Guide*, Springer-Verlag, Berlin Heidelberg, second edition edition.
- Rayleigh L., 1883, *Scientific Papers* (Cambridge University Press, Teddington, England), No. 108, p. 239; Phil. Trans. 175, 1.
- Rayleigh L., 1896, *Theory of Sound* (MacMillan Company, Ltd. , London), Vol. II, p. 217.
- Reichardt H., 1942, *Gesetzmiissigkeiten der freien Turbulenz*, VDI Forschungsheft, 414.
- Rohlfs W., Haustein H.D., Garbrecht O., Kneer R., 2012, *Insights into local heat transfer of a submerged impinging jet: Influence of local flow acceleration and vortex-wall interaction*, Int. J. Heat Mass Tran., 55, 7728-7736
- Roux S., Fénot M., Lalizel G., Brizzi L. E., Dorignac E., 2011, *Experimental investigation of the flow and heat transfer of an impinging jet under acoustic excitation*, Int. J. Heat Mass Tran., 54(15), 3277-3290.
- Russell D.A., Titlow J.P., Bemmen Y.J., 1999, *Acoustic monopoles, dipoles, and quadrupoles: An experiment revisited*, Am. J. Phys, 67, 660-664.
- Rylatt D.I., O'Donovan T.S., 2013, *Heat transfer enhancement to a confined impinging synthetic air jet*, Appl. Therm. Eng., 51, 468-475.
- Sargent S. R., Hedlund C. R., Ligrani P. M., 1998, *An infrared thermography imaging system for convective heat transfer measurements in complex flows*, Meas. Sci. Technol., 9, 1974-1981.
- Schetz J. A., Fuhs A. E., 1999, *Fundamentals of Fluid Mechanics*, Wiley.
- Shuster J.M., Smith D.R., 2007, *Experimental study of the formation and scaling of a round synthetic jet*, Phys. Fluids, 19, 045109.
- Siegel R., Howell J.R., 1992, *Thermal Radiation Heat Transfer*, 3rd edn. Hemisphere, Washington.
- Smith B.L., Glezer A., 1998, *The formation end evolution of synthetic jets*, Phys.Fluids, 10(9), 2281-2297.
- Smith B.L., Swift G.W., 2003, *A comparison between synthetic jets and continuous jets*, Exp. Fluids, 34(4), 467-472.

- Soria J., 1996a, *An adaptive cross-correlation digital PIV technique for unsteady flow investigations*, In Proc. 1st Australian Conf. on Laser Diagnostics in Fluid Mechanics and Combustion (ed. A. Masri & D. Honnery), pp. 29-48. University of Sydney, Sydney, NSW, Australia.
- Soria J., 1996b, *An investigation of the near wake of a circular cylinder using a videobased digital cross-correlation particle image velocimetry technique*, Exp. Therm Fluid Sci., 12 (2), 221–233.
- Soria J., 1998, *Multigrid approach to cross-correlation digital PIV and HPIV analysis*, In Proc. 13th Australasian Fluid Mechanics Conf. (ed. M. C. Thomson & K. Hourigan), Monash University, Melbourne, Australia.
- Soria J., Cater J., Kostas J., 1999, *High resolution multigrid cross-correlation digital PIV measurements of a turbulent starting jet using half frame image shift film recording*, Opt. Las. Technol., 31, 3-12.
- Soria J., Parker K., 2005, *Non-intrusive PIV measurements of turbulence – application to a free round jet*, In Proceedings of the Fourth Australian Conference Australian Conference on Laser Diagnostics in Fluid Mechanics and Combustion, University of Adelaide, Adelaide, SA, Australia, pp. 13–20.
- Therani F.B., Karami M., Jahromi M., 2011, *Unsteady flow and heat transfer analysis of an impinging synthetic jet*, Heat Mass Trans., 47(11), 1363-1373.
- Thomann H., Frisk B., 1968, *Measurement of heat transfer with an infrared camera*, Int. J Heat Mass Tran., 11, 819–826.
- Valiorgue P., Persoons T., McGuinn A., Murray D.B., 2009, *Heat transfer mechanisms in an impinging synthetic jet for small jet-to-surface spacing*, Exp. Therm. Fluid Sci., 33, 597-603.
- van de Hulst H.C, 1957, *Light scattering by small particles,* John Wiley & Sons, Inc., New York (republished 1981 by Dover Publications, New York).
- Violato D., Ianiro A., Cardone G., Scarano F., 2011, *Investigation on Circular and Chevron Impinging Jets by IR Thermography and Time-Resolved Tomographic PIV*, Proceedings ASME-JSME-KSME Joint Fluids Engineering Conference 2011 (AJK2011-FED), July 24 - 29. Hamamatsu, Japan. 12 pp.
- Viskanta R., 1993, *Heat Transfer to Impinging Isothermal Gas and Flames Jets*, Exp. Therm. Fluid Sci. 6, 111–134.

- Wang Y., Yuan, G., Yoon Y.K., Allen, M.G., Bidstrup S.A., 2006, *Large eddy simulation (LES) for synthetic jet thermal management*, Int. J. Heat Mass Tran., 49(13), 2173-2179.
- Webster D.R., Longmire E.K., 1998, *Vortex rings from cylinders with inclined exits*, Phys. Fluids, 10, 400-416.
- Westerweel J., 1994, *Efficient detection of spurious vectors in particle image velocimetry data*, Exp. Fluids, 16, 236–247

List of Publications

Journal Papers

- Avallone F., Greco C.S., Ekelschot D., 2013, *Image resection and heat transfer measurements in hypersonic flows*, QIRT J., 10(2), 188-206. doi:10.1080/17686733.2013.800697.
- Greco C.S., Ianiro A., Astarita T., Cardone G., 2013, *On the near field of single and twin circular synthetic air jets*, Int. J. Heat Fluid Flow, 44, 41-52. doi:10.1016/j.ijheatfluidflow.2013.03.018.
- Greco C.S., Ianiro A., Cardone G., 2014, *Time and phase-average heat transfer in single and twin circular synthetic impinging air jets*, Int. J. Heat Mass Tran., 73, 776-788. doi:10.1016/j.ijheatfluidflow.2013.03.018.
- Girfoglio M., Greco C.S., de Luca L., *Modelling of efficiency of synthetic jet actuators*, Accepted with minor revisions by Sensor Actuat. A-Phys.
- Avallone F., Greco C.S., Schrijer F.F.J., Cardone G., *A low computational cost inverse heat transfer technique for convective heat transfer measurements in hypersonic flows*, Accepted by Exp. Fluids.

Conference Proceedings

- Avallone F., Greco C.S., 2012, *2D Inverse heat transfer measurements by IR Thermography in hypersonic flows*, 11th PEGASUS-AIAA Student Conference, April 11-13, Poitiers (France).
  https://www.pegasus-europe.org/AIAA_Pegasus/Papers/Avallone_uniNA.pdf
- Avallone F., Greco C.S., Ekelschot D., 2012, *2D Inverse heat transfer measurements by IR Thermography in hypersonic flows*, 11th Quantitative InfraRed Thermography, June 11-14, Naples (Italy), QIRT 2012-367.
  http://qirt.gel.ulaval.ca/archives/qirt2012/papers/QIRT-2012-367.pdf

- Greco C.S., Ianiro A., Imbriale M., Astariata T., Cardone G., 2012, *Twin synthetic jets, 15th International Symposium on Flow Visualization*, June 25-28, Minsk (Belarus), 11 pp, ISBN 9789856456759.
  http://www.itmo.by/pdf/isfv/ISFV15-084.pdf
- Greco C.S., Cardone G., 2013, *Phase-average heat transfer measurements in twin circular synthetic impinging air jets*, Italian Association of Aeronautics and Astronautics XXII Conference, September 9-12, Naples (Italy).
- Greco C.S., Ianiro A., Cardone G., 2013, *Average and phase resolved heat transfer in single and twin circular synthetic impinging air jets*, Convective heat transfer enhancement – Eurotherm Seminar N°96, September 17-18, Brussels (Belgium), ISBN 9782875160591
  https://events.vki.ac.be/eurotherm2013/modules/request.php?module=oc_proceedings&action=summary.php&a=Accept&id=17
- Greco C.S., Ianiro A., Cardone G., 2014, *On the heat transfer behavior of impinging synthetic air jets*, 12th Quantitative InfraRed Thermography, July 7-11, Bordeaux (France).
  http://qirt.gel.ulaval.ca/archives/qirt2014/QIRT%202014%20Papers/QIRT-2014-144.pdf
- Paolillo G., Greco C.S., Cardone G., 2015, *Investigation on the flow field of a monopole, dipole and quadrupole synthetic jets*, 10th Pacific Symposium on Flow Visualization and Image Processing, June 15-18, Naples (Italy), Accepted.
- Greco C.S., Cardone G., Soria J., 2015, *Flow field characteristic of high Reynolds impinging synthetic jets*, 10th Pacific Symposium on Flow Visualization and Image Processing, June 15-18, Naples (Italy), 7-10pp. Accepted.
- Greco C.S., Cardone G., Soria J, 2015, *Investigation on the behaviour of high Reynolds round impinging zero-net-mass-flux jets*, 9th International symposium on the turbulence and shear flow phenomena, 30 June – 3 July, Melbourne (Australia), Accepted.
- Crispo C.M., Greco C.S., Avallone F., Vitale L., Cardone G., 2015, *Stereo PIV measurements on circular and chevron synthetic jet*, 11th International Symposium on Particle Image Velocimetry, September 14-16, Santa Barbara (USA). Submitted abstract .

- Castrillo G., Greco C.S., Crispo M.C., Astarita T., Cardone G., 2015; *Impinging single and twin circular synthetic jets flow field*, 11th International Symposium on Particle Image Velocimetry, September 14-16, Santa Barbara (USA). Submitted abstract.